POLITECNICO DI MILANO

SCUOLA DI INGEGNERIA INDUSTRIALE E DELL'INFORMAZIONE
CORSO DI LAUREA MAGISTRALE IN INGEGNERIA BIOMEDICA

GLOBAL RESPIRATORY MOTION MODEL BASED ON 4D CT AND 2D CINE-MRI

Relatore: Prof. Marco Riboldi
Correlatore: Prof. Paul Keall
Dott. Ing. Chiara Paganelli

Tesi di Laurea Magistrale di:
Silvia Albertini matr. 822638
Francesca Iudicello matr. 837621

Anno Accademico 2015-2016

Index

Figure index

Table index

List of abbreviations

3D CRT: 3-Dimensional Conformal Radiotherapy

4D CBCT: 4-Dimensional Cone Beam Computed Tomography

4D CT: 4-Dimensional Computed Tomography

ABC: Active Breath hold

AP: Anterior-Posterior direction

BEV: Beam's Eye View

CBCT: Cone-Beam CT

CC: Correlation Coefficient

CCCS: Collapsed Cone Convolution Superposition

COM: Centre Of Mass

CT: Computed Tomography

CTV: Clinical Target Volume

DAO: Direct Aperture Optimization

DIR: Deformable Image Registration

DMPO: Direct Machine Parameter Optimization

DVF: Deformation Vector Field

DVF^{-1}: inverted Deformation Vector Field

DVH: Dose-Volume Histograms

EBRT: External Beam Radiotherapy

EPID: Electronic Portal Image Devices

FBCT: Fan-Beam CT

FFD: Free Form Deformation

FOV: Field Of View

GTV: Gross Tumour Volume

IGRT: Image-Guided Radiation Therapy

IMRT: Intensity Modulated Radiation Therapy

kV: kilo-Voltage

Linac: linear accelerator

MeV: Mega elettronvolt

MI: Mutual Information

MidP: Mid Position

MLC: Multileaf Collimator

MRI: Magnetic Resonance Imaging

MSE: Mean Square Error

MTB: Mean Tumour Boundary

MU: Monitor Unit

MV: Mega-Voltage

NMI: Normalized Mutual Information

NSCLS: Non-Small Cell Lung Cancer

NTCP: Normal Tissue Control Probability

OAR: Organ At Rrisk

ODM: Opening Density Matrix

PCA: Principal Component Analysis

PET: Positron Emission Tomography

PTV: Planning Target Volume

RBF: Radial Basis Function

RF: Radiofrequency

RL: Right-Left direction

ROI: Region Of Interest

RPM: Real-time Position Management

RT: Radiotherapy

RTOG: Radiation Therapy Oncology Group

SAD: Source-Axis Distance

SBRT: Stereotactic Body Radiation Therapy

SI: Superior-Inferior direction

SIFT: Scale Invariant Feature Transform

SQP: Sequential Quadratic Programming

SSD: Source-Skin Distance

TCP: Tumour Control Probability

TERMA: Total Energy Released per unit Mass

TPS: Treatment Planning System

US: Ultrasound

VMAT: Volumetric Modulated Arc Therapy

XCAT: Extended Cardiac-Torso

Summary

Radiotherapy is a medical treatment that uses ionizing radiation to induce damage to the tumour cells in order to reduce and eliminate neoplastic tissues. At the same time, one of its goals is preserving as much as possible the surrounding healthy tissues (OARs, organs at risk). Usually, a radiotherapy treatment, with the aim of a complete removal of the tumour, is known as definitive treatment and consists in the delivery of a specific amount of dose, quantified in Gray [Gy] (e.g. 60 Gy) in different fractions (e.g. 30 fractions), to treat the target and to allow the recovery of irradiated healthy tissue after the radiation damage. The main phases of radiotherapy could be summarised as:

i. planning phase, where a patient-specific model is developed based on the acquired CT, defining target tumour, OARs and dose to be delivered through a treatment planning system (TPS);
ii. treatment phase, when the treatment plan is effectively delivered.

The development of radiotherapy systems has led to the use of techniques which conform the dose given to the tumour. In this context, the intensity modulated radiation therapy (IMRT) technique, in which the intensity of radiation beam is modulated through a multileaf collimator (MLC), has a great relevance. Another important aspect concerning radiotherapy is the variation in shape and location of the target tumour and OARs due to patient positioning and anatomo-pathological processes, also known as organ motion. Organ motion can be divided in inter-fraction (i.e. it occurs between different fractions of the treatment) and intra-fraction motion (i.e. it occurs within the same fraction). Intra-fraction motion due to respiration is a relevant issue causing uncertainties that affects all tumour sites in the thorax and abdomen. In order to account for inter and intra-fraction motions, margins are added to the tumour itself (gross tumour volume, GTV) during the planning phase and hence a larger zone is irradiated. In this contest, the need to improve the localization and targeting of the tumour has paved the way for the image-guided

radiation therapy (IGRT), which consists in the use of imaging techniques to support the whole radiotherapy workflow and includes several strategies for motion quantification and compensation. The standard clinical practice during planning to account for organ motion consists in the acquisition of time-resolved volumes able to describe the patient-specific respiratory cycle, such as the 4D computed tomography (CT), in which a set of CT images are acquired and then retrospectively sorted through the use of an external respiratory signal (i.e. surrogate). Specifically, for the planning phase image registration is a useful tool for the quantification of organ motion that allows to overlay, compare and fuse different images. In particular, scientific interest has been directed towards the development of deformable image registration (DIR) algorithms, which allows to quantify non-rigid displacements through a deformation vector field (DVF). The DIR for time-resolved volumes is typically performed between each respiratory phase of the 4D CT to allow the description of organ motion due to respiration. However, one of the main issues in radiotherapy is the correct transfer of the planning situation in the in-room scenario in terms of correct correspondence in patient positioning and anatomical alignment of internal structures. In addition, inaccuracies caused by respiratory motion could lead to discrepancies between the planned and delivered dose, affecting the success of the treatment. In this perspective, an in-room real-time monitoring is necessary to track directly or indirectly the target position during treatment. In the clinical routine direct methods based on X-ray imaging are available as well as indirect approaches, such as the one based on local motion models, which are able to find a reliable correlation between the motion of the target and a surrogate data acquired during treatment. The surrogate data can be internal (e.g. implanted markers, image-based surrogates) or external (e.g. based on optical system such as the real-time position management system (RPM)). An improvement of local motion models consists in their extension to the global motion models, which represent a milestone for this thesis project. Global motion models allow the description of the whole motion based on the acquired 4D CT images and not just of the local displacement of the tumour, thus providing additional information about OARs. In this case, a relation between the motion field derived by a DIR between each respiratory phase and a reference volume is defined with a pre-treatment surrogate. Then, the motion model is updated on the basis of the real-time surrogate acquired during treatment. Furthermore, the need to reduce the radiation dose from image acquisition during treatment

has motivated the use of magnetic resonance imaging (MRI) as IGRT technology, which represents another milestone for this work. MRI advantages in being a radiation-free imaging technique, providing good soft tissue contrast and allowing the acquisition of fast images has suggested in the last years the integration of MRI with treatment units, in order to develop an in-room MRI-guidance system for real-time tumour tracking. However, the spatial and temporal trade-off limits in achieving volumetric acquisition is still a challenge; therefore, fast 2D orthogonal slices centred in the tumour (cine-MRI) are typically acquired in order to describe internal anatomy during respiratory motion. This limitation in the volumetric acquisition suggests therefore the use of global motion models, which can be updated according to surrogates derived from in-room cine-MRI data.

The aim of this project is therefore the translation of global motion models typically used for X-ray imaging into the MRI-guided scenario, with the aim to quantify both geometric and dosimetric variations between planning and treatment induced by respiratory motion.

Specifically, we choose and test the models developed by Fayad et al. (2012) and Vandemeulebroucke et al. (2009). Fayad's model is based on a principal component analysis (PCA) approach for the model construction, it considers as reference volume the 0% exhale phase and it requires as input the range of amplitude with respect to the reference value. Instead, the model developed by Vandemeulebroucke is constructed by an interpolation of the DVFs, it uses as reference volume a mean position volume (MidP - an intermediate phase between 0% exhale and 50% inhale) and it requires as input both amplitude and phase information computed by the Hilbert transform. Both motion models are trained on a pre-treatment dataset composed by a 4D CT (10 respiratory phases) and then are updated with different surrogates extracted from the 2D orthogonal sagittal/coronal cine-MRI data acquired during treatment (Figure A).

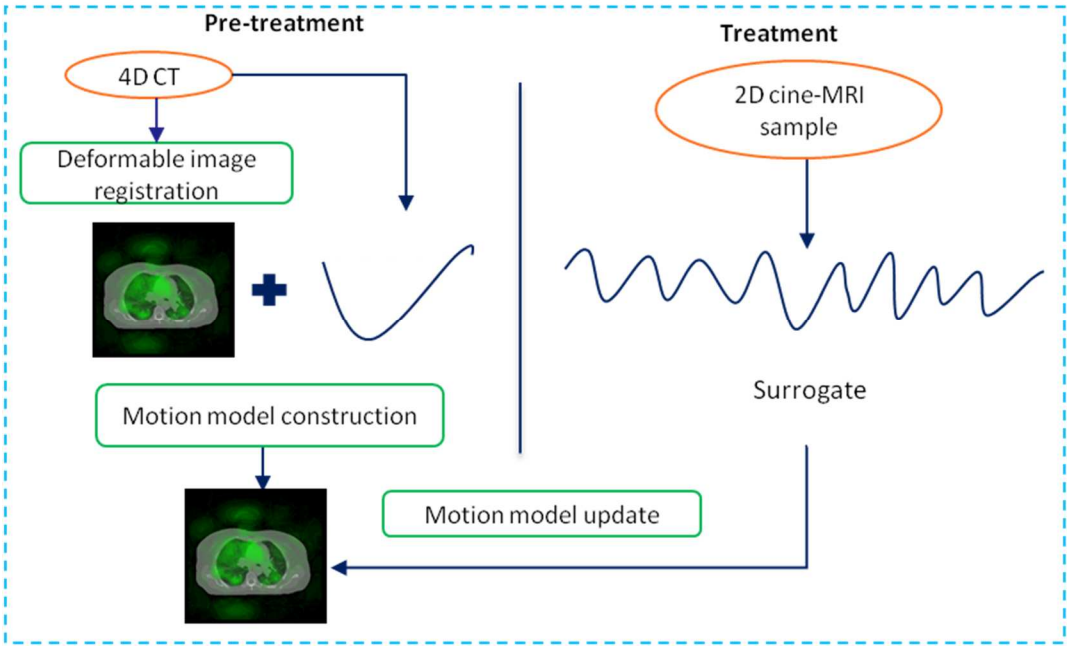

Figure A. Motion model construction: basic steps for the model construction.

The models are tested on a digital CT/MRI phantom and subsequently on two CT/CBCT patients (i.e. patient A, with large tumour in the lower lobe of the right lung, and patient B, with tumour in the upper part of right lung) and a CT/cine-MRI patient (i.e. patient C, with tumour attached to the heart in the left lung). Specifically for CT/CBCT patients, orthogonal slices centred in the tumour are selected within the CBCT data in order to simulate cine-MRI acquisitions. The evaluation of the performance of the models are performed considering a geometric analysis followed by a dosimetric one, in order to provide more information for a preliminary adaptation of the treatment.

The first part of the work is focused on the geometric analysis, which consists in the construction and evaluation of the models (Figure B).

i. Model construction. From the 4D CT dataset, the reference volume (i.e. 0% exhale phase or MidP volume) is identified and a DIR is performed between the reference phase and the other respiratory phases. In this work, we use (i) external surrogate (i.e. RPM signal) and (ii) internal surrogates, by considering the motion of the centre of mass (COM) of the tumour (mean tumour boundary, MTB), the motion of the diaphragm and the motion of lung vessels derived by scale invariant features transform (SIFT), an algorithm for features extractions.

ii. Model update. Once the model is constructed, it is updated with internal and external surrogates (RPM signal, MTB, diaphragm or SIFT) extracted from the treatment dataset.

iii. Geometric quantification. The preliminary analysis consists of the validation of the models on the digital CT/MRI phantom, thanks to the presence of a ground truth (i.e. CT volumes acquired at cine-MRI samples). In order to quantify the geometric error, the model output CT is compared with the ground truth. The geometric quantification is carried out focusing the attention on three regions of interest (ROIs) (i.e. heart, diaphragm and tumour), evaluating the Euclidean distance between the COMs on the model output and the ground truth. Finally, a statistical non-parametric analysis (Friedman test, alpha=5%) is carried out in order to identify which model and surrogates are significantly different. Since for patients, no ground truth is available, we evaluate the models in terms of their capability in reconstructing a specific respiratory phase (i.e. inhale). Also in this case, an evaluation based on ROIs (i.e. diaphragm and tumour) is performed and the difference of the ratio between the model output CT over the pre-treatment surrogate and the ratio between the treatment over the pre-treatment surrogate (Figure B) is computed.

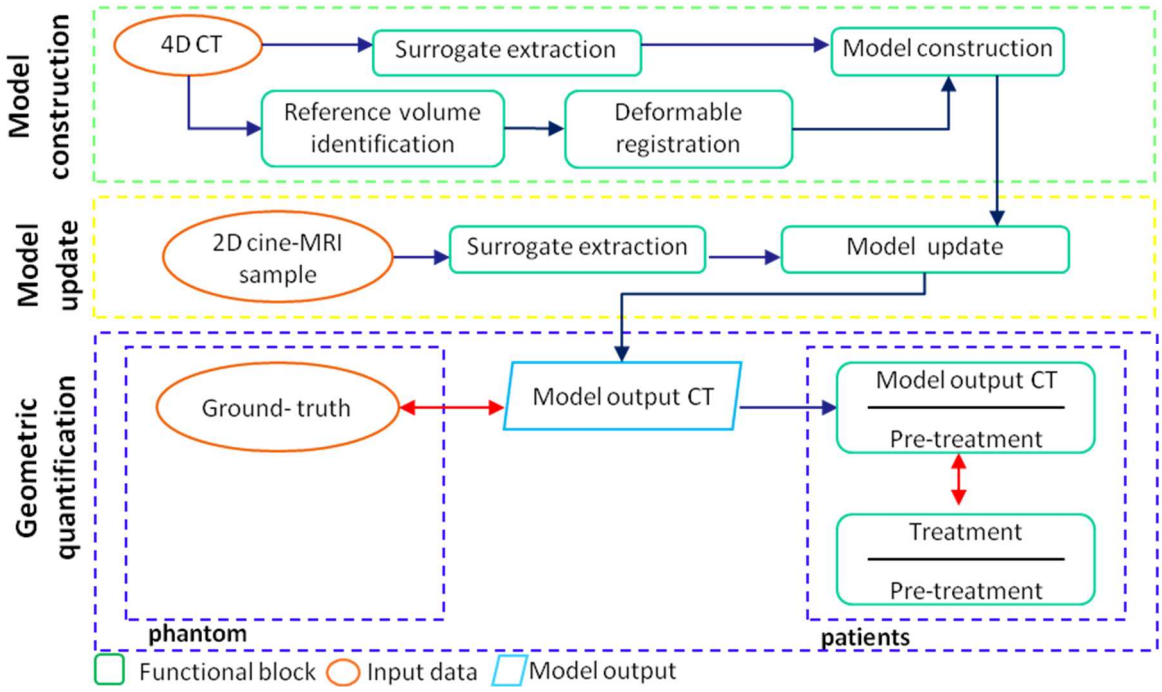

Figure B. Model workflow: essential steps leading to the models validation.

Specifically, for the CT/MRI phantom the models are tested on an entire breathing cycle considering both references (0% exhale and MidP) for each model. Then, different tests are performed (i) considering always both references, (ii) giving the same surrogate in pre-treatment and treatment and (iii) only for Fayad's model, giving the combination of different internal surrogates or internal and external pairs.

For the patients, the fundamental steps leading to model construction and update are similar to the one of the phantom. Differently from the CT\MRI phantom, in which no inter-fraction variabilities is present, in patients inter-fraction changes can be present and needs to be accounted (with the method shown in Figure C) and compensated into the model. Basically, the inter-fraction evaluation is carried out considering an alignment followed by a rigid registration and a DIR (not for the CT/cine-MRI patient) between the 0% exhale in the pre-treatment and the 0% exhale CBCT (cone beam CT) or a gated-MRI (i.e. volume acquired during exhale phase in the treatment situation) according to the availability of the dataset.

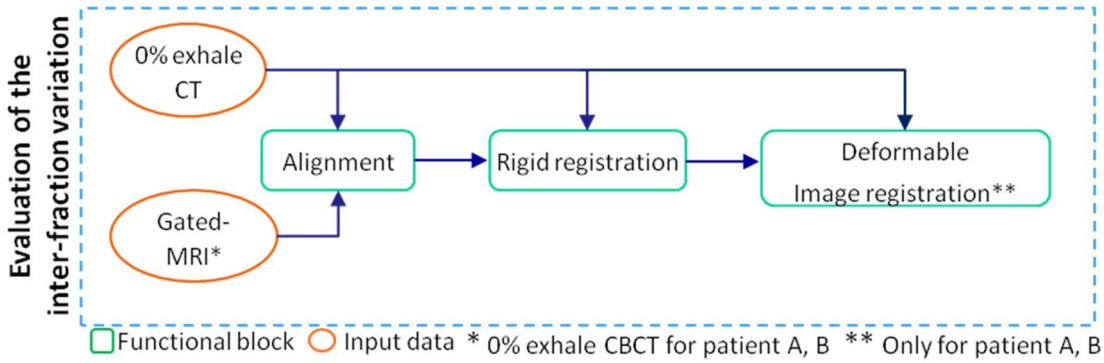

Figure C. Inter-fraction variation: workflow for the evaluation.

Also for patients the same tests (i.e. single surrogate or combination of surrogates), similar to the one performed on the CT/MRI phantom, are carried out. However for patients, both models are constructed considering as reference the 0% exhale phase due to the only presence of a gated-MRI acquired at the 0% exhale phase during treatment for the CT/cine-MRI patient and hence the impossibility to consider the MidP as reference.

As second part of the work, a dosimetric analysis is performed at the University of Sydney in collaboration with the department of the Radiation Therapy Planning unit at Liverpool

Hospital (Sydney, Australia). We use the Pinnacle^3 TPS for the creation and optimization of a patient specific IMRT plan. We manage our analysis firstly on the CT/MRI digital phantom and subsequently on patients, as for the geometric evaluation. For the dosimetric analysis, we create a dosimetric plan, which could be synthesized in the following steps, similar for both phantom and patients.

i. Creation and optimization of the plan on the 0% exhale phase. We realize a dosimetric plan on the 0% exhale phase (reference volume), using as guideline the protocol established by the Radiation Therapy Oncology Group for the treatment of non-small cell lung cancer (RTOG 0617) and also the IMRT plan protocol provided by the Department of Radiation Therapy Planning at Liverpool Hospital. In order to account for tumour motion during planning, we apply the internal target volume (ITV) approach, which consists in the delineation of the ITV considering the maximum range of tumour motion. Once the plan satisfies the protocol requirements, it is ready to be applied to all the other respiratory phases of the 4D CT.

ii. Application of the plan to all the respiratory phases of the 4DCT dataset. In this step, the DIR are used for the translation of target tumour and OARs from the reference volume (0% exhale) to all the respiratory phases. Instead, the ITV, the planning target volume (PTV) and other planning contours remain the same as indicated in the protocol.

iii. Application of the plan to the output of the motion model. After the use of the motion model to create the current CT, the plan, optimized on the 0% exhale phase of the 4D CT, is applied to a group of outputs of Fayad's model. As for the geometric analysis, the dosimetric validation on the CT/MRI digital phantom is carried out. It consists in the updating of the optimized plan on Fayad's model outputs and on the ground truth. The two resultant plans are compared considering relevant metrics (i.e. the same metrics used for the satisfaction of the protocol requirements). For what concern patients, due to the lack of the ground truth, the dosimetric evaluation are carried out comparing the plan resulting on the inhale phase during the pre-treatment planning with the plan updated on the outputs of Fayad's model. In addition, an entire breathing of patient C, the one with the most irregular breathing pattern, is tested.

The geometric evaluation on the entire breathing cycle of the CT/MRI digital phantom highlights that each model works better with its relevant reference phase, as it is fair to expect. Therefore, Vandemeulebroucke's model works better with the MidP as reference (e.g. the mean errors on the entire breathing cycle considering the diaphragm, heart and tumour are respectively 0.78 mm, 1.6 mm, 1.1 mm). While Fayad's model works only with the 0% exhale phase as reference (e.g. the mean errors on the entire breathing cycle considering the diaphragm, heart and tumour are 1.63 mm, 1.25 mm and 1.17 mm respectively). For the analysis of surrogates, when the model is constructed and updated with the RPM motion, a less precise result on tumour with respect to the other surrogates is shown, as already demonstrated in the literature. In addition, if we consider the diaphragm motion to construct and update the model, a bigger error on the heart with respect to the diaphragm is appreciated. Also, the evaluation performed on the CT/MRI phantom, in the test in which the SIFT motion is used, results in a greater errors on the diaphragm, tumour and heart regions than the other tests. A lower error is therefore expected in the lungs, since the SIFT signal describes the motion of the lung vessels. These results suggest that a future implementation of a ROI-based model, in which the surrogate extracted from a specific anatomic region is used to update only that specific region and not the whole volume, could improve the performance.

Analysing the geometric evaluation performed on Fayad's model, where the combination of surrogates is allowed, on the CT/MRI phantom and on patients, we can assert that the combination of coronal and interpolated sagittal value or different signals (internal or internal and external) do not improve the outcome, suggesting to update the model using just the specific surrogate at the correct current sample. However, the combination of different components of motion of the same surrogate shows improved results for the CT/cine-MRI patient. Considering the combination of MTB motion in superior-inferior (SI) and anterior-posterior direction (AP) or in SI and right-left (RL) there is an improvement on tumour motion estimation with respect to the single SI component whereas the outcome does not improve on the diaphragm, suggesting again the implementation of a ROI-based model. Moreover, depending on tumour position and dimension, for both models we can assert that:

i. if the tumour is big and in the lower lobe of the lung (patient A), the diaphragm motion is able to describe accurately also the tumour motion and vice versa, since the main tumour motion is in the SI direction;
ii. if the tumour is little and in the upper lobe of the lung (patient B) or close to the heart (patient C), the RL and AP direction of tumour motion are not negligible. In this case, the diaphragm motion is not able to describe tumour motion.

As already explained, an additional step for inter-fraction evaluation is required for patients. We find negligible variations compared to the voxel dimension, therefore, no inclusion of inter-fraction changes is performed in our study. For all the patients, a rigid alignment between the exhale volumes of pre-treatment and treatment is considered and only for CBCT patients a compensation for non-rigid variations is also performed via DIR. For what concern the CT/cine-MRI patient, nowadays, the implementation of a DIR between MRI and CT volume is still a challenge. Therefore, future studies should require the development and validation of a multi-modal registration algorithm for a more accurate and precise estimation of the inter-fraction variation.

In the second part of the project, the dosimetric evaluation on the protocol metrics proves that the 4D CT leads to an accurate dose estimation. In fact, the dose-volume histogram (DVH) curves of the target tumour and OARs are closed to each other (i.e. distance between inhale and exhale phase on PTV D98 for the CT/MRI digital phantom is around 0.87 Gy). After the evaluation of the 4D CT plan, we apply the dosimetric plan in the in-room scenario on the CT output of the model. The comparison between the DVH curves of Fayad's model outputs and the ground truth for the CT/MRI digital phantom confirms the ability of the model to approximate the ground truth and the results reached with the geometric validation. Therefore, no dosimetric difference is appreciated on the selected metrics when coronal and interpolated sagittal values or surrogates pairs are used to construct and update the model.

In addition, the dosimetric evaluation on Fayad's model output carried out on patients, for the estimation of the inhale respiratory phase, highlights that:

i. if the respiratory motion between pre-treatment and treatment session is similar (as for the CT/CBCT patients), the dosimetric variation is lower or equal to 1 Gy;

ii. if the respiratory motion between the two sessions change and an irregular breathing pattern is present (as for the CT/cine-MRI patient), a greater dosimetric variation is visible. In particular, when the MTB SI motion is combined with MTB RL or AP motion the difference of the inhale model output from the inhale phase of the pre-treatment is equal to 3.14 Gy on PTV D98.

On the CT/cine-MRI patient, as a preliminary approach, since it presents a different respiratory motion between the pre-treatment and the treatment session and an irregular pattern with respect to the other two CT/CBCT patients, we also test an entire breathing cycle. In this case, the cumulative dose on the PTV D98 varies of 1.17 Gy from the pre-treatment to the treatment sessions with the model tested with the diaphragm surrogate.

In conclusion, by validating the global motion models on a CT/MRI phantom and applying them to three patient cases, we prove that motion models offer an efficient strategy for organ motion compensation in terms of both geometric and dosimetric adaptation. Our work confirms the need to accurately establish the actual position and received dose for tumour and OARs quantifying and compensating the movement in order to confirm the effectiveness of the treatment. The fusion of MRI and radiotherapy system units and the integration in the MRI-guidance workflow of motion models, trained on pre-treatment 4D CT and updated with in-room cine-MRI information, suggests therefore a good combination to improve target coverage and healthy tissue sparing during the radiotherapy treatment.

Future studies will rely on the acquisition of new CT/cine-MRI patients through which we can verify the results obtained. Moreover, as previously mentioned, the implementation of a ROI-based model, the development of a multi-modal DIR and the extension of the dosimetric adaptation to others radiotherapy techniques will be also taken into consideration.

Sommario

La radioterapia è un trattamento medico che utilizza radiazioni ionizzanti per danneggiare le cellule tumorali al fine di ridurre ed eliminare i tessuti neoplastici. Contemporaneamente uno dei suoi scopi è preservare il più possibile i tessuti circostanti sani (OARs, organs at risk). Generalmente un trattamento radioterapico che ha lo scopo di rimuovere completamente la lesione tumorale è chiamato definitivo e consiste nella somministrazione di una specifica quantità di dose, espressa in Gy (e.g. 60 [Gy]), in diverse frazioni (e.g. 30 frazioni), per trattare il target e permettere il recupero da parte dei tessuti sani irradiati. Le fasi principali della radioterapia possono essere sintetizzate in:

i. fase di pianificazione, in cui viene sviluppato un modello paziente specifico sulla base delle CT acquisite, definendo il tumore target, OARs e la dose che deve essere somministrata dal sistema di trattamento (TPS, treatment planning system);
ii. fase di trattamento, in cui il piano di trattamento è effettivamente somministrato.

Lo sviluppo dei sistemi di radioterapia ha condotto all'uso di tecniche che adattano il più possibile la dose prescritta al tumore. In questo contesto, è molto rilevante la tecnica IMRT (intensity modulated radiation therapy), in cui l'intensità del fascio di radiazione è modulata attraverso un collimatore multi lamellare (MLC, multileaf collimator). Un altro aspetto molto importante riguardante la radioterapia è la variazione in termini di forma e localizzazione cui sono soggetti il tumore e OARs, dovuta al posizionamento del paziente e a processi anatomo-patologici, anche conosciuto come organ motion (movimento di organi). L'organ motion può essere classificato in movimento inter-frazione (i.e. si verifica tra diverse frazioni del trattamento) e intra-frazione (i.e. si verifica all'interno della stessa frazione). Il movimento intra-frazione dovuto alla respirazione causa incertezze che interessano tutti i tumori del distretto toraco-addominale. Per tener conto di movimenti inter e intra-frazione durante la fase di pianificazione vengono aggiunti dei margini al tumore stesso (GTV, gross tumour volume), irradiando così una zona più larga. La

necessità di migliorare la localizzazione del tumore ha portato allo sviluppo della radioterapia guidata dalle immagini (IGRT, image-guided radiation therapy), che consiste nell'utilizzo di tecniche di imaging durante il processo di radioterapia e include alcune strategie per la compensazione dell'organ motion. Nella pratica clinica, durante la fase di pianificazione, un metodo per tenere in considerazione l'organ motion consiste nell'acquisizione di volumi ad una determinata risoluzione temporale in grado di descrivere il ciclo respiratorio del paziente, come ad esempio le 4D CT in cui un set di CT è acquisito e successivamente ordinato grazie ad un segnale respiratorio esterno (i.e. surrogato). Relativamente alla fase di pianificazione la registrazione di immagini è uno strumento che permette di sovrapporre, confrontare e unire differenti immagini ed è utile per la quantificazione dell'organ motion. L'interesse del mondo scientifico si è rivolto in particolare allo sviluppo di algoritmi per la registrazione di immagini con deformazione (DIR, deformable image registration), che permettono di quantificare gli spostamenti non rigidi attraverso un campo vettoriale di spostamento (DVF, deformation vector field). La DIR, per volumi ad una certa risoluzione temporale, è tipicamente realizzata tra ogni fase della 4D CT al fine di descrivere l'organ motion legato alla respirazione. Tuttavia, uno dei problemi più rilevanti in radioterapia riguarda il corretto trasferimento del piano dalla fase di pianificazione a quella di somministrazione del trattamento, in termini di corretta corrispondenza nel posizionamento del paziente e allineamento anatomico delle strutture interne. In aggiunta, incertezze dovute al movimento respiratorio possono causare discrepanze tra la dose pianificata e quella somministrata, influenzando così la corretta riuscita del trattamento. In questo quadro, è necessario un monitoraggio real-time durante il trattamento per seguire direttamente o indirettamente la posizione del target. Nella pratica clinica sono disponibili metodi diretti basati su imaging a raggi X così come approcci indiretti, come ad esempio quelli basati su modelli di movimento locale, che sono in grado di trovare una correlazione stabile tra il movimento del target e il surrogato acquisito durante il trattamento. Il surrogato può essere interno (e.g. marker impiantati, surrogati basati sulle immagini) o esterno (e.g. basato su un sistema ottico come ad esempio l'RPM, real-time position management). Un miglioramento dei modelli di movimento locale è rappresentato dai modelli di movimento globale, un caposaldo di questo progetto, che permettono la descrizione dell'intero movimento basato sulle immagini 4D CT acquisite e non soltanto dello spostamento locale del tumore, fornendo in questo modo informazioni

aggiuntive sugli OARs. In questo caso si definisce una relazione tra il campo di spostamento derivato dalla DIR (tra ogni fase respiratoria e il volume di riferimento) e il surrogato di pre-trattamento. Successivamente, il modello di movimento viene aggiornato con il surrogato acquisito in real-time durante il trattamento. Inoltre, la necessità di ridurre la radiazione somministrata durante il trattamento, ha motivato l'uso della risonanza magnetica (MRI, magnetic resonance imaging), caposaldo di questo progetto, nell'ambito della tecnologia IGRT. L'MRI è una tecnica di imaging che non utilizza radiazioni, fornisce un buon contrasto per i tessuti molli e permette l'acquisizione di immagini veloci; questi vantaggi hanno suggerito l'integrazione dell'imaging MR con le unità di trattamento, in modo da sviluppare un sistema di MRI-guidance per seguire il movimento del tumore in real-time durante il trattamento. Tuttavia, i limiti legati al trade-off spaziale e temporale per l'acquisizione volumetrica sono tutt'ora un problema; perciò tipicamente, fette 2D ortogonali centrate nel tumore (cine-MRI) sono acquisite in modo da descrivere l'anatomia interna durante il movimento respiratorio. Questo limite durante l'acquisizione geometrica suggerisce quindi l'uso dei modelli di movimento globale, che possano essere aggiornati secondo i surrogati ricavati dalle cine-MRI acquisite durante il trattamento.

Lo scopo di questo progetto è quindi applicare modelli di movimento globale, tipicamente usati per imaging a raggi X, allo scenario MRI-guidance, al fine di quantificare sia dal punto di vista geometrico che dosimetrico le variazioni indotte dal movimento respiratorio tra la fase di pianificazione e quella di trattamento. Specificatamente, abbiamo scelto e testato i modelli sviluppati da Fayad et al. (2012) e Vandemeulebroucke et al. (2009). Il modello di Fayad è basato sull'analisi in componenti principali (PCA, principal component analysis) per costruire il modello, considera come volume di riferimento la fase di espirio e richiede come input il range di ampiezza calcolato rispetto al valore di riferimento. Invece il modello di Vandemeulebroucke è costruito sulla base di un'interpolazione di DVFs, usa come riferimento un volume relativo ad una posizione media (MidP- fase intermedia tra la fase di espirio e quella di inspirio) e richiede come input sia ampiezza che fase calcolati attraverso la trasformata di Hilbert. Entrambi i modelli di movimento sono addestrati su un dataset di pre-trattamento composto da 4D CT (10 fasi respiratorie) e poi aggiornati con diversi surrogati estratti dalle cine-MRI 2D ortogonali (i.e. sagittale/coronale) acquisite durante il trattamento (Figura A).

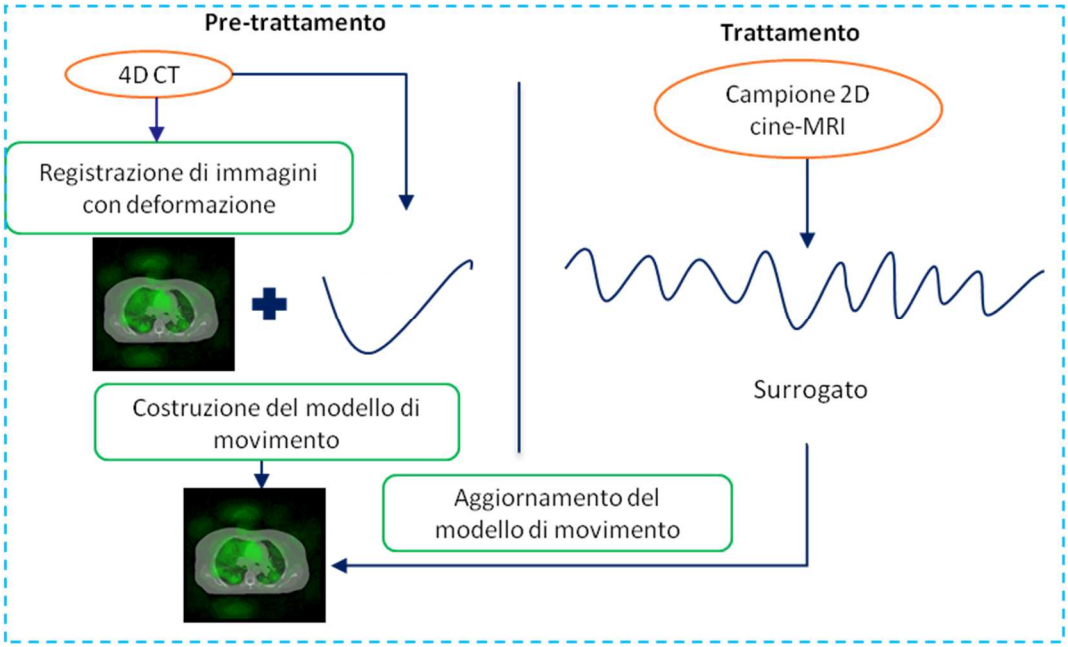

Figura A. Costruzione del modello di movimento: passaggi fondamentali per la costruzione del modello.

I modelli sono testati su un fantoccio digitale CT/MRI e poi su due pazienti CT/CBCT (Cone Beam CT) (i.e. paziente A con tumore nella parte inferiore del polmone destro, paziente B con tumore nella parte superiore del polmone destro) e su un paziente CT/cine-MRI (i.e. paziente C con tumore, nel polmone sinistro, attaccato al cuore). In particolare, per i pazienti CT/CBCT, sono selezionate sulle CBCT fette ortogonali centrate nel tumore, in modo da simulare le cine-MRI. Le performance dei modelli sono valutate geometricamente e dosimetricamente, in modo da ottenere maggiori informazioni per un iniziale adattamento del trattamento.

La prima parte del progetto, riguardante l'analisi geometrica, può essere sintetizzata in (Figura B):

i. <u>Costruzione del modello.</u> Una volta identificato il volume di riferimento (i.e. volume corrispondente alla fase di espirio o alla MidP), è eseguita una DIR tra la fase di riferimento e le altre fasi respiratorie della 4D CT. Abbiamo utilizzato come (i) surrogato esterno il segnale RPM e come (ii) surrogati interni il movimento del centro di massa (COM, centre of mass) del tumore (MTB, mean tumour boundary), il movimento del diaframma e il movimento dei vasi dei polmoni derivati dal SIFT

(scale invariant features transform), un algoritmo per l'estrazione di punti caratteristici.

ii. Aggiornamento del modello. Successivamente alla costruzione, il modello è aggiornato con surrogati interni ed esterni (MTB, diaframma, SIFT, RPM) estratti dal dataset di trattamento.

iii. Quantificazione geometrica. L'analisi preliminare consiste nella validazione dei modelli sul fantoccio digitale CT/MRI grazie alla presenza del ground truth (i.e. CT acquisite ai campioni di cine-MRI). L'errore geometrico è quantificato confrontando la CT di uscita del modello con il ground truth. La quantificazione geometrica è valutata su tre regioni di interesse (ROI, region of interest), ovvero cuore, diaframma e tumore, valutando la distanza euclidea tra i COM sull'uscita del modello e il ground truth. Infine, è effettuata un'analisi statistica non parametrica (test di Friedman, alpha=5%) per identificare quali siano i modelli e i surrogati significativamente differenti. Dal momento che per i pazienti il ground truth non è disponibile abbiamo valutato la capacità dei modelli di ricostruire una specifica fase respiratoria (i.e. inspirio). È stata valutata la differenza tra il rapporto fra l'uscita del modello con il surrogato di pre-trattamento e il rapporto fra il surrogato di trattamento con quello di pre-trattamento (Figura B), considerando due ROIs (i.e. diaframma e tumore).

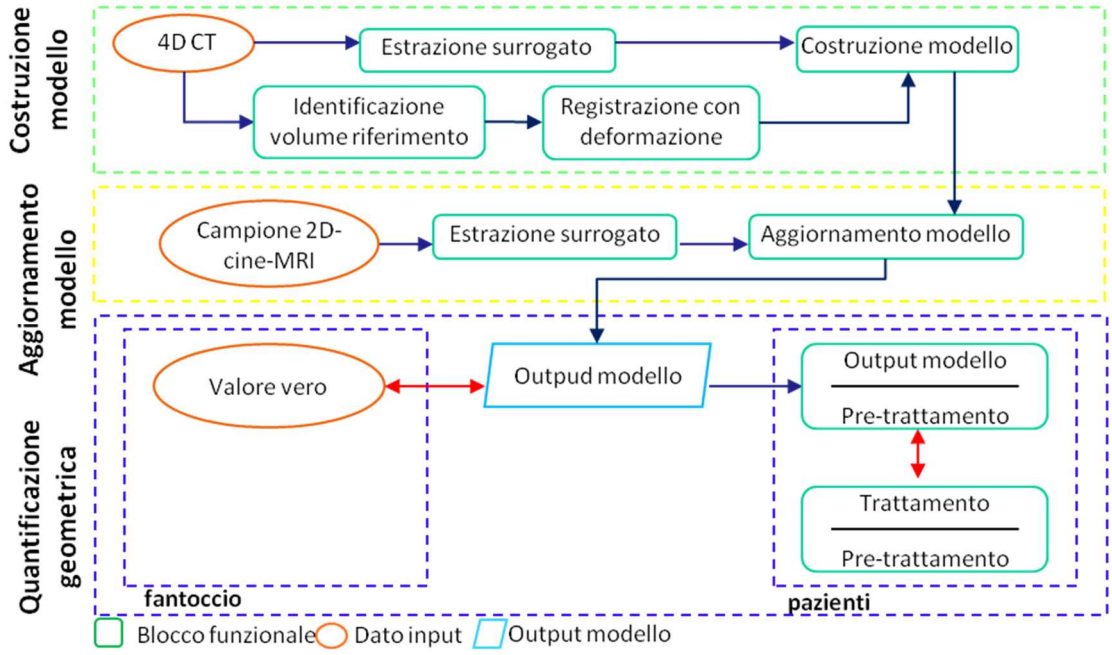

Figura B. Processo del modello: passaggi fondamentali per la validazione del modello

Per il fantoccio CT/MRI i modelli sono stati testati prima su un intero ciclo respiratorio, considerando entrambi i riferimenti (espirio e MidP) per ogni modello. Poi, i test sono eseguiti (i) considerando sempre lo stesso riferimento, (ii) dando lo stesso surrogato in pre-trattamento e trattamento e (iii), solo per il modello di Fayad, dando la combinazione di diversi surrogati interni o surrogati interni ed esterni.

Per quel che riguarda i pazienti, la costruzione e l'aggiornamento del modello è simile a quelli realizzata per il fantoccio, con la differenza che nei pazienti possono essere presenti variazioni inter-frazione che devono dunque essere valutate (metodo mostrato in Figura C). La valutazione della variazione inter-frazione è effettuata considerando un allineamento, seguito da una registrazione rigida e una registrazione con deformazione (solo per pazienti CT/CBCT) tra la fase di espirio in pre-trattamento e la fase di espirio di un volume 3D acquisito durante il trattamento prima delle cine-MRI. Nel caso dei pazienti A e B abbiamo registrato CT con CBCT mentre per il paziente C la valutazione inter-frazione è avvenuta fra CT e gated-MRI (volume acquisito durante la fase di espirio).

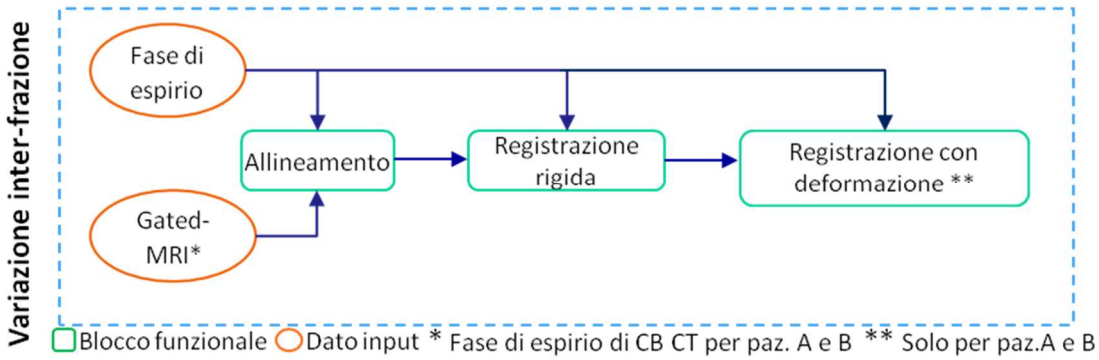

Figura C. Variazione inter-frazione: processo per la valutazione.

Test simili a quelli eseguiti sul fantoccio (i.e singolo surrogato o combinazione di surrogati diversi) sono effettuati per i pazienti. Tuttavia, in questo caso entrambi i modelli sono costruiti considerando come riferimento la fase di espirio, a causa della presenza della sola gated-MRI (per il paziente CT/cine-MRI) acquisita alla fase di espirio durante il trattamento e quindi all'impossibilità di considerare la MidP come riferimento.

Nella seconda parte del lavoro, è stata effettuata un'analisi dosimetrica presso l'Università di Sydney in collaborazione con il dipartimento di radioterapia dell'ospedale di Liverpool (Sydney, Australia). Per la creazione e ottimizzazione di un piano IMRT abbiamo usato il

software Pinnacle[3]. Così come l'analisi geometrica, l'analisi dosimetrica è condotta prima sul fantoccio CT/MRI e poi sui pazienti. In entrambi i casi è creato un piano paziente specifico che può essere riassunto nei seguenti passaggi:

i. Creazione e ottimizzazione del piano sulla fase di espirio. E' realizzato un piano dosimetrico sulla fase di espirio (reference volume), usando come linea guida il protocollo stabilito dal Gruppo di oncologia e radioterapia (RTOG, radiation therapy oncology group) per il trattamento di tumori ai polmoni (RTOG 0617) e il protocollo per la realizzazione di piani IMRT fornito dal dipartimento di radioterapia dell'ospedale di Liverpool. Per compensare il movimento del tumore nella fase di pianificazione è usato l'approccio ITV (internal target volume), che consiste nella delineazione dell'ITV considerando il massimo range di movimento del tumore. Quando il piano soddisfa i requisiti del protocollo, è pronto per essere applicato a tutte le fasi respiratorie del dataset di 4D CT.

ii. Applicazione del piano a tutte le fasi respiratorie del dataset di 4D CT. La DIR è stata usata per propagare i contorni del tumore target e degli OARs dal volume di riferimento (espirio) a tutte le altre fasi. Invece, ITV, PTV (planning target volume) e gli altri contorni di pianificazione rimangono inalterati, come riportato dal protocollo.

iii. Applicazione del piano alle uscite del modello. Dopo aver utilizzato il modello di movimento per creare la CT corrente, il piano, che è stato precedentemente ottimizzato sulla fase di espirio del dataset di 4D CT, è applicato ad un gruppo di uscite del modello. Come per l'analisi geometrica, la validazione dosimetrica viene effettuata sul fantoccio CT/MRI, aggiornando il piano sia sulle uscite del modello di Fayad che sul ground truth. I due piani così ottenuti vengono confrontati considerando metriche rilevanti (i.e. le stesse metriche usate per soddisfare i requisiti del protocollo). Per quanto riguarda i pazienti, a causa della mancanza del ground truth, la valutazione dosimetrica è effettuata confrontando il piano ottenuto sulla fase di inspirio del pre-trattamento con il piano aggiornato sulle uscite del modello di Fayad. In aggiunta, per il paziente C è stato testato un intero ciclo respiratorio.

La valutazione geometrica di un intero ciclo respiratorio per il fantoccio CT/MRI evidenzia, com'è giusto aspettarsi, che ogni modello ha prestazioni migliori quando usa la propria fase di riferimento. Quindi il modello di Vandemeulebroucke funziona meglio con MidP come riferimento (e.g. gli errori medi sull'intero ciclo respiratorio considerando diaframma, cuore e tumore sono rispettivamente di 0.78 mm, 1.6 mm e 1.1 mm), mentre il modello di Fayad funziona solo usando come riferimento la fase di espirio (e.g. gli errori medi sull'intero ciclo respiratorio considerando diaframma, cuore e tumore sono rispettivamente di 1.63 mm, 1.25 mm e 1.17 mm). Inoltre, quando il modello è costruito e aggiornato con il movimento RPM si ottengono risultati meno precisi sul tumore rispetto agli altri surrogati interni, come già dimostrato in letteratura. Considerando invece il movimento del diaframma, per costruire e aggiornare il modello, si osservano errori minori rispetto a RPM, con buone performance di compensazione del movimento del diaframma ma si ha un errore maggiore sulla compensazione del movimento del cuore. Anche la valutazione dei test in cui viene utilizzato il segnale SIFT conferma un errore maggiore su diaframma, tumore e cuore rispetto agli altri test, mentre si prevede un errore minore sulla compensazione del movimento dei polmoni visto che il SIFT descrive il movimento dei vasi e delle biforcazioni polmonari. Questi risultati suggeriscono che con lo sviluppo di un modello basato su regioni di interesse (ROI-based model), ovvero un modello in cui il surrogato estratto da una specifica regione anatomica viene usato per aggiornare solo quella specifica regione e non l'intero volume, le performance dei modelli possano migliorare.

Con la valutazione geometrica condotta sul modello di Fayad, dove è possibile combinare i surrogati, possiamo affermare che, sia per fantoccio che per i pazienti, la combinazione del valore coronale e sagittale interpolato o di differenti segnali (interni o interni ed esterni) non migliora il risultato; questo suggerisce di aggiornare il modello usando solo il surrogato specifico per il corretto campione corrente. Tuttavia, la combinazione di differenti componenti di movimento dello stesso surrogato mostra risultati migliori sul paziente CT/cine-MRI: se si considera la combinazione del movimento del MTB in direzione superior-inferior (SI) e antherior-posterior (AP) o in direzione SI e right-left (RL) si ha un miglioramento sulla stima del movimento del tumore, rispetto all'utilizzo della singola componente SI. In più, a seconda della posizione e della dimensione del tumore, per entrambi i modelli, si può affermare che:

i. se il tumore è grande e nella parte inferiore del polmone (paziente A), il movimento del diaframma è in grado di descrivere accuratamente il movimento del tumore e viceversa, dal momento che il movimento principale del tumore è in direzione SI;
ii. se il tumore è piccolo e nella parte superiore del polmone (paziente B) o vicino al cuore (paziente C), le direzioni RL e AP non sono trascurabili. In questo caso, il movimento del diaframma non è in grado di descrivere il movimento del tumore.

Come già mostrato, nei pazienti è richiesta la valutazione della variazione inter-frazione. Per la valutazione è stato considerato un allineamento rigido tra l'espirio in pre-trattamento e trattamento e, solo per i pazienti CT/CBCT, è stata effettuata anche una compensazione delle variazioni non rigide attraverso una DIR. Per quel che riguarda il paziente CT/cine-MRI, attualmente, si sta ancora cercando di implementare una DIR tra MRI e CT, quindi studi futuri richiederanno lo sviluppo e la validazione di un algoritmo di registrazione multi-modale per una stima più accurata della variazione inter-frazione. Poiché le variazioni trovate sono trascurabili se confrontate con la dimensione del voxel, il nostro studio non include la compensazione delle variazioni inter-frazione.

Nella seconda parte del progetto, la valutazione dosimetrica, considerando le metriche riportate nel protocollo, dimostra che le 4D CT garantiscono un'accurata stima della dose. Infatti, le curve dell'istogramma dose-volume (DVH, dose-volume histogram) del tumore target e OARs appaiono ravvicinate (i.e. la distanza tra inspirio ed espirio sul PTV D98 per il fantoccio CT/MRI è circa 0.87 Gy).

Dopo aver valutato il piano 4D CT, abbiamo applicato il piano alle CT in uscita dal modello. Il confronto tra le curve del DVH delle uscite del modello di Fayad e il ground truth per il fantoccio CT/MRI confermano la capacità del modello, già dimostrata geometricamente, di ricostruire il ground truth. Inoltre, non si apprezzano variazioni dosimetriche sulle metriche selezionate quando sono usati valori coronali e sagittali interpolati o coppie di surrogati per costruire e aggiornare il modello.

Considerando la valutazione dosimetrica dei pazienti sulle uscite del modello di Fayad, in riferimento alla stima della fase di inspirio, si sottolinea che:

i. se il movimento respiratorio tra le sessioni di pre-trattamento e trattamento è simile (come per i pazienti A e B), la variazione dosimetrica è inferiore o uguale a 1 Gy;

ii. se il movimento respiratorio tra le sessioni di pre-trattamento e trattamento cambia ed è presente un andamento respiratorio irregolare (come per il paziente C), si osserva una variazione dosimetrica maggiore. In particolare, quando il movimento MTB SI è combinato con MTB RL o MTB AP la differenza sul PTV D98, tra l'inspirio ricostruito dal modello e l'inspirio del pre-trattamento, è di 3.14 Gy. Questo conferma la necessità di adattare il trattamento per compensare il movimento respiratorio.

Come approccio preliminare, sul paziente CT/cine-MRI, dal momento che il movimento respiratorio tra pre-trattamento e trattamento varia mostrando un andamento irregolare se confrontato con quello dei due pazienti CT/CBCT, è testato anche un intero ciclo respiratorio. In questo caso il modello è testato usando il surrogato diaframma e la dose cumulativa sul PTV D98 varia di 1.17 Gy tra pre-trattamento e trattamento.

In conclusione, validando i modelli sul fantoccio CT/MRI e poi applicandoli ai tre pazienti, abbiamo dimostrato che l'uso dei modelli rappresenta una buona strategia per la compensazione dell'organ motion, in termini di adattamento sia geometrico che dosimetrico. Il nostro lavoro conferma la necessità di stabilire con precisione la posizione attuale del tumore e degli OARs e la dose che essi ricevono, in modo che l'adattamento del trattamento sia efficace. La fusione di MRI con i sistemi di radioterapia e l'integrazione del MRI-guidance nel processo di addestramento dei modelli, costruiti con i dati di pre-trattamento (4D CT) e aggiornati con le cine-MRI di trattamento, sembrano quindi essere un' efficiente strategia per migliorare la copertura del target e preservare i tessuti sani durante il trattamento. Studi futuri prevedono l'acquisizione di nuovi pazienti CT/cine-MRI che confermino i risultati ottenuti. In più, come già menzionato, va anche tenuta in considerazione l'implementazione di un modello ROI-based, lo sviluppo di una registrazione multi- modale con deformazione e l'estensione dell'adattamento dosimetrico anche ad altre tecniche di radioterapia.

Chapter I: Introduction

1.1. Physical basis of radiotherapy

Radiotherapy is a medical therapy consisting of irradiating the tumour (i.e. target) through ionizing radiation with the aim of extinguishing neoplastic cells and avoiding their proliferation in other regions (i.e. metastasis) (Eriksson 2010). Radiotherapy uses radiation to damage the cell via single helix (single-stranded break) and double-helix (double-strand break) of the DNA, as can be seen in Figure 1 (Dewey 1995).

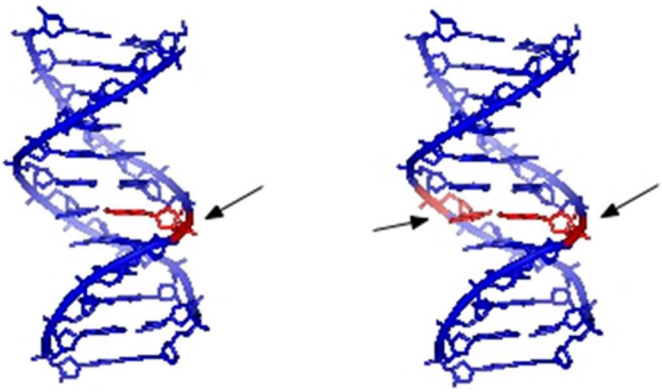

Figure 1. Radiation induced damage in DNA: single-strand break (left) and double-strand break (right).

In both cases, radiation-induced damage can lead to cell-cycle arrest and consequent cell death via either apoptosis (programmed cell death), or necrosis (a passive process which lethally kills cells, disabling any repair and finally any kind of following cellular duplication (i.e. mitosis)) (Cohen E, 1999). Radiotherapy employs ionizing radiation (i.e. electromagnetic waves at high frequency) with energy according to the law:

$$E = h * v$$

With $v = c/\lambda$: frequency

λ: wavelength

c =300 000 000 m/s: speed of light in vacuum

h = 6,624 10^{-34} J/sec: Planck's constant.

The typical ionizing radiation in radiotherapy consists of X-rays with a frequency in the range of 10^{16}-10^{21} Hz, which corresponds to an energy from 4 MeV to 25 MeV. The bremsstrahlung X-Rays (which literally translates as "braking radiation") are one of the most employed in radiation therapy and are generated by accelerated electrons impinging on high Z materials (e.g. tungsten, lead).

Interaction of X-rays with matter

When electromagnetic radiation interacts with matter, the main interactions can be listed as follows (Turner 2007):

i. photoelectric effect: leads to the total absorption of the photon (i.e. primary radiation) by an atom, and one of the atomic electrons of inner shells is ejected;
ii. Compton scattering: the incident photon ejects an outer shell electron from an atom and a photon of lower energy (i.e. scattered photon) is scattered from the same atom;
iii. coherent scattering: all photons energy is scattered (i.e. multiple scattered photons) in an elastic process without energy conversion of electrons into kinetic energy. This interaction is more likely when the primary energy is lower than the electron binding energy;
iv. pair production: if the incident photon energy is greater than 1.022 MeV (twice the electron rest mass) in the presence of an atom nucleus, an electron and positron pair can be generated.

Modern radiotherapy is generally delivered with X-rays between 4-18 MeV. At these energies, the most important interaction is Compton scattering, with pair production becoming more important at higher energies.

1.1.1 Cancer treatment

The main challenge concerning radiotherapy is hitting the tumour cells preserving the surrounding healthy tissues. In radiotherapy, the concept of "hitting tumour cells" involves

the energy that the radiation releases to matter. This energy is called *absorbed dose* (expressed in Gray [Gy]) and is defined by International Commission of Radiation Units (ICRU) 51 as the ratio between:

$$D = \frac{d\varepsilon}{dm}$$

Where $d\varepsilon$ is the imparted energy (ICRU 36) by the ionizing radiation to the matter per unit of mass dm. The goal of radiotherapy is to provide the highest possible dose to the target without damaging the surrounding healthy tissues (Korreman 2012). Generally, the dose is administered in daily fractions, with the aim of protecting the patient from high ionizing radiation and to allow the healthy irradiated tissue to repair the radiation-induced damage. In fact, normal tissue and tumour show a different behaviour: tumour cells grow more rapidly than normal cells and this is due to gene mutation involved in cell proliferation. However, tumour cells have a reduced capacity to repair damage compared to healthy cells, due to the presence of hypoxic cells within the tumour (Withers 1985). The dose-effect curve in Figure 2 shows the probability of inducing lethal effects in the tumour and of complication in the healthy tissue.

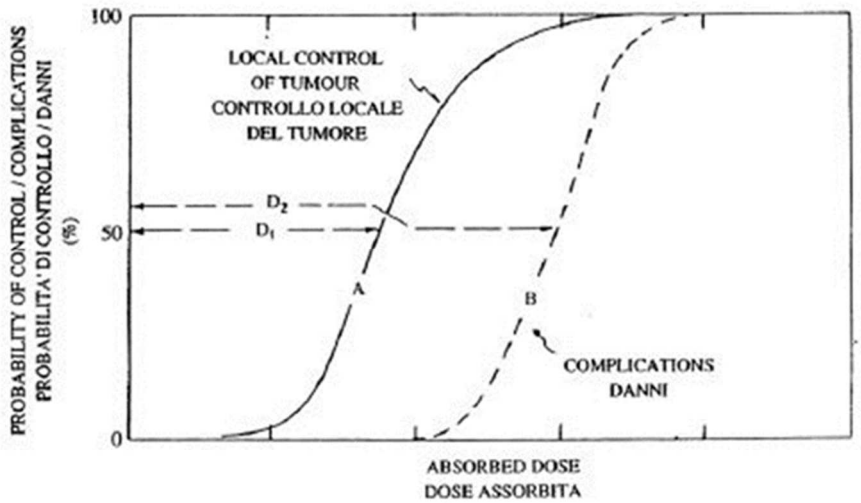

Figure 2. Dose-effect curve: Curve A represents the probability of local control of the tumour, whereas curve B the probability of complications in healthy tissue.

When the probability of tumour control is higher than the probability of complications in healthy tissue, the radiotherapy treatment delivery can be done safely. Another important

issue that has to be taken into account is variations in shape and positions of organ at risk (OAR) and target tumour, which may lead to an ineffective radiotherapy treatment. These variations can take place from fraction to fraction (inter-fraction motion), or can appear in the same fraction (intra-fraction motion). This distinction will be examined in depth in the following paragraph. In order to deal with these uncertainties, the idea is to irradiate a target larger than the tumour itself. With this aim the ICRU 50 defines the margins for any sort of treatment planning (Figure 3):

i. gross tumour volume (GTV): the extension and the position roughly touchable or visible of the tumour;
ii. clinical target volume (CTV): the tissue volume containing the gross target volume and/or microscopic subclinical malignant pathologies which must be eliminated;
iii. internal target volume (ITV): the expansion of CTV for taking into account internal movement (i.e. breathing);
iv. planning target volume (PTV): a geometrical concept defined for selecting the beam dimensions and the appropriate irradiation techniques, by considering the effect of all possible geometrical variations (i.e. patient positioning, ineffective immobilization) and uncertainties (i.e. tumour shrinkage, weight loss) to ensure that the prescribed dose is absorbed actually in the CTV.

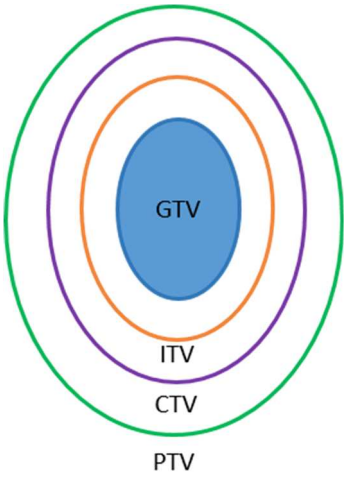

Figure 3. Margins for treatment planning: PTV, CTV, GTV defined by the ICRU 50 and ICRU 62.

1.1.2 External beam radiotherapy

Radiotherapy can be classified into different types, based on the position of the radioactive source and the method of delivery. In brachytherapy, the source is inside the patient, very close to the tumour. External beam radiotherapy (EBRT) instead has the radiation source outside the patient and the accelerator mostly employed in EBRT is the linear accelerator (linac), which is described in section 1.1.1.2. The external beam radiotherapy process consists of two main phases:

i. planning phase: a patient-specific model of the treatment is developed by defining the tumour and OARs margins and the dose to be delivered. This step is supported through the use of a treatment planning system (TPS). The TPS is also able to assess the 3D dose distribution in a 2D format through the dose-volume histogram (DVH), which is a histogram relating radiation dose to tissue volume. Ideally, the 100% of the dose distribution should fall in the 100% of the irradiated volume, thus sparing the surrounding healthy tissues;
ii. treatment phase: the treatment plan is delivered, according to the treatment plan performed. It has to be pointed out that variations with respect to the treatment plan need to be compensated.

1.1.2.1 Linac and multi-leaf collimator

The most commonly used treatment devices in modern radiotherapy are linear electron accelerators (Karzmark et al. 1993). Electrons are generated via thermionic emission and injected into a linear acceleration structure, which consists of a series of radiofrequency resonant cavities. These cavities are excited in the microwave frequency (typically ~3 GHz) and provide an oscillating electromagnetic field to accelerate electrons. The electron accelerator is housed in the gantry, which is the treatment unit that rotates around the patient allowing irradiation from different directions. The linac inside the gantry is installed in a direction parallel to the bed axis for patient's positioning. The gantry rotates symmetrically about one point in space. This point is called the isocentre and it is the intersection between the gantry axis and the central axis of the beam.

In addition to the waveguide, the gantry includes also (Figure 4):

i. bremsstrahlung target: the metal target on which electrons impact, generating X-ray photons;
ii. primary collimator: the first step of radiation beam collimation;
iii. flattening filters: filters used for providing uniform dose profiles;
iv. monitor chamber: the radiation detector with which the dose delivered from the linac is controlled. The delivered dose is measured in monitor units (MUs). One MU is defined as the fluence of a square field that results in a dose of 1cGy at a specific depth in a water phantom;
v. secondary collimator: consists of one or two pairwise-opposed movable metal blocks called jaws, which are positioned in order to block part of the beam not intersecting with the target volume, resulting in a rectangular beam shape;
vi. multileaf collimator (MLC): a system of ~50-100 sliding tungsten leaves which are positioned in order to replicate the target volume to be irradiated from the prospective beam view (i.e. beam eye view). The configuration of leaves and jaws is called segment or aperture.

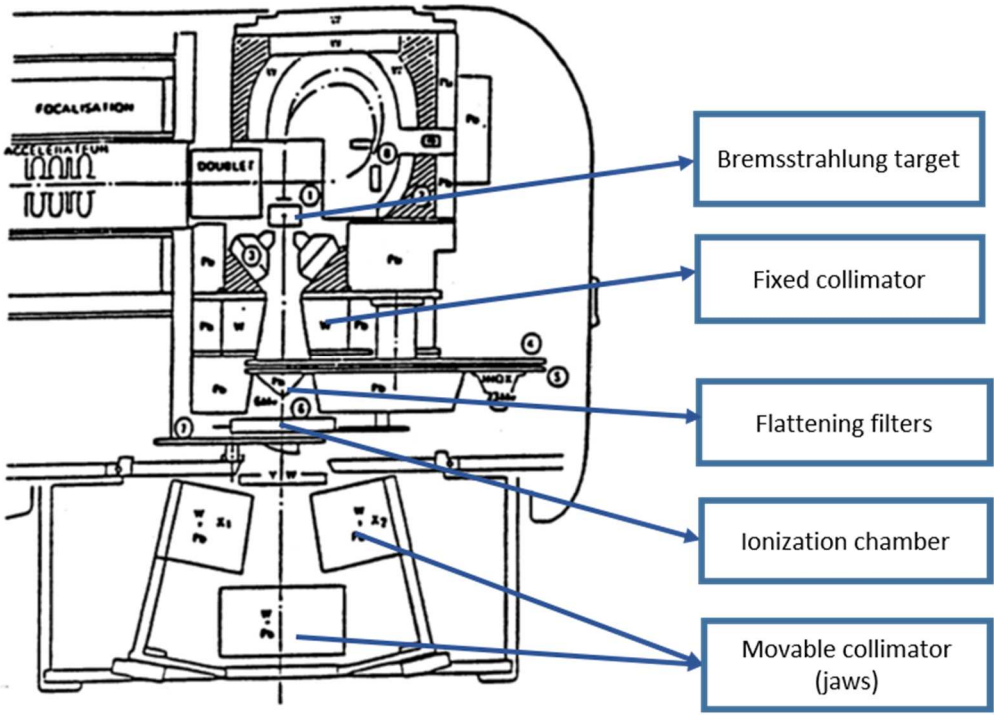

Figure 4. Gantry: representation of the gantry of the linac.

1.1.2.2 EBRT techniques

The evolution of radiation therapy has been strongly correlated with the development of imaging techniques and the main concept that has lead new imaging techniques advancement is using images to better understand location and shape of internal organs and of tumour masses. In the 1970s, computed tomography (CT) has completely transformed radiation therapy allowing the use of image data to build a 3-dimensional (3D) patient model and design 3D conformal radiation treatment (3D CRT). Recent technical advances have enabled the planning and delivery of radiation in three dimensions, so that the dose given to the patient closely conforms to the tumour shape. Within the field of EBRT, a variety of different techniques are used to conform the dose to tumour. One of the most important advances is intensity modulated radiation therapy (IMRT). The basic idea of IMRT is modulating the intensity of radiation beam through the leaves of a MLC (Bortfeld, 2006), thereby delivering a radiation field with a non-uniform intensity to better conform the tumour shape. There are two common methods of IMRT delivery using multi-leaf collimators (Goraj 2012): the static technique known as "step-and shoot" and the dynamic technique. In the first approach, the leaves are set at a fixed position when the radiation beam is switched on and then they change position when the beam is switch off. In the second method instead, the MLC leaves moves continuously while the radiation is on. In contrast with 3D CRT, in IMRT not only the radiation beams are geometrically shaped but they also have a non-uniform radiation fluence to give a pixel by pixel intensity variation within the shaped beam (Webb 2003). In order to better understand the concept of intensity modulation, we should refer to the definitions of radiant energy and energy fluence given by ICRU 33. Radiant energy (R) is the emitted, transferred or received energy (expressed in [J]) and energy fluence ($\boldsymbol{\Psi}$) (expressed in [J m^{-2}]) is the ratio between dR and da, where dR is the radiant energy impinging on a sphere of cross sectional area da.

$$\Psi = \frac{dR}{da}$$

Besides the IMRT technique, other radiotherapy techniques include volumetric modulated arc therapy (VMAT) and stereotactic body radiation therapy (SBRT). VMAT consists of a large number of beam directions from an arc trajectory and delivers doses dynamically

during the rotation of the gantry. As reported by Yu et al. (2011) using the full gantry range provides increased flexibility in generating highly conformal treatment plans. SBRT consists in the delivery of large doses in few fractions (i.e. hypofractionation) with respect to conventional radiation treatment, thus resulting in a highly conformal dose distribution in a relatively short overall treatment time (Benedict et al. 2010). The focus of this thesis project will be on IMRT techniques.

1.1.3 Organ motion

Patient's anatomy and position during the course of radiation therapy varies to some extent from those used for therapy planning process (Langen et al. 2001). This is mainly due to patient movements, inaccurate patient positioning and organ motion. Variation in patient movement and position can be minimized with the help of patient positioning systems and immobilization devices. The term organ motion refers to anatomic-pathological processes that occur during a radiation therapy treatment, causing uncertainties in treatment delivery. There are two main categories in which organ motion can be divided: inter-fraction motion (occurring between treatment sessions) and intra-fraction motion (occurring within a treatment session). Inter-fraction motion is mainly due to anatomic variations such as shrinking or growing of the tumour, patient weight gain/loss and geometric variations (i.e. set up errors and uncertainties related to patient position during treatment). Intra-fraction motion occurs while the patient is irradiated and can be caused by respiratory, muscular, cardiac and gastrointestinal systems. Much interest has been directed towards accounting for respiratory motion, which affects all tumour sites in thorax and abdomen, though the disease of most relevance for radiotherapy is lung cancer (Keall et al. 2006b). Indeed, the management of organ motion due to respiration is one of the main challenges in radiotherapy treatment, especially for abdominal and thoracic regions where respiratory organs are involved (Brander et al. 2006). Respiration implies a non-rigid deformation of the thoracic-abdominal patient anatomy, characterized by a cyclic nature but with an element of irregularity owing to the complex physiological process of breathing (Korreman 2012). In the thorax and abdomen, intra-fraction internal anatomy motion due to respiration is the principal cause for large safety margins. Motion can distort target volumes and results in positioning errors since different parts of the tumour move in and out of the image window with the patient's breathing (Xing et al. 2006). As consequence

of adding safety margins, it should be considered that also the healthy tissues surrounding the target volume are irradiated. Another important issue regarding respiratory motion is the fact that the pattern of breath can significantly vary across patients and within a treatment session given to the same patient. For this reason, there are no general patterns that can be assumed for a particular patient before observation and treatment (Keall et al. 2006b). Keall et al. (2006) report lung tumour motion: 2-30 mm in the SI direction, 1-20 mm in AP direction and 1-10 mm in the right-left direction (RL).

Therefore, the need to quantify and compensate for organ motion is of primary importance in radiation therapy to reduce margins and optimize treatment delivery, thus irradiating the tumour and sparing the surrounding healthy tissues.

1.2 Image Guided Radiotherapy for motion compensation

The need to improve targeting in radiation treatments motivated the use of imaging technologies to guide radiotherapy. Such an approach is known as image-guided radiation therapy (IGRT) (Xing et al. 2006). The term IGRT refers to the steps of patient setup, radiation planning and treatment delivery that integrate new imaging tools, which interface with the radiation delivery system and allow the improvement of treatment accuracy by adjusting the radiation beam based on the actual position of the target (Jaffray et al. 2012). One of the main tasks in IGRT is irradiating tumours more accurately while sparing the normal tissue, thanks to the reduction of safety margins (e.g. CTV and PTV). The precision introduced by IGRT can shorten the duration of radiation therapy by reducing the number of treatment session, increasing uniformity in dose delivered and also decreasing set up errors (Dawson et al. 2006, Jaffray 2012). All these characteristics make IGRT very useful to compensate for anatomical changes in both treatment planning and delivery.

1.2.1 Planning phase

The planning phase in radiotherapy relies on images of the patient (typically CT) in order to build a patient-specific model and to create the treatment plan that will be transferred into the treatment situation. The imaging modality most used in the clinical practice is CT,

thanks to its high spatial resolution and excellent bone structure description. In addition, CT provides information on relative electron density, which is required for dose calculations. The recent development of ultra-fast multi-slice CT has enabled time-resolved (4D) CT imaging of the patient's breathing cycle (Xing et al. 2006). This technique is described in detail in section 1.2.1.1. CT can be categorised by the shape of the X-ray beam and detector used to form images. In alternative to the conventional CT, there are also cone-beam CT (CBCT) and fan-beam CT (FBCT), characterized respectively by a cone-shaped or a fan-shaped X-ray bundle with an X-ray source and detector, rotating around the patient. The main advantages of these techniques are faster acquisition of the dataset of the entire field of view (FOV), a shorter examination time, and a reduction of image unsharpness caused by the translation of the patient. However, due to the increased scatter from the larger beam size, overall image quality is generally lower with these approaches (Scarfe et al. 2008). Other imaging modalities are also used in radiotherapy treatment planning, such as magnetic resonance imaging (MRI), which enhances soft tissues, and positron emission tomography (PET), which provide information on tumour metabolism (Xing et al. 2006). Specifically, MRI provides complementary anatomic information and guarantees an excellent soft-tissue contrast, a good temporal resolution without the use of ionizing radiation. All these characteristics make MRI an attractive technology for target tumour and OARs definition, and it will be at the basis of this thesis project.

1.2.1.1 Imaging of organ motion

Organ motion is one of the main causes of artefacts in 3D static images. The problem of artefacts is extremely relevant because it can consequently affect dose-calculation accuracy (Keall et al. 2006b). The need to account for and reduce the impact of organ motion has resulted in the development of different motion compensation strategies. Among these, there are methods for the reduction of respiratory motion, which include:

i. abdominal compression: realized with a body frame equipped with a small abdominal plate to reduce diaphragm motion;
ii. breath-hold: the patient is asked to interrupt breathing during image acquisition. The disadvantage is that the patient might not be able to hold the breath in a

consistent position for multiple-breath-hold imaging or for the duration of the acquisition process;

iii. active breath hold (ABC): a way to control breath hold thorough an adapted ventilator connected to the patient (Wong et al. 1999). With this method a breath hold of the patient can be initiated and held by controlling the ventilator valves.

There are also methods for CT imaging which allow data acquisition during free-breathing, such as slow CT, inhalation and exhalation breath hold, respiratory gating and four-dimensional CT. In particular:

i. slow CT: allows to obtain the envelop of anatomical structures in a breathing cycle through a very slow CT scanner or acquiring for each slice more than one CT scans (each for a breathing cycle phase) and then averaging them;

ii. respiratory gating (i.e. prospective sorting): a snapshot image of a specific respiratory phase is acquired for reconstructing a motion-free volume with the use of an external surrogate (i.e. a signal representative of respiratory motion) (Kubo et al. 1996). Typically, the respiratory signal is acquired by measuring the displacement of the patient body surface with optical methods, such as the real-time position management (RPM) system (Varian, Palo Alto, California, USA), based on an infrared tracking camera and reflective markers fixed on the patient's thorax. With this system, the respiratory pattern and the range of motion are measured, processed and displayed through a dedicated interface. Another method is the use of an elastic belt equipped with pressure sensors Anzai respiratory gating system AZ-733V (Anzai Medical Co., Ltd, Tokyo, Japan). The advantage of using a respiratory gating approach is highlighted in Figure 5, in which reduced artifacts are visible if the gating approach (Figure 5 B) is used. Both breath-hold and gating acquire an image volume in a single specific respiratory phase, requiring repeated acquisition at multiple reference phases to cover the whole breathing cycle;

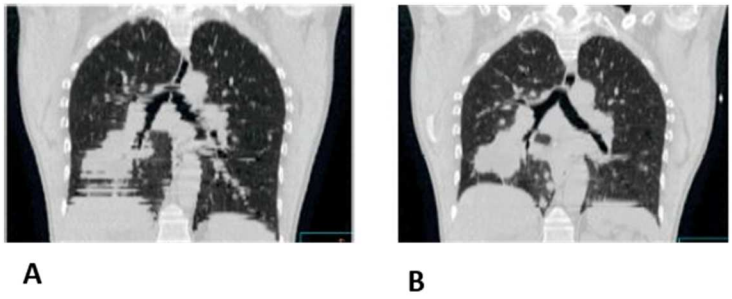

Figure 5. Respiratory gating: coronal view of CT scans of the same patient. A-during free breathing. B-respiratory gating scanning at the end exhalation (from Keall et al. 2002).

iii. four-dimensional CT (4D CT) (i.e. retrospective sorting): is a time-resolved retrospective four-dimensional imaging (4D CT) (Vedam et al. 2003a), which has become a basic component for respiratory motion assessment (Keall et al. 2006b). This method consists of acquiring volumes able to describe the respiratory cycle through the retrospective sorting of 2D slices, acquired in different respiratory states by means of an external surrogate (Figure 6). The entire breathing cycle is typically divided into distinct bins on the phase/amplitude of the respiratory signal and CT images are then sorted into several volumes, according to their corresponding phases/amplitude in the respiratory cycle.

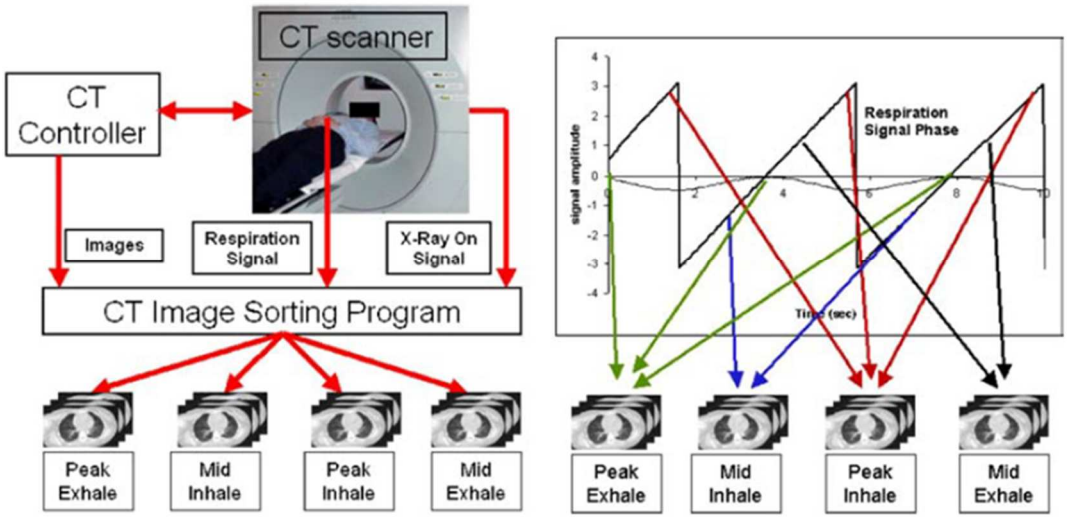

Figure 6. The 4D CT phase-sorting process: the CT images, breathing tracking signal and X-Ray ON signal form the input data stream. The breathing cycle is divided into distinct bins (for example, peak exhale, mid inhale, peak inhale, mid exhale). Images are sorted into these image bins depending on the phase of the breathing cycle in which they were acquired, yielding a 4D CT dataset (from Vedam et al. 2003a).

However, the greater number of slices acquired during the breathing cycle leads to an increase of the ionizing radiation delivered to the patient and the external surrogate may not correlate well with the actual internal motion (Vedam et al. 2003b). A possible solution to overcome the correlation between external and internal signals, is the use of multiple respiratory related signals (Gianoli et al. 2011) or internal surrogates (Zeng et al. 2008), which are expected to improve the 4D reconstruction (Rietzel et al. 2006). Internal surrogates could be derived from implanted markers or, mainly, directly from the acquired images (i.e. image-based surrogates) (Zeng et al. 2008).

Finally, 4D CT volumes are also useful because they can provide the magnitude of the whole motion and on 4D CT the dose calculation can be performed in a way that directly considers the motion information.

1.2.1.2 Quantification of organ motion: deformable image registration

In radiotherapy planning, the expression “image registration” plays an important role with the purpose to align, compare and integrate information from different images (Maintz et al. 1998a, 1998b). Image registration can be used to integrate multi-modality images (i.e. images coming from different systems like CT and MRI) gaining more information or mono-modality images (i.e. images coming from the same system) acquired at different times. Images registration is useful in radiation therapy to quantify organ motion and to transfer the planning situation into the treatment scenario. In general, image registration is an optimization process (Figure 7) for determining a spatial transformation relating the position in one image (reference or fixed image) to the corresponding position in one or more other images (target or moving image).

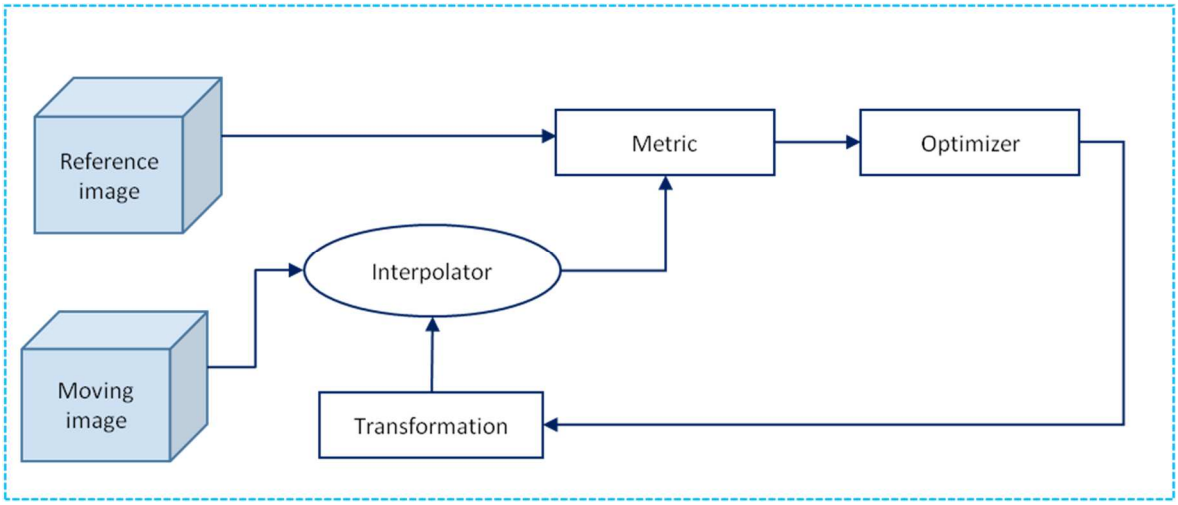

Figure 7. Image registration workflow: fundamental steps of the process.

Considering Figure 7 the blocks of the flowchart are as follows:

- interpolator: transforms the coordinates of the moving image into the physical space of the coordinates of the reference one;
- metric: defines the similarity metric between reference and moving volume depending on mono-modal or multi-modal image acquisition. Example of similarity metrics for mono-modal images are the mean square error (MSE) and the correlation coefficient (CC), whereas for multi-modal images mutual information (MI) and normalized mutual information (NMI) can be used;
- optimizer: finds the optimal parameters of the transformation in order to maximize/minimize the similarity/difference between the reference and moving image;
- transformation: according to this block, registration can be divided in global, applied on the entire image, or local, applied to subsections of the images. Among these, transformation can further subdivided in rigid, affine and deformable (Figure 8).

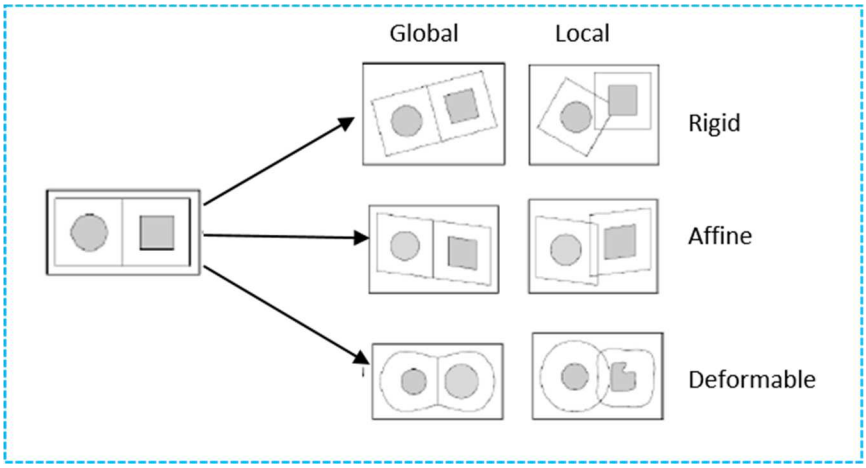

Figure 8. Image registration: type of transformation.

Rigid registration allows only translation and rotation and it is defined by 6 parameters (3 rotational + 3 translational). It preserves straightness of lines and points distance and it is part of most treatment planning systems. It is mainly used to calculate the corrections to apply for differences in patient positioning between planning and treatment. Instead, deformable image registration (DIR) is used to take into account deformation due to the non-rigid nature of the patient body. The output of DIR is described by a deformation model, known as deformation vector field (DVF) (Figure 9), which indicates the displacement between each voxel in the reference image and each corresponding voxel in the target image.

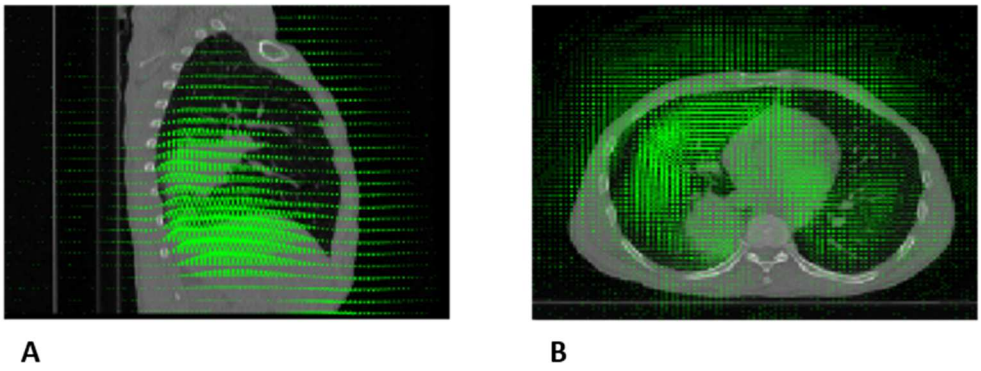

Figure 9. DVF: DVF applied to the image. A-sagittal view. B-coronal view.

There are several ways to compute DVF such as: thin plate splines, radial basis functions (RBF), Demons (based on the intensity conservation between reference and target image)

and free-form deformation (FFD) based on B-splines. In particular, the B-Splines based deformable registration applies a B-spline grid onto the voxel grid of the image (Figure 10). This algorithm obtains interpolated DVFs as result of the interpolation of the B-spline grid on the voxel-grid (Shackleford 2010).

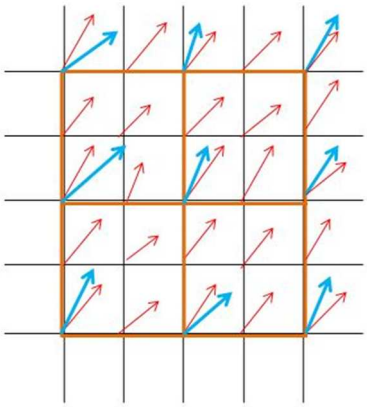

Figure 10. B-Splines DIR: B-spline grid (in orange) applied on the voxel grid (in black) with its vectors (in red) and the resulting interpolated vector field (in light blue).

The DVF is obtained applying the following equation:

$$v(x,y,z) = \sum_{i=1}^{4}\sum_{j=1}^{4}\sum_{k=1}^{4} P(i,j,k)B_i(x)B_j(y)B_k(z)$$

Where:

$B_i(x)B_j(y)B_k(z)$: basis pre-calculated of the B-splines

$P(i,j,k)$: B-splines coefficients to be optimized.

1.2.1.3 Treatment Planning.

Treatment planning refers to the phase in which radiation oncologists and medical physicists create and optimize a patient specific treatment plan. This process is carried out in a virtual environment known as treatment planning system (TPS). From the acquired images, the localization of the target tumour and organs at risk is performed by contouring. Different dose calculation algorithms are used by TPS systems, but all require spatially

accurate electron density information within the patient tissues (i.e. the number of electrons per cubic area). The focus in this project is IMRT plan. Considering IMRT planning techniques, two are the approaches used for the creation of a treatment plan: the forward and the inverse planning. In forward planning the unknown parameter is the dose that has to be prescribed to achieve the purpose of the treatment plan. Once treatment planning images are available, the planner defines the configuration and angles of beams and wedges to obtain the dose distribution. If this dose distribution is acceptable for the specific treatment plan, the plan is ready for being delivered. Conversely, in the inverse planning technique, the planner defines the target dose (i.e. prescribed dose) and the unknown parameters are the weights and the intensity within each beams giving the prescribed dose. A schematic view of the difference between forward and inverse planning is proposed in Figure 11. Although inverse planning is the most used approach for IMRT, they are not synonymous. There are also forward planning approaches that are used, but the inverse one is the most used because the great amount of unknowns to determine (Webb 2003).

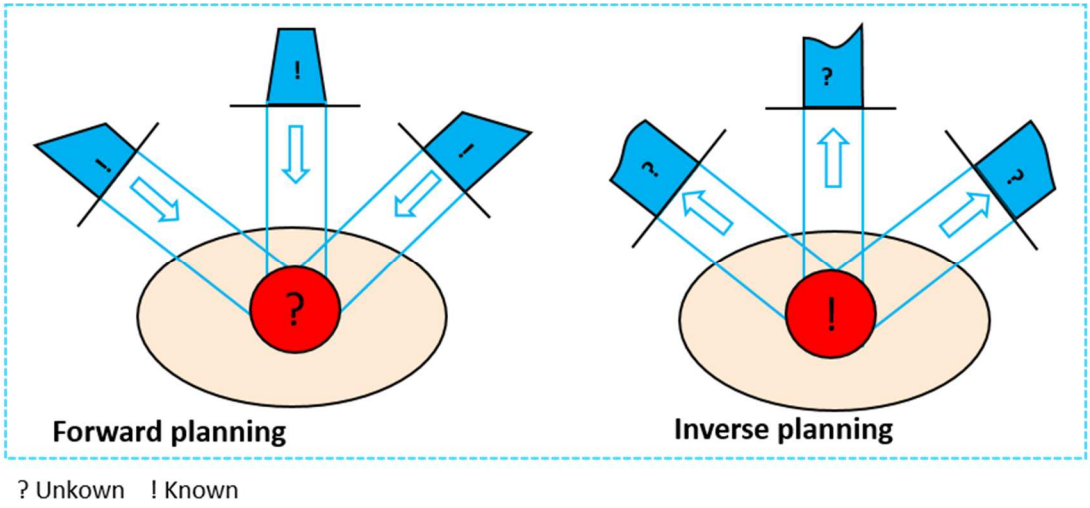

Figure 11. Forward and inverse planning: in forward planning the unknown parameter is the prescribed dose (?) and the beams are the known parameters (!). Conversely, for inverse planning the dose distribution is known (!) while the beams parameters are unknown.

The main issue in inverse planning is the infinite number of beams and their configurations that will give the same dose distribution. For this reason, the inverse planning is also

identified as an ill-conditioned problem. A mathematical formulation for the ill-conditioned inverse problem is given by Webb (2003):

$$\vec{D} = A * \vec{b}$$

Where:

$\vec{D}$: 3D dose distribution

$\vec{b}$: vector of individual beam weights

A: matrix linking each dose-space element to each beam-space element.

In other words, in the inverse problem the prescribed dose D is specified, the matrix A is known and it is required to calculate b:

$$\vec{b} = A^{-1} * \vec{D}$$

However, this is not generally done because there is a large number of vectors $\vec{b}$ that when operate on matrix *A* give the 3D dose distribution $\vec{D}$, and the vectors $\vec{b}$ cannot be negative. A possible strategy for the solution of the ill-conditioned problem is the optimization of a cost function. Basically, in this perspective, the inverse planning problem is represented through a cost function to be optimized. The optimization process means to find the best plan for treating a particular patient with a particular external shape, location of disease and arrangement of internal organs (Webb 2003). A cost function can be defined as:

$$cost\ function = \sum I(x,y,z)[D(x,y,z) - D^P(x,y,z)]^2$$

Where:

$D^p(x, y, z)$: the prescribed dose distribution

$D(x, y, z)$: the actual delivered dose

$I(x, y, z)$: the importance of each voxel.

The optimization problem is an iterative process which continues until the global minimum of the cost function is found. As iterations go on, each beam element (i.e. beamlet) change

and these changes are accepted if they lead to a lower cost function. When the beams are off (number of iterations=0), the cost function is:

$$cost\ function = \sum I(x,y,z)[D^P(x,y,z)]^2$$

Hence, in the following iterations, when the beams are turned on, the cost function gradually decreases while *D(x, y, z)* increases. In Figure 12 A a plot for a generic cost function with a well defined global minimum (red cross) and other local minima (green circle) is shown. In Figure 12 B, a plot for a cost function representing the inverse problem is shown. The wide plateau of the function represents all possible beams arrangements that correspond to the same dose distribution (ill-conditioned problem), where a small dip in the plateau might be present, representing the best value of the cost function.

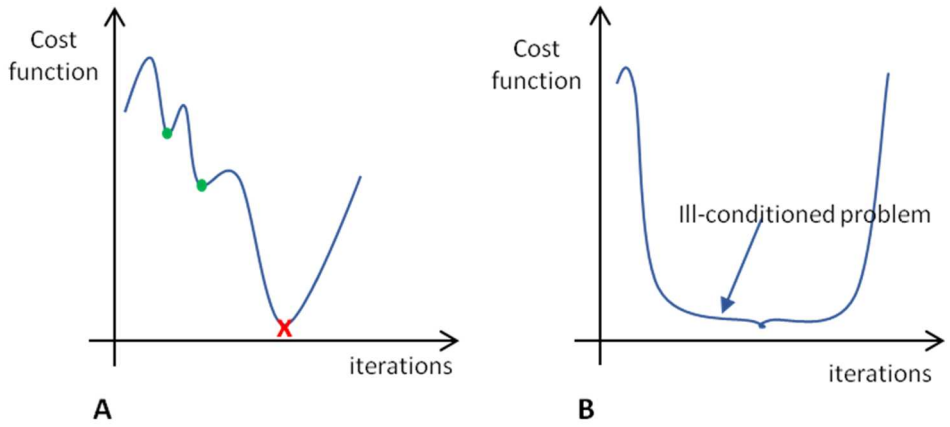

Figure 12. Cost function representation: A-a generic cost function with global minimum (red cross) and local minima (green circles). B-a cost function representing the inverse problem.

Before the optimization process, each beam is divided in a number of smaller beamlets and the corresponding dose distributions are computed (Dobler et al. 2009). Each beamlet has a specific weight. This process is also known as beamlet-based inverse planning and consists of the steps illustrated in Figure 13.

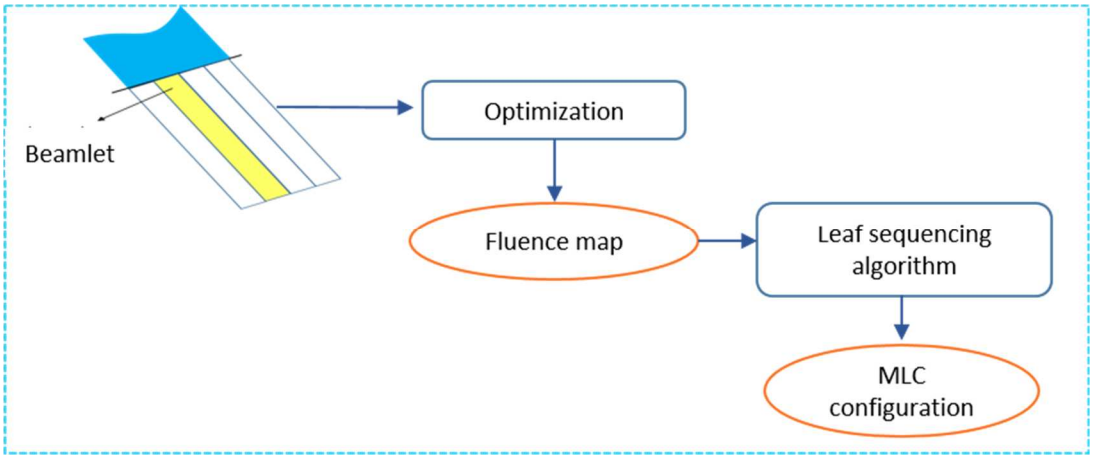

Figure 13. Workflow of the beamlet-based inverse plan: fundamental steps of the process.

Specifically:

i. beamlet weights are optimized to produce an optimized fluence map for each beam direction;
ii. a leaf sequencing algorithm is applied to translate each optimized fluence map into a set of deliverable aperture shapes of the MLC.

The beamlet-based optimization requires a large number of segments and monitor units, which can require also long treatment times. For this reason, the direct aperture optimization (DAO) or the direct machine parameter optimization (DMPO) algorithms, in which the MLC setting is produced during the optimization (see section 2.3.1 in Chapter II), are preferred. Another important aspect of the optimization process is the definition of objective functions and constraints, which drive the optimization. The objective function represents the function to be minimized in order to obtain the optimum plan. Keall et al. (2006a) report a table of dose-volume constraints for IMRT treatment planning that give acceptable plans over a range of tumour volumes and locations (Table 1).

Table 1. Dose volume constraints proposed by Keall et al. (2006a) for IMRT plans. In this case the prescribed dose is 74 Gy in 37 fractions to the 95% of the PTV.

Structure	Constraint type	Dose [Gy]	Volume [%]	Weight
PTV	Min DVH	74	95	100
PTV	Min Dose	66.6	-	40
PTV	Max Dose	88.8	-	40
Lungs minus GTV	Max DVH	20	30	20
Spinal cord	Max Dose	45	-	50
Heart	Max DVH	55	50	20
Oesophagus	Max DVH	55	30	40

Objective functions can be divided in (Carlsson 2008):

- physical functions: based on the direct measures in the dose domain. The functions that belong to this category are (i) the maximum dose, which is typically used for OARs since only voxels with dose exceeding the prescribed dose level are penalize, (ii) the uniform dose, (iii) the minimum dose, which is used for target tumour and (iv) the maximum or minimum dose that a percentage of the interested volume should receive, which are the Max DVH and Min DVH;
- biological functions: based on radiobiological models that predict the clinical outcome of the dose distribution. In this category there are (i) the "tumour control probability" function (TCP), which is the probability of local control given the planned dose distribution, and (ii) the "normal tissue complication probability" function (NTCP), which is the probability of some defined undesirable effect on the patient due to irradiation (Brahme 1999).

Instead, the constraints place restrictions on the set of solutions, which are considered feasible. They define what is an acceptable solution, driving the optimization process.

Different TPS systems are available in the clinic. For this project the attention will be focused on the Pinnacle^3 TPS which uses a gradient iterative method to find the best solution. More details will be given in Chapter II, section 2.3.1.

1.2.2 Treatment delivery

In this phase, the patient receives the target dose assessed by doctors and radiation oncologists in the planning. One of the main challenges is to correctly transfer the planning situation in the in-room scenario, in terms of correspondence in patient positioning and anatomical alignment of internal structures to ensure the correct position of the patient at the time of each radiation treatment. This is the reason why in-room real-time monitoring, able to directly or indirectly observe the target position during treatment, is necessary. In clinical routine, different approaches are available. Simple approaches are non-image-based, in which the patient is positioned and moved by inferring the location of internal anatomy from surface landmarks (e.g. optical tracking) (Bentel et al. 1999). The disadvantage of this approach is due to the presence of uncertainties in deriving the target position, because the external surrogate may not correlate well with the internal anatomy. Also, approaches based on CBCT, that uses a rotating gantry through which the X-Ray source and the detector rotate around the patient, could be useful (Scarfe 2008). The cone-shaped source of ionizing radiation is directed through the target volume onto an X-Ray detector on the opposite side. During the gantry rotation, sequential planar projections images of the field of view (FOV) are acquired. These series of planar images are, then, subject to a tomographic reconstruction (Bissonnette et al. 2009), hence ensuring the acquisition of the whole volumes useful to verify soft-tissue position. Accurate placement of the radiation beam at the prescribed location on the patient can be achieved through the use of electronic portal image devices (EPID) to measure the X-ray intensity transmitted through a patient from a radiation port during a treatment session (Herman et al. 2001). The great advantage of this technique is that internal structures such as the diaphragm are visible with mega-voltage (MV) images (i.e. EPID) and can be correlated with tumour location. However, kilo-voltage (kV) radiography or fluoroscopy yield higher contrast images for a lower energy (Xing et al. 2006), allowing more frequent imaging. Also ultrasound (US) techniques, in which conventional systems are employed in conjunction with a tracking system (optical or robotic) to allow US images of internal anatomy, providing real-time information, can be useful. US systems have the advantage of low cost, easy integration within the RT process and lack of ionizing radiation. However, bones or air cavities can generate reflections which interfere with the US signal from soft-tissue targets. In addition, this technique is severely operator-dependent.

1.2.2.1 Management of organ motion

The presence of organ motion due to respiration during treatment delivery causes a blurring of the static dose distribution and consequently a shift between the desired and the delivered dose. Therefore, the compensation for organ motion during treatment delivery is of primary importance in order to increase the treatment accuracy. A first method is respiratory gating, in which the compensation for organ motion consists of turning on the beam only in specific respiratory states. However, it has been shown that a better way to treat a moving target may be dynamic MLC tracking, in which the MLC is used to track the tumour motion (Keall et al. 2001). Real-time image-guidance strategies require a method to directly or indirectly observe the target position continuously during treatment. Direct localization strategies entail the real-time measurement of the target position. Fluoroscopy at kV energies can be employed to localize radio-opaque fiducials implanted into (on near to) the tumour volume: a frequency of 30 images per second is reached by Shirato et al. (2000) with an accuracy better than 1.5 mm. However, a relevant non-therapeutic dose is delivered to the patient if fluoroscopy is applied for the whole treatment duration and the implantation of radio opaque fiducials, which is required to cope with the low tumour contrast in kV images, represents an additional risk, especially for lung cancer patients. EPID can be also used to track internal markers; a recent real-time solution proposed by Fuangrod et al. (2013) utilizes a comprehensive physics-based model to generate a series of predicted transit EPID image frames as a reference dataset and compares these to measured EPID frames acquired during treatment. Indirect strategies to follow target position during treatment are explained in the next paragraph.

1.2.2.2 Dose assessment during treatment

A major issue with the current practice of radiotherapy is that anatomical variations can introduce large uncertainty in the delivered dose. Discrepancies between planned and delivered dose to tumours and normal tissues can lead to unsafe and/or ineffective treatments; as such, techniques enabling the calculation of the delivered dose incorporating anatomical motion are of great importance. Several methods have been reported to assess the delivered dose during treatment. Among these, some approaches have been developed to link EPID images to actual delivered dose thanks to the fact that EPIDs are available on existing clinical equipment and require no additional imaging dose (Cai et al. 2015). A

dose estimation method based on MV images acquired by EPID was proposed by Berbeco et al. (2007) and by Aristophanous et al. (2011). Elmpt et al. (2009, 2010) combined CT with images recorded by EPID during treatment to verify the delivered dose. Other approaches, reported by Veiga et al. (2015), proposed the use of DIR as a tool to assess the delivered dose at each time of the treatment. This technique is known as "dose warping" and entails the application of the DVF to the fraction by fraction dose maps to deform them with respect to a reference in order to appreciate dose variations. The choice of the DIR algorithm leads to uncertainties in dose warped, especially for regions with poor imaging quality (Veiga et al. 2015).

1.3 Motion models

An alternative to direct X-ray imaging involves the indirect motion monitoring through the use of motion models. Motion models attempt to find a relationship between the motion of interest (i.e. organ motion) and surrogate data, used when it is not possible to directly measure the motion of interest. Surrogate data have an important role in the definition of a motion model and they should be easy measurable, have a strong correlation with the motion of interest and a sufficiently high temporal resolution. There are different sources and physical measurements that can be used to obtain surrogate data, such as respiratory bellows, that describe the movement of the chest and the spirometer, that measures the air flow to and from the lung, used together with an optical tracking signal (Lu et al. 2005). Moreover, there are optical tracking technologies, such as the RPM system, that track the motion of one or more points on the surface of the chest or the abdomen. Alternatively can be employed electromagnetic or laser based tracking systems. Therefore, the basic idea is to track external markers or breathing signals (i.e. surrogates for the indirect motion monitoring) spatially and temporally correlated with tumour motion (Vedam et al. 2003b). A patient specific correlation model is used to infer the tumour position as a function of the surrogate and it is periodically updated with the information on the actual tumour position acquired with the imaging system (Murphy et al. 2006). The main issue regarding the indirect solution is establishing a reliable correlation between internal and external surrogates, especially when tumour motion is irregular. In addition, it should be stressed out that patients' breathing patterns can vary in amplitude, period and regularity during

treatment sessions and there could also be systematic changes in the respiratory baseline. Moreover, motion features may be markedly different between patients, suggesting a customized approach to respiratory management. Nowadays, there are several models in X-ray radiotherapy that clinical implement this correlation, such as the CyberKnife system (Accuracy, Sunnyvale, California, USA) (Kilby et al. 2010) and the VERO system (Vero GmbH, Germany) (Kamino et al. 2006). In the CyberKnife, a linac mounted on a robotic manipulator delivers treatment beams with high precision. The system compensates organ motion thanks to a model correlation between the configuration of three infrared external surface markers (surrogate signal) and the internal target position. Image acquisition, target localization and alignment corrections are repeated continuously during treatment delivery, typically every 30–60 s (the imaging interval can be adjusted during treatment based on the stability of the target position). For targets that move due to respiration an additional tracking system enables beams to move in real-time to follow the target. The second example is the Vero system (Vero GmbH, Germany), that has a gimbaled irradiation head and predicts motion by means of models which uses real-time infrared monitoring of patient's surface points and periodical imaging verification. It performs adaptation of the correlation model to moving pattern similarly to the CyberKnife system.

In addition to clinically implemented solutions in the literature global image-based respiratory motion models have been proposed. The motion is estimated from the imaging data (e.g. using image registration) and the motion model approximates the relationship between the surrogate data and the motion (Figure 14). Therefore, the construction of global motion models is able to describe the whole internal anatomy and can improve the description of the motion and the identification of tumour with respect to the surrounding healthy structures (McClelland et al. 2013).

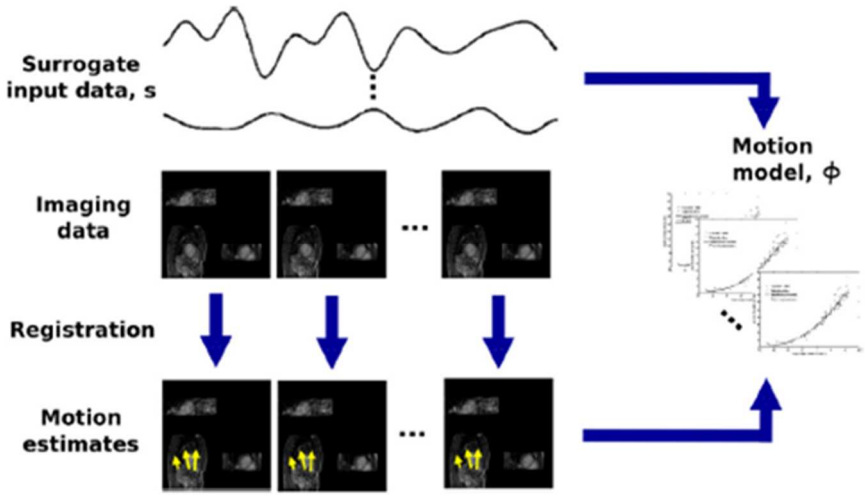

Figure 14. Motion Model: creation of motion model (from McClelland 2012).

Most of the respiratory motion models presented in the literature are patient specific, based on 4D CT (Vandemeulebroucke et al. 2009, Fassi et al. 2015) or MRI dataset (Fayad et al. 2012). Specifically, Fayad's model is based on principal component analysis (PCA) and uses 4D MRI imaging for the model creation step. Subsequently, the model is updated with two "breath hold" 3D MRI volumes and 2D MRI images which are using a 2D image navigator which relates to the internal organ motion described by the motion fields. This model is similar to the one previously developed by Fayad et al. (2009) which is 4D CT based and requires the use of external surface patient acquisitions. Vandemeulebroucke et al. (2009) proposed a method for estimating respiratory motion from the 2D cone beam (CB) projection sequence acquired during treatment. First, the parametric patient-specific motion model is created from the 4D CT acquired pre-treatment for irradiation treatment planning and then the model is fitted to the CB projection by optimizing the parameters in order to maximize the similarity between the 2D CB projection and the simulated projection of the model. These two motion models will be described in details in sections 2.2.1 and 2.2.2, since these models are the basis of this project. In this framework, Cai et al. (2015) proposed an approach to assess actual 3D delivered dose for patients with significant respiratory motion during SBRT treatment through the reconstruction of 3D images of the patient using kV or MV projection images. These images are acquired at sampled timepoints during treatment, and at each timepoint the 3D dose distribution is calculated and then the deformed doses are accumulated to assess the actual delivered dose

to tumour and critical organs. Recently, Hurwitz et al. (2014) proposed to reconstruct the 3D images of respiratory phases during treatment using external surrogate signals, based on which the actual delivered dose can be calculated for the entire volume.

1.4. Magnetic Resonance Imaging and its role in image-guidance

The development of next-generation IGRT systems integrating the use of MRI is currently showing important progress (Jaffray 2012). The reasons why MRI has become an attractive technology for target and organs at risk definition are numerous: the absence of ionizing radiation, the high contrast of soft tissues and the good temporal resolution in dynamic acquisition modality. In addition, MRI imaging systems can offer functional information. Diffusion-weighted imaging has the ability to monitor physiological changes during treatment and dynamic contrast enhanced imaging is an accurate assessment of the tumour environment.

1.4.1 In-room MRI systems

The exquisite properties of MRI motivated several recent technological developments towards the integration of MRI with radiation therapy treatment units, raising the prospect of fully MRI-guided treatments (Menard et al. 2014). Different groups are working on the integration of in-room MRI into radiotherapy guidance (Figure 15) and these systems will be available soon in different clinical centres.

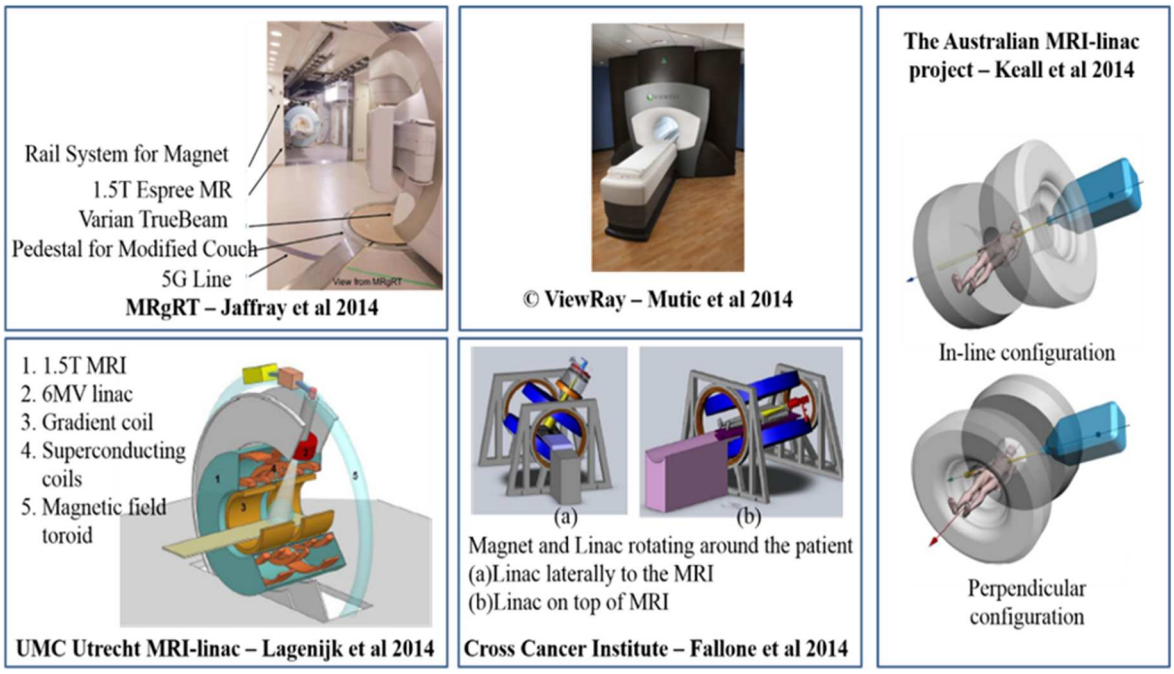

Figure 15. In-room MRI configurations: different systems developed.

The system proposed by Jaffray et al. (2014) consists of a 1.5T MRI scanner on rails which can be moved into and out of a treatment room with a 6MV linac. This configuration however does not allow real-time MR imaging during treatment delivery, as the MRI scanner cannot be in the treatment room during treatment. The ViewRay™ system (Mutic et al. 2014) is already in clinical use and is based on three Cobalt-60 units equipped with MLC positioned in a ring in the mid transversal plane of the MRI system: the system can rotate 120° to allow radiation delivery from each gantry position. Limitations are linked to:

i. the characteristic of the Co-60 radiation beam, which provides beams with lower output, less penetration, larger penumbra, and higher surface doses than a linear accelerator even if the radioactive decay does not interfere with operation of an MRI unit;
ii. low-field MRI of 0.35 T, which is known to provide images with less signal-to-noise ratio and shorter relaxation times even if magnetic susceptibility artefacts, heating and perturbation of the dose distribution are prevented.

Other groups are developing systems in which an MRI and a linear accelerator are integrated into one system. This is the case of Fallone et al. (2014), Keall et al. (2014) and

Lagendijk et al. (2014), which provide an MRI-guided system with a 6MV linac in a conventional bunker with different field strength and magnet configurations. Specifically, the UMC Utrecht prototype system (Lagendijk et al. 2014) consists of a modified 1.5T MRI and a 6MV accelerator in a ring in the mid-transversal plane around the MRI for continuous rotation in either directions (Raaymakers et al. 2009). In this case, active shimming is required to compensate for magnetic variations that occur at different gantry angles. These variations are the result of the movement and position of magnetic linac components. In fact, rotating the gantry while imaging, adds a further layer of variability to the scanner magnetic field. Two ways in which image distortions can be minimized are the dynamic adaptation of the scanner's magnetic field (i.e. dynamic shimming) and advanced image reconstruction methods (Crijns et al. 2014). In the configuration proposed by Fallone et al. (2014) the accelerator is positioned laterally to the MRI (0.56T), so the beam enters through the open side of the magnet. In this way the beam transmission is facilitated and the variability due to linac components in the magnetic field is reduced. To allow irradiation from multiple beam angles the accelerator has to rotate together with the MRI around the target. The accelerator can be positioned either laterally to the MRI, so the beam enters through the gap, or on top of the MRI, where a dedicated hole in the MRI allows the beam to enter. The Australian MRI-linac proposed by Keall et al. (2014) is a specifically designed 1T open-bore MRI (Agilent) with a 6 MV linac system (Varian Linatron), designed to provide both in-line (i.e. beam parallel to the external magnetic field) and perpendicular (i.e. beam perpendicular to the external magnetic field) orientations as shown in Figure 15. The in-line approach provides also the possibility to rotate both the MRI-linac and the patient, in the horizontal and the up-right planes as shown in Figure 16.

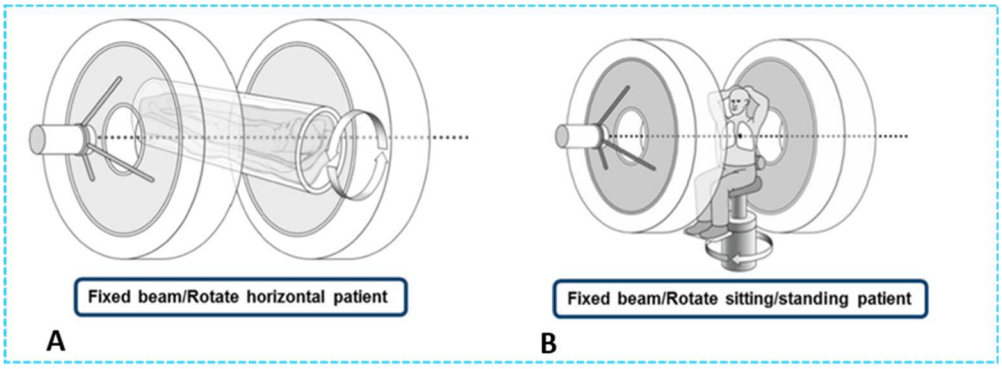

Figure 16. Configuration options for in-line approach: A-patient rotation in the horizontal plane. B-patient rotation in the upright plane (from Keall et al. 2014).

A major obstacle in MRI linac development are the electromagnetic interactions which occur between the MRI and the linac. Various authors have investigated these effects; Kolling et. al (2013) report MLC (Varian Millennium 120 leaf MLC) influences on the imaging volume homogeneity, showing that (i) the MLC does not induce significant field inhomogeneity if the source-axis distance increases (i.e.140cm or more) in both the in-line and the perpendicular orientations, (ii) the different positions of the MLC leaves during treatment does not induce inhomogeneity that is sufficient to require dynamic shimming and (iii) the force between the MLC and the magnet is manageable. Studies on the effect of the magnet on the linac focusing on the electron gun were carried out by Constantin et al. (2011). It was demonstrated that (i) the magnetic field affects an unshielded electron gun and (ii) in the in-line configuration the primary beam current does not vanish but a large reduction of beam current (up to 77.1%) is observed at higher field strengths (from 0 to 0.16 T). (ii) In the perpendicular configuration the current vanishes due to beam bending under the Lorentz force. Modifications to the gun can potentially improve the performance (Keall et al. 2014). Studies on skin dose were also performed on a water phantom by Oborn et al. (2010), showing that significant skin doses at the beam central axis are reported for large positive surface angles and strong magnetic fields. In addition, electron contamination from the linac may cause considerable skin dose increase or hot spots at the beam central axis in the longitudinal field. This depends heavily on the properties of the magnetic fringe field entering the linac beam collimation system, the MRI coil thickness and the isocentre distance of the linac (Oborn et al. 2012). Furthermore, the potential for MRI to guide adaptive radiotherapy to account for tumour deformation using an MLC has

been demonstrated (Ge et al. 2012). Specifically, the deformation was actuated to deformable phantoms by a linear motion platform and the intra-fractional images were acquired by the on-board kV imager. Using a deformable image registration software, the sequential motion fields were used to interpolate the displacement at the end points of each leaf of the MLC, thus proposing a real time dynamic MLC tracking prototype system capable of adapting the beam aperture to the deforming target.

1.4.2 In-room MRI-guidance

Nowadays the first implementation of an MRI-guided system (Mutic et al. 2014) delivers radiotherapy irradiating the patient in a specific breathing phase (i.e, gated approach) ensuring that the desired radiation dose is delivered to the tumour and that normal tissues and other OARs are spared. However, the potential improvement in MRI-guidance is the achievement of a real-time tumour-tracking approach. Initial works on tumour tracking in MRI studied the use of MRI navigator signals as surrogates to track tumour motion. These signals provide high temporal information on a 1D dimensional scale and have been evaluated both for gated delivery (Crijns et al. 2011) and for real-time tracking (Crijns et al. 2012). The real-time tracking of the tumour motion and deformation can be difficult with this approach due to the 1D signal extracted from the navigator. This problem can be overcame through the acquisition of 2D fast cine-MRI images, which allow continuous imaging during respiration and tracking of internal anatomical structures. Several studies propose tumour tracking relying on the template matching technique: following manual selection of a region of interest (i.e. tumour, internal structure), the template matching approach tries to find the same region of interest (ROI) in the series of 2D cine-MRI (Tryggestad et al. 2013a, Cervino et al. 2011). Moreover, the capability of MRI to work on different planes permits the acquisition of orthogonal cine-MRI slices intersecting on the target thus obtaining the 3D position of the tumour. However, all these approaches are time consuming and suffer from inter-operator variability. As an alternative, several algorithms for automatic feature extraction have been developed, such as the scale invariant feature transform (SIFT). As reported by Paganelli et al. (2015a), the SIFT-based method has been used for the extraction of distributed features in cine-MRI images, providing accurate motion quantification as function of breathing related variables. This method is widely reported in the literature for image registration purposes (Allaire et al. 2008), for tracking

region of low-contrast in cine-MRI images (Mazur et al. 2016) and, as mainly required in radiation therapy applications, for organ motion quantification (Paganelli et al. 2012).

1.5 Aim of the project

In the last 20 years, technological innovations have enabled the integration of biomedical images into the radiotherapy system with the aim to quantify and compensate for organ motion (Jaffray 2012), with a specific interest in the use of Magnetic Resonance Imaging (Plathow et al. 2004).

Nowadays, the clinical practice for organ motion management in treatment planning is derived typically from pre-treatment 4D CT images, allowing the simulations and optimization of all the geometric, radiological, and dosimetric aspects. The integration of additional images during the treatment itself with in-room units allows treatment adaptation, thus achieving highly accurate and precise radiotherapy to the constantly changing anatomy of a cancer patient (Xing 2007). Recent attention has been specifically direct to the integration of MRI directly in the treatment scenario, thanks to its exquisite properties. However, the transfer of the treatment planning in the treatment delivery situation and the on-line adaptation of the treatment is still a challenge, since inter and intra-fractional changes cause uncertainties in the dose delivered to the tumour. A possible solution, presented in the literature, is the use of global motion models, which allow the update of a model built on the pre-treatment data through a surrogate acquired during treatment. In this work, we translate the use of global motion models typically used for X-ray-based imaging in an MRI-guided scenario: the model trained on pre-treatment 4D CT is updated on the basis of different surrogates derived from cine-MRI slices acquired during treatment. Specifically, two different patient-specific motion models have been tested for validation purposes on a digital anthropomorphic CT/MRI phantom and subsequently applied to different patients. Quantifications are then performed in terms of both geometric and dosimetric variations between pre-treatment and treatment, in order to provide a preliminary approach for treatment adaptation.

Chapter II: Methods and materials

The main purpose of this study is the evaluation of the geometric and dosimetric variations between the treatment planning and delivery, where cine-MRI samples are acquired. In this chapter, after the description of the image datasets, two patient specific motion models are described in detail, along with the geometric experiments that were carried out. Then, after the description of the selected dosimetric approach, the dosimetric experiments based on the previous geometric results are described.

2.1 Image datasets

Three different scenarios are tested in this study: (i) a digital anthropomorphic CT/MRI phantom, which is used to validate and test the motion models, and (ii) two patients having 4D CBCT throughout treatment, and (iii) one patient having cine-MRI images taken throughout treatment. These data sources are described in detail below.

2.1.1 CT/MRI digital phantom

The pre-treatment 4D CT dataset of the digital phantom is derived from the extended cardiac-torso (XCAT) phantom (Segars et al. 2010). The 4D CT consists of 10 respiratory volumes of the entire thorax (an example is shown in Figure 17), with a matrix of 384×384×384 voxels and a resolution of 1 mm in all directions, representing the mean respiratory cycle of a patient respiratory signal.

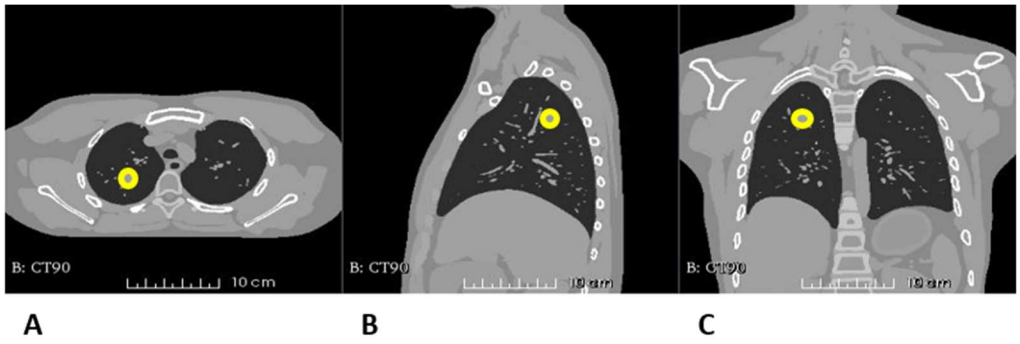

Figure 17. CT volume-CT/MRI phantom: a slice centred in the tumour (underlined in yellow). A-axial plane. B-sagittal plane. C-coronal plane.

The treatment dataset is derived by the MRI version of the XCAT (Paganelli et al. 2015) from 1024 CT volumes (temporal resolution: 150 ms, matrix size 384×384×384, resolution 1×1×1mm). Therefore, the treatment dataset consists of 1024 2D orthogonal cine-MRI slices, acquired alternatively in sagittal (AP vs. SI direction) (Figure 18 A) and coronal plane (RL vs. SI direction) (Figure 18 B) every 150 ms, achieving 3D information around the tumour. The 1024 CT volumes represent the ground truth, which is used to validate the model output.

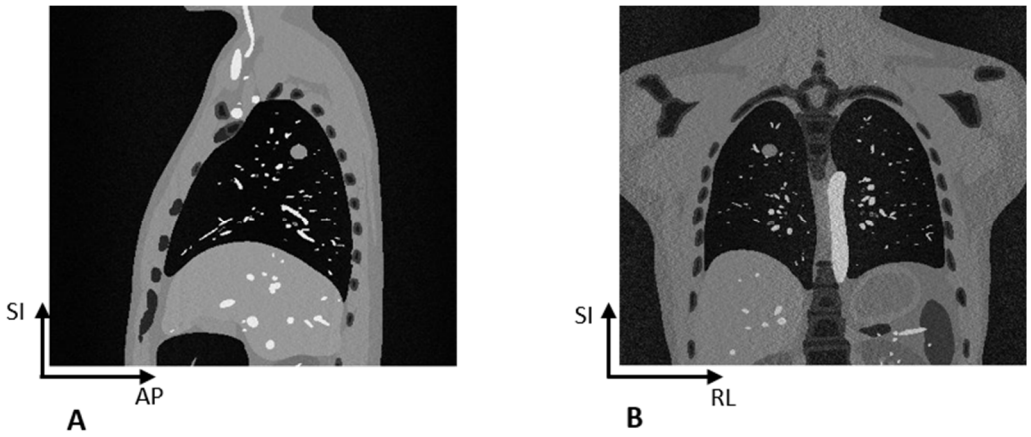

Figure 18. MRI orthogonal sample-CT/MRI phantom: A-sagittal plane. B-coronal plane.

The CT/MRI digital phantom, with a tumour of 7.55 mm radius in the right lung, is generated with a diaphragm motion in SI and AP direction of 16 mm and 4 mm respectively during treatment, while the tumour has a motion of 8 mm and 4 mm in SI and AP direction respectively.

2.1.2 CT/CBCT patients

The pre-treatment 4D CT dataset of the first group of patients (patient A and patient B) consists of 10 respiratory volumes of the whole thorax (with a resolution of [0.98 0.98 3] mm in RL, AP and SI directions) and an average CT volume. From the average CT, which represents the mean position of the anatomy during the breathing cycle, the lungs and tumour boundaries has been contoured by an expert (Figure 19). The CT volume of patient A is 512×512×131 pixels. This patient has a large tumour (with a volume at the 0% exhale phase of 111.6 cm^3) in the lower part of the right lung close to the spinal cord. Patient B is composed by a matrix of 512×512×77 pixels and a smaller tumour (volume at the 0% exhale phase of 13.35 cm^3) in the upper part of the right lung.

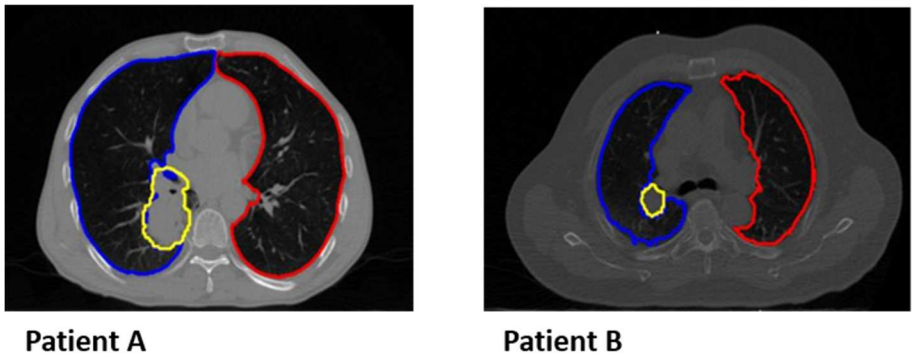

Figure 19. Average CT boundaries-CT/CBCT patients: the red lines show the manual contours of the left lung, the blue lines surround the right lung and the yellow lines highlight the tumour.

The treatment dataset consists of 4D CBCT (10 phases, included the 0% exhale phase) patient projections, reconstructed through a respiratory signal (RPM signal), a binning method (respiratory phase binning) and McKinnon-Bates (MKB) reconstructed algorithm (McKinnon et al. 1981), that is a common approach for reducing noise (Shieh at al. 2014).

A matrix of 450×450×220 pixels and a resolution of 1 mm in all directions (Figure 20) characterizes the CBCT dataset of the two patients. As already explained, in our work the attention is focused on 2D cine-MRI acquired in treatment, therefore these reconstructed volumes will be used to simulate orthogonal cine-MRI acquisitions (i.e. orthogonal slices centred in the tumour are extracted from the CBCT dataset).

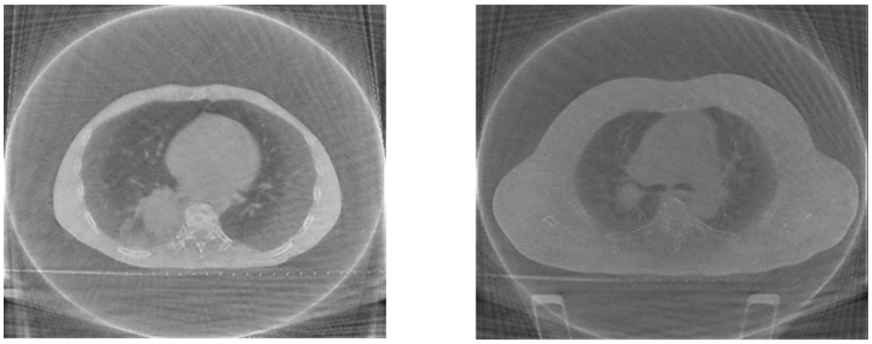

Figure 20. CBCT slice-CT/CBCT patients: slice centred in the tumour taken from the 0% exhale phase.

2.1.3 CT/cine-MRI patient

For the third patient (Patient C) the pre-treatment 4D CT dataset consists of 10 respiratory volumes. On the exhale phase, an expert has manually delineated the tumour boundaries (yellow line in Figure 21 A). Each phase of the 4D CT volumes consists of a matrix of 512×512×65 pixels (resolution of [0.78 0.78 2] mm). This patient has a tumour in the left lung (volume in the 0% exhale phase of 23.37 cm^3) close to the heart. Unfortunately, as shown in Figure 21 B on the sagittal view, the 4D CT volumes are truncated (only the right diaphragm is visible and the upper regions of the lungs are cut).

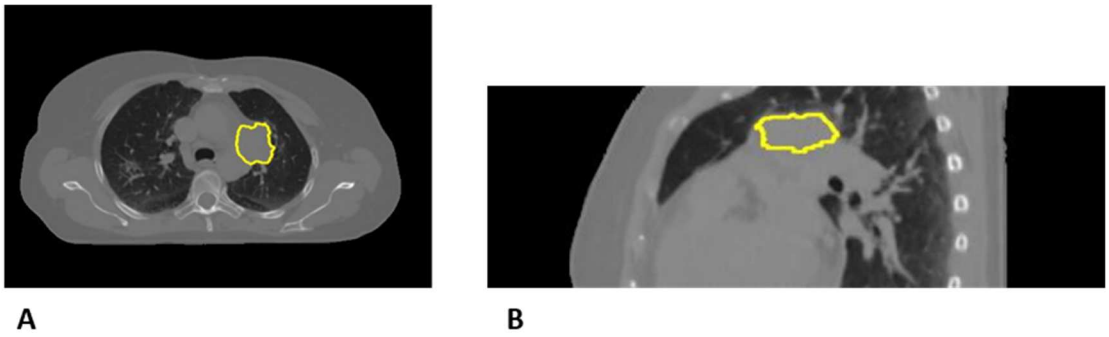

Figure 21. CT boundaries-CT/cine-MRI patient: slice taken from the 0% exhale phase. A-axial plane. B-sagittal plane.

The treatment dataset (Figure 22) consists of 512 2D cine-MRI orthogonal samples and a gated-MRI acquired at the 0% exhale phase. The 2D cine-MRI samples, from which the tumour boundaries were segmented by an automatic segmentation process (Lee et al. 2012), are acquired alternatively every 300 msec in sagittal and coronal plane achieving, in

this way, 3D information around the tumour. Every cine-MRI sample is composed by a matrix of 256×256voxels with a resolution of [1.48 1.48 5] mm.

In addition, the RPM signal is recorded in both planning and treatment, as external surrogate to resort the 4D CT and to provide a surrogate (in addition to the internal ones derived from the cine-MRI data) for the treatment situation.

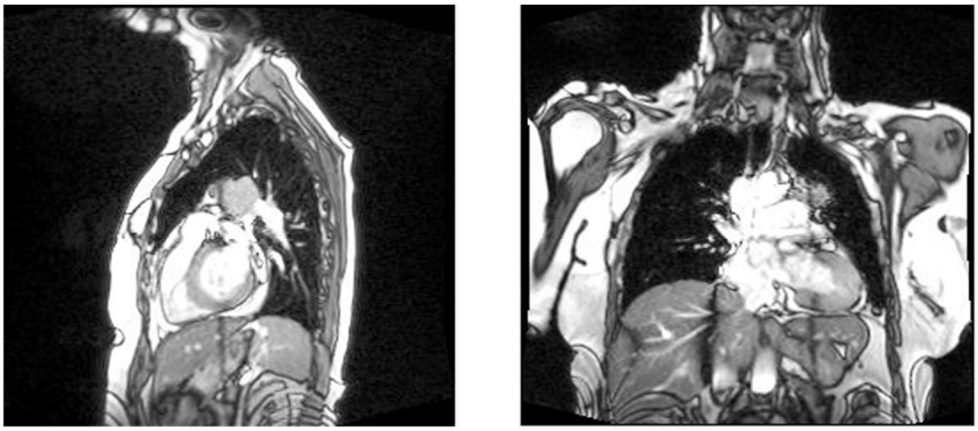

Figure 22. 2D cine-MRI samples-patient C: A-sagittal plane. B-coronal plane.

In Table 2 are summarised the image dataset and the different features for each patient.

Table 2. Summary of image dataset and tumour location and volume of each patient.

DATASET			TUMOUR	
Patient	**Pre-treatment**	**Treatment**	**Location**	**Volume**
Patient A	4D CT	CBCT	Lower lobe of the right lung	111.6 cm^3
Patient B	4D CT	CBCT	Upper lobe of the right lung	13.4 cm^3
Patient C	4D CT	2D cine-MRI samples	Left lung, attached to the heart	23.7 cm^3

2.2 Geometric adaptation

As described in section 1.3, a motion model is a process that, taking a surrogate data as input, produces a motion estimate as output (McClelland 2013). The general idea of a global motion model approach is shown in Figure 23. The motion model is constructed starting from the training 4D CT: a relationship between the motion field derived by a DIR between each respiratory phase and a reference volume, is defined with a pre-treatment surrogate. Then, the motion model is updated on the basis of the real-time surrogate acquired during treatment. In the literature, different types of models are available; in this section, two surrogate driven motion models are described.

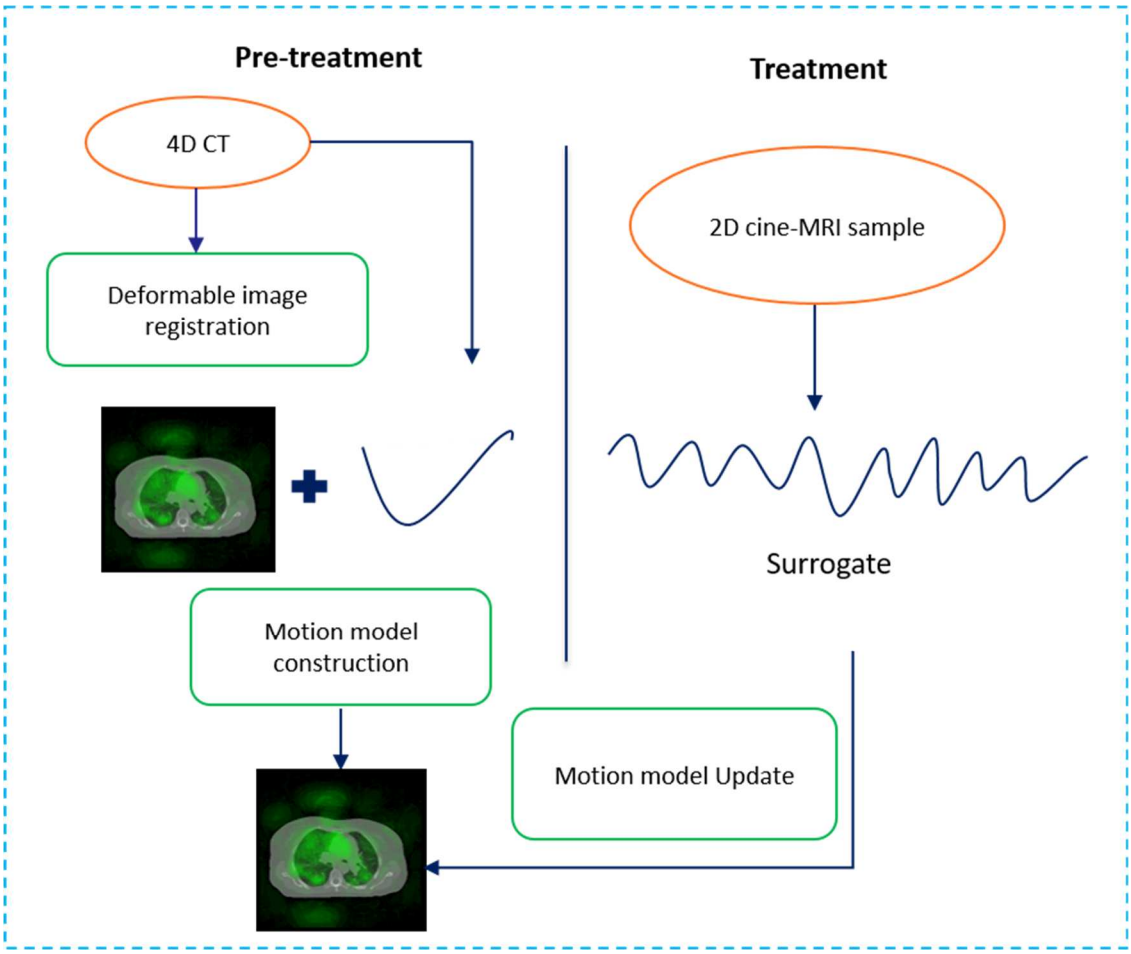

Figure 23. Motion model: the motion model construction is based on a DIR between all the respiratory phases and a reference phase and a respiratory signal. Then the model is updated in treatment sessions, employing a respiratory signal.

2.2.1 Description of Vandemeulebroucke's model

The first motion model used is the one developed by Vandemeulebroucke et al. in 2009. The adaptation to the available data has led the model to the layout shown in Figure 24.

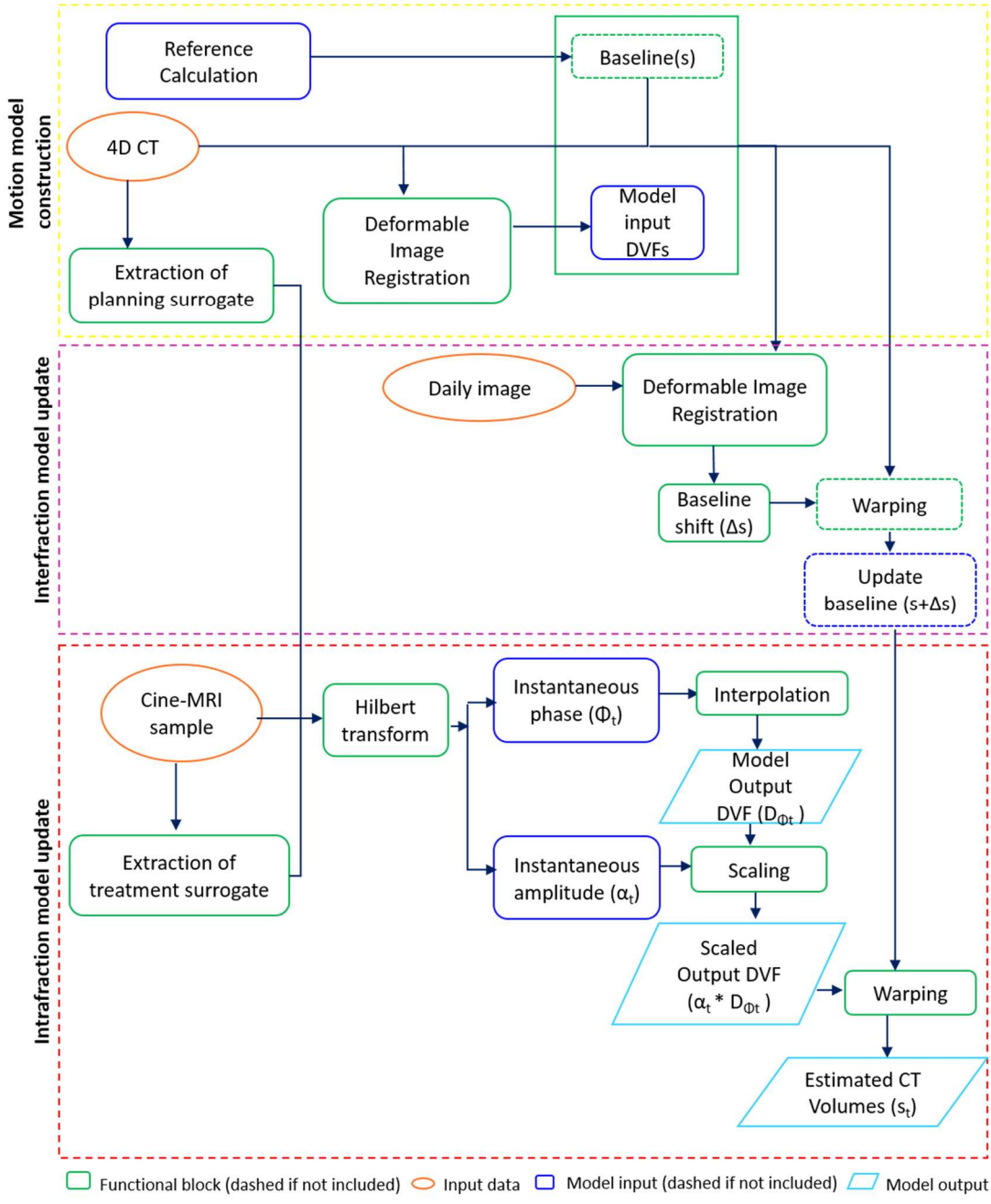

Figure 24. Vandemeulebroucke's model: yellow box-model construction during planning. Purple box-interfraction model update. Red box-intrafraction model update.

The input data for the model construction are:

i. the reference volume used for motion estimation;
ii. the DVFs derived from DIR of each CT volume on the reference volume;
iii. the amplitude and phase values (described through the Hilbert transform), derived from a surrogate signal in pre-treatment and treatment sessions.

The mid position phase (MidP) is used as the reference frame, which represents the time-average position of the anatomy during the 4D CT breathing cycle (see the section 2.2.1.1 for details).

Once the reference volume is identified, the displacement between this reference and all the other respiratory phases is computed using a multi-stage B-splines algorithm in Plastimatch (http://plastimatch.org/, Shackleford et al. 2010): as a result, the corresponding DVFs are computed.

The respiratory motion model provides a specific motion state S_t, function of time and four parameters:

i. the baseline (s);
ii. the baseline shift (Δs);
iii. the instantaneous amplitude (α_t);
iv. the instantaneous phase (Φ_t).

The motion state function is therefore calculated as:

$$S = s + \Delta s + \alpha_t * D_{\phi t}$$

In our work, to take into account the Δs, we quantify the inter-fraction variation between the reference phase in pre-treatment and in treatment (i.e. daily image (e.g. gated-MRI or CBCT)). Since no relevant inter-fraction variations are present, the baseline shift is not included (see section 2.2.3.2.2 for further details on this aspect).

Instantaneous phase Φ_t and amplitude α_t are computed at every time that a sample in treatment is acquired by the Hilbert transform (Fassi et al. 2015), a spectral analysis technique specifically suited for the analysis of non-linear and non-stationary processes.

The Hilbert transform $X(t)$ of a time series x(t) is defined as the convolution of the signal $x(t)$ with the signal 1/t:

$$X(t) = H\{x(t)\} = \frac{1}{\pi} P \int_{-\infty}^{+\infty} \frac{x(\tau)}{t-\tau} d\tau$$

where P indicates the Cauchy principal value of the integral.

The analytical signal associated with x(t) can be written as:

$$z(t) = x(t) + iX(t) = A(t)e^{i\varphi(t)}$$

where $A(t) = \sqrt{x(t)^2 + X(t)^2}$ and $\varphi(t) = \arctan(\frac{x(t)}{X(t)})$.

The polar coordinate expression explicates the nature of the Hilbert transform representation: it is the best local fit of an amplitude and phase varying trigonometric function of $x(t)$. The amplitude and phase parameters helps to model variations of the trajectory shape and breathing level (Vandemeulebroucke et al. 2009). Once the instantaneous amplitude and phase information are computed, the model requires as input the ratio of the treatment over the pre-treatment.

The term $D_{\Phi t}$ in the motion state above, represents the results of the B-splines interpolation of the model input DVFs in correspondence of the phase Φ_t, where Φ_t varies from 0 to 1. A new DVF, describing the displacement between the motion acquired at the phase Φ_t and the reference, is obtained as output. The output DVF is scaled according to the amplitude factor α_t. The last step is the transformation (i.e. warping) of the reference image according to the new DVF. As a result, the estimated model output CT volume is obtained.

2.2.1.1 Mid position

The 3D MidP scan represents all anatomy in the time-weighted mean position over the respiratory cycle (Wolthaus et al. 2008). The whole process for achieving the 3D volume is summarised in Figure 25. Once the 4D CT dataset is acquired and the reference frame, typically the 0% exhale respiratory phase, is defined, a DIR between the reference and each frame of the 4D scan is computed. New DVFs are obtained as the difference between the original DVFs, resulted from DIR, and the average DVF (i.e. mean among the original

DVFs). Each frame of the 4D CT scan is warped with the new DVF, transforming each frame to the time-weighted mean position. The resulting set of 10 CT volumes are finally averaged to obtain the MidP volume.

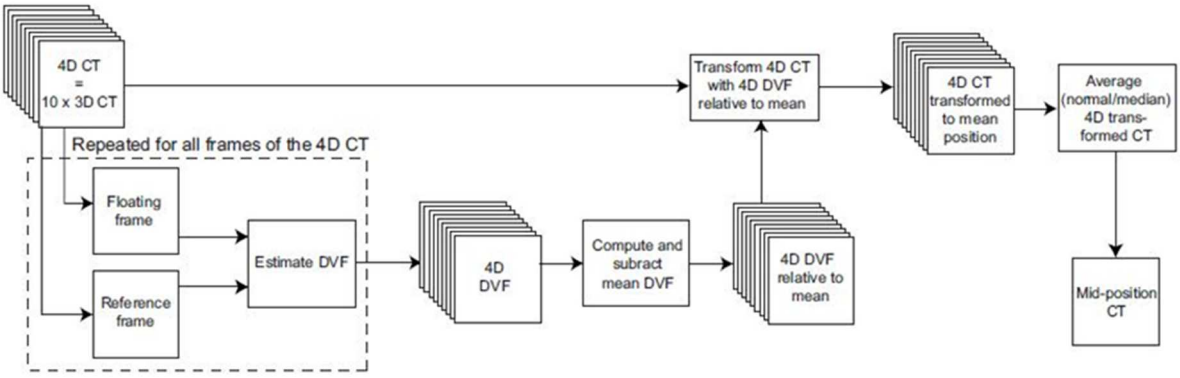

Figure 25. MidP construction: From the 4D CT scan, at every step, two frames are selected: the maximum exhalation and the floating frame, which are registered to each other with deformable registration. This process is repeated for all 10 frames with the same reference frame. The resulting deformation vector field DVF is recomputed to deform all CT frames to the time-weighted mean position. The deformed frames are averaged to obtain a high quality MidP CT scan (from Wolthaus et al. 2008).

2.2.2 Description of Fayad's model

The global motion model proposed by Fayad et al. (2012) is based on the principal component analysis (PCA), a statistical procedure used to simplify data, determining the least number of variables able to describe the given data.

The required input dataset required:

i. the reference volume for motion estimation;
ii. the DVFs derived from DIR of each CT volume on the reference one;
iii. the amplitude value (in mm), derived from surrogates signal in pre-treatment and treatment sessions.

The DVFs are computed using a multi-stage B-splines algorithm in Plastimatch, performing a DIR between the reference volume and all the other 4D CT phases. Fayad et al. (2012 a) suggest to consider the 0% exhale phase as reference. The obtained DVFs and the surrogates are placed in a vector, as follows:

$$Mapped\_motion = [dvf_{1\_1}\ dvf_{2\_1} \dots\ dvf_{m\_1}$$
$$dvf_{1\_2}\ dvf_{2\_2} \dots \dots$$
$$dvf_{1\_3}\ dvf2_{\_3} \dots \dots$$
$$dvf_{1\_4}\ dvf2_{\_4} \dots \dots$$
$$dvf_{1\_5}\ dvf2_{\_5} \dots\ dvf_{m\_n}$$
$$\dots \dots \dots \dots$$
$$s_1\ s_2 \dots\ s_n]$$

Where:

i. dvf_{i_j} is the DVF of the i_{th} phase of the j_{th} 4D CT
ii. m is the number of phase bins (m = 10-1)
iii. n is the number of 4D CT used to train the model (n = 1)
iv. s_i is the surrogate value of the i_{th} phase, computed as the range of motion between the value of the i_{th} phase and the value of the reference volume.

This model allows inserting in the mapped-motion above more than one surrogates, attaching, therefore, more information. The PCA is applied to the mapped-motion and the eigenvectors and the corresponding eigenvalues of the covariance matrix are computed. By applying the PCA, the output can be divided in two different information, one derived from the vector field (M_{vf}) and the other from the surrogate (M_s):

$$M_{dvf} = mapped\_motion\left(1{:}\left(size\left(mepped\_motion(1, end-1)\right)\right)\right)$$

$$M_s = mapped\_motion(end)$$

and the model can be derived as

$$M = \frac{M_{dvf}}{M_s}$$

Finally, when a new or more surrogates are available during treatment (i.e. by computing the range of movement between the value at the i_{th} amplitude and the reference value) the model is updated. As output, a new DVF is computed as:

$$DVF_{new} = M * S_{new}$$

with $S_{new}=[s_{1\_new}\ s_{2\_new} \dots\dots\dots\ s_{m\_new}]$.

The DVF_{new} needs to be inverted ($(DVF_{new})^{-1}$), since it describes the displacement between the treatment and the reference frame acquired in pre-treatment, and then the model output CT is obtained by warping the reference frame with the $(DVF_{new})^{-1}$.

In Fayad's model no inclusion of the baseline is present, conversely to Vandemeulebroucke's model. However, the inter-fraction variation can be compensated by increasing the number of 4D CT included (n>1) or by creating a model of the exhale reference volume and then use this estimated reference volume to build the overall motion model, as proposed by Paganelli et al. 2015c.

2.2.3 Experiments for geometric adaptation

The main purpose of this study is the evaluation of the geometric and dosimetric variations between the treatment planning and delivery. The CT\MRI digital phantom is used for the evaluation of the models performance thanks to the presence of the CT volumes at cine-MRI samples (i.e. ground truth). The models are tested by considering as reference volume: (i) the 0% exhale phase (as suggested by Fayad et al. 2012), since it is expected to have reduced imaging artefacts due to the minor tumour motion and higher reproducibility of tumour position (Wolthaus et al. 2008), and (ii) the MidP (as suggested by Vandemeulebroucke et al. 2009). Figure 26 shows a schematic representation of the two compared options.

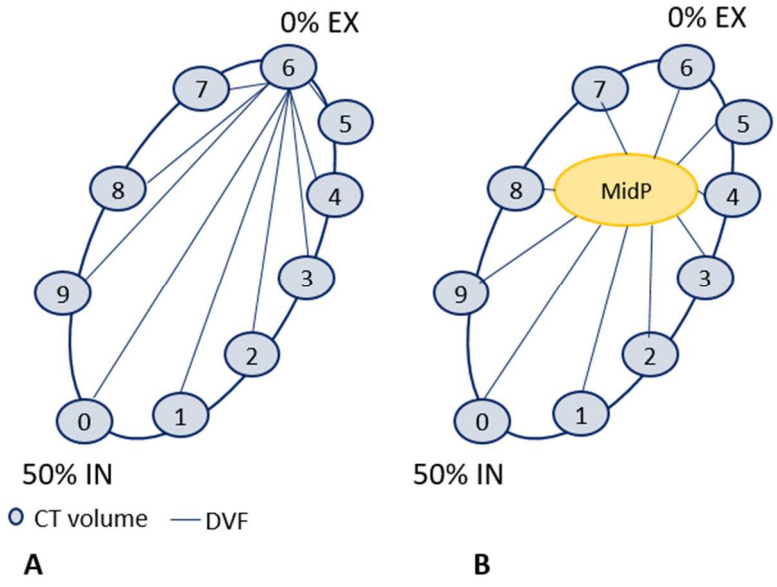

Figure 26. Reference volumes: A-0% exhale phase. B-MidP volume.

Subsequently additional studies are performed on three patients, testing the model only considering the 0% exhale phase as reference, due to the lack of data for identifying the MidP reference in treatment for the CT/cine-MRI patient.

2.2.3.1 Validation of the models on the CT/MRI digital phantom

Even if the models chosen are different, they require similar data. In this section the necessary steps for model implementation are described. Subsequently, the different tests carried out on the models and their validation are described. The workflow is shown in Figure 27; each block will be described in detail in the following paragraphs.

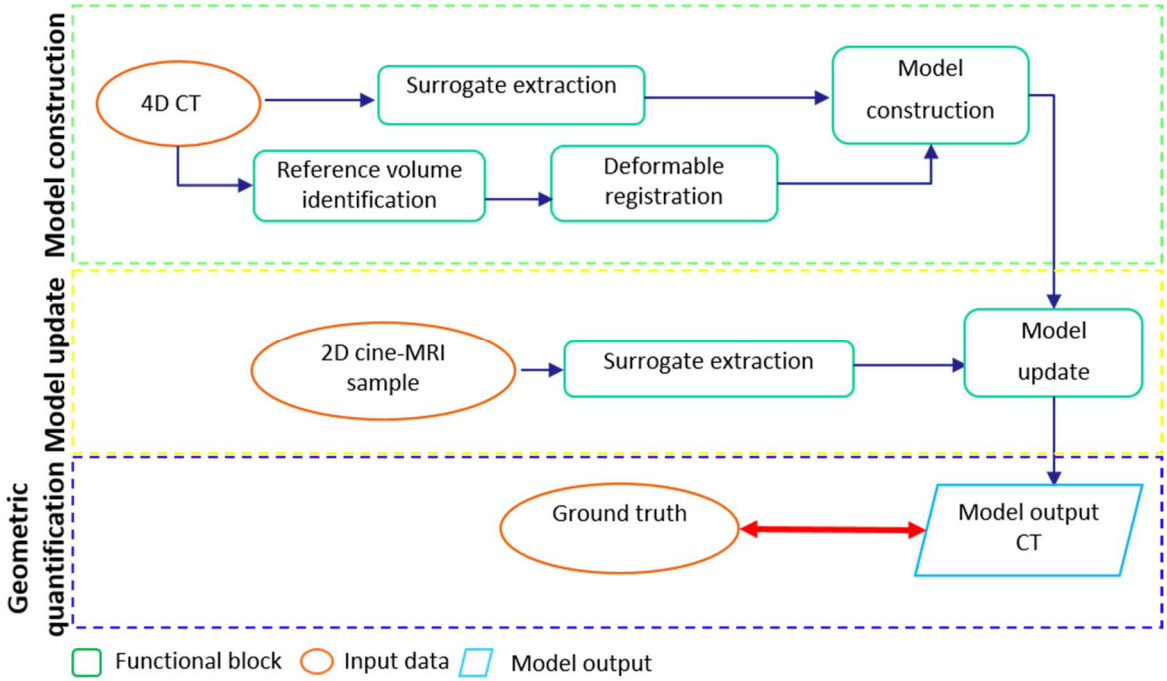

Figure 27. Model workflow: essential passages leading to the model validation.

2.2.3.1.1 Model construction

The essential passages leading to model construction are summarised in the green box above (Figure 27).

i. Identification of the reference volume.

As previously described, two different reference volumes are used: the 0% exhale and the MidP. During exhalation, the diaphragm relaxes and reaches its highest

position, therefore, the exhale phase is identified as the one in which the diaphragm achieves the higher excursion. The identification process is described in detail in Appendix B. The computation of the MidP volume is explained above in section 2.2.1.1.

ii. Deformable image registration.

Once the reference image is available a multi-stage B-spline DIR algorithm is applied. In order to evaluate DIR, features points on the reference image and the 50% inhale CT (maximum range of motion) are extracted using the Scale Invariant Feature Transform (SIFT), a method able to extract stable landmarks (i.e. features) from 3D images and to quantify internal non-rigid motion (Paganelli et al. 2013a, Paganelli et al. 2013b). The median accuracy (± interquartile range) between the extracted features is evaluated.

iii. Surrogate extraction.

The last data needed for model construction is the respiratory signal derived in pre-treatment. In this work internal and external signals are evaluated.

- An external signal (RPM signal), simulating the RPM system (see section 1.2.1.1), describes the AP displacement of the thorax.
- As internal signals we consider:
    - the SI and AP motion of the centre of mass (COM) of the tumour, identified as mean tumour boundary (MTB);
    - the SI respiratory motion of the diaphragm, identified with the approach explained in Appendix B;
    - the SI motion of the lung vessels derived through the SIFT method. In order to identify the SIFT signal, since the respiratory motion is higher in the lower lobe of the lung, different regions are considered. Therefore, the sagittal volume is split into two different regions, one on the top and the other on the bottom, and the coronal volume is instead split into four different regions (Figure 28). Two regions with the higher range of motion are chosen for model implementation.

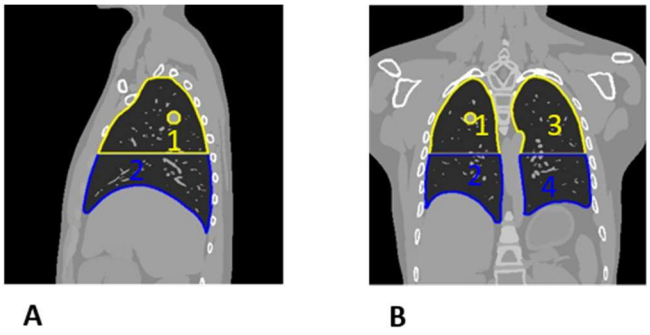

Figure 28. SIFT region-CT/MRI phantom: A-sagittal view. B-coronal view.

The signals extracted from the 4D CT dataset, which describe the mean respiratory movements, are used, in addition with the DVFs, to create the models.

An additional step is needed for implementing Fayad's model; as explained in section 2.2.2, the model needs as input the distance in amplitude of each phase with respect to the 0% exhale phase.

2.2.3.1.2 Model update

Once the model is generated, the update in the treatment scenario is performed. The essential step leading to the model updates are summarised in the yellow box in Figure 27 and are described in detail below.

i. Surrogate extraction.

From the treatment dataset, the same surrogates (external and internal) listed above for the pre-treatment session are considered: the RPM signal; the MTB signal; the diaphragm and SIFT signals (Paganelli et al. 2015b).

The RPM (AP direction of the thorax) and MTB (AP and SI tumour motion) signals are the same signals used for the phantom generation. The extraction of the highest point of the diaphragm (SI motion) is executed with the process describe in Appendix B, but modifying the code for the available data (i.e. ROI selected, opening and closing operation (Appendix A)). The SIFT signals (SI motion) are extracted with the same process explained above.

Since the SI motion is visible on both coronal and sagittal plane, for every surrogates describing the SI motion, two signals are available (i.e. one extracted

from the coronal plane and one from the sagittal plane). Instead, if the direction investigated is the RL or the AP, only coronal or sagittal signal is available, respectively.

Because the 2D cine-MRI slices are alternatively acquired in sagittal and coronal plane, the respiratory signal is composed of 1024 samples, split into 512 sagittal and 512 coronal samples. A cubic interpolation is applied to all signals in order to obtain the sagittal and coronal values every 150 msec (Figure 29).

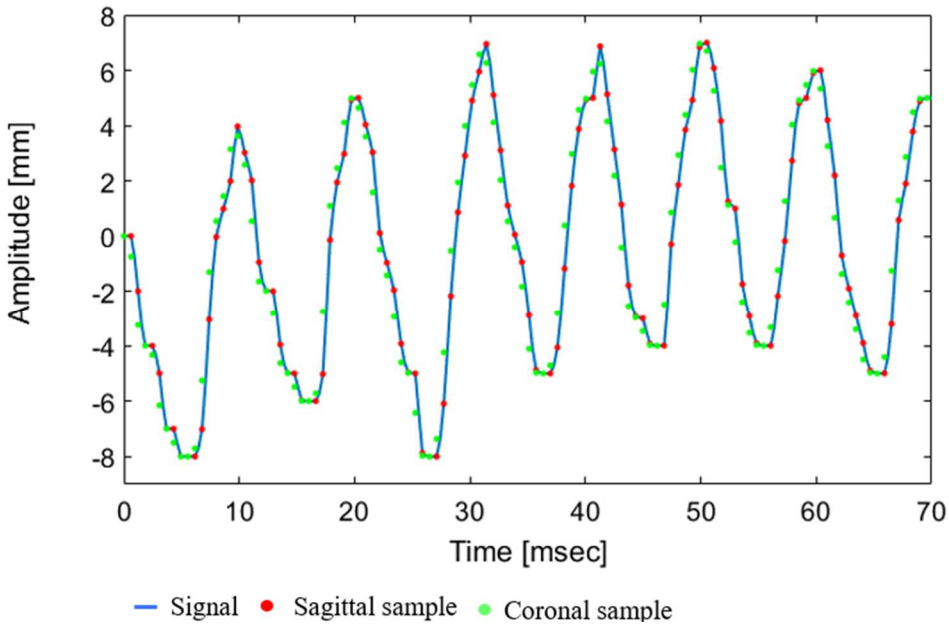

Figure 29. Interpolated signal: six respiratory cycles of the diaphragm signal in sagittal plane after interpolation. This process is shown for the diaphragm signal but is computed for all the surrogates, both on coronal and sagittal planes.

For applying Vandemeulebroucke's model the amplitude and phase ratio of each sample is obtained through the Hilbert transform, as already explained in section 2.2.1, and used to update the model.

For Fayad's model, in order to assign the amplitude input as the range of motion with respect to the reference phase, the cine-MRI sample acquired at the reference phase has to be identified. The process leading the identification is explained in detail in Appendix C. The accuracy of the overlap between the selected cine-MRI sample and the correspondent 0% exhale CT slice (or the MidP CT slice) is evaluated by computing the median distance (± interquartile range) between the boundary points of the diaphragms.

2.2.3.1.3 Tests performed

Below we describe the different tests carried out on the models are listed. In order to compare the different tests and the models, we consider always the same coronal or sagittal sample for the model update.

Vandemeulebroucke's model:

A preliminary check on the consistency of the model, relies on testing the model with an amplitude value equal to 1 and phase value corresponding to the 50% inhale (equal to 0.4) (Test 0 in Table 3). Then, the ability of the model to reconstruct an entire breath is examined. Subsequently, in order to better understand which reference volume and which surrogate fit best, all the different surrogates are tested, considering the coronal or the sagittal sample respectively. Since the same tests are performed using the MidP and the 0% exhale phase as reference, we test the capability of the model to reconstruct the 50% inhale phase. The only difference, between the tests performed using the different references, is the use of different types of DVFs, which are computed applying DIR considering the MidP volume or the 0% exhale volume respectively as fixed volume. Table 3 illustrates all the tests performed focusing on the estimation of the 50% inhale phase. In the second and third columns, the signals used for the model implementation are listed, while in the last two columns the amplitude and phase ratio gave as input to the model are shown.

Table 3. List of tests performed using Vandemeulebroucke's model for both references.

TEST	PRE-TREATMENT SURROGATE	TREATMENT SURROGATE	AMPLITUDE [mm/mm]	PHASE [rad/rad]
0	Diaphragm SI	---	1	0.4
1	Diaphragm SI	Diaphragm SI, coronal sample	1.47	0.31
2	Diaphragm SI	Diaphragm SI, sagittal sample	1.39	0.37
3	MTB SI	MTB SI, coronal sample	0.69	0.25
4	MTB SI	MTB SI, sagittal sample	0.86	0.34
5	SIFT SI	SIFT SI, coronal sample	1.75	0.26
6	SIFT SI	SIFT SI, sagittal sample	1.91	0.33
7	RPM AP	RPM AP, sagittal sample	1.6	0.34

Fayad's model:

Also for Fayad's model, the first test entails the estimation of the 50% inhale of the pre-treatment scenario, in order to check the consistency of the model considering as reference the 0% exhale phase (Test 0 in Table 4) or the MidP volume.

Later, we focus our attention on 0% exhale as reference. As already explain, the output DVF required to be inverted (DVF^{-1}), before warping the reference image to obtain the estimated CT volume, therefore, a series of tests to evaluate the error due to this additional inversion step are performed. In particular, the overlap between the 50% inhale volume and the model output CT, obtained by warping the 0% exhale volume with the DVF^{-1}, is compared with the overlap of the model output CT, obtained without inverting the DVF, with the 0% exhale phase, using the same amplitude value for the model construction and update. Moreover, as for the other model, we tested the ability of the model to estimate an entire breathing cycle. Then, since the different construction of Fayad's model allows the combination of multiple surrogates, all the meaningful combinations are examined, focusing always on the 50% inhale phase. In particular, the tests performed can be divided into three categories.

- Same surrogate in pre-treatment and in treatment.

  We consider alternatively the coronal, the sagittal sample or both, using, in this latter case, the coronal value and the interpolated sagittal one (Table 4). In the fourth column of Table 4 the amplitude values used to update the model in the treatment scenario are listed.

Table 4. Test performed on Fayad's model using the same signal in training and treatment.

TEST	PRE-TREATMENT SURROGATE	TREATMENT SURROGATE	AMPLITUDE [mm]
0	Diaphragm SI	---	9.62
1	Diaphragm SI	Diaphragm SI, coronal sample	8.24
2	Diaphragm SI	Diaphragm SI, sagittal sample	7.58
3	Diaphragm SI	Diaphragm SI, coronal and sagittal sample	coronal: 8.24 sagittal: 7.03
4	MTB SI	MTB SI, coronal sample	4.39
5	MTB SI	MTB SI, sagittal sample	4.02
6	MTB SI	MTB SI, coronal and sagittal sample	coronal: 4.39 sagittal: 4.48
7	MTB AP	MTB AP, sagittal sample	0.44
8	SIFT SI	SIFT SI, coronal sample	2.4
9	SIFT SI	SIFT SI, sagittal sample	4.65
10	SIFT SI	SIFT SI, coronal and sagittal sample	coronal: 2.40 sagittal: 4.55
11	RPM AP	RPM AP, sagittal sample	4.02

- Combination of different internal surrogates in pre-treatment and treatment.

  These signals describe always the SI movement but referring to anatomical structures with different range of motion (e.g. tumour vs. diaphragm motion) or different motion direction (e.g. MTB AP vs. MTB SI). For taking into account these differences, the signals, both in pre-treatment and in treatment, are previously normalized with respect to the maximum range of motion. In Table 5 the tests are listed, the last column shows the amplitude value used for model update in the treatment scenario.

Table 5. Tests performed on Fayad's model using different combinations of internal surrogates in training and treatment.

TEST	PRE-TREATMENT SURROGATE	TREATMENT SURROGATE	AMPLITUDE [mm]
1	Diaphragm SI and MTB SI*	Diaphragm SI*, coronal sample	7.86
2	Diaphragm SI and MTB SI*	MTB SI*, coronal sample	6.72
3	Diaphragm SI and MTB SI*	Diaphragm SI*, coronal sample MTB SI*, coronal sample	Diaphragm SI*: 7.86 MTB SI**: 6.72
4	MTB SI and MTB AP**	MTB SI**, sagittal sample, MTB AP**, sagittal sample	MTB SI**: 4.02 MTB AP**: 0.43
5	MTB SI and SIFT SI**	SIFT SI**, coronal sample	4.91
6	MTB SI and SIFT SI**	MTB SI**, coronal sample	4.22
7	MTB SI and SIFT SI**	SIFTSI**, coronal sample MTB SI**, coronal sample	SIFT SI**: 4.91 MTB SI**: 4.22

*Normalized on diaphragm SI **Normalized on MTB SI

- Combination of external and internal surrogate in training and in treatment.
  Also in this latter case, the surrogates are normalized with respect to the maximum range of motion. In Table 6 the two tests carried out are listed, highlighting always the amplitude value used for the model update (last column of the table).

Table 6. Tests performed on Fayad's model using a combination of internal and external surrogates.

TEST	PRE-TREATMENT SURROGATE	TREATMENT SURROGATE	AMPLITUDE [mm]
1	MTB SI and RPM AP*	RPM AP*, sagittal sample	1.44
2	MTB SI and RPM AP*	RPM AP*, sagittal sample MTB SI*, sagittal sample	RPM AP: 1.44 MTB SI: 3.82

*Normalized on MTB SI

Finally, in order to evaluate if the first principal component of the PCA is able to summarise the main characteristics of the data, the model is also implemented with four principal components, testing the model using the diaphragm as surrogate.

2.2.3.1.4 Geometric accuracy

The great advantage of the CT/MRI phantom is the presence in the treatment scenario of the ground truth (CT acquired at cine-MRI sample), which allows to directly evaluate the model performance (blue box in Figure 27). The comparison between the ground truth and the estimated output model CT is performed focusing on three different ROIs: the heart, the tumour and the diaphragm. First, the ROIs are segmented (see Appendix A) and then the Euclidean distance in mm between the COM is computed.

Finally, a statistical non-parametric analysis (Friedman test, alpha = 5%), is carried out in order to identify which model and which surrogates are significantly different. Three populations are considered: the first population contains the geometric quantifications on the diaphragm, the second on the tumour and the last on the heart. First, significant differences are searched between Vandemeulebroucke's model, using both the MidP and the 0% exhale as reference, and Fayad's one. Then, statistic differences between all the tests performed on Fayad's model considering the 0% exhale as reference are evaluated.

2.2.3.2 Evaluation of the models on patients

As previously discuss (section 2.1) patients are split in two groups (two CT/CBCT patients (patient A and B) and one CT/cine-MRI patient (patient C)) depending, essentially, on the

treatment data made available. Even if the treatment dataset is different, all the steps leading to the models construction and update are similar (Figure 30). Therefore, all the patients are merged in a unique description, highlighting the different steps when necessary. Finally, all the tests performed and the geometric quantifications are described.

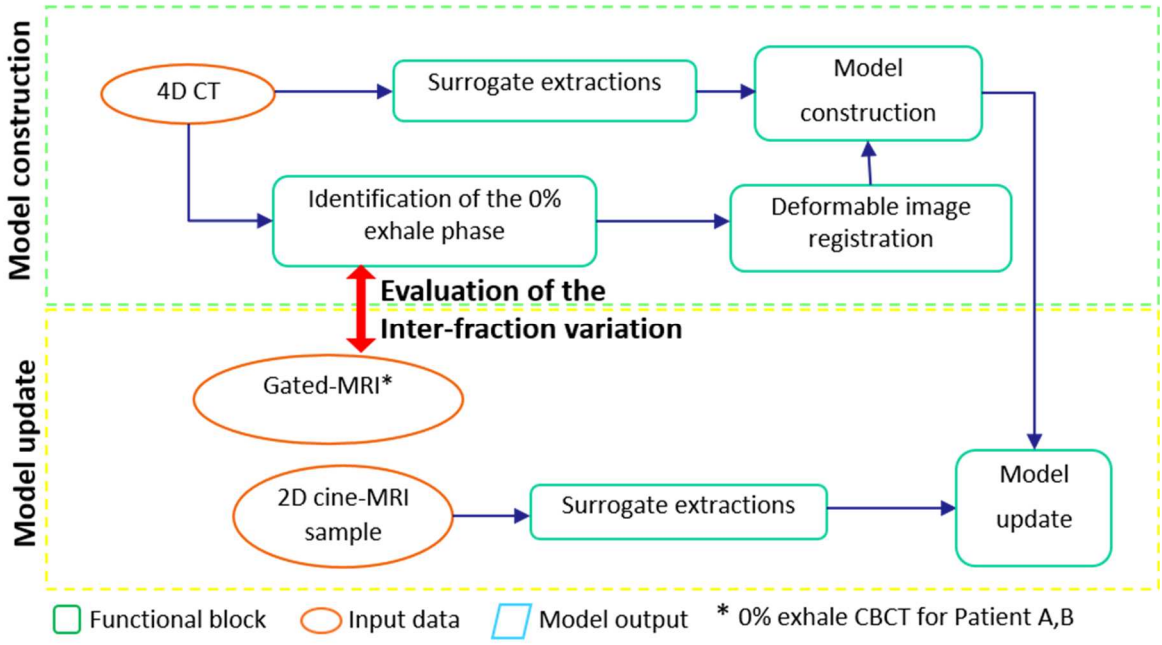

Figure 30. Model workflow for patients: green box-model construction. Yellow box-model update.

As shown in Figure 30 above, an additional step (i.e. evaluation of the inter-fraction variation) is required, conversely to the CT/MRI digital phantom. For patient C only a gated-MRI acquired at the 0% exhale phase is available so, during treatment the evaluation of the inter-fraction variation, considering the MidP volume as reference, is not possible. Therefore, the motion models are tested considering as reference only the 0% exhale phase. For patients A and B, a volumetric CBCT at the exhale phase is used instead of the gated-MRI (see section 2.3.3.2.2 for details).

2.2.3.2.1 Model construction

The fundamental steps for the model construction are summarised in green in Figure 30.

i. Reference volume identification.

   As for the CT/MRI digital phantom the reference phase is identified looking at the motion of the highest point of the diaphragm.

For the CT/CBCT patients the lung contours, defined manually by an expert on the average CT, are used as starting point for diaphragm identification. Specifically, a B-spline DIR between the average CT and each CT volume is performed, followed by lung contour warping. The validation of the DIR is performed, as for the CT/MRI phantom study, through the use of SIFT (see the following step for details). Then, a thin and narrow ROI (107×16 pixels) is applied (Appendix A) on the lungs boundary and the highest point of the diaphragm is identified (see Appendix B).

For the CT/cine-MRI patient a ROI containing the right diaphragm is selected and a morphological operation (i.e. dilation (Appendix A)) allows the identification of the highest point of the diaphragm (see Appendix B).

ii. Deformable image registration.

The same multi-stage B-spline DIR algorithm used for the CT/MRI digital phantom is applied. In order to evaluate DIR, features points on the reference image and the 50% inhale CT (maximum range of motion) are extracted using SIFT. The median accuracy (± interquartile range) between the extracted features is evaluated.

iii. Surrogate extraction.

CT/CBCT patient

The only investigated respiratory motions are: (i) the SI movements of the highest point of the diaphragm (see Appendix B), (ii) the MTB (for patient A only the SI motion while for patient B also the AP and RL motion). The extraction of the tumour boundary is carried out starting from the tumour boundary on the average CT, with the same method explained above (i.e. DIR with the other 10 respiratory phases and warping).

CT/cine-MRI patient

Internal and external respiratory signals are considered, in a similar fashion to the CT/MRI phantom study, for the CT/MRI patient.

- The external signal describes the mean AP displacement of the thorax and it is acquired using the Varian RPM system; so we refer to it as the RPM signal.

From the acquired signal, each respiratory breath (i.e. the signal included between two consecutives minima) is identified and divided into 10 bins. Last, the mean motion of each respiratory phase is computed.

- As internal signals we consider:
  - the SI, AP and RL movements of the tumour. The tumour COMs are computed, using Plastimatch, from the boundaries available on each CT volume;
  - the SI movement of the highest point of the diaphragm, extracted with the method explained in Appendix B;
  - the SI motion of lung vessels derived by SIFT. In order to extract the SIFT signal a coronal and sagittal slices, correspondent to the cine-MRI samples, are selected on the CT volumes with the method described in Appendix D. Only the regions (the same considered in treatment) with the most regular motion are studied.

An additional step is needed for implementing Fayad's model because, as explained in section 2.2.2, the model needs as input the distance in amplitude of each phase with respect to the 0% exhale phase.

In Table 7 the different surrogates available for each patient are summarised.

Table 7. Surrogate studied and direction of motion investigated for each patient.

Surrogate	Patient A	Patient B	Patient C
RPM AP	N.A.	N.A.	A.
MTB RL	---	A.	A.
MTB AP	---	A.	A.
MTB SI	A.	A.	A.
Diaphragm SI	A.	A.	A.
SIFT SI	N.A.	N.A.	A.

N.A. = not available A. = available

2.2.3.2.2 Model update

Once the model is generated, the update in the treatment scenario is performed. The essential steps leading to the model construction and update are summarised in the yellow box shown in Figure 30.

i. Evaluation of the inter-fraction variation.

Differently from the CT\MRI phantom, in which no inter-fraction variability is present, in patients these changes may occur and need to be accounted for and compensated into the models, as proposed by Fassi et al. 2010. The main steps leading to the evaluation of the inter-fraction variations are shown in Figure 31.

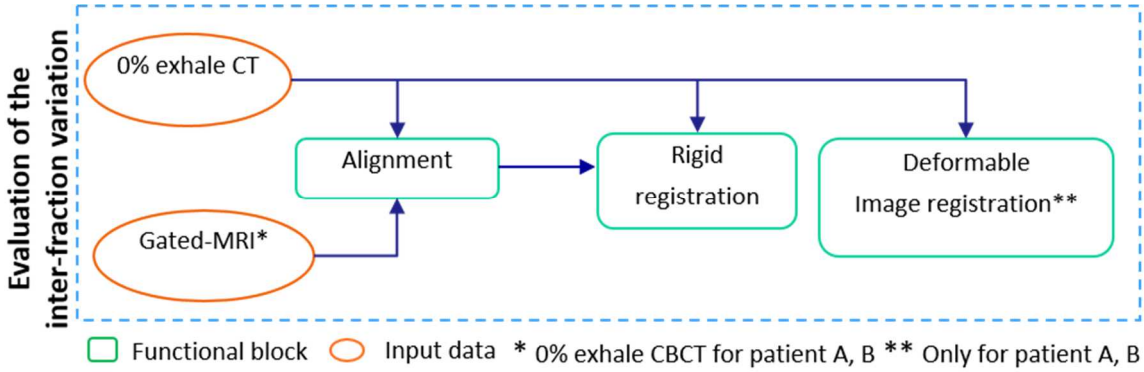

Figure 31. Inter-fraction variation: workflow for the evaluation.

First, the centre alignment of the two exhale volumes is performed using Amira 3D (http://www.fei.com/software/amira-3d-for-life-sciences/). Then, for evaluating the setup errors, a rigid registration of the two exhale volumes is performed using 3D Slicer (https://www.slicer.org/). The transformation maps the 0% exhale treatment CT to the pre-treatment volume and consists of 3 translations and 3 rotations. The rigid transformation is evaluated computing the median accuracy (± interquartile range) of the highest point of the diaphragm (identified as explained in Appendix B) and the tumour COM (only for the CT/CBCT patients) between the output volume of the registration and the 0% exhale pre-treatment CT. Then, for the CT/CBCT patients two-stages B-spline DIR between these two volumes is performed using Plastimatch to account for any non-rigid change and the mean motion of the DVF is the evaluated.

ii. surrogate extraction

Due to the different data available, the surrogate extraction requires different steps, depending on the considered patient.

CT/CBCT patients

To simulate cine-MRI samples, sagittal and coronal slices centred in the tumour are selected from every treatment volume. The consistency of the selections is evaluated computing the mean difference (± standard deviation) of tumour (only for patient A) and diaphragm motion at the intersection of the sagittal and coronal slices. Then, the same surrogates extracted from the pre-treatment dataset are extracted from the simulated cine-MRI samples. So, the extraction of the diaphragm is realized, for both patients, with the same process explain in Appendix B, focusing only on the right part of the diaphragm due to low quality of the images. For patient A, the MTB (SI motion) is extracted automatically selecting a ROI centred in the tumour and applying morphological operations (i.e. filling the holes (see Appendix A)). The precision of the segmentation is validated comparing the boundaries just found with the one obtained warping the exhale phase boundaries (the method is described in detail in Appendix E). Due to the low image quality, the automatic segmentation of the tumour (RL, AP, SI directions) for patient B is not carried out, but the signal is extracted by warping the exhale phase boundaries (see Appendix E for details).

CT/cine-MRI patient

The same surrogates of the pre-treatment dataset (external and internal) are extracted: the RPM signal (AP motion), MTB signal (RL, AP and SI direction), the diaphragm signal (SI motion) (see Appendix A) and the SIFT signals. Using the SIFT algorithm the SI movements of the lung vessels in six different regions are obtained. However, for the model update, only two regions (one in coronal and one in sagittal plane), with the biggest range of motion and with the most regular pattern, are considered.

Since the cine-MRI slices are alternatively acquired in sagittal and coronal plane, a cubic interpolation is applied to all signals in order to obtain the sagittal and coronal

values every 150 msec. In addition to the signals extracted from patient C a moving average filter is applied to achieve a more regular pattern.

One last step is necessary for Fayad's model, since the model needs as input the distance in amplitude of each sample with respect to the 0% exhale phase. In order to identified the cine-MRI sample acquired at the 0% exhale phase the comparison between the cine-MRI samples and the gated-MRI (acquired at the 0% exhale phase) is carried out for patient C (see Appendix C). The accuracy of the overlap between the selected cine-MRI sample and the correspondent 0% exhale CT slice is evaluated by computing the median distance (± interquartile range) between the boundary points of the diaphragm. This processed is not necessary for the CT/CBCT patients, since the 0% exhale phase during treatment is known.

2.2.3.2.3 Tests performed

Below the different tests carried out on the patient models are listed, first on Vandemeulebroucke's model and then on Fayad's model, considering as reference only the 0% exhale phase. In order to compare the different tests and models, for each respiratory signal, we consider always the same coronal or sagittal sample.

Vandemeulebroucke's model

Since the ability of the model to reconstruct an entire breathing cycle is tested and evaluated for the CT/MRI digital phantom, where the ground truth for the direct geometric evaluation is available, the first test for patients entail the reconstruction of the 50% inhale phase of the pre-treatment scenario (Test 0 in Table 8). Then all the respiratory surrogates are tested (Table 8).

Table 8. Tests performed on Vandemeulebroucke's model for patients.

	TEST	PRE-TREATMENT SURROGATE	TREATMENT SURROGATE	AMPLITUDE [mm/mm]	PHASE [rad/rad]
	0	---	---	1	0.4
	1	Diaphragm SI	Diaphragm SI, coronal sample	1.18	0.41
PATIENT A	2	Diaphragm SI	Diaphragm SI, sagittal sample	0.73	0.39
	3	MTB SI	MTB SI, coronal sample	1.07	0.40
	4	MTB SI	MTB SI, sagittal sample	0.84	0.39
	0	---	---	1	0.4
	1	Diaphragm SI	Diaphragm SI, coronal sample	0.89	0.41
	2	Diaphragm SI	Diaphragm SI, sagittal sample	0.88	0.41
PATIENT B	3	MTB SI	MTB SI, coronal sample	0.73	0.41
	4	MTB SI	MTB SI, sagittal sample	0.74	0.46
	5	MTB RL	MTB RL, coronal sample	0.23	0.41
	6	MTB AP	MTB AP, sagittal sample	1.66	0.46
	0	---	---	1	0.4
	1	Diaphragm SI	Diaphragm SI, coronal sample	0.51	0.31
	2	Diaphragm SI	Diaphragm SI, sagittal sample	0.58	0.38
	3	MTB SI	MTB SI, coronal sample	0.62	0.85
PATIENT C	4	MTB SI	MTB SI, sagittal sample	0.45	0.87
	5	MTB RL	MTB RL, coronal sample	0.29	0.16
	6	MTB AP	MTB AP, sagittal sample	1.06	0.73
	7	SIFT SI	SIFT SI, coronal sample	0.41	0.30
	8	SIFT SI	SIFT SI, sagittal sample	0.72	0.37
	9	RPM AP	RPM AP, sagittal sample	0.59	0.67

Fayad's model

Also for Fayad's model the first test entails the estimation of the 50% inhale of the training (i.e. built on the pre-treatment session), to check the consistency of the model (Test 0 in Table 9). Then, since the different construction of Fayad's model allows the combination of multiple surrogates all the meaningful combinations are examined, focusing always on the 50% inhale phase. In particular, the tests performed can be divided into three categories.

- Same surrogate in training and in treatment.

  The model is tested considering alternatively the coronal sample, the sagittal one or both, using, in this latter case, the coronal value and the interpolated sagittal. In Table 9 are described the test carried out on patients (different tests are done according to the available surrogates).

Table 9. Tests performed considering only one surrogates on Fayad's model for patients.

	TEST	PRE-TREATMENT SURROGATE	TREATMENT SURROGATE	AMPLITUDE [mm]
PATIENT A	0	Diaphragm SI	---	10.55
	1	Diaphragm SI	Diaphragm SI, coronal sample	16.25
	2	Diaphragm SI	Diaphragm SI, sagittal sample	12
	3	Diaphragm SI	Diaphragm SI, coronal and sagittal sample	coronal: 16.25 sagittal: 12
	4	MTB SI	MTB SI, coronal sample	6.69
	5	MTB SI	MTB SI, sagittal sample	8.06
	6	MTB SI	MTB SI, coronal and sagittal sample	coronal: 6.69 sagittal: 7.8
PATIENT B	0	Diaphragm SI	---	10.55
	1	Diaphragm SI	Diaphragm SI, coronal sample	10.5
	2	Diaphragm SI	Diaphragm SI, sagittal sample	10
	3	Diaphragm SI	Diaphragm SI, coronal and sagittal sample	coronal: 10.5 sagittal: 9.33
	4	MTB SI	MTB SI, coronal sample	5.81
	5	MTB SI	MTB SI, sagittal sample	5.82
	6	MTB SI	MTB SI, coronal and sagittal sample	coronal: 5.81 sagittal: 3.85
	7	MTB RL	MTB RL, coronal sample	0.19
	8	MTB AP	MTB AP, sagittal sample	0.93
PATIENT C	0	Diaphragm SI	---	12,5
	1	Diaphragm SI	Diaphragm SI, coronal sample	3.46
	2	Diaphragm SI	Diaphragm SI, sagittal sample	1.9
	3	Diaphragm SI	Diaphragm SI, coronal and sagittal sample	coronal: 3.46 sagittal: 3.20
	4	MTB SI	MTB SI, coronal sample	1.99
	5	MTB SI	MTB SI, sagittal sample	0.12
	6	MTB SI	MTB SI, coronal and sagittal sample	coronal: 1.99 sagittal: 0.16
	7	MTB RL	MTB RL, coronal sample	0.13
	8	MTB AP	MTB AP, sagittal sample	0.43
	9	SIFT SI	SIFT SI, coronal sample	1.14
	10	SIFT SI	SIFT SI, sagittal sample	2.05
	11	SIFT SI	SIFT SI, coronal and sagittal sample	coronal: 1.14 sagittal: 3.02
	12	RPM AP	RPM AP, sagittal sample	0.1

- Combination of different internal surrogates.

  As for the CT/MRI digital phantom the different signals, that describe the motion of different anatomical structures, are normalized with respect to the maximum range of motion. In Table 10 the test carried on patients are listed. In particular for patient B different directions of motion (SI, RL and AP) are evaluated. The amplitude value that appears in Table 10 is used for the model update.

Table 10. Test carried out on Fayad's model for patients combining internal surrogates.

	TEST	PRE-TREATMENT SURROGATE	TREATMENT SURROGATE	AMPLITUDE [mm]
PATIENT A	1	Diaphragm SI and MTB SI	Diaphragm SI, coronal sample	16.25
	2	Diaphragm SI and MTB SI	MTB SI, coronal sample	9.69
	3	Diaphragm SI and MTB SI	Diaphragm SI, coronal sample MTB SI, coronal sample	Diaphragm SI: 16.25 MTB SI: 9.69
PATIENT B	1	Diaphragm SI and MTB SI	Diaphragm SI, coronal sample	10.5
	2	Diaphragm SI and MTB SI	MTB SI, coronal sample	5.81
	3	Diaphragm SI and MTB SI	Diaphragm SI, coronal sample MTB SI, coronal sample	Diaphragm SI: 10.5 MTB SI: 5.81
	4	MTB SI and MTB RL	MTB SI, coronal sample MTB RL, coronal sample	MTB SI: 5.81 MTB RL: 0.93
	5	MTB SI and MTB AP	MTB SI, sagittal sample MTB AP, sagittal sample	MTB SI: 5.81 MTB AP: 0.93
PATIENT C	1	Diaphragm SI and MTB SI*	Diaphragm SI*, coronal sample	7.48
	2	Diaphragm SI and MTB SI*	MTB SI*, coronal sample	0.87
	3	Diaphragm SI and MTB SI*	Diaphragm SI*, coronal sample MTB SI*, coronal sample	Diaphragm SI: 7.48 MTB SI: 0.87
	4	Diaphragm SI and SIFT SI**	Diaphragm SI*, coronal sample SIFT SI*, coronal sample	Diaphragm SI: 9.15 SIFT SI: 7.48
	5	MTB SI and MTB AP**	MTB SI**, sagittal sample MTB AP**, sagittal sample	MTB SI: 4.34 MTB AP: 5.01
	6	MTB SI and MTB RL**	MTB SI**, coronal sample MTB RL**, coronal sample	MTB SI: 3.41 MTB RL: 4.71

*Normalized on diaphragm SI **Normalized on MTB SI

- Combination on internal and external surrogates.

  Only for the CT/cine-MRI patient, the RPM signal (external) is combined with the MTB or with the diaphragm, focusing on the coronal samples (Table 11). Moreover, we study also the combination of different tumour direction (i.e. SI motion combine with RL or AP motion). Also in these latter cases, the signals are normalized with

respect to the maximum range of motion. The amplitude value that appears in Table 11 is used for model update.

Table 11. Test carried out on Fayad's model for patients combining internal and external surrogates.

	TEST	PRE-TREATMENT SURROGATE	TREATMENT SURROGATE	AMPLITUDE [mm]
PATIENT C	1	MTB SI and RPM AP*	MTB SI*, coronal sample RPM AP*, coronal sample	MTB SI: 1.66 RPM AP: 1.43
	2	Diaphragm SI and RPM AP*	Diaphragm SI**, coronal sample RPM AP**, coronal sample	Diaphragm SI:7.48 RPM AP: 4.31

*Normalized on MTB SI

2.2.3.2.4 Geometric accuracy

Unlike for the CT/MRI digital phantom, for which the ground truth for the direct comparison with the models output is available, for patients this piece of data is missing. However, the relationship between the pre-treatment and treatment surrogates (e.g. diaphragm) is known. Hence, by extracting the same surrogate from the output model CT we can approximatively evaluate if the model is able to maintain such a relationship. Therefore, the ratio between the treatment over the pre-treatment surrogate and the ratio between the model output surrogate over the pre-treatment surrogate is compared: if the model is able to reconstruct correctly the output CT, the difference between the ratio should be approximately zero. As already explained, for CT/CBCT patients only the diaphragm and tumour motion are evaluated, therefore we evaluate the variations on the diaphragm and tumour for each model output, also when these surrogates are not used for the model construction.

Finally, the same non-parametric statistical analysis carried out on the CT/MRI phantom (i.e. Friedman test, alpha = 0.5) output is performed to identify significant differences between the models. For patients two population are considered: the first contains the diaphragm quantifications, the second the tumour ones.

2.3 Dosimetric adaptation

During the planning phase of radiotherapy, the creation and optimization of a patient specific treatment plan is carried out in a virtual computer environment known as a treatment planning system (TPS). In this work we use the Pinnacle^3 treatment planning system in the research version v.9.10 to create IMRT plans. For the aim of this work, we first create a treatment plan on the 4D CT and then we apply it on Fayad's model output in order to appreciate dosimetric changes.

2.3.1 The Pinnacle^3 treatment planning system

As previously mentioned in section 1.2.1.3 in Chapter I, IMRT plans are typically designed using inverse planning, which begins by specifying the desired dose to the target tumour. This aim is achieved through different objective functions and constraints (see the definition in section 1.2.1.3, Chapter I). In this work, we use the P^{3}IMRT® (i.e. the inverse planning software), which is integrated into the Pinnacle^3 TPS. In P^{3}IMRT® multiple objective functions and constraints can be specified for a given IMRT plan, as well as multiple objectives and constraints may be specified for the same structure, since it may be difficult to synthesize the treatment goals for a structure through a single function. For example, if the prescribed dose is 60 Gy the ITV should receive a uniform dose as close as possible to 60 Gy, as well as the PTV should receive at least a dose which guarantees treatment success, but at the same time this dose must not exceed a certain value. The optimization algorithm attempts to minimize the objective function $F(\tau)$ which is the sum of n different objectives F^k, $k=1,...,n$.

$$F(\tau) = \sum_{k=1}^{n} F^k$$

Where τ is the set of parameters to be optimized. In the optimization problems are defined also m functions that are constraints and are represented by the constraint vector function $C(\tau)$. A general expression for an objective function may be formulated as:

$$F^k = w^k \sum_{i \in V} f(d_i, d^k) \left(\frac{d_i - d^k}{d^k} \right)^2 \Delta v_i$$

Where:

w^k= weight relevant to the k objective function

V= the considered ROI

d_i= the dose in the voxel i

d_k= the dose criteria (e.g. maximum dose, minimum dose)

v_i= voxel volume

Δv_i= the voxel volume relative to the ROI volume.

When:

$f(d_i,d^k)=max(d_i-d^k, 0)$, F^k is defined as the "Max Dose function"

$f(d_i,d^k)=min(d^k-d^i, 0)$, F^k is defined as the "Min Dose function"

$f(d_i,d^k)=1$, F^k *is* defined as the "Uniform Dose function".

Is it possible also to define the "maximum dose received by a % of the ROI volume", also reported as "Max DVH function" or the "minimum dose received by a % of the ROI volume", the "Min DVH function". Both functions are an extension of the concept of the Max/Min Dose functions. In this case, the ROI volume is divided in two: the high dose sub-volume V_H and the low dose sub-volume V_L. The separation between these two volumes is determined by the specified fraction (μ) of the ROI volume that receive at most (max DVH) or at least (min DVH) dose d_k.

Here below in details the dose calculation steps and the optimization approach.

Dose calculation

The Pinnacle^3 treatment planning system uses the Collapsed Cone Convolution Superposition (CCCS) algorithm developed by Mackie et al. (1987, 1990) for the dose computation. The CCCS dose model is a 3D dose computation that handles the effects of patient heterogeneities on both primary and scattered radiation. The essential steps of CCCS dose computation are summarised in the Figure 32.

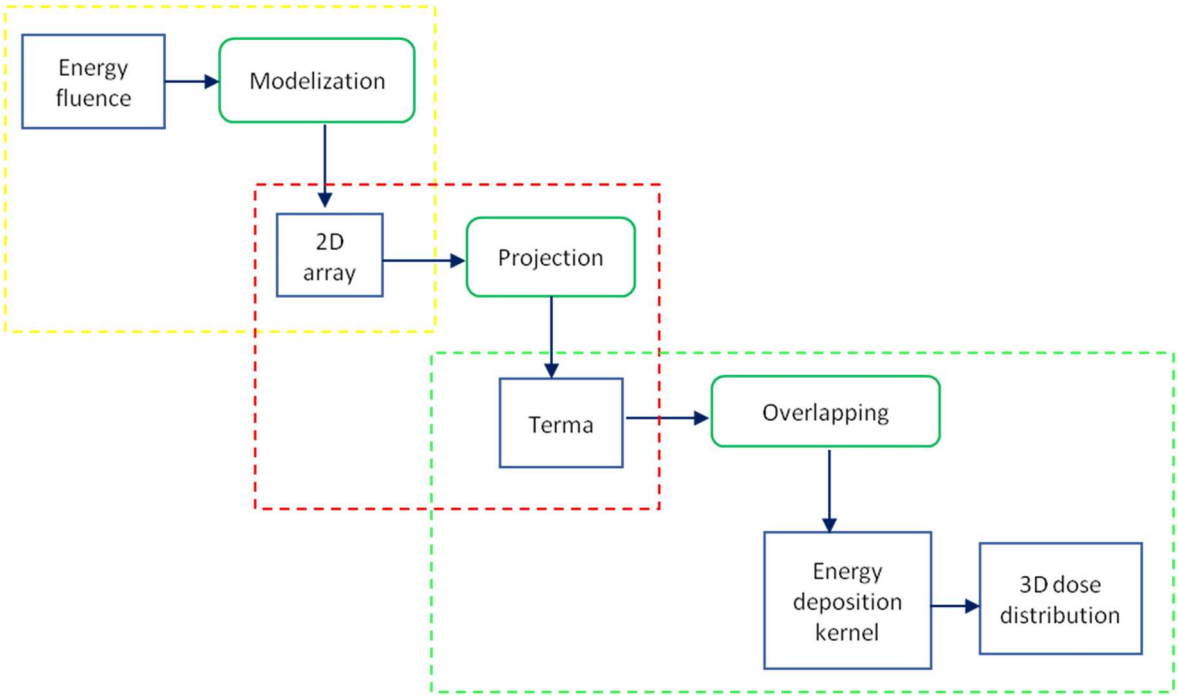

Figure 32. Dose calculation: description of the basic steps for CCCS dose computation.

The first step of the algorithm (yellow dashed box in Figure 32) is the modeling of the incident energy fluence exiting from the head of the linac as a 2D array. This modelization takes into account the intensity variation in the beams produced by the flattening filter (i.e. horns of the beam), the geometric penumbra and beams modifiers such as blocks, wedges and compensator. Then, this energy fluence plan (e.g. the 2D array) is projected through the patient density volume (red dashed box in Figure 32) to compute the total energy released per unit mass (TERMA) volume. The TERMA volume is computed using a ray-tracing technique in which a given ray is determined based on the position of the radiation source and the particular location in the 2D array. At each voxel along the ray path, the TERMA is computed using the attenuated energy fluence along the ray and also considering (i) the mass attenuation coefficient, to consider patient heterogeneities, and (ii) the radiological depth dependence, to take into account beam hardening through the patient.

The third part of the process (green dashed box in Figure 32) entails superimposing the TERMA volume with the energy deposition kernel to get the 3D dose distribution in the patient. The energy deposition kernel describes the energy deposited by charged particles

set in motion by primary, first scattered, second scattered, multiple scattered and bremsstrahlung annihilation photons (Mackie et al. 1988). In other words, it represents the spread of energy from the primary photon interaction site throughout the associated volume. The superposition is performed with a ray-tracing technique, similar to that mentioned in the second part of the process. The algorithm described above computes the dose for a single beam, but multiple beams dose calculations can be done independently and then the entire 3D dose distribution is creating by summing the dose from each beam according to the corresponding beam weight. The algorithm used for dose computation is the Adaptive Convolution Superposition, which is basically identical to CCCS, with some differences in order to increase the speed of computation by a factor of 2-3, without compromising the accuracy of CCCS. This is achieved by adaptively changing the resolution of the dose computation grid (i.e. grid overlapped to the patient on which the dose is computed) depending on the curvature of the TERMA distribution and dose distribution (McNutt 2007).

The optimization problem

The traditional inverse planning problem in IMRT is a fluence-based optimization problem. The optimization algorithm divides each beam into a series of finite-sized beamlets (see section 1.2.1.3, Chapter I). The corresponding weights of the beamlets are optimized to produce a fluence map for every beam. Furthermore, dose is expressed as a function of the fluence distribution and during the optimization process the fluence maps are optimized to produce the desired dose distribution. Then, these fluence maps are converted into MLC settings. A problem with this workflow is the machine capability parameters that are not included in the initial optimization problem, and as such the plan quality is often degraded in this final step, or overly complex plans generated (Ahnesjo 2006). The mathematical expression for the traditional inverse problem posed and solved by P^{3}IMRT is:

$$min_{\tau}\ F(\tau)$$

with

$$\begin{cases} C(\tau) \leq 0 \\ \tau \geq 0 \end{cases}$$

where F is the objective function, τ the set of parameters to be optimized (e.g. the fluence) and C the constraint function. The condition $\tau \geq 0$ ensures non-negative fluences. The condition $C(\tau) \leq 0$ specifies if the condition on the objective function has been met or exceeded. The fluences and hence the dose resulting from the solution of the optimization problem cannot be delivered to the patient directly but they need a conversion in control points, that define the position of the leaves of the MLC. To avoid this problem a new formulation of the inverse problem has been developed: the direct machine parameter optimization (DMPO). With the DMPO approach, the machine parameters are directly taken into account in the optimization problem (Ahnesjo 2006).

Direct machine parameter optimization (DMPO)

In Pinnacle[3], the DMPO optimization problem has been described by Hardemark et al. in 2004. The DMPO optimization problem can be formulated as:

$$min_{x,w}\ F(x,w)$$

with

$$\begin{cases} C(x,w) \leq 0 \\ Ax \leq b \\ w \geq 0 \end{cases}$$

In this new formulation, the fluence τ can be calculated from a set of control points described by the leaf positions *x* and the segment weights *w*, where the segments describe a specific configuration of jaws and MLC. The condition $w \geq 0$ ensures non negative fluence, *A* and *B* are coefficients set based on the available machine and the condition $Ax \leq b$ describes machine-specific requirements on the leaf positions. The DMPO problem is harder to solve than the fluence-based one, because it has a greater degree of non-linearity and it is subject to numerous linear constraints. The optimization algorithm for the DMPO is performed by the so-called RayOptimizer® (Lof et al. 2003) and its optimization core is a sequential quadratic programming algorithm (SQP), which is a basically gradient-based optimizer. Hence, every iteration the optimizer uses the gradient of the objective function defined in *x* and *w* to find an update of the parameters that will improve the objective function. The basic steps of the optimization are:

i. first of all, a few iterations are performed to find a set of control points which meet the user and the machine specific requirements. An initial estimation is produced by assigning a uniform fluence to the beam's eye view of the target for each beam;

ii. in the following iterations, the gradient of the objective function is computed through several steps (Figure 33 below):

   a. with respect to the dose : $\frac{\mathrm{d}\,F}{\mathrm{d}\,d}$

   b. with respect to the fluence : $\frac{\mathrm{d}F}{\mathrm{d}\tau} = \frac{\mathrm{d}\,F}{\mathrm{d}\,d}\frac{\mathrm{d}d}{\mathrm{d}\,\tau}$

   c. with respect to leaf position : $\frac{\partial\,F}{\partial x} = \frac{\mathrm{d}\,F}{\mathrm{d}d}\frac{\mathrm{d}d}{\mathrm{d}\tau}\frac{\partial\tau}{\partial x}$ and

   segments weights : $\frac{\partial\,F}{\partial w} = \frac{\mathrm{d}\,F}{\mathrm{d}d}\frac{\mathrm{d}d}{\mathrm{d}\tau}\frac{\partial\tau}{\partial w}$.

   In this step, the optimization of MLC leaf positions, of the segment weights and the conversion of fluence maps into the MLC settings are also performed. Then, the fluences are modeled with a grid which divides the beam's cross section into small elements, known as opening density matrix (ODM). The ODMs are then resampled to match the MLC leaves. In this way, the fluence values are constrained to a number of fluence intensity level and they are also decomposed into smaller elements used to build the segments. At the end, jaws positions are assigned to the segments and the remaining requirements set by the objective functions are processed. The jaws also allow to avoid leakage by conforming as close as possible the MLC aperture;

iii. at the end of this stage, when the optimization process reaches the optimal solution (i.e. minimizing the cost function), the plan is feasible to be delivered without any post-processing.

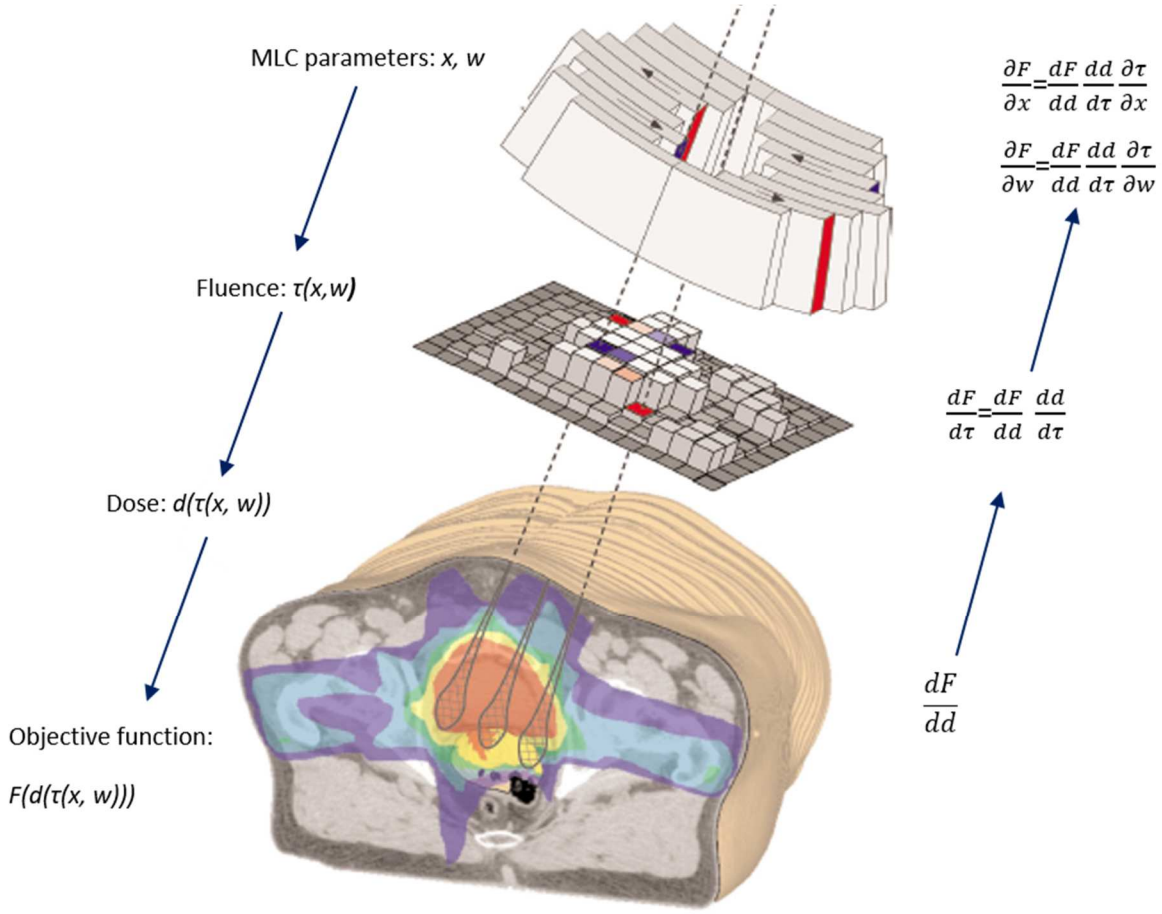

Figure 33. Gradient-based algorithm: The figure shows the objective function and its gradients calculated through several steps, taken from Hardemark et al. 2004.

2.3.2 Description of the dosimetric plan

2.3.2.1 The ITV approach

Each treatment plan is tumour specific and depends on the type of treatment to be delivered (e.g. palliative, adjuvant, definitive). All treatment plans should conform to the Radiation Therapy Oncology Group guidelines for treatment planning based on each disease category (RTOG 0617, 2016). In this work, we follow the guidelines presented in the RTOG 0617, which concerns the treatment of non-small cell lung cancer (NSCLS). This document presents also some methods to account for tumour motion during planning. The one used in this project is the internal target volume (ITV) approach. The ITV is defined by the maximum observed range of tumour motion. If we consider the 0% exhale and 50% inhale as the two extremes of respiratory motion, the ITV should contain the GTV designed in the 0% exhale and the GTV designed in the 50% inhale phases. It has to be pointed out that for the 4D CT plan the delineation of the ITV is fundamental for the placement of the isocentre of the beams, which are placed in the centre of the ITV. The ITV is by definition the same in all respiratory phases.

2.3.2.2 Plan optimization

In this section we will explain the basic stages used for the creation and optimization of the 4D CT treatment plan on the 0% exhale. Since part of this project has been carried out at the Radiation Physics Laboratory at the University of Sydney, which also collaborates with the Liverpool Hospital and the Ingham Institute (Liverpool, Sydney), we also use as guideline for the implementation of the plan, the IMRT plan protocol used at the department of Radiation Therapy Planning at Liverpool Hospital. This protocol includes all the specifications of the RTOG 0617 and it was used as reference for the evaluation of the acceptability of the elaborated plans. The creation and optimization process of a treatment plan can be represented with the decision tree shown in Figure 34.

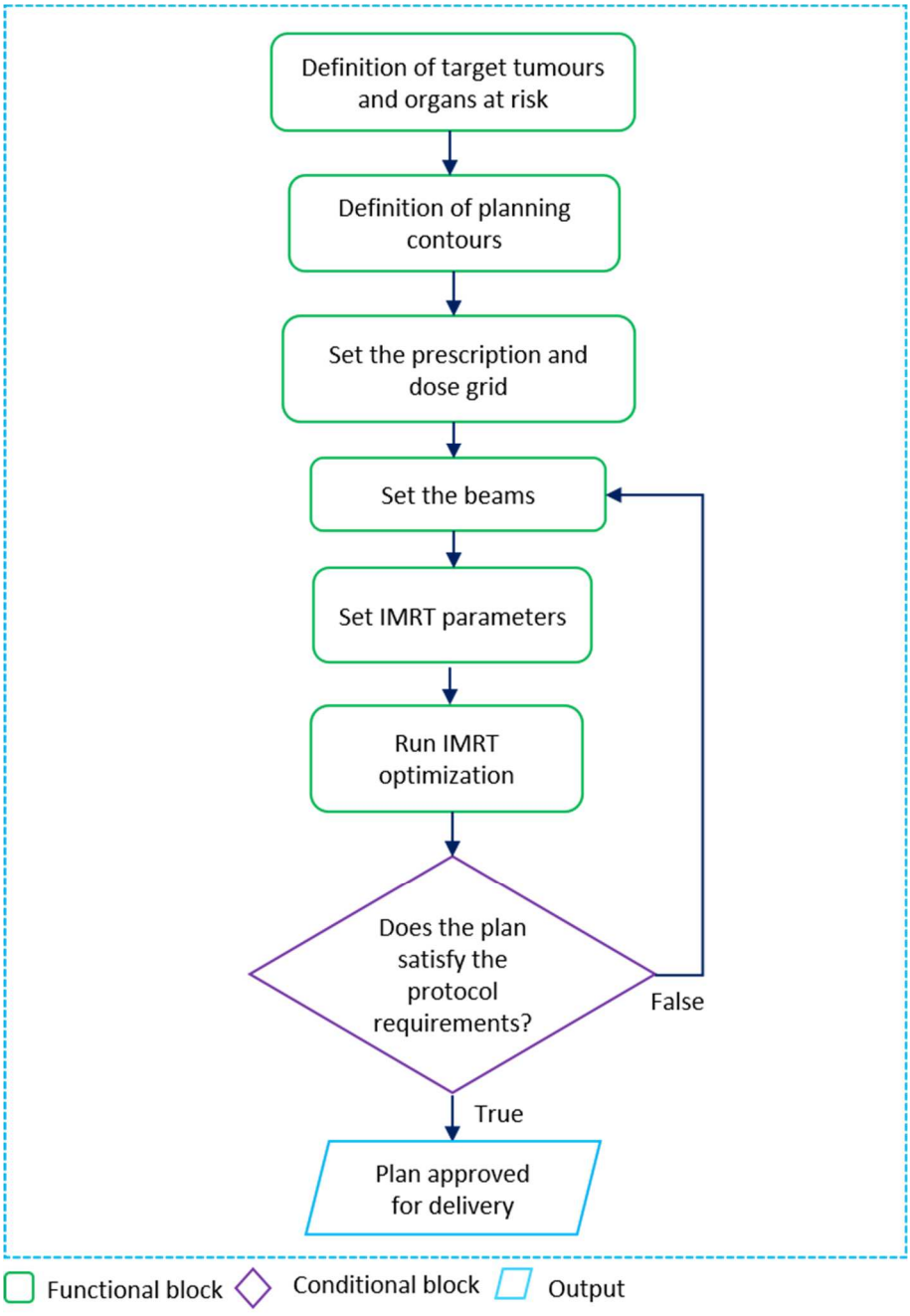

Figure 34. Optimization: flowchart of the plan optimization process.

The key points for the creation of the plan are:

i. Definition of target tumour and organs at risk.

   In this phase, the target (i.e. tumour) is delineated by an expert and labelled as GTV. Then the critical structures surrounding the tumour are also delineated.

Considering that our focus is lung tumour, the organs at risk taken into account are: lungs, heart, spinal cord and oesophagus.

ii. Definition of planning contours.

The planning contours to be defined are the ITV, the PTV and a series of rings with growing diameters, which are defined starting from the ITV. ITV and PTV are delineated in order to account for tumour motion and set up uncertainties (see section 1.1.1, Chapter I). The rings are fundamental during the optimization process to push the dose to the GTV, sparing the surrounding healthy tissues. RTOG 0617 suggests that the PTV should include the ITV with a margin at least of 0.5 cm in all directions.

iii. Prescription and dose grid.

The dose prescribed for a specific treatment is specific to the treatment in question. Three major categories of treatment can be individuated: adjuvant, palliative and definitive. The prescribed dose for a definitive treatment is 60 Gy to the 95% of the PTV as suggested by the RTOG 0617 study. In this step, the dose grid on which the dose is computed is defined. In this work the resolution has been set to [0.25x0.25x0.25] cm^3.

iv. Beams.

In our study, the beams are modelled based on the Elekta Versa (Elekta, Sweden) machine, with an energy of 6 MV for each beam and a dose rate of 550 MU/min. The position and the number of beams around the patient are variable and defined by the planner. What does not change is the distance from the source of photons to the isocentre, also known as source-axis distance (SAD), which for the linac is 100 cm. Instead, the distance from the source of radiation of the treatment machine to the surface of the patient (source-skin distance, SSD) continually changes while the gantry is rotating around the patient. Usually for lung cancer, the idea is avoiding placing beams that enter in the contra-lateral lung (i.e. the lung without the tumour) and also ensuring that beams are at least 20 degrees apart from each other and not opposing. IMRT is planned in “Step & shoot” (see section 1.1.2.2 in Chapter I). In this way, the leaves of the MLC try to conform the shape of the PTV, in order to protect normal tissues outside of the target volume. An example of MLC’s leaves shaping the PTV is shown in Figure 35.

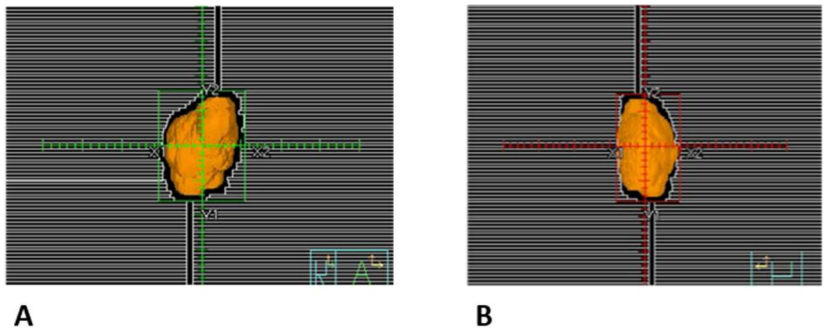

Figure 35. MLC's leaves: Beams Eye View (BEVs) for two different beams and the positioning of the MLC leaves in order to shape the tumour. A- beam 1. B-beam 2.

v. IMRT optimization parameters.

At this step, the planner sets the parameters regarding the IMRT optimization algorithm configuration. The first parameter to choose is the optimization type; all the dosimetric plans in this project is performed using DMPO optimization (section 2.4.1.3). After choosing the optimization type, other parameters used in this study are listed in the Table 12. The parameters "Minimum segment area" and "Minimum segment MU's" that appear in Table 12 depend on the tumour volume and machine capability parameters.

Table 12. List of parameters to set before running the optimization

Max iterations	Set the default number of times that the software should refine the optimization
Max number of segments	Set the maximum number of segments created during the optimization
Minimum segment area	Set the default minimum contiguous area that should be exposed by any MLC control points
Minimum segment MU's	Set the default minimum MU's required for each MLC control points
Compute final dose	Select whether the software automatically computes dose when the conversion is complete

vi. Define IMRT problem.

In this last step, the user has to define a list of dose volume constraints on specific ROI that will give an acceptable plan (see point vii). For each ROI, the planner can define an objective function that has to be optimized. A number of desired dose metrics are entered; each may have a different weighting factor, according to how important it is to satisfy the plan requirements. For instance, usually the ITV has a

very high weighting factor in order to push the optimization to give the maximum dose to the target tumour (see Table 1 in section 1.2.1.3 (Keall et al. 2006a)). If some structures have dose volume constraints that "conflict" with other constraints on other structures (e.g. two overlapping structures and one is supposed to get Max Dose but at the same time the second one should get Min Dose) the optimization will be stopped without giving any results. This was the most "trial and error stage" of the optimization process because standardized parameters or constraints value do not exist and so the planner has to attempt different solutions before getting the best one.

vii. Satisfaction of protocol requirements.

During treatment optimization, the identification of the best plan solution is achieved if the plan satisfies the requirements proposed in the protocol. These requirements concern the dose that critical structures should receive. The first requirement to be satisfied, as suggested by the RTOG 0617, is that the PTV should receive at least the 95% of the prescribed dose. There are also other requirements on the PTV (e.g. D98 that is the dose received by the 98% of the volume and D2), on the ITV (e.g. V100 that is the % of volume which receive the 100% of the dose and V98) and on the Max Dose or Mean Dose received by organ at risk. In Table 13 the requirements used in this work for the acceptance evaluation of the plan are reported. These requirements are chosen according to RTOG 0617. After the plan has been approved, it is ready for treatment delivery.

Table 13. Protocol requirements that the treatment plan has to satisfy to be acceptable.

Structure	Metric	Requirements
PTV	D98	At least 95% of target dose
PTV	D2	<107% of target dose
ITV	V100	Should receive 100% of target dose
ITV	V98	Should receive 98-99% of target dose
Spinal cord	Max Dose	45 Gy
Lungs	Mean Dose	15 Gy
Oesophagus	Mean Dose	28 Gy
Heart*	Max Dose	40 Gy

*if heart is close to the PTV, the D50 on the heart should be inferior of 60 Gy at least.

2.3.2.3 4D dosimetric plan

The need to account for respiratory motion during the planning phase of radiotherapy has resulted in the rapid growth of 4D radiotherapy, which is defined as the "explicit inclusion of the temporal changes in anatomy during the imaging, planning and delivery of radiotherapy" (Keall 2004). In this 4D radiotherapy scenario, there is the need to design a treatment plan on the 4D CT dataset suitable for all the respiratory phases, known as 4D CT treatment planning. The basic stages for the creation of a 4D CT treatment planning are shown in Figure 37.

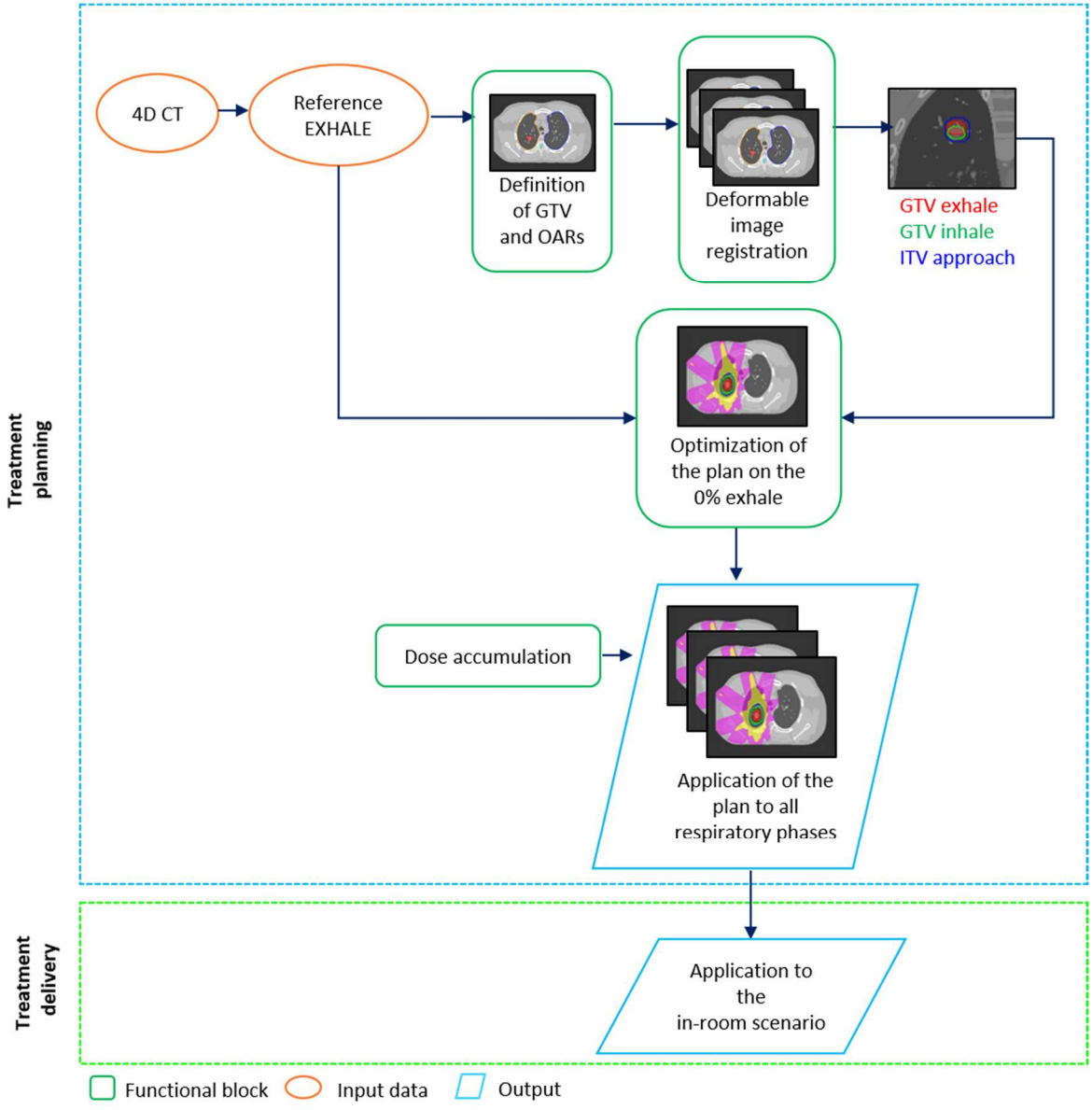

Figure 36. 4D CT treatment planning: basic steps of the approach used to create a 4D CT dosimetric plan.

In the first step of the 4D CT planning, we choose as reference the 0% exhale phase, on which we delineate the contours of the target and critical structures and then we propagate these contours to all other phases by applying the DIR mentioned in section 2.3.3.1.1. The plan is optimized on the 0% exhale phase and then applied to all other phases. Since the Pinnacle^3 does not currently have the ability to plan on a 4D CT dataset, after the plan optimization on the 0% exhale, each phase is considered independently, creating on it an individual plan, and subsequently integrated with the plans on the other phases, as reported by Colgan et al. 2008.

2.3.3 Experiments for dosimetric adaptation

The focus of this part of the project is the evaluation of the dosimetric variations between the pre-treatment and the treatment scenario caused by anatomical changes and motion. The plan, created and optimized on the 0% exhale of the 4D CT dataset, is applied on the model outputs of Fayad's model. At the beginning, the CT/MRI digital phantom is used for the dosimetric validation of the model performance thanks to the presence of the CT acquired at the cine-MRI samples (i.e. ground truth). Then the treatment plans are also optimized for the two CT/CBCT patients (patient A and B) and the CT/cine-MRI patient (patient C).

2.3.4.1 Dosimetric simulation on the digital phantom

In this section the steps for the creation and optimization of the 4D CT treatment plan on the CT/MRI digital phantom are presented. The plan is updated with respect to the ground truth and to the outputs of Fayad's model, according to the different surrogates (as reported in section 2.2.3.1.3).

2.3.4.1.1 4D CT treatment plan

As mentioned in the section 2.2.1 the tumour in the CT/MRI digital phantom is located in the upper part of the right lung with a radius of 7.55 mm. After the segmentation of the tumour and organ at risk on the 0% exhale phase, we apply the DVFs used during the model construction phase (section 2.3.3.1.1) to warp the contours of the tumour and the anatomic structures on all the other respiratory phases. Once get the GTV contour on all the phases, the ITV is delineated. Figure 37 shows the ITV derived for the CT/MRI

phantom. The ITV is expanded from the GTV in 0% exhale and the GTV in 50% inhale adding a margin of 3 mm in SI, AP and RL direction. The ITV is always the same for all the respiratory phases (see section 2.4.2.1).

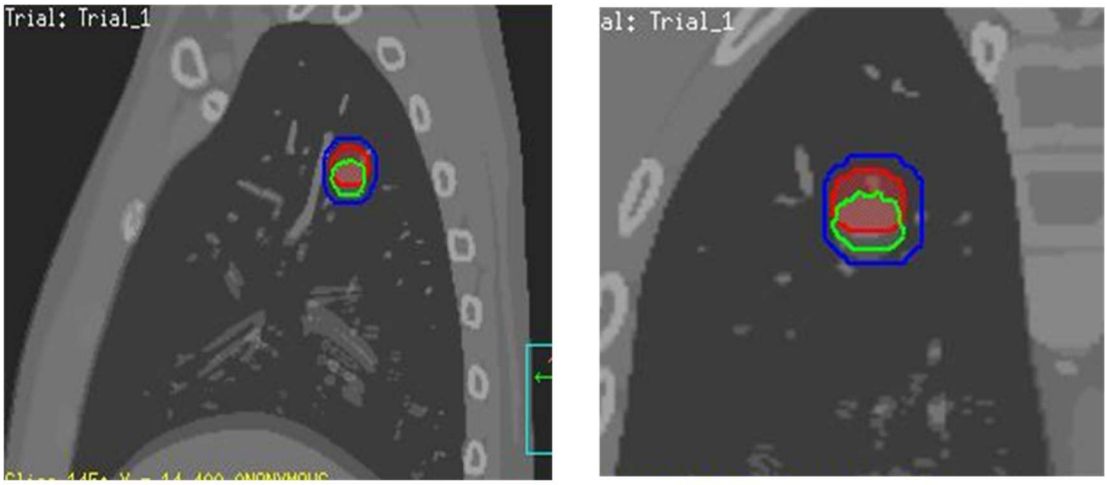

Figure 37. ITV approach: The ITV (blue) comprehends the GTV I the 0% exhale (red) phase and in the 50% inhale phase (green). A-sagittal view. B-coronal view.

After the delineation of the ITV, other planning contours are designed. They are reported in Table 14.

Table 14. Planning contours for the CT/MRI phantom

Source	New ROI	Expansion AP, SI, RL [mm]
ITV	PTV	5
PTV	PTV_02	2
PTV_02	RING_10	10
RING_10	RING_20	10
RING_20	RING_30	20
RING_30	RING_50	20

For the CT/MRI phantom 6 beams are used to hit the tumour, with angles and energies reported in Table 15, and the target dose is prescribed to the 95% of the PTV. In Figure 38 the position of the beams is shown.

Table 15. Beams setting for CT/MRI phantom

Beams	Gantry angle	Beam energy
1	22°	6 MV
2	342°	6 MV
3	183°	6 MV
4	228°	6 MV
5	256°	6 MV
6	298°	6 MV

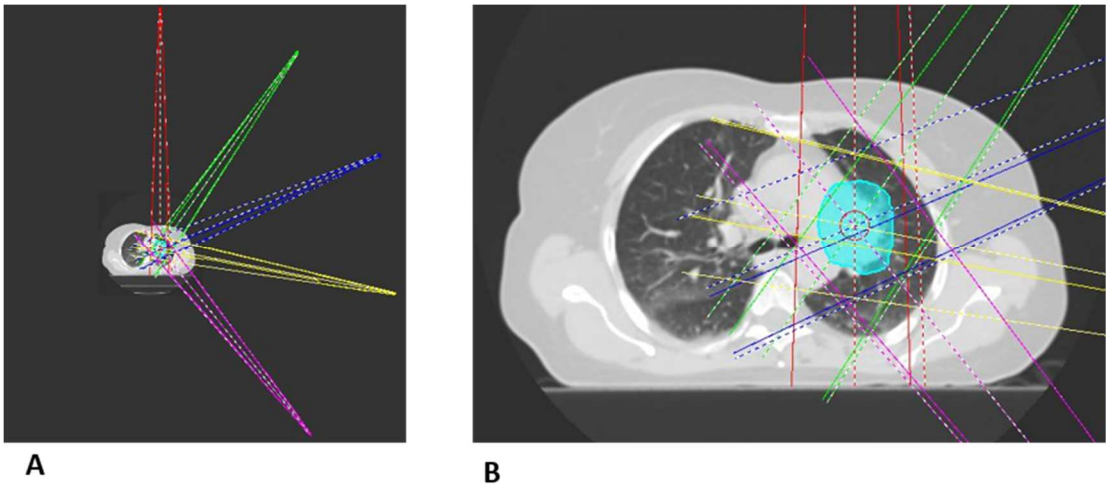

Figure 38. Beams for CT/MRI phantom: position of the 6 beams used to hit the tumour.

In this way the IMRT parameters are set considering the size of the tumour and are reported in Table 16.

Table 16. IMRT parameters for CT/MRI phantom

Max iterations	40
Max number of segments	30
Minimum segment area	8 cm^2
Minimum segment MU's	8
Compute final dose	Yes

The last step of the treatment plan is the definition of the dose volume constraints on critical structures. In Table 17 the objective functions defined for achieving an acceptable plan on the CT/MRI phantom are reported.

Table 17. Dose volume constraints for the CT/ MRI phantom

Structure	Constrain Type	Dose [Gy]	Volume [%]	Weight
ITV	Uniform dose	62	--	65
PTV_02	Min dose	60	--	45
PTV_02	Max dose	61.5	--	45
Spinal cord	Max dose	20	--	10

In this way the treatment plan realized on the CT/MRI phantom satisfies the protocol requirements reported in section 2.3.2.2.

2.3.4.1.2 Application of the plan to the ground truth and model outputs

The 4D CT plan is subsequently applied to the CT acquired at the cine-MRI sample (ground truth) and to the output of Fayad's model. In this process, the plan does not change and it is simply updated to the ground truth CT or to the specific output of the model. The only things that change is the contour, according to the specific respiratory phase in CT. In this case the ITV and hence the other planning contours are updated as well. With

reference to the tests carried out on the Fayad's model in section 2.2.3.1.3, the 4D CT plan is updated on:

- all the tests listed in Table 4 (except for test 0). These tests are performed giving the same surrogate in pre-treatment and treatment;
- tests 3, 4, 7 in Table 5 These tests are performed giving combination of internal surrogates in pre-treatment and treatment;
- test 2 in Table 6. This test is performed giving combination of internal and external surrogate.

2.3.4.1.3. Dosimetric validation

Since for the digital phantom the treatment data also includes the ground truth, the comparison between the plan updated on the outputs of Fayad's model and the plan updated on the ground truth is carried out in order to validate the dosimetric results generated on the model outputs. The comparison considers the difference between the output of the model and the ground truth in terms of "relevant metrics", which are the same of the plan evaluation. In Figure 39 a schematic process for the dosimetric validation is represented.

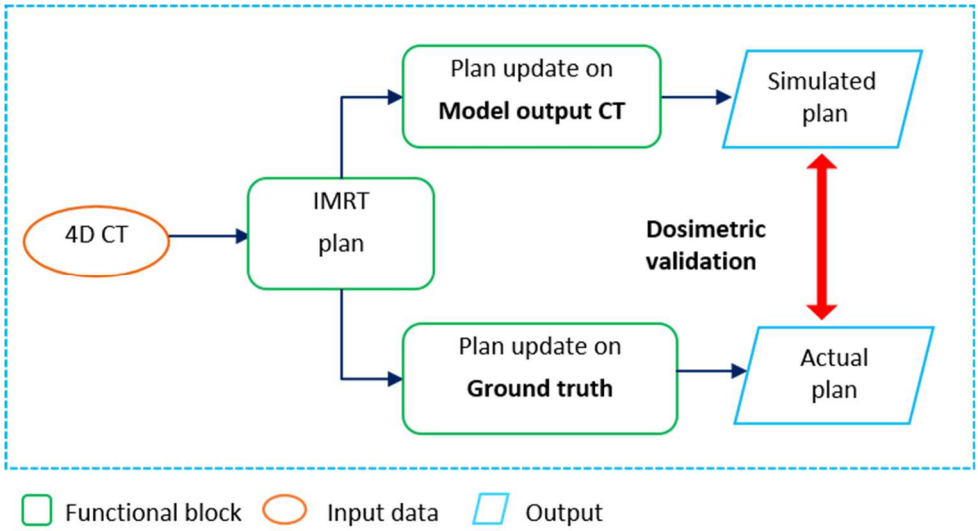

Figure 39. Dosimetric validation: schematic process of the dosimetric validation for the CT/MRI digital phantom.

2.3.4.2 Dosimetric plan on patient cases

In this section the creation and optimization of the 4D CT treatment plan on the CT/CBCT patients (patient A and patient B) and for the CT/cine-MRI patient (patient C) is described. The plan is adapted to the outputs of Fayad's model afterwards.

2.3.4.2.1 4D CT treatment plan

For all the patients, after the segmentation of the tumour and OARs on the 0% exhale phase, a DVF^{-1} obtained by the DIR used during the model construction phase (section 2.3.2.1) is applied, in order to obtain the contour of the tumour and anatomical structures on all other phases. After the delineation of the GTV on all the phases, the ITV is derived. In all the patients, the ITV is expanded from the GTV in the 0% exhale and from the GTV in the 50% inhale. The specific margins added for the three patients are reported in the Table 18.

Table 18. Margins added in AP, SI, RL direction in order to obtain the ITV for the patients.

	AP [mm]	**SI [mm]**	**RL [mm]**
Patient A	10	10	10
Patient B	5	5	5
Patient C	5	5	5

The ITV considered is always the same for all the respiratory phases. In Figure 40 the ITVs (in blue) designed for patient A, B and C are shown.

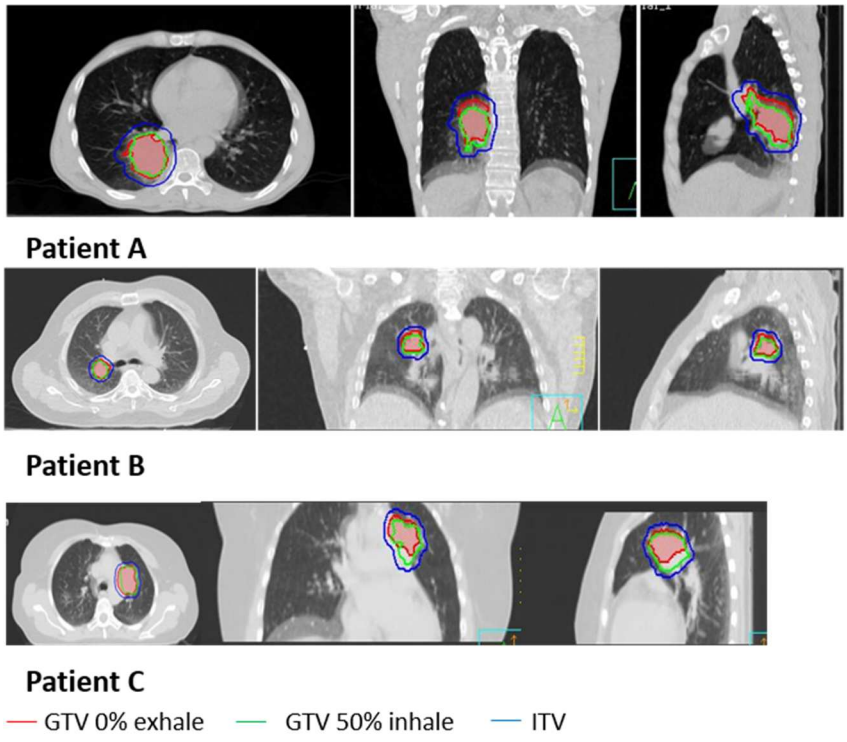

Figure 40. ITV approach: axial, coronal and sagittal view of the patients. The ITV (blue) comprehends the GTV in 0% exhale (red) and the GTV in 50% inhale (green).

Other planning contours are designed after the ITV by considering a contour as source and extending it to obtain the new one. They are reported in the Table 19.

Table 19. Planning contours designed for patients A, B and C.

		Patient A	Patient B	Patient C
Source	**New ROI**	**Expansion in AP, RL, SI[mm]**	**Expansion in AP, RL, SI [mm]**	**Expansion in AP, RL, SI [mm]**
ITV	PTV	5	5	5
PTV	PTV_02	2	2	2
PTV_02	RING_10	10	10	8
RING_10	RING_20	10	10	10
RING_20	RING_30	20	20	10
RING_30	RING_50	20	20	20

The number of beams, their energy and gantry angles are listed in the following Table 20. In the Figure 41 are instead shown the position of the beams for each patient.

Table 20. Number of beams, their position and energy for the patients.

	Beams	Gantry angle	Beam energy
Patient A	1	180°	6 MV
	2	334°	6 MV
	3	304°	6 MV
	4	267°	6 MV
	5	230°	6 MV
Patient B	1	0°	6 MV
	2	207°	6 MV
	3	274°	6MV
	4	315°	6 MV
Patient C	1	0°	6MV
	2	35°	6 MV
	3	67°	6 MV
	4	101°	6 MV
	5	141°	6 MV

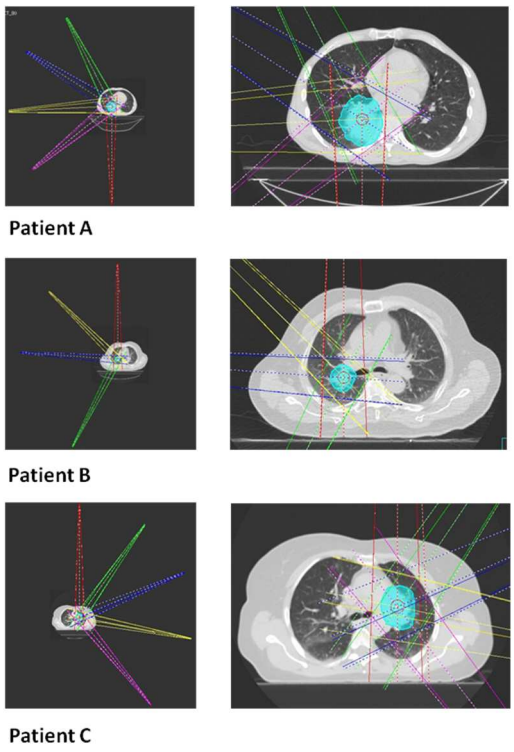

Figure 41. Beams position: beams positioned around the patients and zoom view of the beams.

The IMRT parameters are set considering the size of the tumour and are reported in Table 21.

Table 21. IMRT parameters for patients.

	Patient A	**Patient B**	**Patient C**
Max iterations	40	40	40
Max number of segments	50	30	30
Min segment area	8 cm^2	8 cm^2	8 cm^2
Min segment MU's	8	8	8
Compute final dose	Yes	Yes	Yes

The last step of the treatment plan is the definition of the dose volume constraints on critical structures. In the Table 22 are reported the objective functions defined for an acceptable plan for patients, in order to satisfy the RTOG requirements. The treatment plans realized satisfy the protocol requirements reported in section 2.3.2.2.

Table 22. Dose and volume constraints for patients.

	Structure	Constraint type	Dose [Gy]	Volume [%]	Weight
Patient A	ITV	Uniform Dose	62	-	80
	PTV_02	Min Dose	60.5	-	60
	PTV_02	Max Dose	61.5	-	60
	Heart	Max DVH	6.2	80	30
	Spinal cord	Max Dose	20	-	40
	Ring_10	Max DVH	57	5	25
	Ring_20	Max DVH	50	30	25
	Ring_30	Max Dose	40	-	20
	Ring_50	Max Dose	40	-	20
Patient B	ITV	Uniform Dose	62	-	65
	PTV_02	Min Dose	59.5	-	45
	PTV_02	Max Dose	61.5	-	45
	Spinal cord	Max Dose	20	-	10
	Heart	Max DVH	6.2	80	30
	Ring_10	Max DVH	57	5	10
	Ring_20	Max DVH	50	30	13
	Ring_30	Max Dose	45	-	18
	Ring_50	Max Dose	35	-	22
Patient C	ITV	Uniform Dose	62	-	80
	PTV_02	Min Dose	59.5	-	65
	PTV_02	Max Dose	61.5	-	65
	Spinal cord	Max Dose	20	-	25
	Heart	Max DVH	6.2	80	30
	Oesophagus	Max DVH	6.2	80	30
	Ring_10	Max DVH	57	5	25
	Ring_20	Max DVH	50	30	30
	Ring_30	Max Dose	40	-	20
	Ring_50	Max Dose	6.2	80	30

2.3.4.2.2. Application of the plan to the outputs of Fayad's model

The 4D CT plans for patient A, B and C are subsequently applied to the output of Fayad's model. In this application the plan does not change, it is simply updated to the particular output of the model. The only things that changes are the contours, obviously according to the CT. In this case the ITV and hence the other planning contours are updated too, considering the CT. With reference to the tests carried out on the Fayad's model in section 2.2.3.2.3, the 4D CT plan are updated on:

- patient A: all the tests listed in Table 9 (except for test 0) and test 3 in Table 10;
- patient B: all the tests listed in Table 9 (except for test 0) and tests 3, 4, 5 in Table 10;
- patient C: all the tests in Tables 9 (except for test 0), tests 3,4,5 and 6 in Table 10 and all tests in Table 11.

2.3.4.2.3 Dosimetric evaluation

In contrast to the CT/MRI phantom, the dataset of both CBCT/CT patients and CT/cine-MRI patient do not include ground truth data. However, it is possible to compare the plan applied on the inhale phase during the 4D CT planning with the plan updated on the outputs of the Fayad's model. The comparison evaluates the difference between the plan on the model output and plan on the inhale phase considering the "relevant metrics", which are the same considered for the evaluation of the treatment plan. In Figure 42 a schematic process for the dosimetric evaluation is represented. For the sake of consistency, for patient C (the CT/cine-MRI patient) we also consider a "mean 4D CT plan", which can be explained as the mean trend of all the plans on all the ten phases.

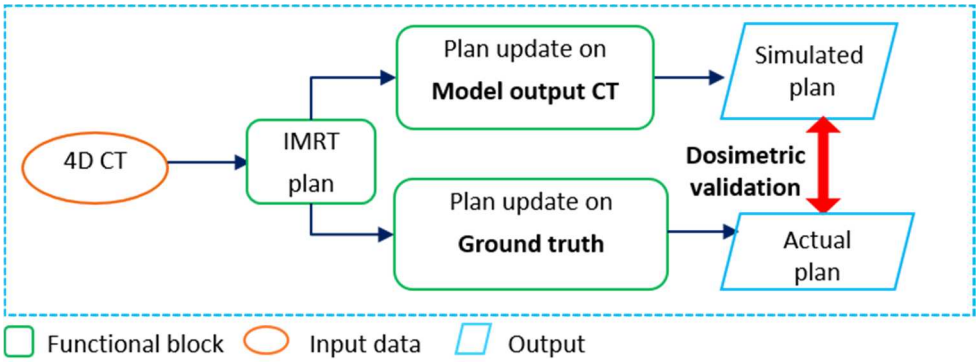

Figure 42. Dosimetric evaluation: schematic process of the dosimetric evaluation for the patient.

Chapter III: Results and discussions

3.1 Geometric adaptation

Starting from the model construction and then moving to model outcomes, in this section we discuss all results. The CT/MRI phantom measurements provide an assessment of the accuracy of the model and, even if the motion applied by the phantom is a simplification of clinical reality, results are confirmed by the patient dataset.

3.1.1 Results on the CT/MRI digital phantom

3.1.1.1 Model construction

For the models construction, the input data required are the DVFs, describing the motion with respect to the reference phase (e.g. the 0% exhale phase or the MidP), and the surrogates extracted from the 4D CT pre-treatment dataset.

i. Identification of the reference volume.
   In Figure 43 we show the MidP volumes overlapped with the 0% exhale volume (Figure 43 A) and with the 50% inhale volume (Figure 43 B); the MidP correctly occupies an intermediate position, as visible around the diaphragm region. Figure 43 C represents the overlap between the 50% inhale phase and the 0% exhale phase, where the diaphragm reaches its highest position.

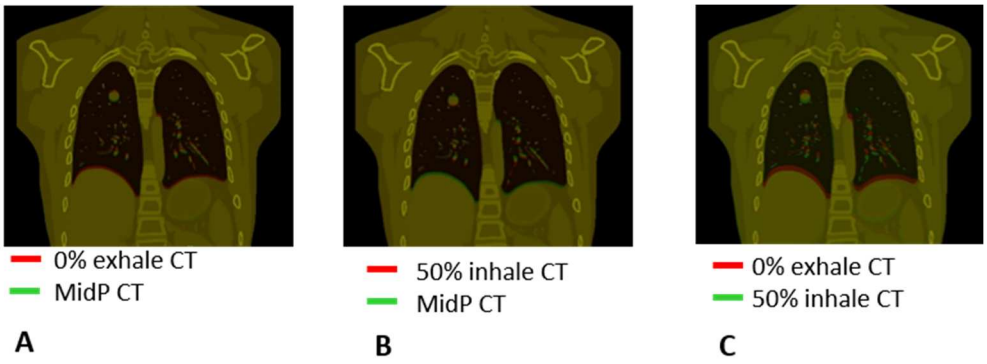

Figure 43. Reference volume-CT/MRI phantom: A-overlap between the MidP volume and the 0% exhale CT. B-overlap of the MidP volume and the 50% inhale CT. C-overlap of the 50% inhale CT and the 0% exhale phase.

ii. Deformable image registration.

In Figure 44 an example of the resulting DVF describing the displacement between the 50% inhale phase and the 0% exhale phase is shown. The features points (1061 points) on the 0% exhale CT (Figure 45 A) and the 50% inhale CT (Figure 45 B) result in a median accuracy (± interquartile range) of 1±1.4 mm. Comparing the voxel size ([1 1 1] mm) with the median accuracy (± interquartile range), we can assert that the DIR achieves acceptable results. Performing accurate DIR is important because the accuracy of the motion model partly depends on the accuracy of DIR.

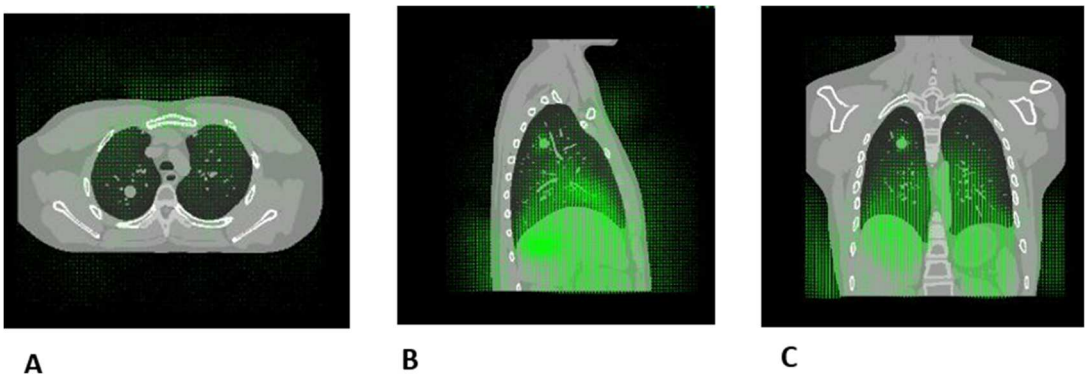

Figure 44. DVF-CT/MRI phantom: overlap between the 0% exhale phase and the DVF. A-axial plane. B-sagittal plane. C-coronal plane.

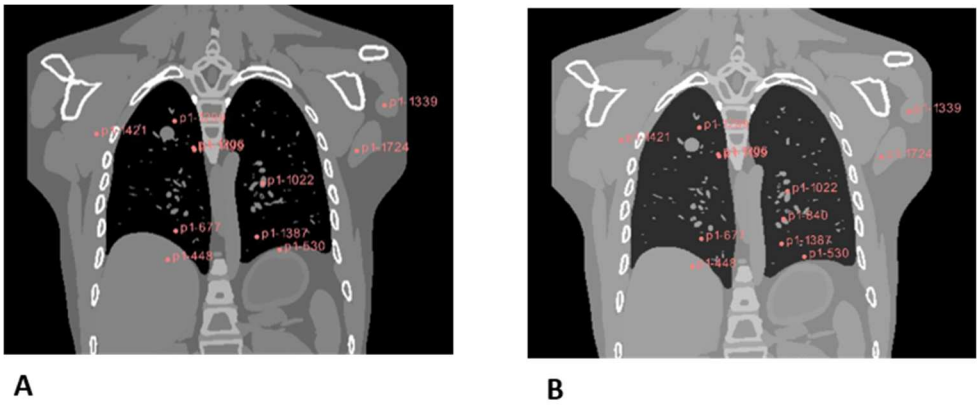

Figure 45. Extracted features by SIFT: example of the extracted points by SIFT. A-0% exhale CT. B-50% inhale CT.

iii. Surrogates extraction.

In Figure 46 the mean respiratory signals are shown, as a function of the respiratory phase, as extracted from the 4D CT.

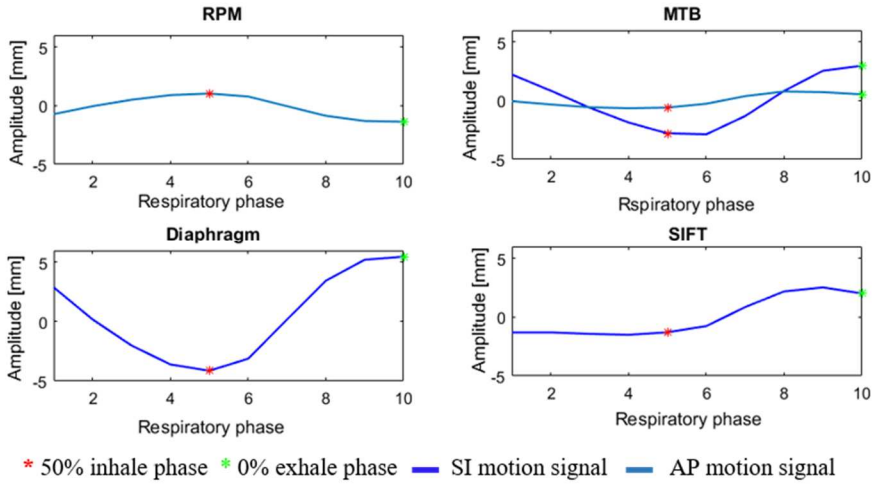

Figure 46. Pre-treatment signals-CT/MRI phantom: mean respiratory signals extracted from the 4D CT.

For all the signals, except for the SIFT, the 50% inhale (red star in Figure 46) corresponds exactly to the 5th CT volume, while the 0% exhale phase (green star in Figure 46) corresponds to the 10th CT volume. Diaphragm and MTB, when SI motion is considered, have a similar pattern but different range of motion: the diaphragm fluctuates in a range of 9.6 mm, whereas the GTV swings in 5.8 mm range. Comparing the SI direction and the AP direction (range of motion: 1.43

mm) of the MTB (blue and light blue lines in the upper right plot in Figure 46) can be asserted that the SI motion direction is dominant. The RPM signal (range of motion: 2.4 mm) has a reverse pattern compared to the diaphragm: indeed, during the inspiration the diaphragm contracts and the chest wall expands. The pattern of the SIFT signal is different from other internal signals because only two regions, with the highest range of motion and regular pattern, are taken into account (region 1 in sagittal and 4 in coronal plane (Figure 28 in Chapter II)). Furthermore, the CT/MRI phantom has an irregular respiratory motion in the lungs region.

3.1.1.2 Model update

Figure 47 shows the resulting signals on sagittal and coronal plane, after the cubic interpolation, as a function of acquisition time. The RPM fluctuates in a 4 mm range, like the MTB in AP direction (pink lines in Figure 47). As shown in Figure 47, the SI motion (MTB and diaphragm) on coronal and sagittal planes are very similar; the diaphragm has the biggest range of motion (16 mm), while the MTB moves of 8 mm. The SIFT signal on sagittal and coronal plane (range of motion: 9 mm and 4.6 mm respectively) are different because two regions, the same indicated above, are analysed.

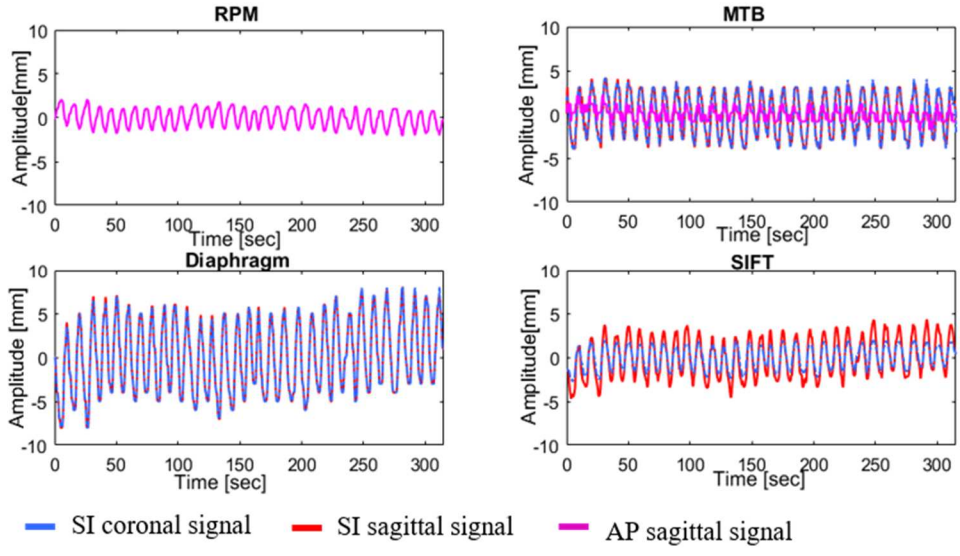

Figure 47. Treatment signals-CT/MRI phantom: respiratory signals extracted from the cine-MRI.

In Table 23 the motions of each signal in both pre-treatment and treatment session are summarised.

Table 23. Comparison between the ranges of motion of each surrogate in pre-treatment ad treatment.

Pre-treatment		Treatment	
Surrogate	**Mean signal [mm]**	**Coronal [mm]**	**Sagittal [mm]**
RPM AP	2.4	N.A.	4
MTB SI	5.84	8	8
MTB AP	1.43	N.A.	4
Diaphragm SI	9.6	16	16
SIFT SI	4	4.6	9

N.A.=not available

The last step necessary for Fayad's model is the identification of the cine-MRI sample more similar to the 0% exhale phase (Figure 48 A) and the MidP (Figure 48 B) (sample 487 and 320 respectively) (identified with the method described in Appendix C).

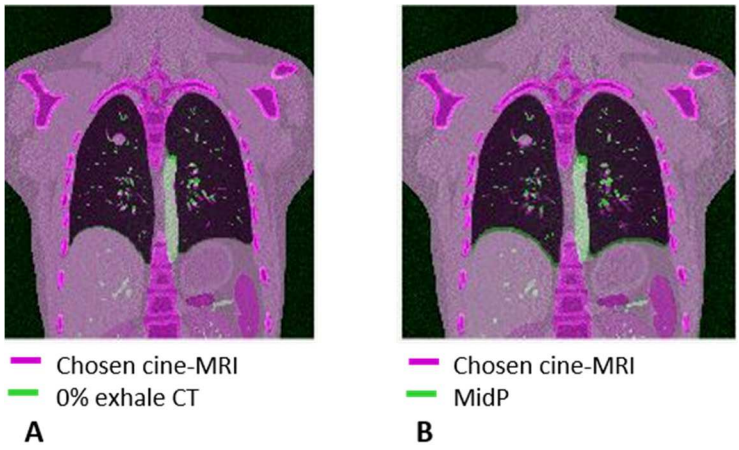

Figure 48. Cine-MRI samples-CT/MRI phantom: A- overlap between the chosen cine-MRI sample and the 0% exhale volume. B-overlap between the chosen cine-MRI sample and the MidP.

The median accuracy (± interquartile range) in the region containing the diaphragm boundaries (Table 24) has a maximum error in the neighbourhood of the double of the voxel size ([1 1 1] mm).

Table 24. Median accuracy (± interquartile range) on the diaphragm between the chosen cine-MRI sample and the reference CT.

Reference	Median accuracy (± interquartile range) [mm]
0% exhale	2±0
MidP	2.83±1.64

3.1.1.3 Tests performed and evaluations

In this section the most meaningful outcomes are reported, highlighting the comparison between Vandemeulebroucke's model and Fayad's model, in terms of the reference volume to use and the surrogate configuration.

For Fayad's model, considering as reference the MidP, Test 0 (reconstruction of the 50% inhale phase of the pre-treatment session) does not achieve satisfactory results. Using the MidP as reference, the mean motion of DVFs used to construct the model is lower than the case in which the 0% exhale phase is used as reference. Since the model updating is obtained giving the model an amplitude value, when the model is updated with a greater value than the mean DVF (i.e. mean DVF motion 0.03 vs. amplitude value 10.33) the model is not able to reconstruct the output CT (Figure 49). Due to this reason, in the following discussion Fayad's model, constructed with the MidP as reference, is no longer considered.

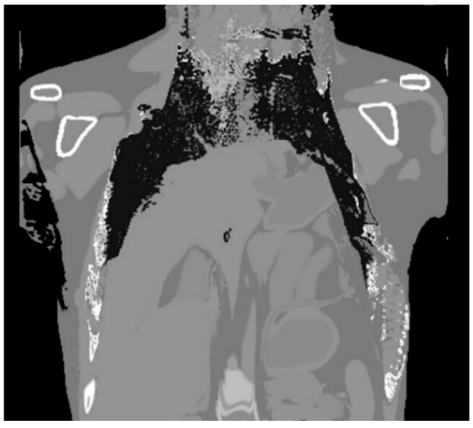

Figure 49. MidP as reference-Fayad's model: model output CT of Fayad's model when the MidP volume is used as reference.

The models are then tested considering an entire breathing cycle, using the diaphragm motion to construct and update the models. The geometric quantification obtained are shown in Figure 50, where in each histogram bar the variation of the three specific ROIs (diaphragm, heart and tumour) is summed and in the last bar the mean variation of each ROI is shown. In Vandemeulebroucke's outcomes, results are better on the diaphragm than on the heart, where the error is higher especially when the reference is the 0% exhale phase (middle histogram in Figure 50). In Figure 51 A and B the overlap and the difference volume, between Vandemeulebroucke's outcome (reconstructing the inhale phase) and the ground truth, are shown. In Fayad's model, the variations on heart are lower than the variations on Vandemeulebroucke's model (Figure 51 C). Vandemeulebroucke's model performs better when the MidP is considered as reference, as highlighted by the mean error shown in Figure 50. Comparing Fayad's model with Vandemeulebroucke's model, considering as reference the 0% exhale, the first model performs better: this result is expected since Fayad's model is constructed to work with the 0% exhale phase as reference, while Vandemeulebroucke's model with the MidP.

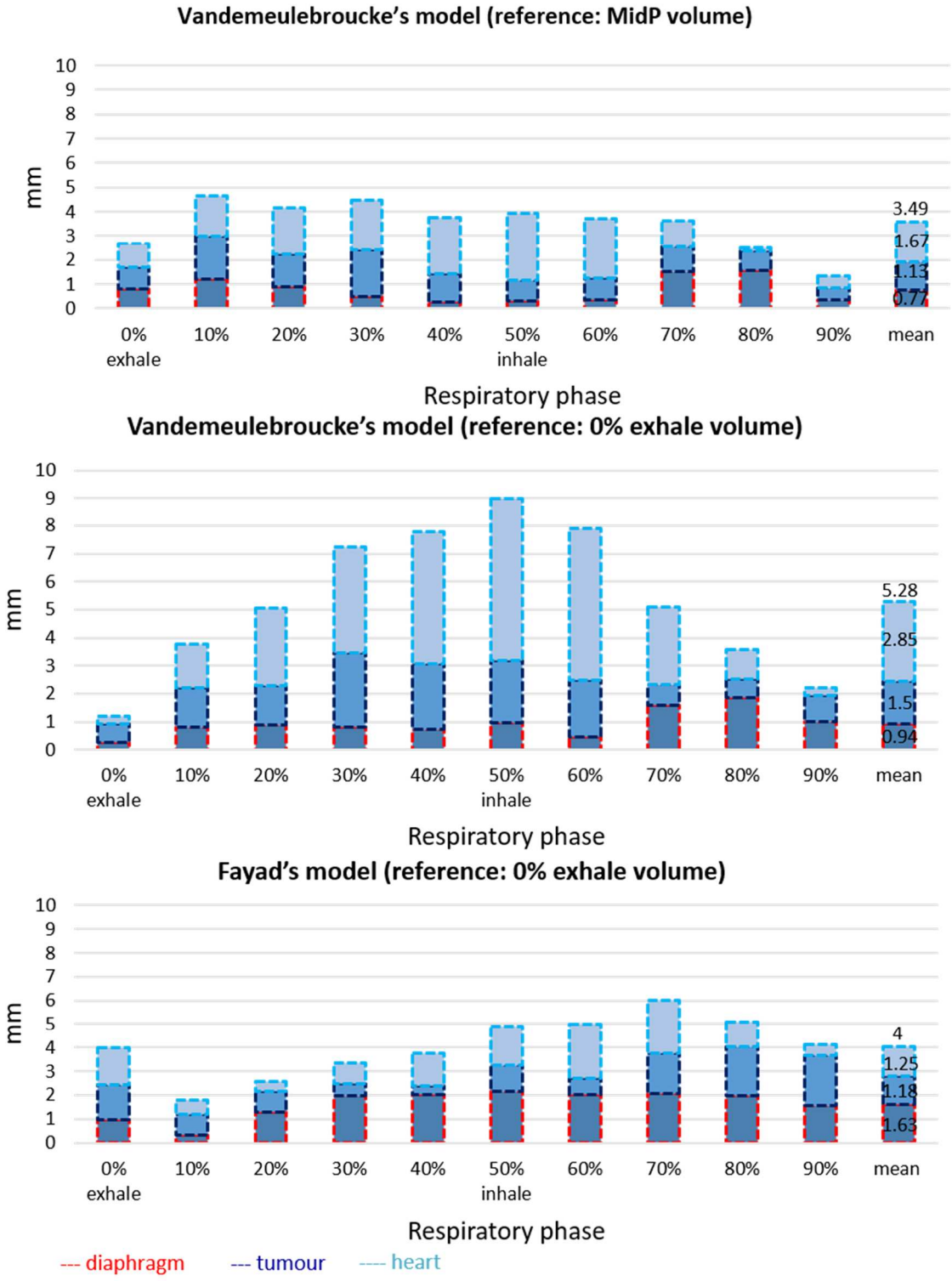

Figure 50. Breathing cycle geometric quantification: geometric quantification of an entire breathing cycle for Vandemeulebroucke's model, considering the MidP volume (upper case) or the 0% exhale phase (middle case), and for Fayad's model (lower case).

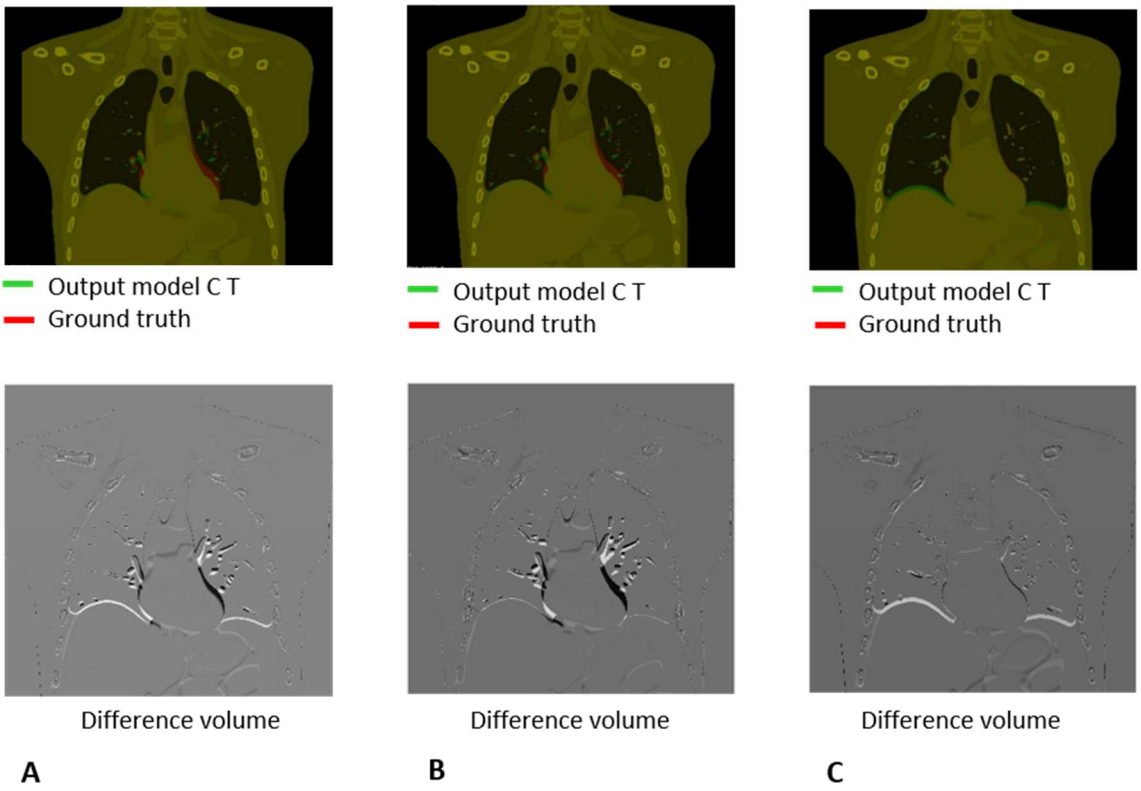

Figure 51. Inhale phase-CT/MRI phantom: reconstruction of the inhale phase. A-Vandemeulebroucke's model (reference: MidP). B- Vandemeulebroucke's model (reference: exhale). C-Fayad's model.

For what concerns Vandemeulebroucke's model, it performed better using the MidP as reference instead of using the 0% exhale also considering all the other surrogates. In Figure 52 A we report, as indicative values of all the evaluations, the geometric variations on Vandemeulebroucke's model, constructing and updating the model with the RPM signal. In Figure 52 B the correspondent model output CT overlapped with the ground truth is shown: the greatest difference is appreciated on the heart, as confirmed also by the geometric evaluation. Figure 52 C shows the difference between the model output CT and the ground truth, where, as it can be observed, the greatest difference between the two options is on the heart.

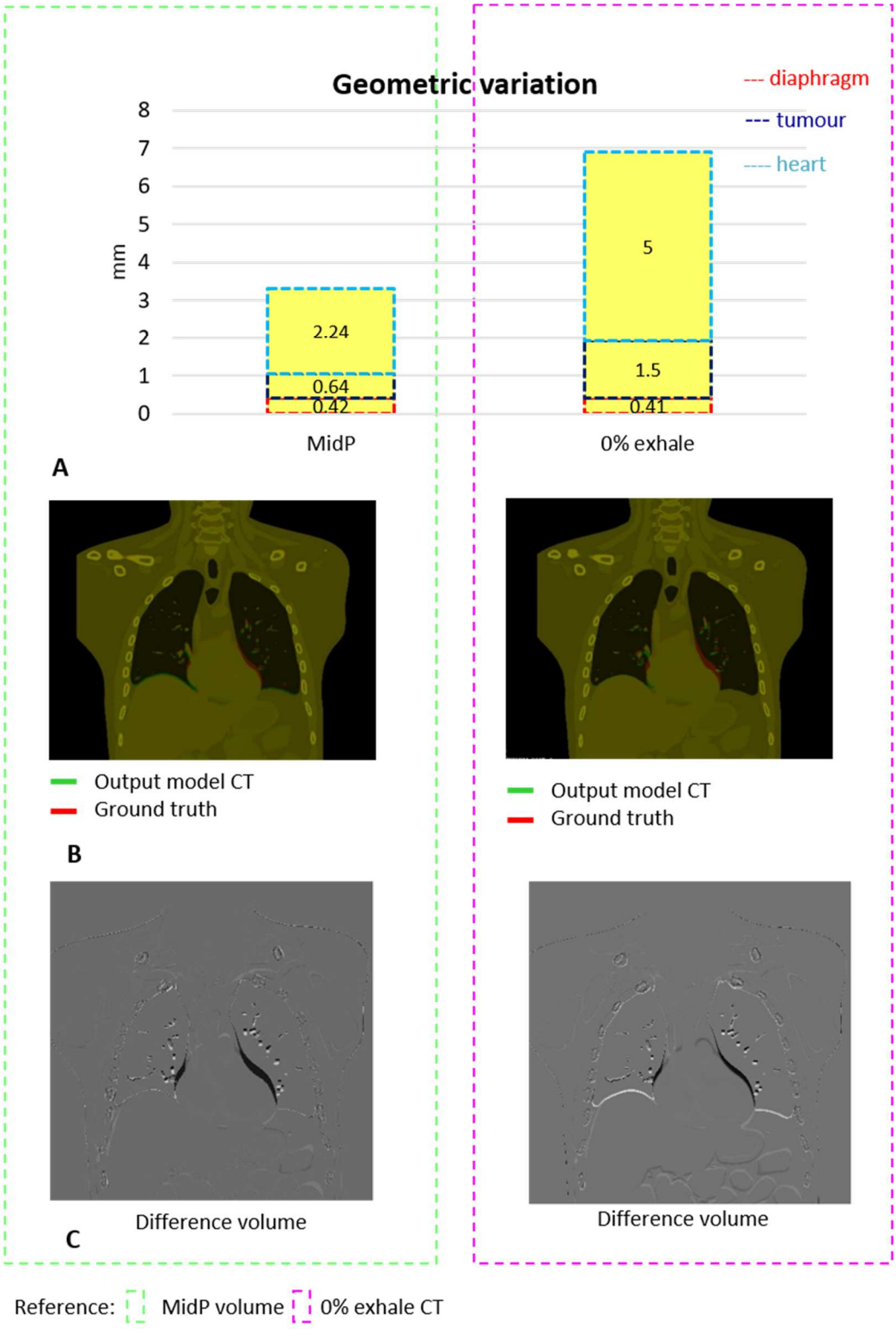

Figure 52. Vandemeulebroucke's model output-CT/MRI phantom: A-geometric variation. B-overlap of the model output and the ground truth. C-difference between the output volume and the ground truth.

For what concerns Fayad's model, before the evaluation of its behaviour with respect to the specific surrogate, we also have to evaluate the error introduced by the inversion of the vector field (DVF^{-1}). By comparing the overlap of the model output CT and the 50% inhale volume (obtained with the DVF^{-1}) and the overlap of the model output CT (obtained with the DVF) with the 0% exhale phase, we can assert that the inversion of the DVF does not add significant errors. In Table 25 the geometric evaluation for the three ROIs and the mean errors are reported.

Table 25. Geometric variation due to the DVF^{-1} to construct Fayad's model.

	Diaphragm [mm]	**Tumour [mm]**	**Heart [mm]**	**Mean [mm]**
DVF^{-1}	0.08	1.18	1.64	0.97
DVF	0.92	1.18	1.29	1.13

On Fayad's model (using the 0% exhale as reference) no important differences between the surrogates are appreciated. If we consider the same signal to construct and update the model, the tests in which the model is updated with the coronal value performed better and the combination of coronal and interpolated sagittal values seems not to improve the performance. This lack of improvement could be due to the sagittal value that, when it is combined with the coronal value, is interpolated, thus not adding additional information to the surrogate. In fact, the phantom was built using as internal surrogate the signal coming from interleaved cine-MRI slices of a patient, in which only the coronal surrogate was given as input with an interpolation at the sagittal samples. The geometric quantifications are shown in Figure 53; the different colours indicate the surrogate used to construct the model, the dashed boxes point out the specific evaluated ROI and the dashed grey line divides the tests in which only one surrogates is used (left part) from the one in which coronal and sagittal samples are considered (right part). In the tests performed using SIFT (light blue bars in Figure 53) we appreciate an overall error higher than 5 mm. This is because the signal describes the lung vessel motion and this region is not directly evaluated. Therefore, better results could be appreciated in the lung compared to the other model outputs.

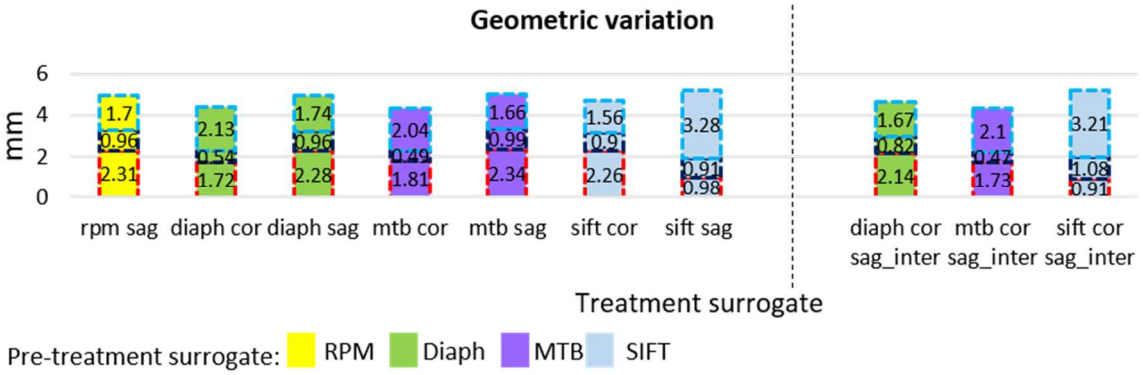

Figure 53. Fayad's model-CT/MRI phantom: geometric variation in mm computed as difference between the model output CT and the ground truth when the same surrogate is used to construct and update Fayad's model.

Figure 54 reports the overlap (Figure 54 A) and the difference (Figure 54 B) between the output model CT (updated with the coronal value of the MTB) and its correspondent ground truth: the model performs better on the tumour with respect to the diaphragm (as can be observed looking at the difference image).

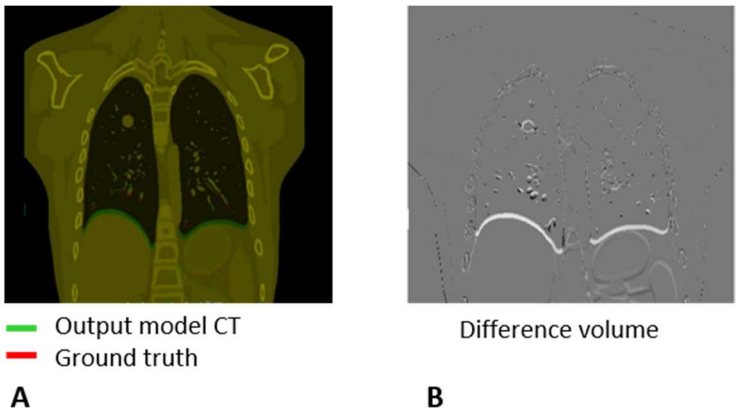

Figure 54. Fayad's model output CT-CT/MRI phantom: A-overlap of output model CT and the ground truth. B-difference volume.

Since Fayad's model allows the combination of different signals, other tests are performed with different combinations to evaluate if an improvement of the model is provided by attaching additional information. However, no improvement can be appreciated. An example of the geometric quantification is shown in Figure 55. The quantification, examined when the diaphragm or only the MTB (coronal samples) are considered (Figure 55 A), are compared with the quantifications obtained combining the surrogates (Figure 55

B). In the light orange bars in Figure 55 B we highlight the assessments done when the model is constructed using both diaphragm and MTB and then updated only with the diaphragm value (first bar on the right), with the MTB value (middle bar) or with both (left bar). By constructing the model with two signals and updating the model only with one, results worsen (especially on the diaphragm). Instead, by attaching two signals also in treatment, the outcome is similar to the one obtained in the upper histogram of Figure 55 A (i.e. using just one surrogate). So, the outcomes obtained when the model is constructed and updated with only one surrogates are comparable to the ones in which two surrogates are involved.

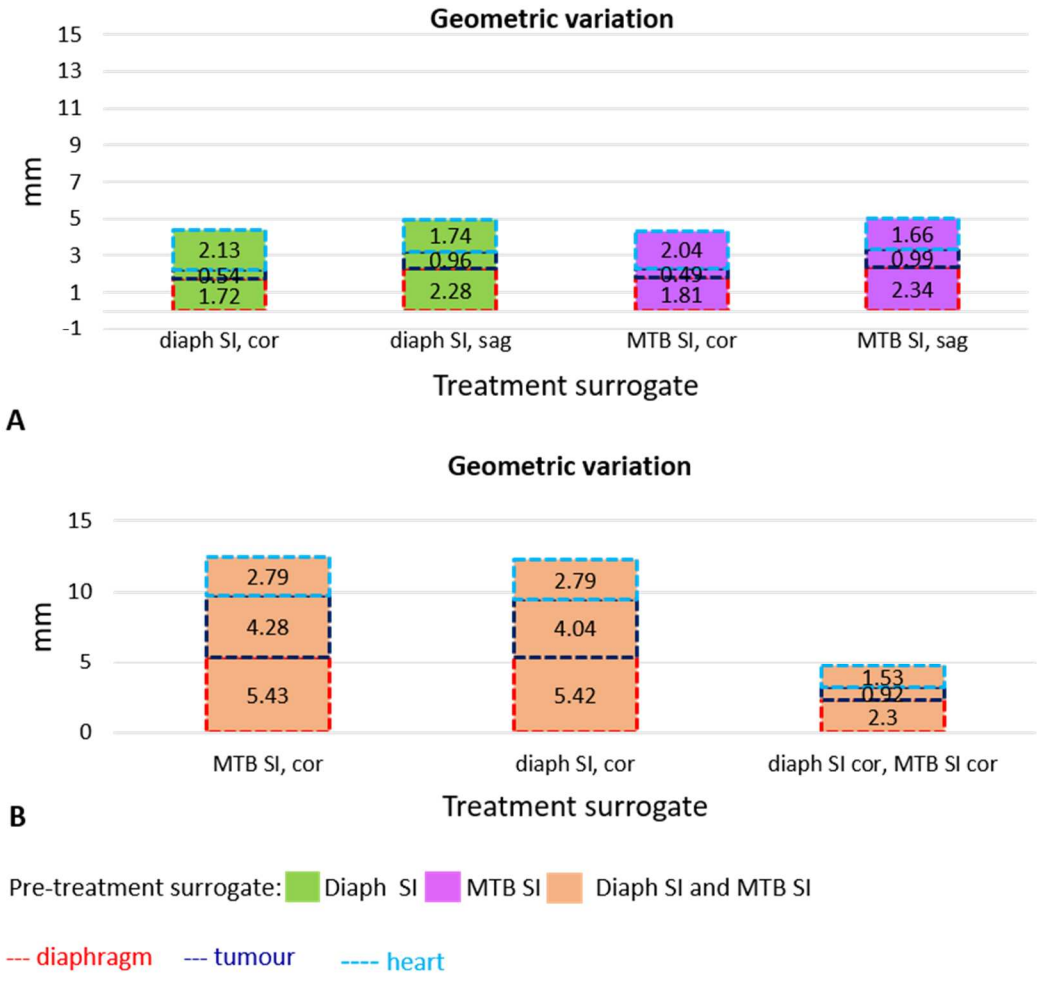

Figure 55. Surrogates combination-Fayad's model: comparison between the geometric variations when A-the same surrogate is used in pre-treatment and treatment; B-internal surrogates are combined.

These results are also confirmed by the combination of other internal surrogates (e.g. diaphragm and SIFT) and of internal and external signals (e.g. MTB and RPM). The reason could be linked to the signal normalization with respect to the maximum range of motion accomplished when more surrogates are use (e.g. in the test shown in Figure 55 B the signals are normalized with respect to the diaphragm motion). Moreover, Fayad's model in literature was tested considering only one surrogate (the same during pre-treatment and treatment).

In addition, considering the first four principal components to run the PCA, no differences can be appreciated. Therefore, the first principal component of the PCA is sufficient to describe the data.

Finally, a statistical Friedman's test is performed. In Figure 56 we show the results obtained considering three populations (two for Vandemeulebroucke's model and one for Fayad's model) including the geometric quantification on the tumour. Using the 0% exhale phase as reference, Vandemeulebroucke's model is statistically different from the case in which the MidP is considered as reference and from Fayad's model. Considering instead the heart, we have already underlined with the geometric quantification that Vandemeulebroucke's model obtains better results using the MidP as reference and the result is confirmed also by the statistical analysis. In particular, considering all the tests (same test for Vandemeulebroucke's and Fayad's models), using as reference the 0% exhale phase, the mean variation with respect to the ground truth is lower for Fayad's model than Vandemeulebroucke's one (tumour: 0.78 vs. 1.56 mm, heart: 2.02 vs. 3.92 mm).

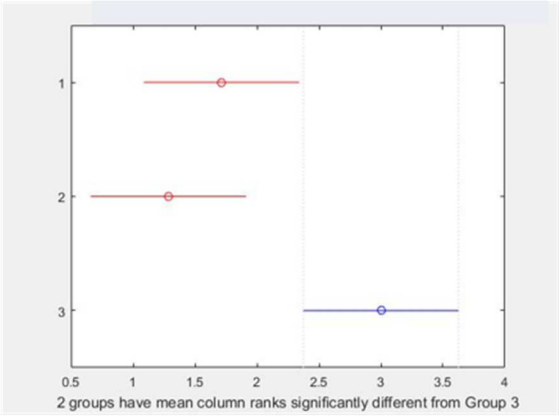

1: Fayad's model, reference 0% exhale phase
2: Vandemeulebroucke's model, reference MidP
3: Vandemeulebroucke's model, reference 0% exhale phase

Figure 56. Statistical analysis-CT/MRI phantom: comparison of the models, considering the geometric quantification on the tumour.

Considering the entire tests performed on Fayad's model, the geometric results are proved by the statistical ones: no improvement is assessed when coronal and sagittal values are used together or when different surrogates are combined.

In conclusion, analysing the geometric quantification computed on the phantom, we can assert that:

i. Vandemeulebroucke's model reaches the lowest variations with respect to the ground truth when the MidP volume is considered as reference;
ii. Vandemeulebroucke with the MidP and Fayad with the 0% exhale do not result significantly different, even if a slightly better performance is observed in Vandemeulebroucke model;
iii. when the 0% exhale phase is the reference volume, Vandemeulebroucke' s model performance is lower than Fayad's model;
iv. Fayad's model works only with the 0% exhale phase as reference;
v. the combination of coronal and interpolated sagittal values or different signals do not improve the outcomes of Fayad's model;
vi. Better performance in the reconstructed volume are achieved on the specific organ when the relevant surrogate is used.

In particular for the last observation (point vi), analysing the results we noticed that a possible future improvement could be in the implementation of a ROI-based model. The basic idea is that the surrogate, which describes the motion of a specific anatomical structure, is used to construct and then update the model.

3.1.2 Results on patients

In this paragraph the results obtained on patients, which confirmed the evaluation found on the CT/MRI digital phantom, are described. Results are presented following the structure of Chapter II. Specifically, analysis with the 0% exhale is only applied to the patient dataset, since for one patient (CT/cine-MRI patient) the "daily image" for inter-fraction quantification is acquired at the exhale phase, thus not providing a daily MidP to compare with the pre-treatment MidP.

3.1.1.1 Model construction

i. Identification of the reference volume.

Since the DIR between the 0% exhale phase and the average CT is performed for the identification of the diaphragm boundaries of the CT/CBCT patients, Table 26 shows the evaluation performed using SIFT. Comparing the results with the voxel size ([0.98 0.98 3] mm), the accomplished registrations can be considered accurate.

Table 26. Evaluation of the DIR between the average CT and a CT volume based on SIFT.

Patient	Extracted features	Median accuracy (± interquartile range) [mm]
Patient A	874	0.98 ± 1.38
Patient B	619	1 ± 2.2

After that, the highest point of the diaphragm in every respiratory phase is identified, in order to select the exhale respiratory phase. Figure 57 shows the overlap between the 50% inhale phase, the one in which the diaphragm reaches its lowest position, and the 0% exhale phase.

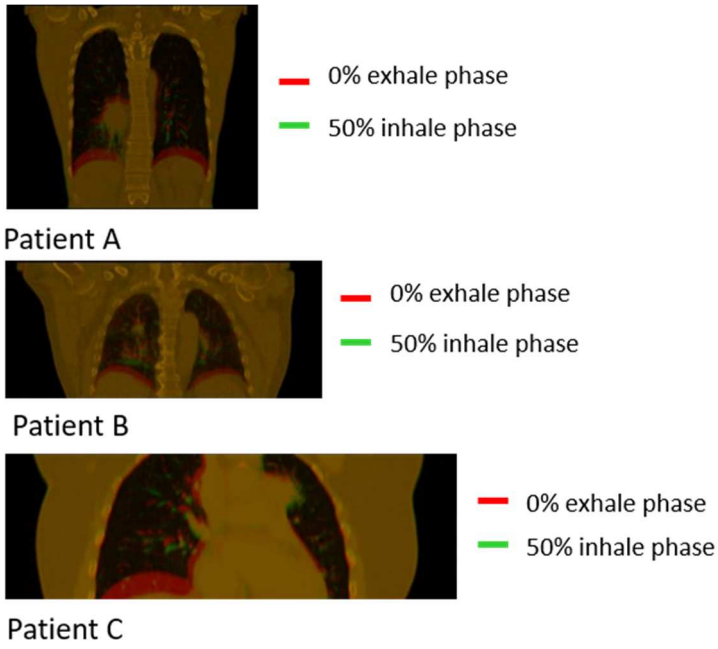

Figure 57. Inhale/exhale overlap-Patients: overlap between the 0% exhale phase and the 50% inhale phase for each patient.

ii. Deformable image registration.

The DIR, evaluated by SIFT landmarks, results in a median accuracy (± interquartile range) between extracted features shown in Table 27. Also in this case the performed DIR procedures are accurate, because within the voxel size (CT/CBCT patients: [0.98 0.98 3] mm, patient C: [0.78 0.78 2] mm).

Table 27. DIR evaluated by SIFT.

Patient	Extracted features	Median accuracy (± interquartile range) [mm]
Patient A	853	1 ± 1.4
Patient B	592	0.9 ± 1.4
Patient C	384	0.78 ± 1.56

iii. Surrogates extraction.

Depending on tumour position (e.g. lower or higher lobe), tumour size and data availability, different respiratory signals are extracted from the pre-treatment dataset. In Figure 58 all the respiratory signals of each patient are shown.

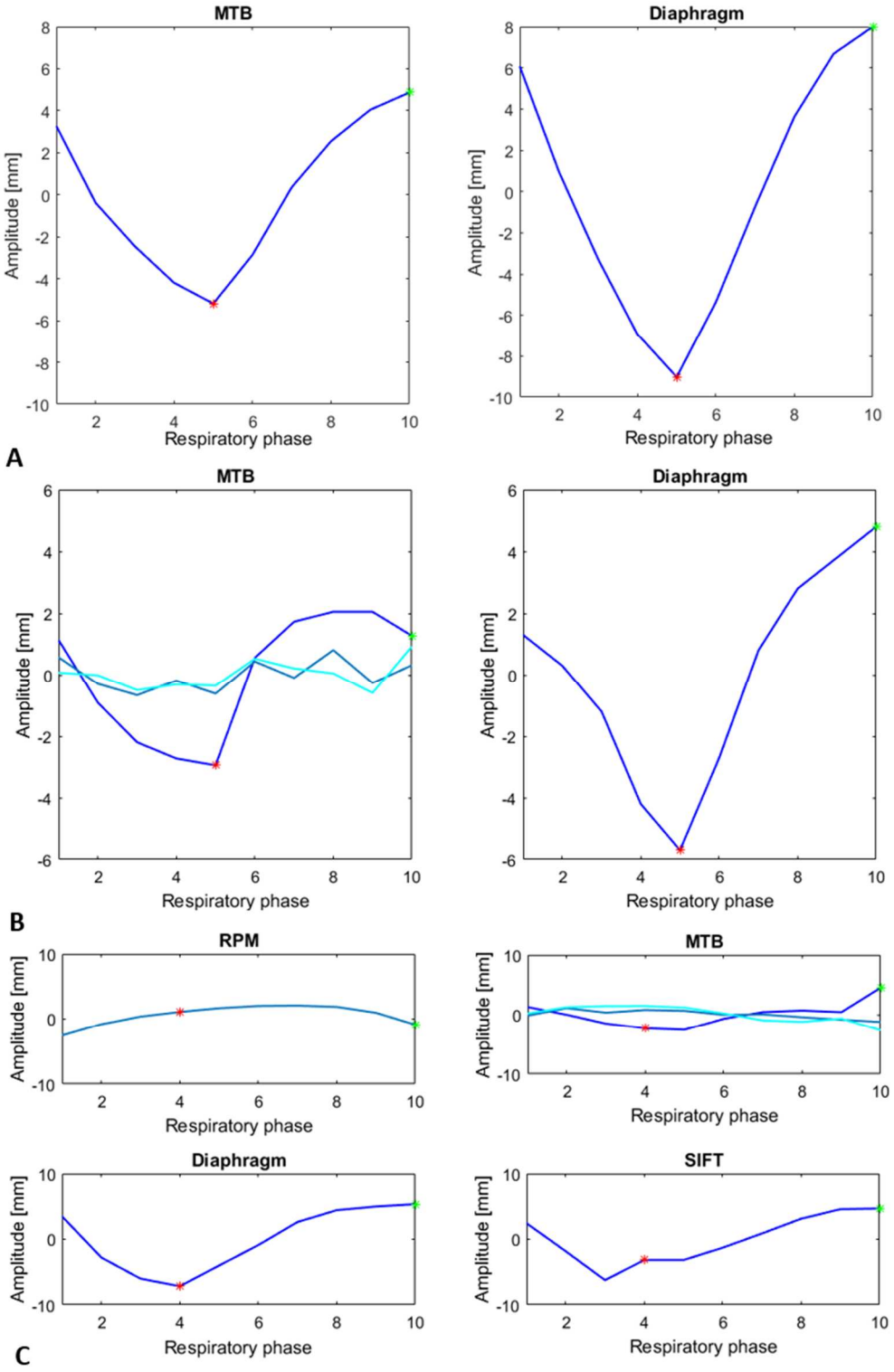

Figure 58. Pre-treatment surrogates-Patients: surrogates extracted from 4D CT. A-patient A. B-patient B. C-patient C.

In particular, for patient A (Figure 58 A) the diaphragm and the MTB have a similar pattern but different range of motion: the diaphragm moves more than the

MTB in SI direction (17.02 mm vs. 10 mm). For this patient the only tumour direction investigated is the SI, since the tumour has little motion in RL (1.7 mm) and AP (0.5 mm) directions.

The tumour of patient B (Figure 58 B) moves sufficiently in the AP direction (range of motion: 3.6 mm) and less in the RL direction (range of motion: 1.51 mm), but the main motion is always in the SI direction (motion: 6.4 mm). Patient B has a little tumour in the upper region of the right lung; therefore, tumour motion in SI direction is not equal to diaphragm motion (range of motion: 10.67 mm).

For patient C, to extract the SIFT signal two slices (one on coronal plan and one sagittal plan) are selected, as the more similar to the cine-MRI samples acquired in treatment (applying the method in Appendix D). Evaluating the distance of the tumour COMs, the selected coronal slice (Figure 59 A) is the 170^{th} (Euclidean distance equals to 3.41 mm) while the selected sagittal slice (Figure 59 B) is the 138^{th} (Euclidean distance: 5.9 mm). Figure 59 also highlights in pink the two regions that are considered. Comparing more than one structures (e.g. tumour and diaphragm), the selection could be more accurate, but is not possible since the diaphragm disappears during the breathing cycle. Diaphragm motion (12.5 mm) has the most regular pattern: the diaphragm reaches its highest excursion at the 0% exhale phase (green star in Figure 58 C) and the lowest at the 50% inhale phase (red star in Figure 58 C). The RPM pattern is rightly opposite to the diaphragm motion, despite the little range of motion (4.2 mm). Also in this case, the SI tumour motion is dominant (7.09 mm) but, since the tumour is attached to the heart, remarkable motion is observed also in RL and AP directions (4.12 mm and 2.32 mm respectively). The SIFT signal instead varies in a range of 10.91 mm.

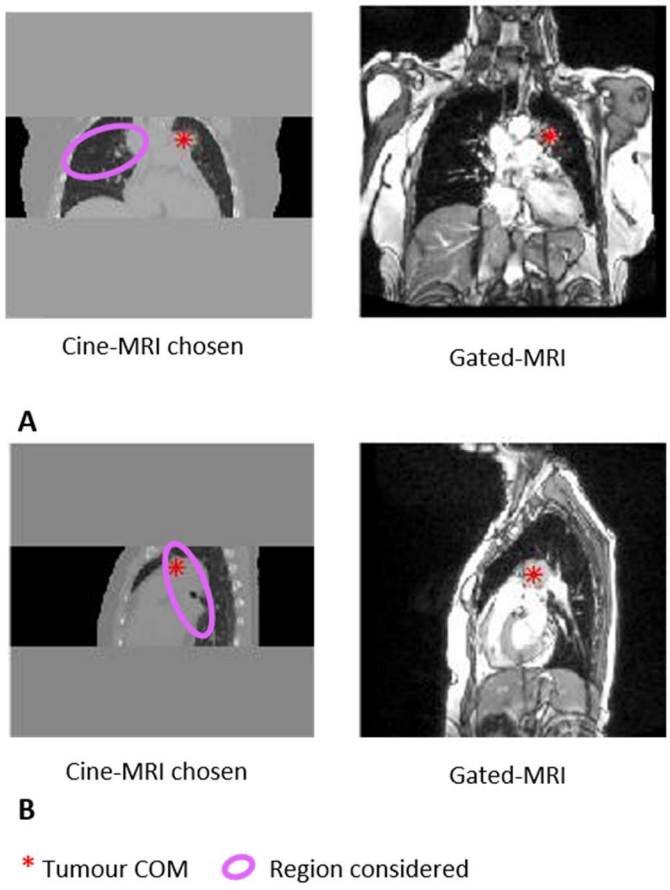

Figure 59. SIFT extraction-Patient C: the CT slices chosen are shown on the left part while the correspondent cine-MRI samples are shown on the right. A-coronal. B-sagittal.

3.1.1.2 Model update

i. Evaluation of the inter-fraction variations.

As already explained in paragraph 2.2.3.2.2, the inter-fraction variation is quantified by performing a rigid registration between the exhale phase of the 4D CT and a "daily volume" (CBCT for patient A, B or gated-MRI for patient C), followed by a DIR (if possible) to account for non-rigid variations. Comparing the median accuracies (Table 28) of CT/CBCT patients with the voxel size ([0.98 0.98 3] mm) the inter-fraction variation is not significant.

Table 28. Evaluation of the inter-fraction variation.

Rigid registration			Deformable registration
	Median error ± iqr [mm]		Mean DVF [mm]
Patient	**Diaphragm**	**Tumour**	
Patient A	4.3 ± 0.6	2.9 ± 1.7	2.67
Patient B	1.5 ± 0.32	0.9 ± 1	0.5
Patient C	1.56 ± 1.95	N.A.	N.A.

N.A. = not available.

The results on patient A are worst because this patient moves more than patient B. An example of the corresponding rigid registration for patient A is shown in Figure 60, where the tumour and diaphragm boundaries (extracted with the method explained in Appendix A) are also highlighted on the 0% exhale CT (in red) and on the output of the rigid registration (in yellow).

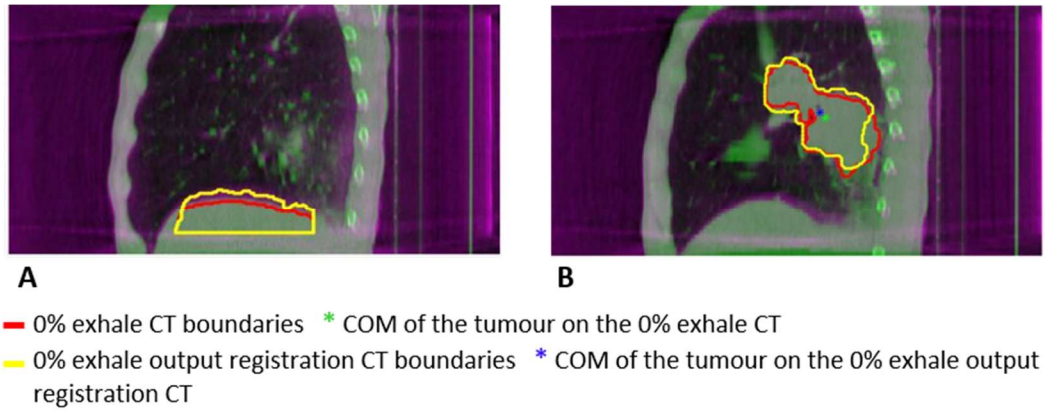

Figure 60. Rigid registration-CT/CBCT patients: overlap of the 0% exhale volume (in purple), resulting from the rigid registration, and the 0% exhale CT (in green) for patient A. A-diaphragm. B-tumour.

The median variation (± interquartile range) of patient C, compared with the voxel size ([0.78 0.78 2] mm), is an acceptable result. The corresponding rigid registration is shown in Figure 61.

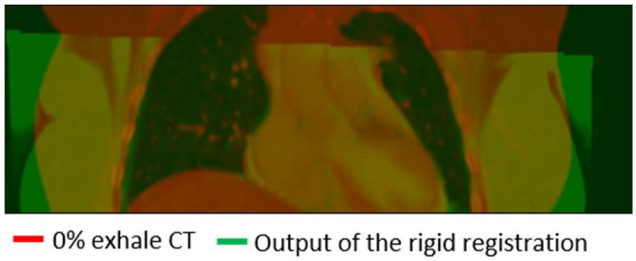

Figure 61. Rigid registration CT/gated-MRI: overlap of the 0% exhale CT and the aligned gated-MRI.

As it can be observed from Figure 61 above, the registration performed between the CT and the gated-MRI is not completely satisfactory. A better result can be achieved by performing a DIR between these volumes but, nowadays, the DIR between MRI and CT volumes is still a challenge and not the focus of this thesis project. Nonetheless, the corresponding motion after the rigid registration is comparable to the voxel size.

In conclusion, considering the mean DVF motion, we do not appreciate a relevant inter-fraction variation, so we decide to not apply any shift correction to the models.

ii. Surrogates extraction

Since for CT/CBCT patients the cine-MRI samples are simulated, starting from the 4D CBCT acquired in treatment, only one respiratory cycle is studied, while for patient C, 25 breaths are acquired during treatment.

CT/CBCT patients

To simulate cine-MRI samples, sagittal and coronal slices centred in the tumour are selected. The evaluations of the consistency of the selections are shown in Table 29. For an accurate selection, the motion patterns identified on the sagittal and coronal samples should be identical: observing the patterns and the mean differences (± standard deviation), we can assert that the selection done is accurate, being below the voxel size. As shown in Table 29 the evaluation of tumour motion is performed only for patient A due to the low quality and contrast of CBCT images of patient B, which does not allow a reliable tumour boundary segmentation with

the process described in Appendix A. The surrogates derived from the treatment data are shown in Figure 62; the range of motion is comparable with the motion appreciated on the pre-treatment signals.

Table 29. Evaluation of the coronal and sagittal slices selected on CT/CBCT patients.

	Diaphragm	**Tumour**
Patient	**mean difference (± standard deviation) [mm]**	**mean difference (± standard deviation) [mm]**
Patient A	0.32 ± 0.25	0.22 ± 0.24
Patient B	1 ± 0.7	N.A.

N.A. = not available

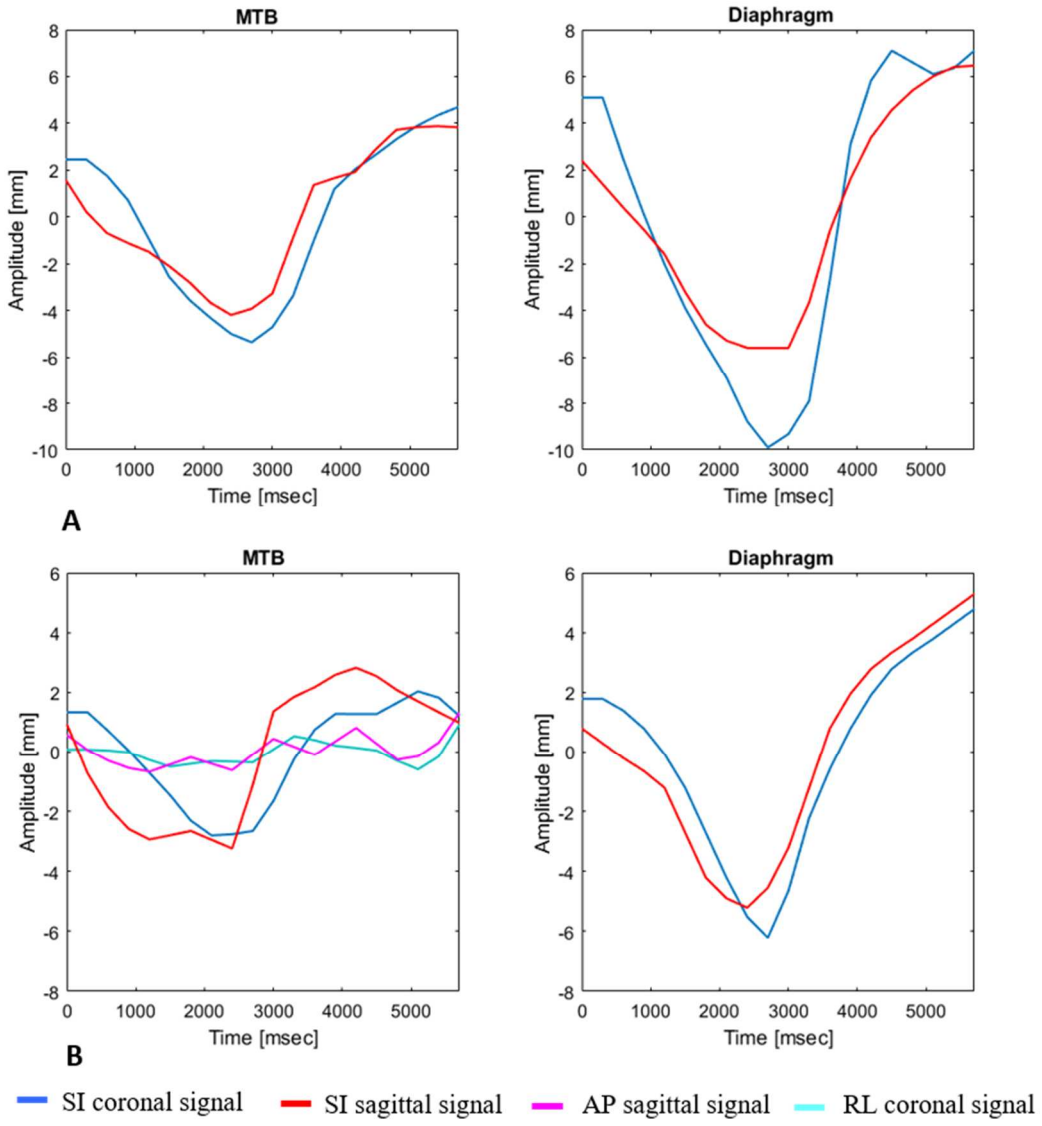

Figure 62. Treatment signals-CT/CBCT patients: respiratory motion signals extracted in treatment. A-patient A. B-patient B.

CT/cine-MRI patient

Figure 63 shows the SI motion of diaphragm, SIFT and MTB on coronal plane. As clearly visible, the MTB is not synchronized with the other signals. This is due to the tumour position that is attached to the heart and so tumour motion is influenced by heartbeat. Patient C is characterized by a lower range of motion during treatment compared to pre-treatment but, like in pre-treatment, the SI motion of the diaphragm is bigger than SIFT and MTB motions (11.84 mm, 4.97mm and 3.4 mm respectively). The range of motion in the sagittal plane is similar; in particular the

MTB swings in SI direction of 5.3 mm, the SIFT moves 8.65 mm and diaphragm of 11.32 mm. The SIFT signal has the main difference between coronal and sagittal plane because two different regions, the same chosen on the pre-treatment dataset, are selected.

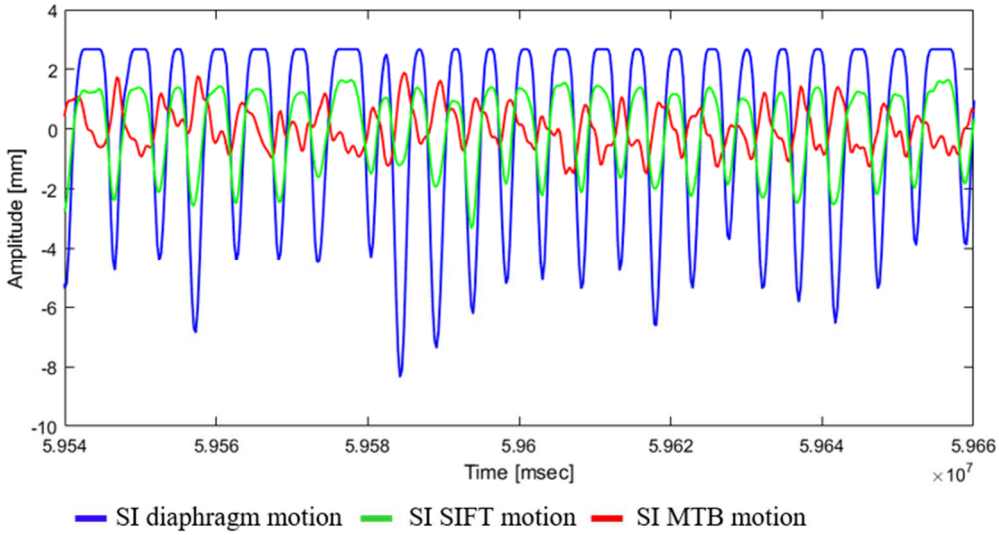

Figure 63. SI treatment signals-Patient C: SI motion of diaphragm, SIFT and MTB on coronal plane during treatment.

Figure 64 shows the motion recorded on the sagittal plane for the RPM (motion equal to 5 mm) and MTB, considering the AP motion direction; in this direction the tumour moves roughly as on SI direction (4.47 mm vs. 5.3 mm) and the RL tumour motion is around 4.37 mm.

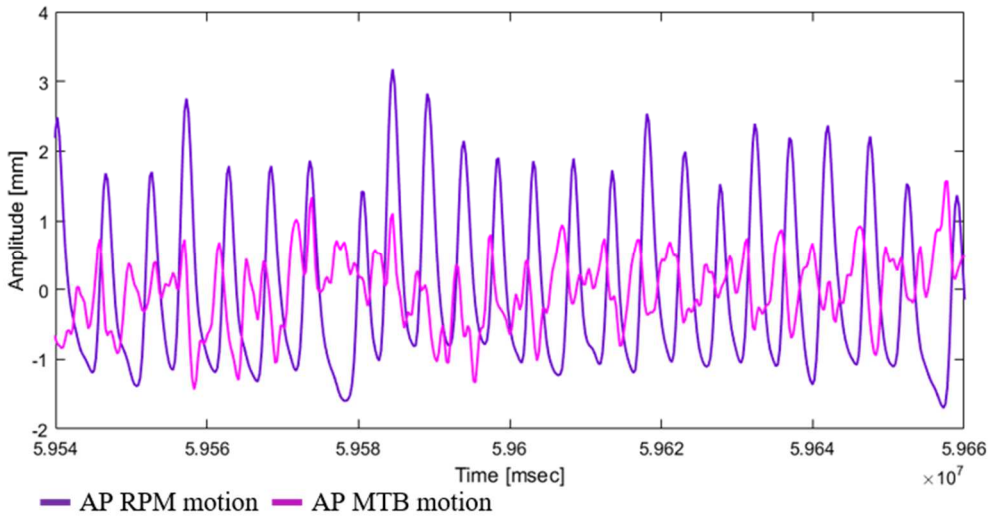

Figure 64. AP treatment signals-Patient C: AP motion on sagittal plane of MTB and RPM signals.

The last step for Fayad's model is the determination of the cine-MRI sample more similar to the gated-MRI acquired at the 0% exhale (see Appendix C for details). The cine-MRI chosen on coronal plan is the 134th sample, with a median accuracy (± interquartile range) between diaphragms boundaries of 2.09 ± 1.48 mm (voxel size [1.48 1.48 5] mm). The overlap of the 134th cine-MRI sample on coronal and sagittal plane and the gated-MRI (in violet) is shown in Figure 65.

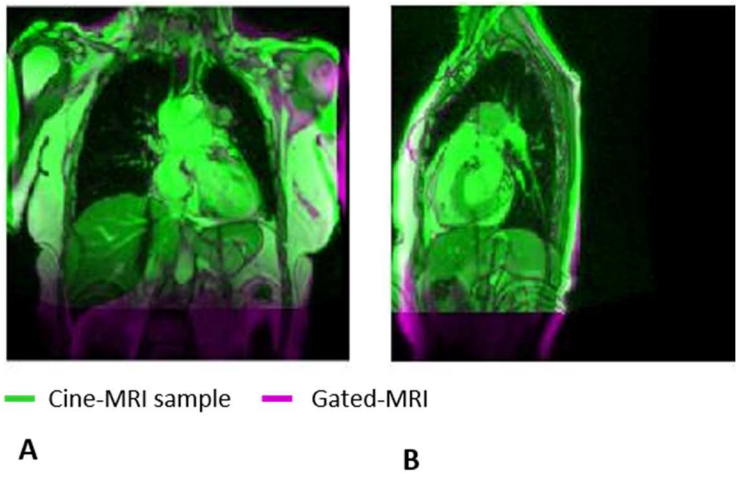

Figure 65. Exhale cine-MRI sample-Patient C: overlap between the 134th cine-MRI sample and the gated-MRI. A-coronal plane. B-sagittal plane.

3.1.1.2 Tests performed and evaluations

All the tests confirm the results found on the CT/MRI digital phantom. Therefore, evaluating the outcome on the diaphragm and tumour, we can confirm that Fayad's model performs better than Vandemeulebroucke's model, since only the 0% exhale phase is considered as reference. As already explained, since for patient C the "daily image" for inter-fraction quantification is acquired at the exhale phase, thus not providing a daily MidP to compare with the pre-treatment MidP, Fayad's model with the 0% exhale phase as reference is applied for patients.

For Fayad's model, all the possible meaningful combinations of surrogates are tested. The combination of different signals (i.e. MTB and diaphragm) or coronal and interpolated sagittal values do not improve the model performance. An exception appears in patient B and C, considering different tumour directions to test the model (see below).

In particular, testing both models on patient A, the evaluation carried out on diaphragm and tumour highlights that the model performance does not vary constructing and updating the model only with diaphragm signal or MTB signal (Figure 66). This result is due to the tumour position and dimension, that is big (volume of 111.6 cm^3) and in the lower lobe of the right lung. Therefore, for patient A, the diaphragm motion is able to describe also tumour motion and vice versa. In addition, testing the model with two surrogates (last bar in Figure 66) the obtained outcome is worse.

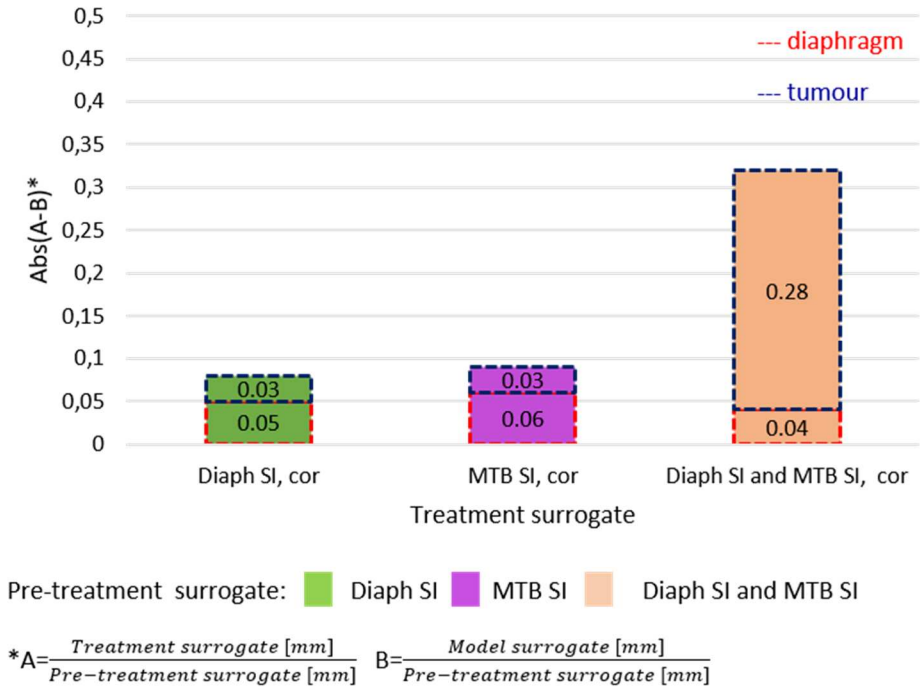

Figure 66. Fayad's performances-Patient A: evaluation of Fayad's model performances.

The same result, regarding the motion of diaphragm and tumour, can not be asserted for patient B, featuring a small tumour (volume of 13.35 cm^3) in the upper lobe; so diaphragm motion is not comparable to tumour motion. In addition, for this patient, all the tumour motion directions are studied. In Figure 67 meaningful results are reported; where the dashed line divides the model outcomes obtained using only one surrogate from the model outcome obtained using more surrogates. As it can be observed in Figure 67, worst results on tumour are obtained by considering only the SI motion to construct and update the model, compared with the case in which only the AP or RL signals are used (first three histogram bars in Figure 67). This patient in fact, presents also a relevant motion in the AP direction (as described above), therefore the inclusion of also this motion component allows to better describe tumour motion. Combining SI motion on coronal and sagittal plane the outcome does not improve significantly. In the last two bars in Figure 67, we can analyse the outcome appreciated on the tumour when the SI motion is combined with AP or RL motion. An improvement is obtained combining AP and SI motion direction (i.e. main respiratory motion directions), even if it is not different from the outcome obtained

using only the AP direction. Combining RL and SI motion the model performance worsens.

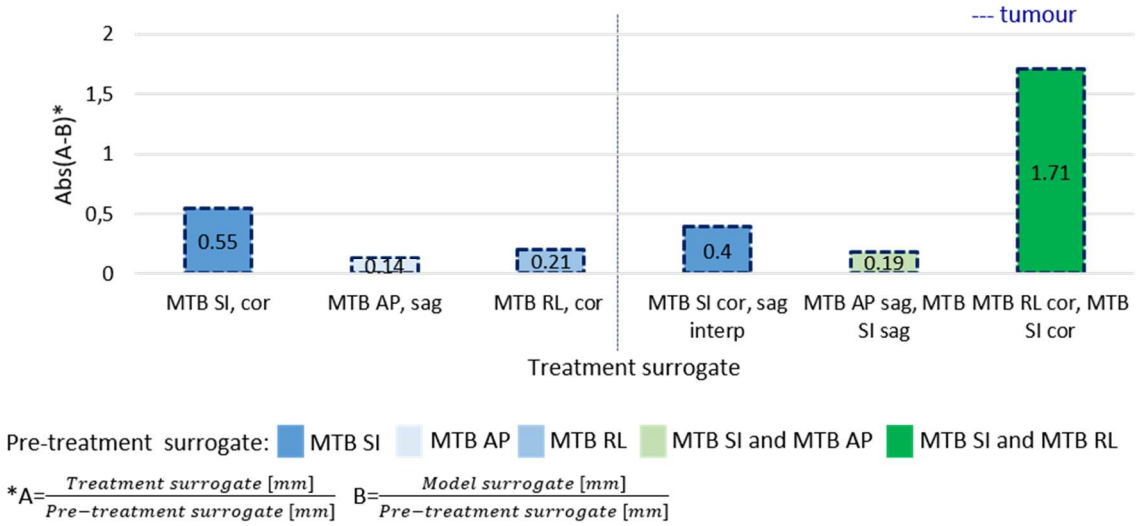

Figure 67. Fayad's performances-Patient B: evaluation of Fayad's models on tumour using the different motion directions of MTB signal.

Figure 68 shows the evaluation performed on tumour and diaphragm considering the different tumour directions alone or combined (divided by the dashed line) on patient C. It is confirmed that the combination of coronal and interpolated sagittal value does not improve the model performance (as show in Figure 68 comparing the first and fourth bars). Moreover, since patient C has the tumour attached to the heart, the combination of SI motion with the AP motion or RL motion improves the model performances on the tumour but not on the diaphragm. This confirms that implementing a ROI-based model can potentially improve the overall performance.

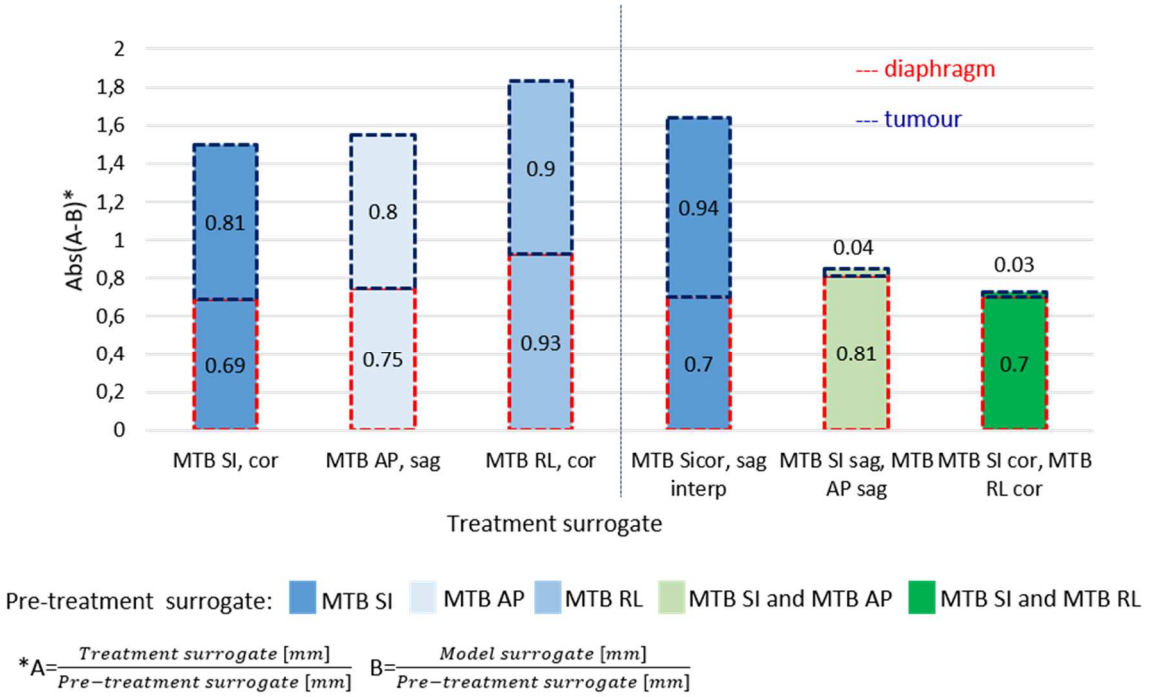

Figure 68. Fayad's performances-Patient C: geometric evaluation on Fayad's model considering the different tumour directions.

Concerning Vandemeulebroucke's model, the same trend highlighted on Fayad's model appears for CT/CBCT patients. Therefore, for patient A the diaphragm motion is able to describe also the tumour motion and vice versa, whereas the tumour motion for patient B is not described by the diaphragm. For patient C, as shown in Chapter II (Table 8) the phase values used to implement Vandemeulebroucke's model are different, depending on the chosen surrogate (i.e. diaphragm vs. MTB). Since the model required as input both amplitude and phase values, if the signals are not synchronized this ambiguity appears, as opposed to Fayad's model, that requires as input only the amplitude value. Figure 69 shows the breath used to test the models: the stars highlighted the 35th sample that for the diaphragm represents an exhale phase, whereas for the MTB signal represents nearly an inhale phase.

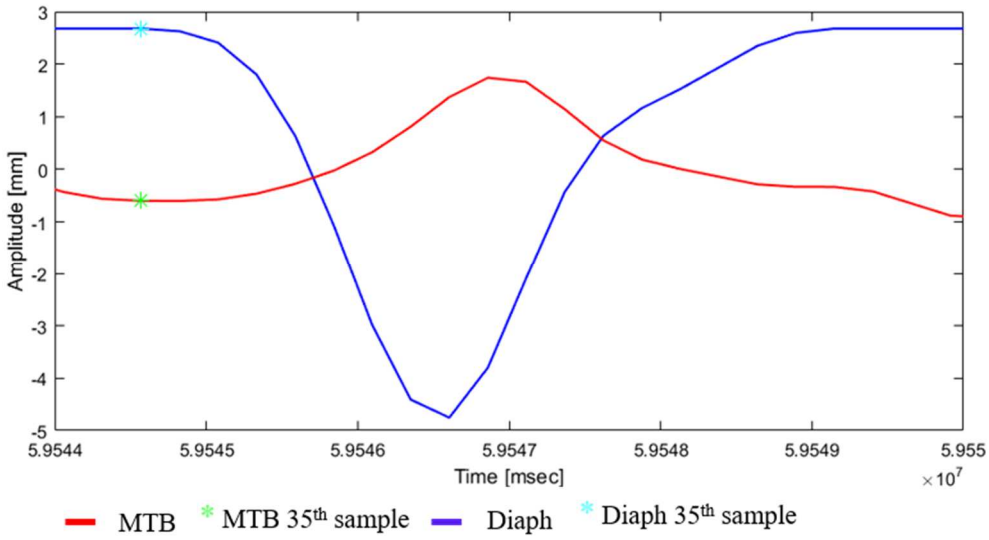

Figure 69. Desynchronized signals-Patient C: respiratory breath used to test the models.

Considering the evaluation on both models, the differences between treatment/pre-treatment ratio ([mm]/[mm]) and model outcome/pre-treatment ratio ([mm]/[mm]) on the CT/CBCT patients are smaller than the one obtained on the CT/cine-MRI patient. For example, the mean differences on the tumour, considering all tests, appreciated for Fayad's model on patient A is 0.19, for patient B is around 0.59 and for patient C is 0.96. The greater difference on patient C is reasonable, since the voxel size in treatment is bigger than the others ([1.48 1.48 5] mm vs. [0.98 0.983] mm). Since the purpose of this work is to analyse the differences between the two models when they are implemented with 4D CT and 2D cine-MRI, the results on patient C are the most relevant but new patients dataset, with the entire thorax acquired in pre-treatment, are required to check the conclusions.

Finally, considering two populations (one for Fayad's model and one for Vandemeulebroucke's model) the statistical tests highlights a significance difference on diaphragm for all patients across the models. In particular, the mean geometric variation for CT/CBCT patients on Fayad's model is lower than Vandemeulebroucke's model (e.g. 0.02 ([mm]/[mm]) vs. 0.21 ([mm]/[mm]) for patient B). Therefore, Fayad's model, considering the CT/CBCT patients, performs better on the diaphragm. For the CT/cine-MRI patient the result found is opposite but for this patient we have to take into account the issue of not perfectly synchronized signals, which may shift the results towards better

performance with the Vandemeulebroucke's model, which include the information of both amplitude and phase of the surrogate. Finally, the statistical test regarding only Fayad's model (considering one population on the diaphragm and one on the tumour) highlights a significant difference for patient B and C; Fayad's model performs better on the diaphragm than on the tumour.

3.2 Dosimetric adaptation

In this section, the dosimetric results obtained on the CT/MRI digital phantom and then on patients are reported. The validation of dosimetric simulations on the CT/MRI phantom confirms the results reached with the geometric validation.

3.2.1 Validation of dosimetric simulation on the CT/MRI digital phantom

In this section, the discussion is split in two part: the 4D CT treatment planning and the plan application during treatment.

4D CT treatment plan

Figure 70 shows the isodose curves of the optimized plan on the 0% exhale phase and the ITV boundaries in black. The ITV receives almost entirely 95.0% of the prescribe dose (60 Gy) and, moving far from the tumour, the dose progressively decreases.

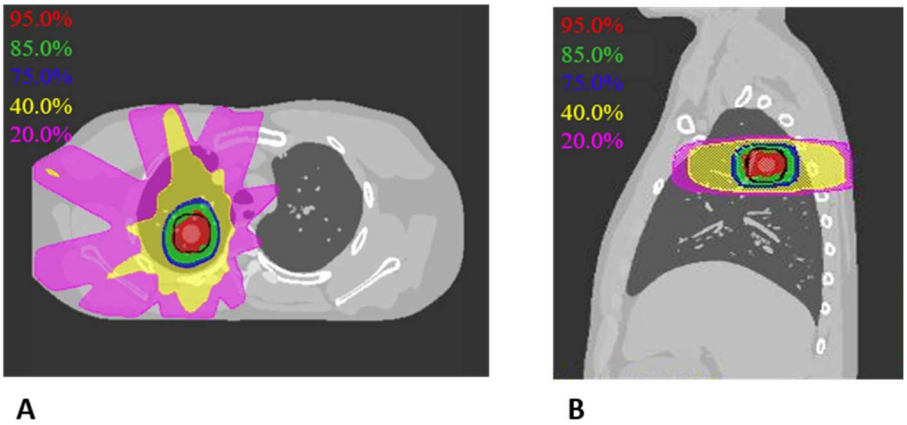

Figure 70. Isodose curves-CT/MRI phantom: obtained on the 0% exhale phase of the CT/MRI digital phantom. A-axial view. B-sagittal view.

Figure 71 instead shows the DVH curves of all the metrics taken into consideration to satisfy the protocol requirements (see Table 13 in Chapter II for details). For example, the PTV D98 reaches 57.33 Gy (protocol requirement: at least 57 Gy), the maximum dose received by the heart is 4.56 Gy (protocol requirement: maximum dose 40 Gy), the maximum dose on the spinal cord is 18.9 Gy (protocol requirement: maximum dose 45 Gy).

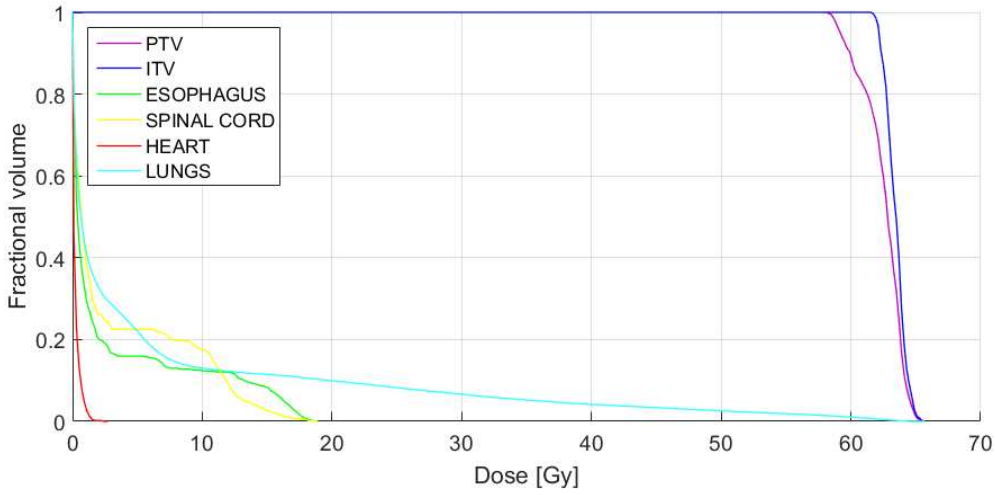

Figure 71. DVH 0% exhale-CT/MRI phantom: obtained on the 0% exhale phase for the CT/MRI digital phantom.

The 4D CT leads to an accurate dose estimation, as expected due to the regular breathing pattern and due to the ITV approach used (explained in 2.3.2.1). Therefore, the DVH curves obtained for each respiratory phase are very similar; in Figure 72 we report the DVH curves on the PTV (Figure 72 A) and on the spinal cord (Figure 72 B), as indicatives of the whole OARs. The distance between the 0% exhale phase and the 50% inhale (maximum distance) on PTV D98 is 0.87 Gy, on PTV D2 is 0.73 Gy and on the maximum dose received by spinal cord is 0.42 Gy. A greater difference between the curves appears on the DVH curves of the heart (Figure 72 C) with respect to the spinal cord. This variation is due to the organ motion during respiration that is negligible for the spinal cord but not for the heart.

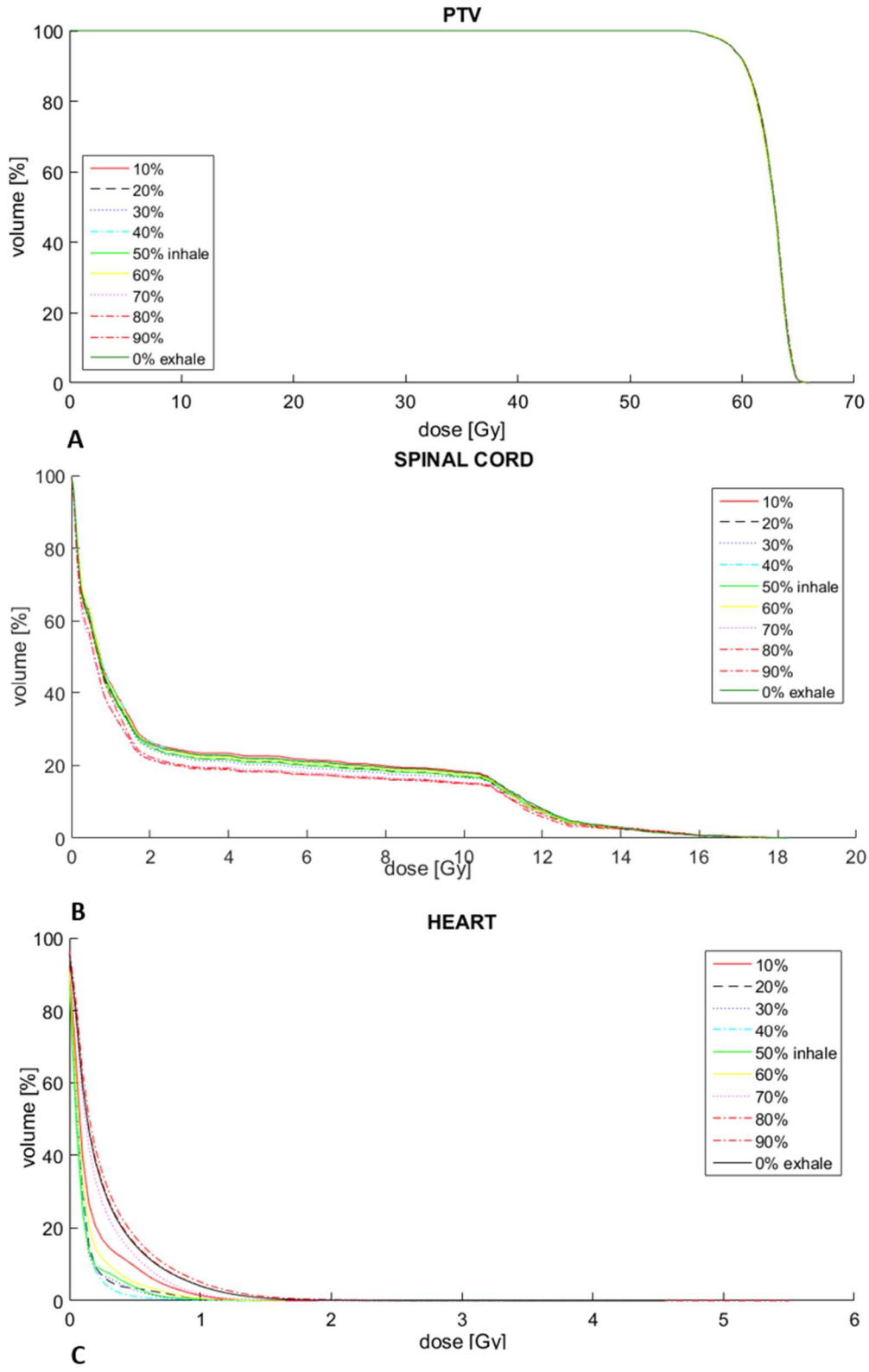

Figure 72. 4D CT DVHs-CT/MRI phantom: A- ITV. B-spinal cord. C-heart.

Application of the plan to the ground truth and model output

Since no big dosimetric differences are appreciated considering the different surrogates, Figure 73 shows the comparison between the delivered dose (on three model outputs) and the dose calculated on the ground truth, as representative of all the results found.

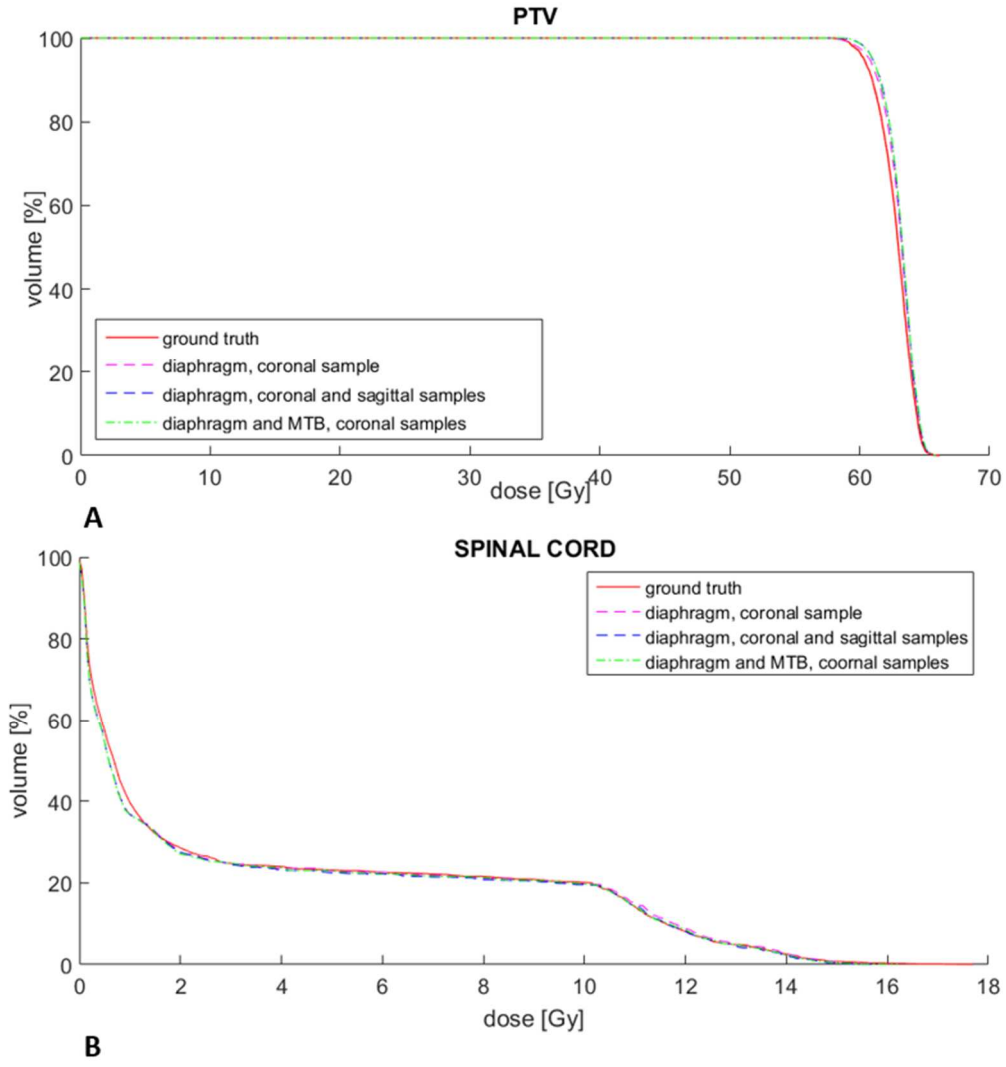

Figure 73. Model outputs DVHs-CT/MRI phantom: comparison of the DVHs of the ground truth and of three model outputs. A-PTV. B-spinal cord.

Since all the DVH curves are closed to the ground truth curve (red line in Figure 73), Fayad's model ability to approximate the ground truth is confirmed on the PTV constraints. In addition, a further proof is the fact that for all the model output plans the ITV V100, a strenuous metric to satisfy, reaches the 100% of the volume. Moreover, the

dosimetric evaluation confirms that the combination of the coronal and sagittal values (blue dashed line in Figure 73 A and B) does not get different or better outcomes than updating the model only with the coronal value (pink dashed line in Figure 73 A and B). The result is also confirmed by the other tests that were carried out (shown in Table 30): for example looking at the PTV D98 of test 1 versus test 2 (0.08 Gy vs. 0.68 Gy) or test 3 compared with test 4 (0.5 Gy vs. 0.4 Gy). The same outcomes are also obtained when the model is constructed and updated with two surrogates (green dashed line in Figure 73 A and B). Taking into account the PTV D98, the variation appreciated when coronal values of the diaphragm and MTB (test 9 in Table 30) is greater than the one obtained only with diaphragm or MTB (respectively test 1 and 3 on Table 30).

In Figure 73 B the DVHs curves of the spinal cord are reported, as representative of one of the OARs. Taking into account the maximum dose received by the spinal cord, a difference is appreciated with respect to the other OARs, as highlighted also in Table 30. Even if differences drop considering the mean dose (less sensible to the error), this variation suggests that the DVFs used to create the model can introduce an error. Indeed, the magnitude of dosimetric errors can be affected by several factors and the accuracy of the DIR used to derive DVFs is a primary cause of error (Weixing et al. 2015) (see 3.2.2 for additional detail).

Moreover, as shown in Table 30, similar variations are appreciated for all the surrogates tested and the mean variation for all the evaluated metrics is 0.11 Gy. In particular, constructing and updating the model using the SIFT signals, better outcome is appreciated in the lungs, as it is fair to expect since the SIFT signals describes the lungs vessels motion, but the results obtained at the spinal cord is worse. Furthermore, when the external surrogate (i.e. RPM) is used a greater variation appears on the PTV (variation on D98 equal to 1. 13 Gy for the RPM while the mean variation for the other model outcomes is 0.55 Gy). The same result is appreciated looking at the geometric variation on tumour; the variation obtained using the RMP signals on Fayad's model is equal to 0.97 mm, whereas the mean variation of all the internal surrogates is 0.79 mm. In the phantom case, the RPM signal can be considered as an internal surrogate, since it was used to generate the phantom itself. Therefore, this variation can be associated to the fact that the RPM signal is

describing the AP motion and not the full SI motion of the tumour, confirming that the external surrogate is not able to describe the internal motion completely.

Table 30. Dosimetric results on the CT/MRI digital phantom.

			OESOPHAGUS	**HEART**	**ITV**	**LUNGS**	**SPINAL CORD**	**PTV**	
TEST	**PRE-TREATMENT SURROGATE**	**TREATMENT SURROGATE**	Mean Dose [Gy]	Max Dose [Gy]	V100 [%]	Mean Dose [Gy]	Max Dose [Gy]	D2 [Gy]	D98 [Gy]
1	Diaphragm SI	Diaphragm SI, coronal sample	0.11	0.53	0	0.26	-1.39	-0.1	0.08
2	Diaphragm SI	Diaphragm SI, coronal and sagittal samples	0.09	0.42	0	0.29	-1.82	0.1	0.68
3	MTB SI	MTB SI, coronal sample	0.09	0.75	0	0.24	-0.57	-0.1	0.5
4	MTB SI	MTB SI, coronal and sagittal samples	0.04	0.79	0	0.27	-1.36	0.08	0.4
5	MTB AP	MTB AP, sagittal sample	0.15	0.12	0	0.41	0.29	0	0.63
6	SIFT SI	SIFT SI, coronal sample	-0.16	0.18	0	0.24	-1.56	0.1	0.65
7	SIFT SI	SIFT SI, coronal and sagittal samples	-0.38	2.01	0	0.01	-3.4	0.4	0.46
8	RPM AP	RPM AP, sagittal sample	0.14	1.45	0	0.32	0.53	0	1.13
9	Diaphragm SI and MTB SI*	Diaphragm SI* and MTB SI*, coronal samples	0.09	0.81	0	0.3	-1.7	0.15	0.7
10	MTB AP** and MTB SI	MTB** AP and MTB SI, sagittal samples	0.06	0.19	0	0.59	0.09	0.2	0.39
11	MTB SI and RPM AP**	RPM AP** and MTB SI**, sagittal samples	-0.24	1.05	0	0.35	-0.25	0.2	0.81

* Normalized signal on diaphragm SI ** Normalized signal on MTB SI

3.2.2 Evaluation of dosimetric simulation on patients

Here the meaningful results appreciated on patients are reported. The discussion in split into treatment plan and treatment delivery.

4D CT treatment plan

As shown in Table 31, where the protocol parameters are listed, all the metrics on the 0% exhale phase are satisfied.

Table 31. Value of each protocol parameter on the 0% exhale phase.

	OESOPHAGUS	**HEART**	**ITV**		**LUNGS**	**SPINAL CORD**	**PTV**	
Patient	Mean Dose [Gy]	D50 [Gy]	V100 [%]	V98 [%]	Mean Dose [Gy]	Max Dose [Gy]	D98 [Gy]	D2 [Gy]
Patient A	27.95	10.19	99	99.9	16.93	36.79	58.2	63.51
Patient B	18.93	1.59	100	100	13.13	20.64	58.75	62.5
Patient C	20.75	2.35	93	99.4	12.92	21.13	57.12	63.94
Protocol requirements	28*	60*	100%**	98%**	15-20*	45*	64.2*	57*

*dose permitted **should receive 100% (or 98%) of target dose

Figure 74 shows the isodose curves of the 0% exhale phase for each patient on the axial view and the ITV boundary in black. The tumour size and position of patient A and patient C does not allow to hit uniformly the ITV with the 95.0% of the prescribe dose, but with the 90.0% dose (reported in red).

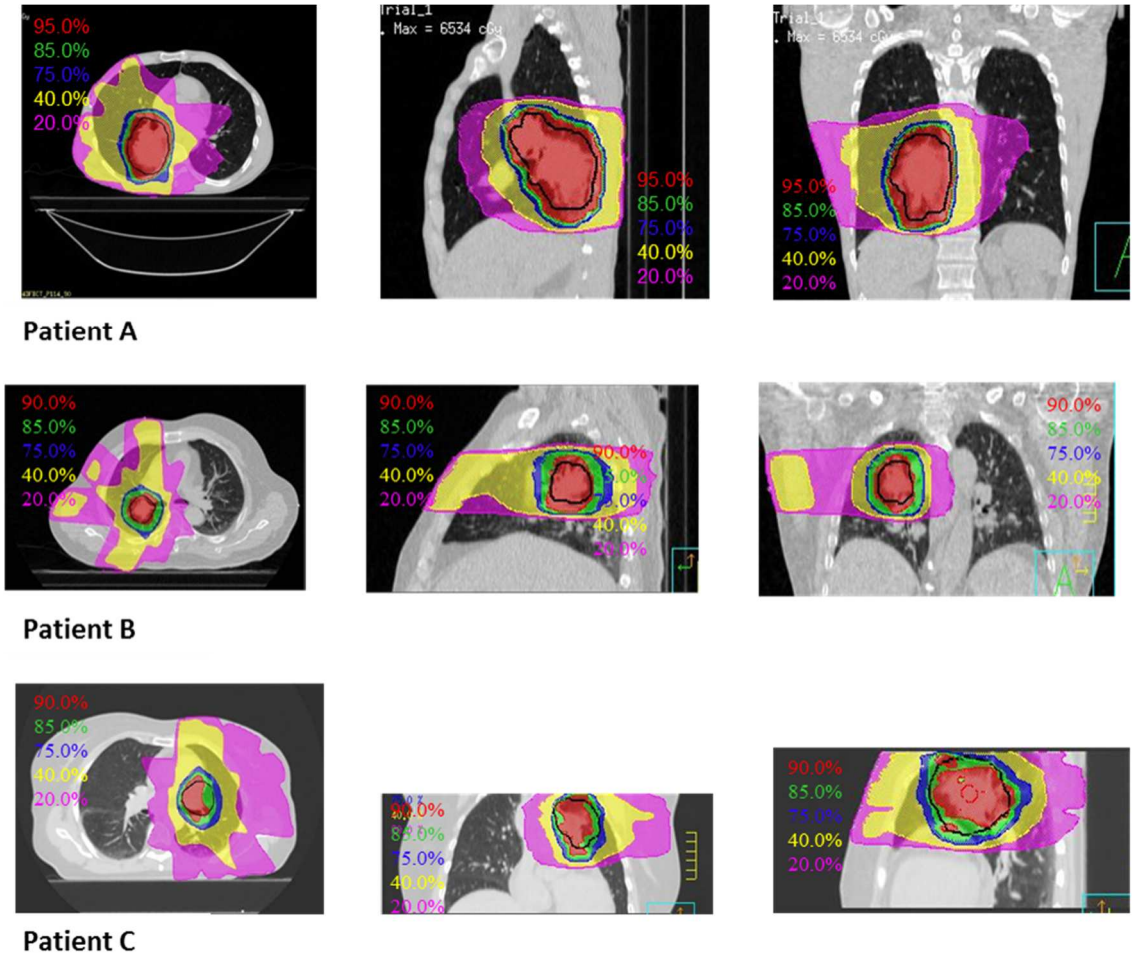

Figure 74. Optimized plan-Patients: isodose curve and ITV boundaries (in black) on the 0% exhale phase for each patient.

Evaluating the chosen metrics for each respiratory phase, as it is fair to expect, the selected metrics are similar. For example, the PTV D98 for the patient A varies of 0.55 Gy between 0% exhale phase and 50% inhale phase (bigger variation), for patient B varies of 0.32 Gy and for patient C the variation is 0.38 Gy. Figure 75 shows the DVHs curves of the PTV and of the heart for patient A, the one with the higher respiratory motion in planning session. For the PTV the curves are close to each other; in particular in Figure 75 we show the zoom on the parameters observed by the protocol (PTV D98, PTV D2). Conversely for the heart, a greater variation can be appreciated. This difference is linked with the ITV approach (see paragraph 2.3.2.1 for details) and respiratory motion; the ITV is delineated considering the maximum range of tumour motion (range of motion between the 50%

inhale and 0% exhale phase) and it is the same for every respiratory phase, while the heart boundary changes for every phase.

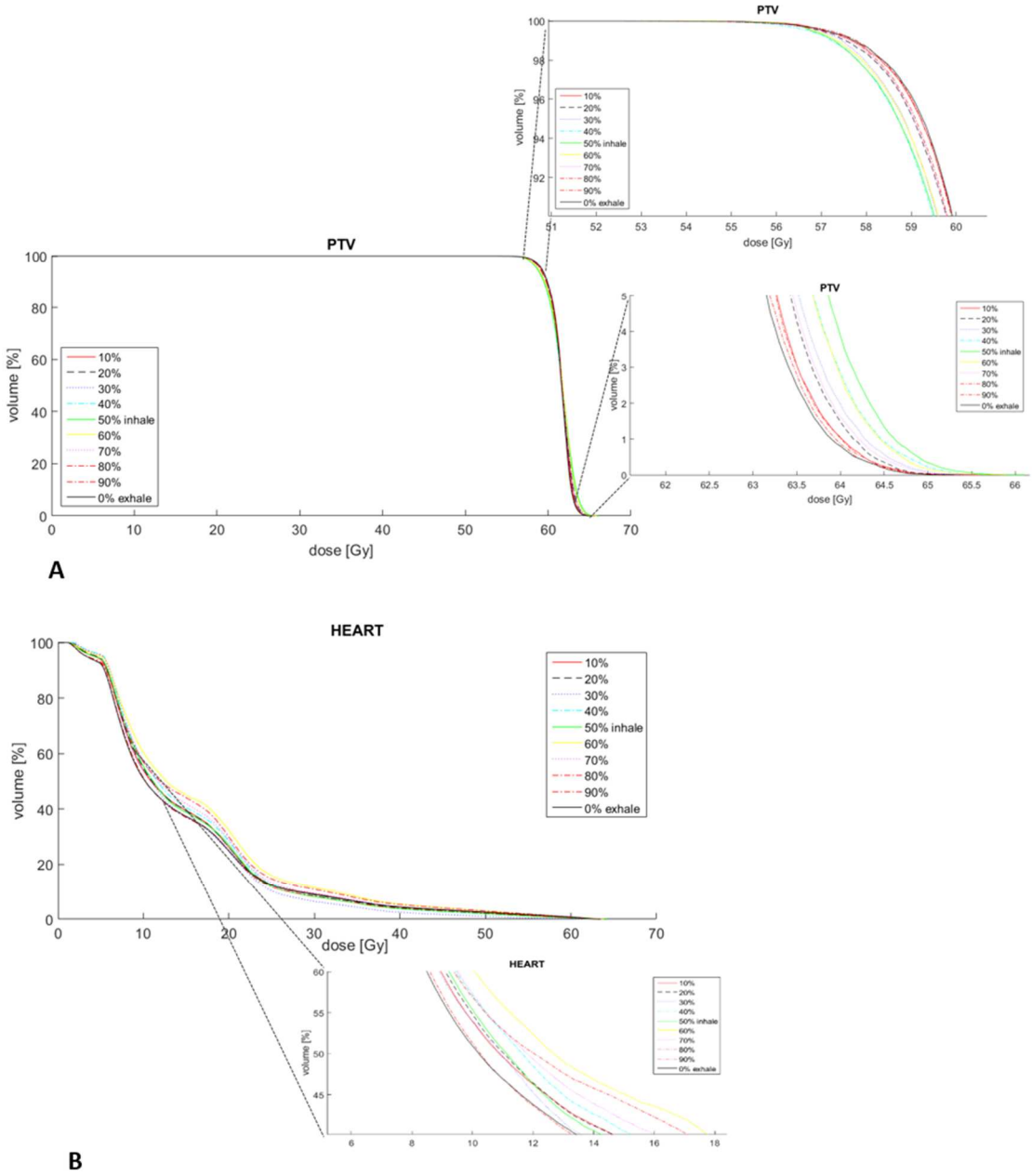

Figure 75. 4D CT DVH-Patient A: A-PTV. B-heart

Instead, Figure 76 shows the DVH curves of the PTV and the spinal cord for patient C, as indicative of all the OARs. As it can be observed in both histograms, the curves have a similar pattern for each phase.

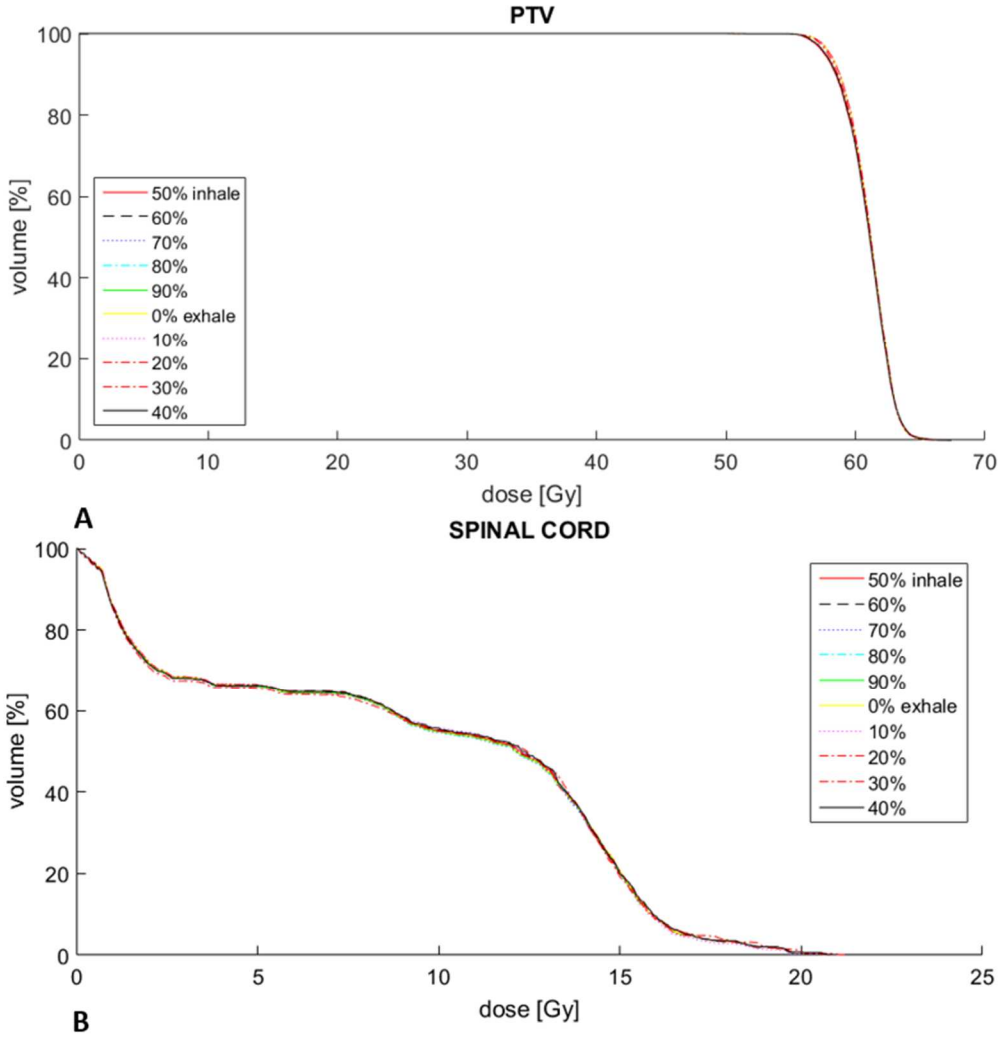

Figure 76. 4D CT DVH-Patient C: A-PTV. B-spinal cord.

A different behavior across patients is observed on the spinal cord: for patient B and C the spinal cord curves are close to each other, as it is fair to expect since it is a fixed organ, but bigger variations are appreciated for patient A. On patient A, taking into consideration the maximum dose received by the spinal cord, a gap (equal to 3.11 Gy) is present between the 0% exhale phase and the following one. In order to better understand the reason of this variation regarding a fixed structure, we compare the segmentation found automatically by the Pinnacle^3 system and the boundaries obtained by warping the contours of the 0% exhale phase (i.e. the ones used for our simulations). Figure 77 A shows the segmentation performed on the 10% phase, where a difference between the two methods is visible, showing inaccuracy in the warping of the spinal cord structure with the DVF obtained by

the DIR procedure. The spinal cord volume found by Pinnacle^3 is 22.27 cm^3 and the COM coordinates are [3.67 71.37 -28.33] mm. Conversely, with the contours warping, the volume is 13.77 cm^3 and the COM coordinates are [3.71 72.33 -36.60] mm. Comparing the volumes at the 0% exhale phase (22.52 cm^3) the better outcomes is reached by the Pinnacle^3 system, as confirmed also by the COM variations (coordinates of the 0% exhale phase: [3.68 70.88 -24.19] mm). Therefore, considering the Pinnacle^3 spinal cord boundaries on the 10% phase, the gap on the maximum dose between the two consecutives phases disappears. To check the consistency of the boundaries of the other OARs, the same comparison is carried out, evaluating the volumes and COM variations on patient A and on the CT/MRI phantom. Only for the oesophagus and the spinal cord, that are thin organs, the segmentations are different. For patient A the results obtained by the Pinnacle^3 system are better, otherwise for the CT/MRI phantom the warping strategy provides better results. In fact, for the CT/MRI digital phantom, as highlighted in Figure 77 B, the Pinnacle^3 automatic segmentation stops almost at the middle height of the spinal cord. Regarding the CT/MRI phantom, the COM coordinates of the spinal cord found by Pinnacle^3 system are [187.52 225 297.93] mm (volume: 8.62 cm^3), whereas the COM found by contour warping is [190.51 249.68 188.66] mm (volume: 13.37 cm^3). Therefore, the step of segmentation or warping (after the DIR) of the structures, requires to be checked carefully in order to avoid error propagation in the dosimetric assessment.

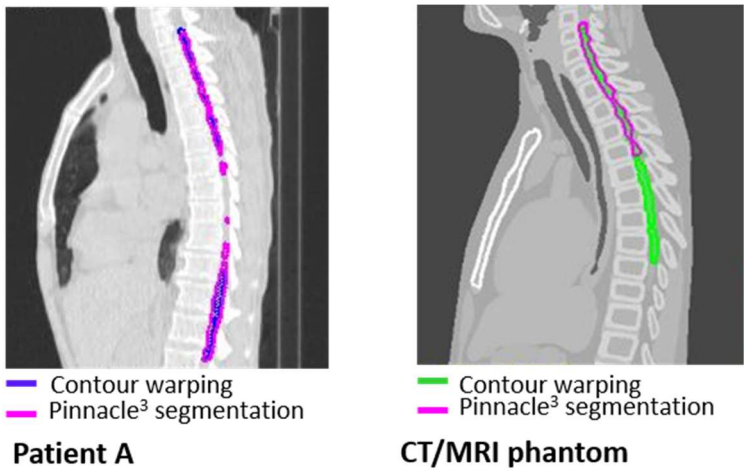

Figure 77. Warping vs. Pinnacle^3 segmentation: comparison of the spinal cord segmentation. A-Patient A. B-CT/MRI digital phantom.

Application of the plan to the model outputs

In Figure 78 the DVH analysis of three models output of each patient on the PTV are reported. For the patients, as already explained in Chapter II, the ground truth for the direct model comparison is not available, so we compare the plan on the model outcome, reconstructing a 50% inhale phase in treatment, with the 50% inhale plan of the pre-treatment CT. For CT/CBCT patients, the red lines in Figure 78, which indicates the curves obtained on the 50% inhale phase during pre-treatment, are similar to the model output curves, since the range of motion does not vary between pre-treatment and treatment session. Differently, patient C reports greater difference since the range of motion between pre-treatment and treatment varies (e.g. the larger variation on the PTV D98 is 3.14 Gy). The other curves in Figure 78 represent the dosimetric outcome on PTV when only one surrogate is used, when both coronal and sagittal values are considered and when two surrogates are tested. In particular, in order to underline that any surrogates combination is similar, we report:

- for patient A (Figure 78) the outcome obtained considering the diaphragm motion or the combination of diaphragm and MTB motion (i.e. two different internal surrogates). The results confirm the one previously highlighted through the geometric evaluation; no improvement is appreciated combining coronal and sagittal samples or different (internal) surrogates;
- For patient B (Figure 78) the outcome evaluated using only the MTB SI or combing with the MTB RL motion direction (same surrogate but different motion direction) are shown. The curve obtained combining the signals is the most distant from the red curve and, as already shown, this model output presents the highest geometric variation. Also in this case, the results confirm the one previously highlighted through the geometric evaluation;
- The geometric analysis on patient C highlights an improvement on tumour evaluation when the MTB SI motion is combined with the MTB RL or AP motion. In these cases, we also appreciate a greater dosimetric variation with respect to other tests (i.e. considering the combination of SI and AP direction the difference of the model output from the 50% inhale of pre-treatment is equal to 1.82 Gy on PTV D2 and 3.14 Gy on PTV D98). In Figure 78 we reported, as indicative, the

comparison between the MTB SI direction alone or combined with the AP direction.

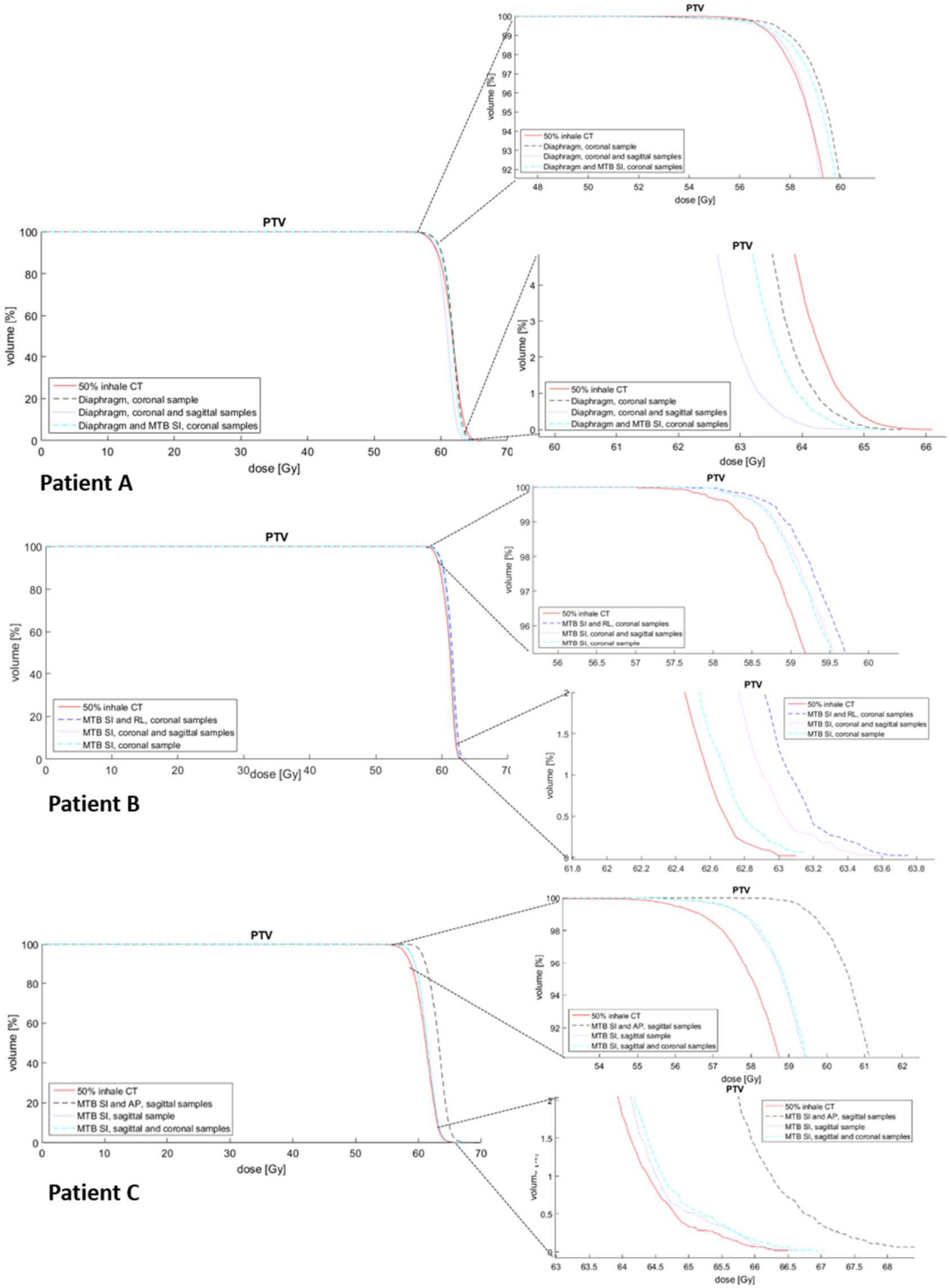

Figure 78. DVH curves of PTV-Patients: curves for each patients of three selected model output and the 50% inhale phase of pre-treatment.

Figure 79 shows instead the DVH curves on the heart of each patient, as indicative of the OARs. Also in this case, the curves for the CT/CBCT patient are close to the 50% inhale curve, whereas patient C reports greater variations.

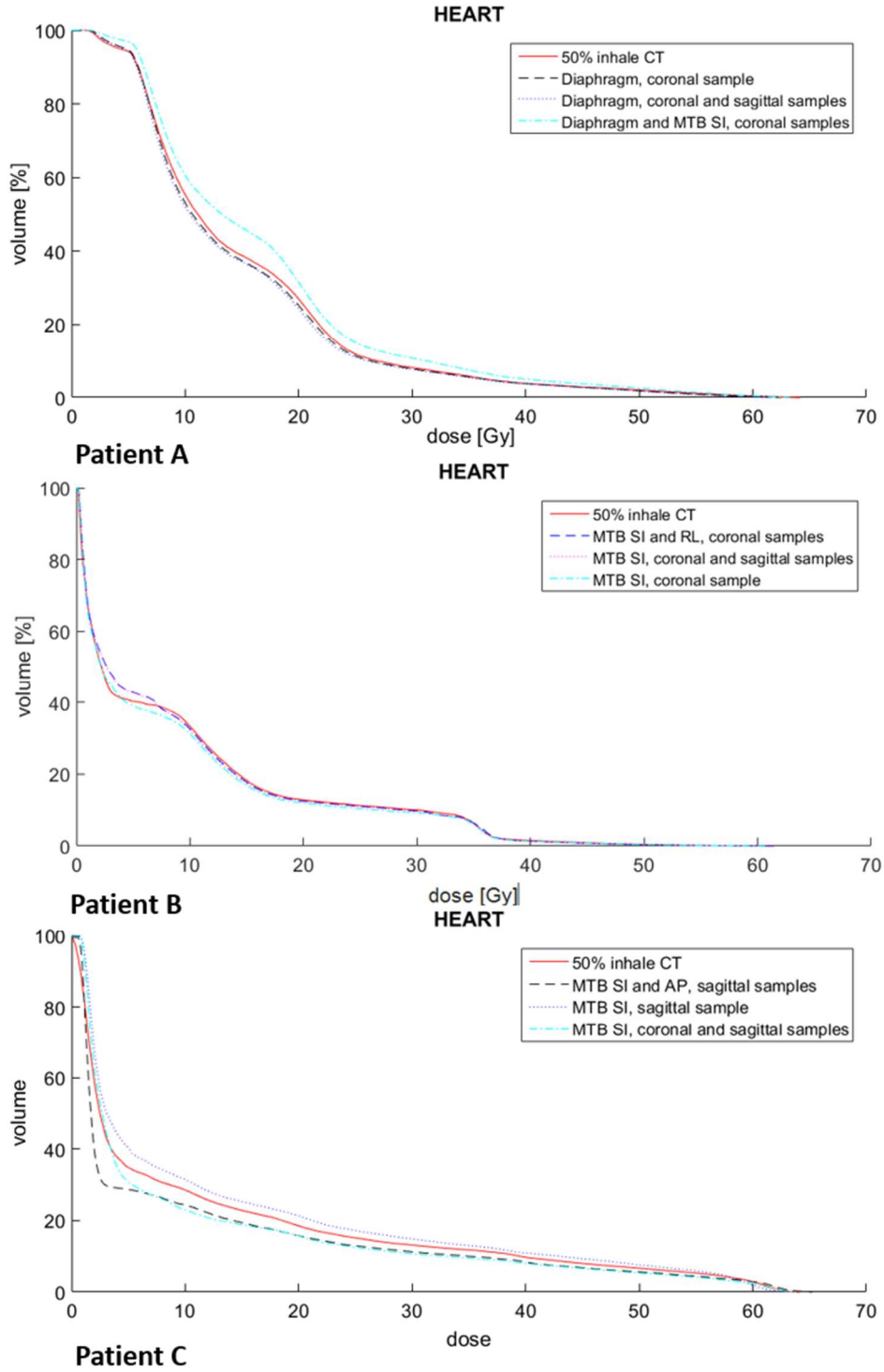

Figure 79. DVH curves of heart-Patients: curves for each patients of three selected model output and the 50% inhale phase of pre-treatment.

Therefore, evaluating all the dosimetric plans on Fayad's model output, we can assert that:

i. if the respiratory motion between pre-treatment and treatment session is similar, the dosimetric variation are lower or equal to 1 Gy. This is the case of the CT/CBCT patients, where, for example, the tumour motion in SI direction of patient A in pre-treatment is equal to 10 mm and mean motion (of sagittal and coronal signals) in treatment is equal to 9.17 mm;
ii. if the respiratory motion between the two sessions change, a greater dosimetric variation is visible. For example, for patient C the highest difference from the 50% inhale plan of pre-treatment is equal to 3.14 Gy (on the PTV D98);
iii. combing coronal and sagittal samples or two surrogates the dosimetric evaluation reaches the same value obtained when only one surrogate is used, as already noted with the geometric assessment. An exception, as already said, appears for patient C for what concern the combination of different motion directions.

It should be pointed out that the highlighted discrepancies between the planned and delivered dose can lead to unsafe or ineffective treatments, caused by increased dose to OARs and decrease dose to the tumour, as recently noticed by Cai et al, 2015. Therefore, the development of a method to calculate the actual dose delivered to patients has an important role for effective and safe treatments.

3.2.2.1 Breathing cycle

As already explained, patient C is the only one with a different motion between pre-treatment and treatment, thus leading to geometric and dosimetric uncertainties. Therefore, an entire breathing cycle is tested on patient C, considering the model outcome CT obtained with the diaphragm signal. The values on the PTV D98 (Figure 80 A) change according to tumour motion, following the respiratory pattern (as shown in Figure 80 B). In particular, the maximum variation from the exhale phase (10^{th} value in Figure 80 B) is reached near the 50% inhale phase (indicated as respiratory phase 5 in Figure 80 B).

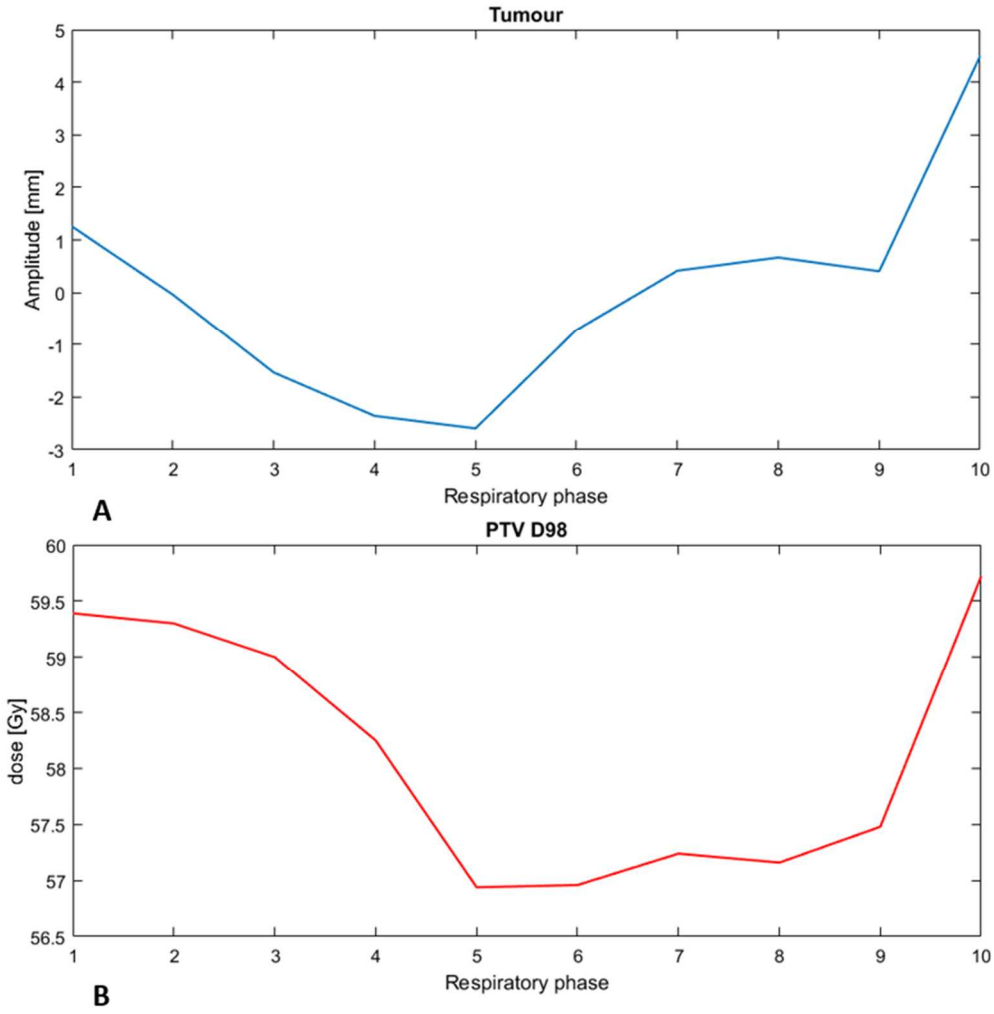

Figure 80. Breath-Patient C: A-pre-treatment tumour motion. B- PTV D98.

This result depends on the fact that Patient C is characterized by a higher range on motion on pre-treatment with respect to treatment (differently from CT/CBCT patients): for the chosen breathing cycle the pre-treatment motion is equal to 12 mm while the treatment one is equal to 7.43 mm, thus leading to dosimetric differences between the two sessions.

In addition, in order to evaluate the dosimetric changes on the whole respiratory cycle of patient C, we compute the dosimetric differences between each respiratory phase of the treatment with respect to the correspondent pre-treatment one (Figure 81). The greatest variation appears at the 0% exhale phase (10^{th} respiratory phase in Figure 81); this is due to the different tumour motion. In fact, the amplitude reached at exhale in pre-treatment is 4.98 mm and in treatment is -0.51 mm. Therefore, even if the inter-fraction component

between the pre-treatment CT and the daily image (i.e. gated MRI) was quantified to be negligible (see Table 28), for this specific breathing cycle, a variation of the respiratory motion is visible as for an irregular patient.

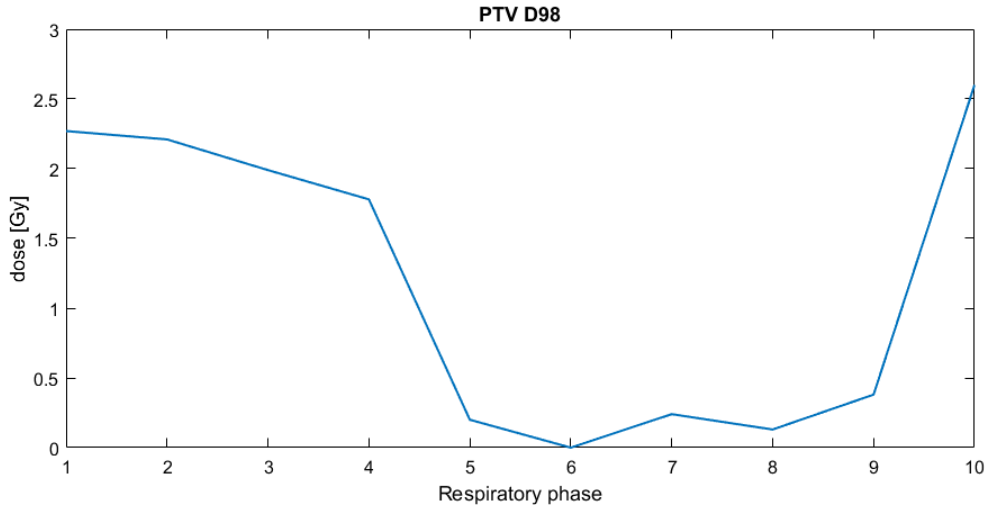

Figure 81. Correspondent phases-Patient C: difference between the treatment phase and the correspondent pre-treatment phase.

Table 32 shows indeed the mean value of each protocol requirements of the pre-treatment and treatment. The mean dose that reaches the PTV D98 in planning is equal to 56.96 Gy while in treatment is 58.14 Gy. This difference on the mean PTV D98 is due to the different range of motion (indicated above) between the considered sessions.

Table 32. Cumulative dose in pre-treatment and treatment session

	Oesophagus	**Heart**	**ITV**	**Lungs**	**Spinal cord**	**PTV**	
	Mean Dose [Gy]	D50 [Gy]	V100 [%]	Mean Dose [Gy]	Max Dose [Gy]	D2 [Gy]	D98 [Gy]
Pre-treatment	22.43	2.27	91.1	12.46	21.19	63.95	56.97
Treatment	22.9	2.1	96.05	12.24	20.32	65.03	58.14

Therefore, this preliminary analysis shows dosimetric changes according to the breathing cycle, suggesting that the need of updating the dose delivered to patients is of primary importance in the treatment of tumours in which respiratory motion is involved.

Chapter IV: Conclusions and future developments

The goal of this project is to define the groundwork to join respiration motion compensation and detailed 4D dosimetric description for tumours in the thorax region. We implement a workflow to adapt the geometric and dosimetric changes caused by respiratory motion involving MRI in treatment. In this section, we report the main conclusions reached and the future development of the method adopted, focusing first on the geometric accuracy of motion models and then on dosimetry.

Geometric evaluation

In the first part of the thesis, we have compared two motion models: Vandemeulebroucke's and Fayad's models. The use of these motion models linking fast 2D orthogonal-MRI during radiation treatment with patient-specific characterization of 4D motion derived from 4D CT, confirms that the two motion models can estimate accurately the motion of tumour and OARs during the radiation treatment. The models are tested on a CT/MRI digital phantom and then applied to two CT/CBCT and one CT/cineMRI patients.

The first comparison, regarding the reconstruction of an entire breathing cycle of the CT/MRI digital phantom, considering both the MidP volume and the 0% exhale phase as reference, confirms that each model works better with its relevant reference phase. Therefore, better performance are reached by Vandemeulebroucke's model when the MidP is considered as reference (as suggested by Vandemeulebroucke et al. 2009) with respect to the 0% exhale phase. The reason of this is inherent with the model construction, which specifically for Vandemeulebroucke et al. is based on the interpolation of the DVFs. Therefore, by considering the MidP, which represents an intermediate position of the anatomy during the breathing cycle, a better outcome is obtained. Conversely Fayad's

model works only with the 0% exhale phase as reference (as suggest by Fayad et al. 2012a). In this case, the motion is described through the use of PCA, thus needing the description of the whole range of motion and not of the only intermediate position.

For each model we tested different external and internal surrogates, derived from external acquisitions or directly from imaging data. As reported in the results session to estimate the entire breathing cycle, the diaphragm motion can be used to construct and update the model. In this case, better results are highlighted on the diaphragm rather than the heart, especially considering Vandemeulebroucke's model. A similar trend is observed when analyzing other surrogates, performing better in the region where they are extracted. This suggests that a future development can be the implementation of a ROI-based model, in which each signal extracted from a specific ROI is used to update not the whole volume but only the specific anatomical region. In this way, combing the motion of different ROIs, a more precise approximation of the anatomy can be obtained. The implementation of the ROI-based model is suggested also by the model evaluation computed on the CT/MRI digital phantom when the SIFT signal is used. In this case a worst evaluation appears on the diaphragm, tumour and heart but a lower error is visible at the lung vessels, from which the SIFT signal is extracted.

Recently, two works by Harris et al. (2016) and Stemkens et al. (2016) propose as possible solutions the inclusion of the positional information of the surrogates. Specifically, Harris et al. developed a technique to estimate volumetric cine-magnetic resonance imaging (VC-MRI) useful for inter and intra-fraction evaluation of moving targets. Three major respiratory pattern are extracted from the pre-treatment 4D MRI based on PCA and then, the 2D MRI acquired during treatment, are used to estimate the VC-MRI. Stemkens et al. propose a method to estimate 3D DVFs based on fast 2D imaging and a subject-specific motion model based on MRI. The 3D DVFs, computed through a DIR between the 4D-MRI acquired in pre-treatment, is parameterized using PCA. Then, the 3D motion is updated in treatment warping the pre-treatment MRI volume with the incoming 2D MRI slice.

A future development of our motion models could be therefore to include the motion field derived from the cine-MRI directly in the model, without the need of extracting specific surrogates.

The tests carried out on the CT/MRI digital phantom show that Vandemeulebroucke's model performance (when the reference is the MidP volume) are better than Fayad's model (with the 0% exhale phase as reference). However, since for the CT/cine-MRI patient the construction of the MidP is not possible, we compare the performance of the two models by considering the 0% exhale phase as reference. In this case, considering all the tests carried out on patients and on the CT/MRI digital phantom, better performance are reached by Fayad's model, as confirmed also by the statistical analysis. Future studies should consider a CT/cine-MRI patient dataset in which the construction of the MidP is possible, thus providing the geometric and dosimetric study of Vandemeulebroucke's model with the MidP.

However, a problem regarding Vandemeulebroucke's model with the 0% exhale as reference appears on patient C, where the different surrogate signals resulted desynchronized. In fact, Vandemeulebroucke's model requires as input both amplitude and phase information, computed through the Hilbert transform. Therefore, due to desynchronized signals, the samples acquired at a specific time on different signals belong to different respiratory phases. We expect that this problem could be also observed if the MidP would be used instead of the 0% exhale phase, thus limiting the applicability of the Vandemeulebroucke's model. This does not appear for Fayad's model, which requires as input only the amplitude value, thus not linking the range of motion to a specific respiratory phase when irregularities are present.

Moreover, as opposed to Vandemeulebroucke's model, Fayad model allows the combination of more surrogates. Different tests are performed by combining different surrogates. No improvement is pointed out by considering both coronal and interpolated sagittal pairs, thus suggesting to use the original sample at the specific timestamp to update the model. Instead, if the model is constructed with two surrogates (e.g. diaphragm and MTB) and updated only with one (e.g. diaphragm) results worsen. In general, we do not appreciate any significant difference in combing different normalized surrogates, considering the same signals in construction and updating steps. Better results may be reached by normalizing in a different way (i.e. not with respect to the biggest range of motion) the respiratory signals; but a normalization process is required because the signals describe the motion of different anatomical structures or different motion directions.

Nevertheless, the combination of different components of motion of the same surrogate appears on patient B and patient C. For patient B a little improvement on the tumour is visible when the AP and SI tumour motion (i.e. main respiratory motion directions) are combined. On patient C the geometric evaluation on tumour improves combining the SI direction with AP or RL tumour direction but not the one on the diaphragm. Therefore, for patients that breathe deeply and feature small tumours in the upper lobe of the lung, the integration of different motion direction, allowed only by Fayad's model, could improve the model outcome. Moreover, the lack on the improvement on diaphragm confirms that implementing a ROI-based model the model performances can potentially improve.

An additional analysis on new patients in which the RPM signal is available, can be accomplished as well. As a matter of fact, the study carried out on the CT/MRI digital phantom highlights a less precise result on the tumour when the RPM signal is used with respect to internal surrogates (e.g. MTB). This is because the RPM signal describes the AP motion direction and not the SI motion direction (i.e. dominant component for the respiratory motion). Ionascu et al. (2007) analysed the correlation of internal and external surrogates, founding that the SI motion is well correlated, whereas the AP motion (the one described by the RPM signals) reveals larger time shifts. Moreover, since the RPM signal of the CT/MRI digital phantom is used to create the phantom itself, analysis on new patients are required. For what concerns patient C, where the AP tumour direction is not negligible, the geometric variation on the tumour when the RPM signal is used to construct the model are bigger than the one appreciated when the MTB (AP motion direction) is used. Therefore, internal surrogates seem able to describe more precisely the anatomical motion as already confirmed in the literature.

Another difference between the models is the fact that Fayad's model requires the computation of the DVF^{-1}, but our analysis suggests that this additional step does not add appreciable errors.

Up to here, the differences between the two models have been highlighted but we can underline comparable behaviour linked to tumour position and size for the three analysed patients. In particular, for what concerns the scenarios studied we can assert that:

- if the patient (such as patient A) has a big tumour in the lower lobe of the lung, close to the diaphragm, diaphragm motion is able to describe accurately also tumour motion and vice versa;
- if the patient (such as patient B) has a small tumour in the upper lobe of the lungs, the situation is opposite. Hence, diaphragm motion is not able to describe tumour motion and vice versa. In particular, since the tumour is small, the AP direction of tumour motion cannot be neglected in the model construction;
- if the tumour is attached to the heart (is the case of patient C), tumour motion is influenced by heartbeat. Therefore, in order to better describe tumour motion, the AP and RL directions have to be taken into account, especially in addition to SI motion for Fayad's model.

However, as already suggested before, a deeper analysis is required on a larger CT/cine-MRI patient dataset, in order to provide a more accurate evaluation according to different respiratory motion patterns.

For what concerns inter-fraction variations, we quantify the motion between the planning volume and an intra-session volume. For our patient cases, negligible variations are found, therefore, no inclusion of inter-fraction changes is performed in our study. However, better performances are expected on both models if inter-fraction variations are included, especially for patients with irregular breathing patterns. Both rigid and non-rigid variations are considered for CT/CBCT patients, whereas for the CT/cineMRI patient just a quantification of the rigid displacement is performed. Therefore, the development of a DIR between MRI and CT volume (nowadays still a challenge in terms of algorithms and validation) is required for a more accurate and precise estimation of the inter-fraction variation.

Dosimetric evaluation

For quality assurance in radiotherapy, the validation of the actual dose received by the patient is crucial (Glitzner et al. 2015) because subject-specific motion can vary during the radiation treatment or between fractions (Keall et al. 2006) and the inhomogeneity in dose distribution within the tumour introduces large variations in the tumour and in the OARs dose coverage. Therefore, in the second part of our project, we create a 4D CT treatment

plan and we study the actual dose received by tumour and OARs, when the motion model is updated to obtain the actual CT volume.

For what concerns the 4D CT plan, the ITV approach, in which the ITV boundary contains the over-all tumour motion (i.e. motion between inhale and exhale phase), is used to create the plan. The IMRT dosimetric plan is optimized on the 0% exhale phase and then applied to all the other respiratory phases using the Pinnacle^3 system. For all the scenarios studied, the regular breathing during the planning phase leads to an accurate 4D CT plan. Therefore, analysing the DVH curves of each OAR at every respiratory phase, the curves are close to each other: the PTV and ITV curves are very similar with a mean variation of PTV D98 across all the phases around 0.5 Gy. A greater variation on the heart is observed due to the ITV approach, in which the ITV boundaries are fixed across all the respiratory phases but not the boundaries of the other OARs (e.g. the heart).

We also have to highlight that the organs boundaries on patients are extracted by warping the contours of the 0% exhale phase. Acceptable results are achieved with all the propagated contours. However, for patient A, a gap of 3.11 Gy appears on the maximum dose received by the spinal cord between the 0% exhale phase and the consecutive phases. We therefore perform a comparison of the OARs boundaries extracted by warping and the one extracted by the Pinnacle^3 automatic segmentation tool for patient A and for the CT/MRI digital phantom, to evaluate the performance of our warping strategy and the automatic segmentation. Differences between the two methods appear for the spinal cord and the oesophagus, as confirmed by the volume and the COM coordinates. For what concerns the spinal cord for patient A, the COM coordinates and volumes of the 0% exhale phase and the consecutive one are similar with the Pinnacle^3 segmentation tool and, in this case, the dose gap disappears. Conversely, the automatic segmentation of Pinnacle^3 system of the CT/MRI digital phantom stops around a halfway of the length of the spinal cord. This suggests the need to select the best patient-specific approach (i.e. warping vs. automatic segmentation) in order to avoid errors in the dose estimation.

The treatment plan created is then applied on Fayad's model outputs (where the 0% exhale phase is the reference) for studying the dosimetric variation between treatment and pre-treatment caused by organ motion. The tests on the CT/MRI digital phantom compare the dose model output with the dose received by the ground truth. The DVHs curves of each

OARs of the model output CT are close to the DVHs curve of the ground truth (mean variation of 0.11 Gy for the metrics recommended by the RTOG 0617). Therefore, the ability of the model to reconstruct the ground truth is confirmed by the dosimetric quantification. Moreover, depending on the surrogate used to construct the model, the dose of the different OARs improves. Using the RPM signal as a surrogate, a greater variation on the PTV D98 appears with respect to the mean difference of other surrogates (i.e. difference from the ground truth of 1.13 Gy for the RPM signal and of 0.55 Gy for other surrogates). Therefore, internal surrogates are able to describe more precisely the anatomic motion rather than external surrogates, as confirmed by the geometric evaluation. Indeed, considering the SIFT signal, that describes the motion of lung vessels, a slightly improvement is appreciated on the mean dose received by the lungs, suggesting therefore the need of an ROI-based model.

For what concerns patients, we focus the attention on the reconstruction of the inhale phase by providing the dosimetric comparison of the dosimetric plan on the model outputs with the 50% inhale phase of the planning session. All the tests carried out confirm the results found through the geometrical analysis. Therefore, the combination of coronal and interpolated sagittal samples does not show any difference with respect to the use of the only coronal or sagittal sample, as well as, in general, no differences are appreciated in the combination of different surrogates (internal or external). An exception is appreciated on patient C, where in the test in which the SI tumour motion is combined with the AP or RL motion a greater variation, especially on PTV, can be appreciated (i.e. the variation with respect to the inhale phase on PTV D98 is equal to 3.14 Gy). This result is expected since, as already explained, the geometric evaluation on the tumour improved in these correspondent tests.

So, analysing the different patient scenarios, we can assert that:

- if the patient's breath is similar in pre-treatment and treatment session (as for patient A and B), the dosimetric variation are lower or around 1 Gy;
- if the patient's breath changes between pre-treatment planning and treatment session following an irregular pattern (as for patient C), dosimetric variation are bigger. For example on the PTV D98 the maximum variations is 1.73 Gy when

only one surrogate is considered, or 3.14 Gy when different tumour directions are combined.

Cai et al. (2015) implemented a feasible method to calculate the actual dose delivered during radiation treatment for patients with significant respiratory motion. Also in their work, an accurate dose estimation was achieved testing their method on a phantom with a regular breathing pattern, while if the breath follows an irregular pattern a variation of approximatively 2 Gy on the reconstructed dose with respect to the 4D CT plan is evaluated.

For patient C, we also provide a preliminary analysis on an entire breathing cycle by testing the model on the diaphragm surrogate. The PTV D98 follows a respiratory pattern and the maximum variation appears between the exhale and inhale phase. The difference between the correspondent respiratory phases of pre-treatment and treatment shows the highest variation on the exhale phase. This variation is due to the different tumour motion between the considered breathing cycles. Even if the inter-fraction variation is quantified as negligible, this patient presents breathing irregularities, which cause a deviation of the exhale phase to the planning one, thus suggesting the need to account for this variation and to provide a geometric and dosimetric compensation, as achieved by motion models. Future studies should extend this analysis also considering the other different surrogates extracted from the cine-MRI, since the combination of the AP/RL and SI component of the tumour surrogate improves the geometric outcome of the model.

In conclusion, the results reached in our work confirm that motion models offer a solution to the problem of organ motion since they are able to adapt the geometric variation due to respiration, rising the effectiveness and safeness of the dosimetric treatment. Moreover, the fusion of MRI and radiotherapy systems enables new options for motion management, providing the fast acquisition of internal anatomy during treatment. The use of a motion model trained on a 4D CT and updated on fast cine-MRI slices, provides a method to compute the motion of tumour and OARs during radiation treatment, thus allowing the computation of the actual delivered dose. Further improvement with a ROI-based model can provide a more comprehensive adaptation of the whole volume, as similarly proposed in the recent publication by Stemkens et al. (2016).

Finally, further patient data are needed to investigate the feasibility, accuracy and usefulness of our approach and to confirm results. In particular the new patients should breathe differently between planning and treatment phase, have an entire thorax 4D CT and orthogonal 2D cine-MRI samples acquired in treatment. Future studies can also compare the results found in this work using the IMRT plan, in which the beam angles are fixed, with the one obtained with the VMAT plan, in which the gantry rotates during treatment, in order to provide an analysis on the different dosimetric plans.

Appendix A

Morphological image processing

Morphological image processing is defined as a collection of non-linear operations related to the shape or morphology of features in an image. In our work, these techniques are used to extract the boundaries of selected ROIs (e.g. tumour). The workflow followed, shown in Figure 82, is implemented using the image processing toolbox of Matlab (http://au.mathworks.com/products/image/).

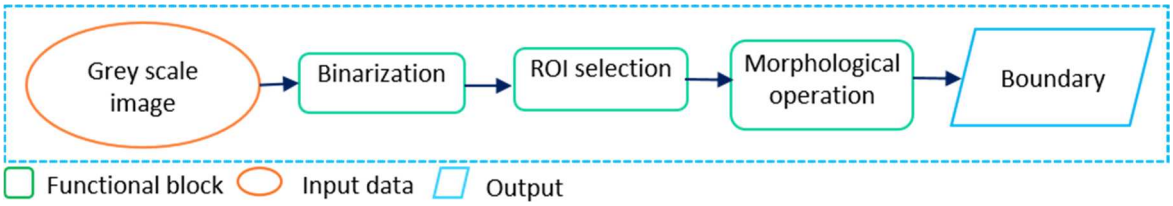

Figure 82. Morphological image processing: workflow.

The greyscale images (e.g. CT or cine-MRI) are converted into binary images (i.e. binarization). The simplest method replaces in an image with a black pixel if the image intensity is less than a fixed constant T or a white pixel if the image intensity is greater than T. Then, in order to focus the attention on a precise anatomical structure (e.g. diaphragm) a ROI is selected. To segment properly the ROI (i.e. boundary identification), two morphological operations are used: erosion and dilation. Dilation grows the selected object in an image in a way controlled by a shape element (e.g. diamond, rectangular shape) known as structuring element. Erosion, on the contrary, shrinks objects in a binary image in a way controlled by the structuring element. The combination of these operations provides to maintain the relative size of an object, deleting the imperfections (e.g. boundary discontinuity or noise). Binary opening (i.e. erosion followed by a dilation) removes the pixels in a region too small to contain the structuring element. The closing

operation (i.e. dilation followed by erosion) fills the holes smaller than the structuring element. Once the ROI is segmented, a set of information (e.g. area in pixel, COM) can be extracted.

Appendix B

Highest point of the diaphragm

The highest point of the diaphragm is extracted as suggested by Rit et al. in 2012. In this work the method is applied both to the pre-treatment CT and to the treatment dataset. Below the method implemented on the pre-treatment CT of the CT/MRI digital phantom is described in detail.

The first step is the selection of a ROI containing the diaphragm (Figure 83 A) in every slice of the CT volume. After the creation of a mask, the diaphragm boundaries are computed (Figure 83 B and Figure 83 C), applying the process explained in Appendix A. By summing each voxel along the raw from the vector, as the one shown in Figure 81 D, the highest point of the diaphragm in each frame is derived. Once the highest point is identified in every frame of the CT volume, the mean highest point is computed. The same process is applied to every respiratory phase to obtain the mean highest point of the diaphragm in each respiratory phase.

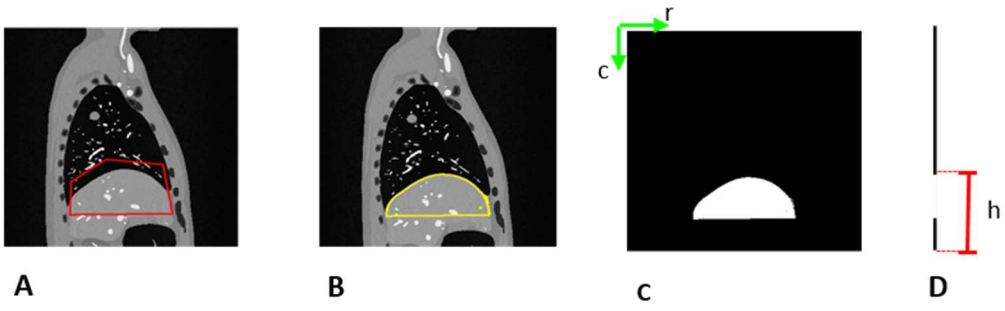

Figure 83. Diaphragm extraction: A-ROI (in red) applied for the extraction of the diaphragm. B-the boundary of the diaphragm (in yellow). C-mask containing only the diaphragm. D- summing each voxel along the raw (r) the vector shown is obtained, where h specifies the height found.

If the method is applied to the treatment dataset, the average highest point is not computed, since during treatment a real-time signal is extracted. Depending on the image type (e.g. CT or cine-MRI) and quality the morphological operation (e.g. dilation, erosion) needed to segment the diaphragm can vary, as detailed in the text.

Appendix C

Cine-MRI sample acquired at the reference phase

Below (Figure 84) we describe in detail the implemented method, considering as reference the 0% exhale phase on the CT/MRI digital phantom. Since the method is repeated for the coronal (light blue dashed box in Figure 84) and sagittal slices (red box in Figure 84), we focus the explanation on the sagittal plane. First, a sagittal slice centred in the tumour from the 0% exhale CT volume is extracted, the diaphragm is segmented (see Appendix A for details) and the area (B_s) is computed. By segmenting the diaphragm on each cine-MRI sample the vector A_s, containing the areas, is computed. The first comparison is the identification of the cine-MRI samples having the diaphragm area more similar to the reference; in this way, from the vector A_s (size(1,m), where m is the number of samples (e.g.512)), k cine-MRI samples are selected (where k<m). Then, from these k selected cine-MRI samples and from the reference slice, the highest point of the diaphragm is computed (see Appendix B), obtaining respectively the vector C_s (size(1,2)) and R_s (size(1,k)). The second comparison is the identification of the smaller distance between the selected k cine-MRI samples and the reference sagittal slice. As a result, a cine-MRI sagittal sample is selected. Once the same process is repeated for the coronal slices, if the selected cine-MRI samples are different, the sample with the smaller distance from the reference CT slice is chosen.

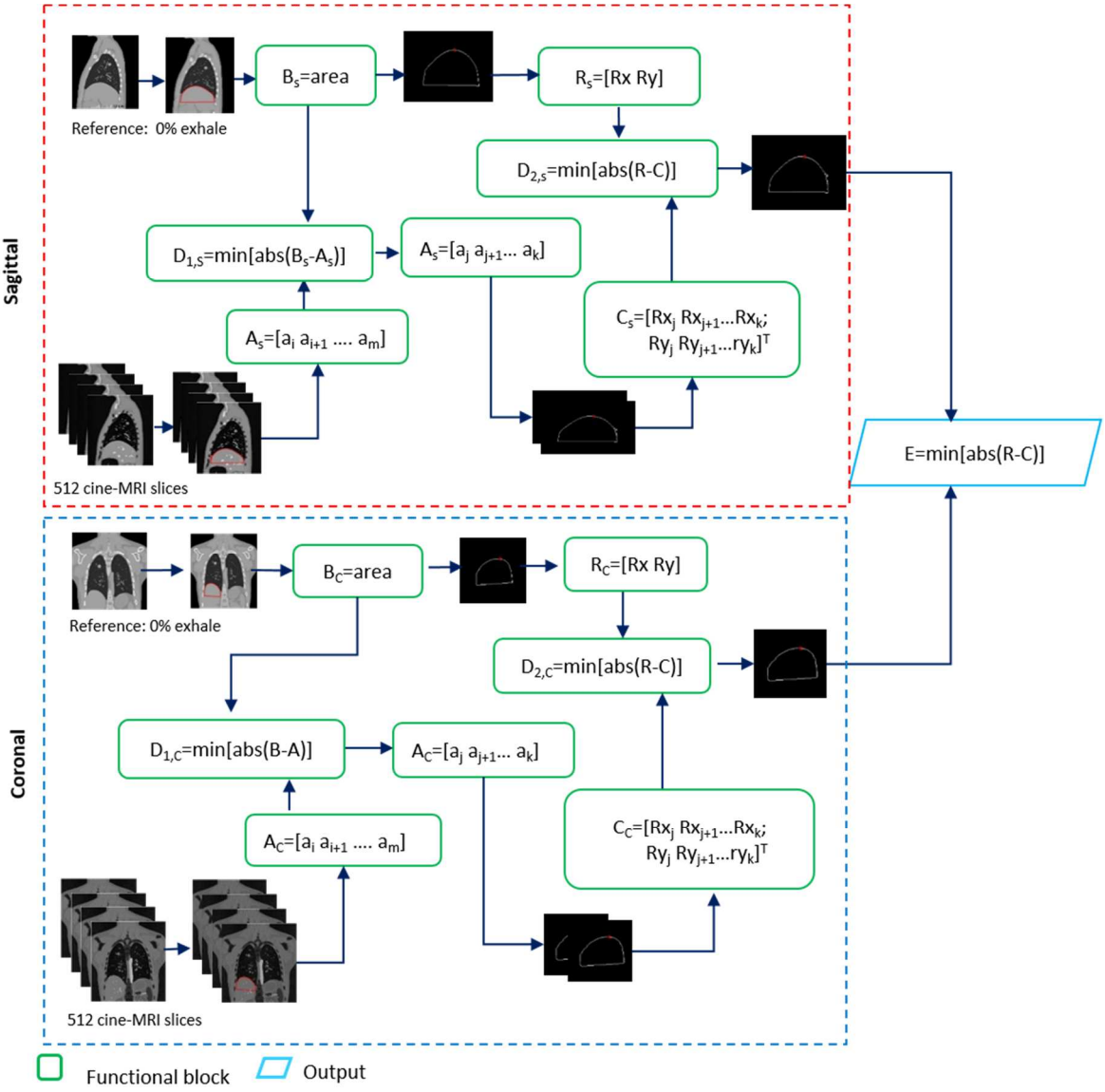

Figure 84. Reference cine-MRI: algorithm implemented for determining the 0% exhale in the cine-MRI dataset. Red box-sagittal plane. Blue box-coronal plane.

The same method is applied also considering the MidP as reference and also for patient C to identify the cine-MRI sample more similar to the gated-MRI, changing, in this case, the starting reference slice.

Appendix D

CT slices correspondent to cine-MRI samples

As a first step, the cine-MRI sample more similar to the gated-MRI (acquired at the exhale) is identified (see Appendix C). Once the coronal and sagittal sample at the exhale phase are identified (circled in orange in Figure 85) the same method is applied on both coronal and sagittal planes. So, an automatic alignment and a rigid registration between the pre-treatment 0% exhale CT and an in-room slices is performed. In this way, corresponding slices between the in-room scenario and the pre-treatment session are selected (light blue boxes in Figure 85). Following this step, the tumour COM is extracted on the 0% exhale CT volume and on the aligned volumes, identifying the sagittal and coronal CT slices with the minimum Euclidean distance from the cine-MRI samples. Finally, the slice (indicated as I in the Figure) with the lower Euclidean distance between the chosen sagittal and coronal slices is selected. The slice I is extracted on coronal and sagittal planes in all the 10 CT volumes.

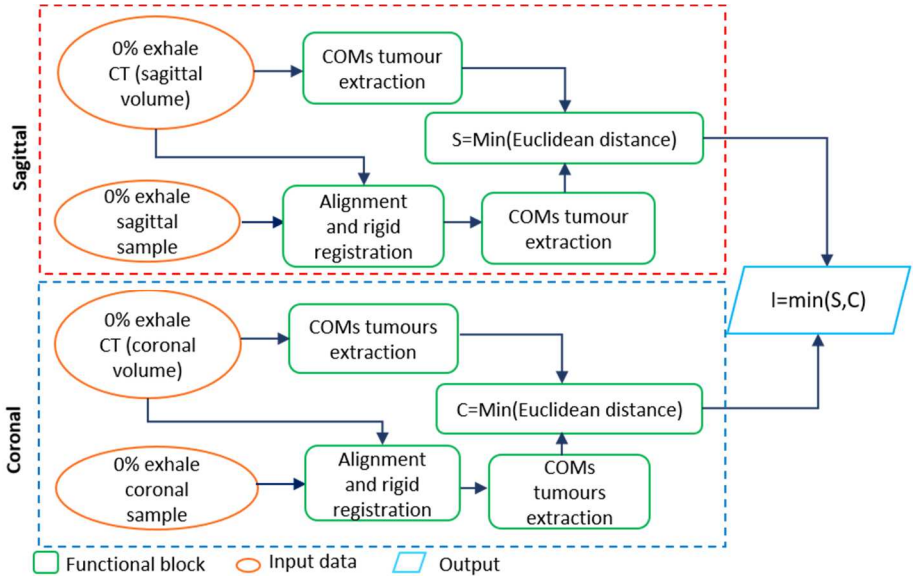

Figure 85. CT correspondent to the cine-MRI sample: schematic summary of the method leading the identification of the CT slice more similar to the cine-MRI sample.

Appendix E

Warping of tumour contours

The method implemented to obtain the tumour boundaries in treatment starting from the pre-treatment boundaries is shown in Figure 84(where the images shown belong to the patient B). First, we extract the tumour boundary of the 0% exhale phase during treatment (green box in Figure 86) and then we extract the tumour in the other respiratory phases (pink box in Figure 86). Therefore, exploiting the DVF resulting from the DIR between the 0% exhale in pre-treatment and treatment (upper blue box in Figure 86) and warping the tumour boundaries of the 0% exhale CT with the DVF^{-1}, the boundaries on the 0% exhale CBCT are obtained (upper light blue box in Figure 86). Next, a DIR between the other respiratory phases and the 0% exhale CBCT volumes is applied (lower blue box in Figure 86). Finally, by warping the contours on the 0% exhale CBCT with the DVF^{-1}, the tumour boundaries on each respiratory phase are found (lower light blue box in Figure 86).

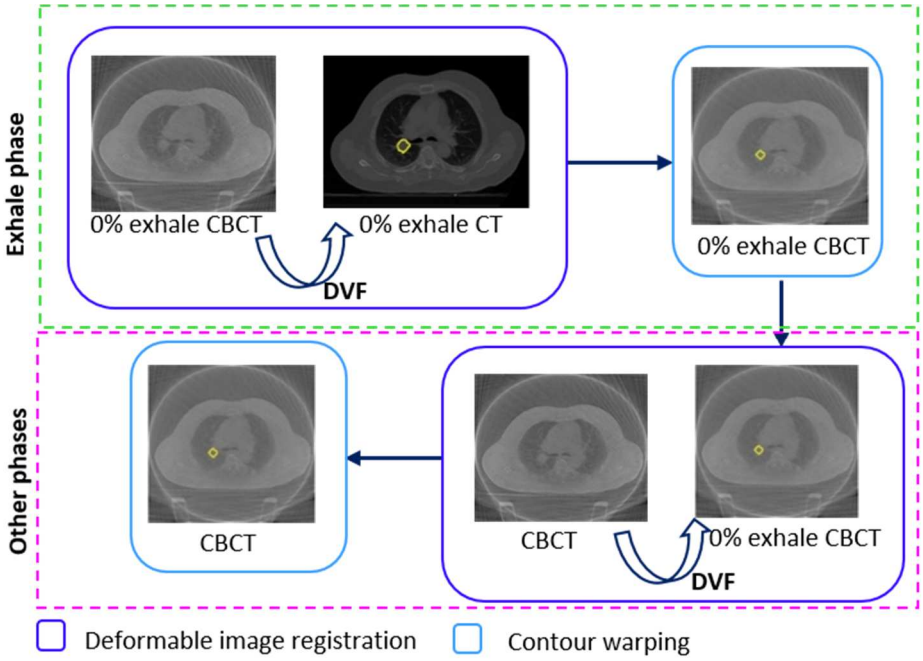

Figure 86. Tumour warping: essential step for the tumour boundaries extraction, starting from the pre-treatment data.

Bibliography

Admiraal M.A., Schuring D., Hurkmans C.W., Dose calculations accounting for breathing motion in stereotactic lung radiotherapy based on 4D-CT and the internal target volume, Radiotherapy and Oncology 86, p.55–60, 2008.

Ahnesjo A., Hardemark B., Isacsson U., Montelius A.: The IMRT information process-mastering the degrees of freedom in external beam therapy. *Phys Med Biol*, 51:R381-402, 2006.

Allaire S., Kim J.J., Breen S.L, et al. Full orientation invariance and improved feature selectivity of 3DSIFT with application to medical image analysis. IEEE Computer Society Conference on Computer Vision and Pattern Recognition Workshops. June 23-28 2008.

Aristophanous M., Rottmann J., Court L.E., and Berbeco R.I., ″EPID guided 3D dose verification of lung SBRT,″ Med. Phys. 38, 495–503 (2011).

Benedict SH., Yenice KM, Followill D., et al. Stereotactic body radiation therapy: The report of AAPM Task Group 101. Med Phys. 37: 4078-4101, 2010.

Bentel GC., Patient positioning and immobilization in radiation oncology. McGraw-Hill. 1999.

Berbeco R. I., Hacker F., Ionascu D., and Mamon H., ″Clinical feasibility of using an EPID in cine mode for image-guided verification of stereotactic body radiotherapy,″ Int. J. Radiat. Oncol., Biol., Phys. 69(1), 258–266 (2007).

Bissonnette JP., Purdie TG., Higgins JA., et al. Cone-Beam Computed Tomographic Image Guidance for Lung Cancer Radiation Therapy. Int J Radiat Oncol Biol Phys. 73: 927-934, 2009.

Bortfeld T., IMRT: a review and preview, Phys Med Biol.;51(13):R363-79, 2006.

Brahme A., Optimized radiation therapy based on radiobiological objectives. Seminars in radiation oncology, 9(1):35_47, 1999.

Brander E.D., Andrew Wu, Hungcheng Chen, Dwight Heron, Shalom Kalnicki, Krishna Komanduri, Kristina Gerszten, Steve Burton, Irfan Ahmed, Zhenyu Shopu, Abdominal organ motion measured using 4DCT, Int. J. Radiation Oncology Biol. Phys., Vol. 65, No. 2, pp. 554–560, 2006.

Cai W., Hurwitz M.H., Williams C.L., Dhou S., Berbeco R.I., Seco J., Mishra P. and John H. Lewis 3D delivered dose assessment using a 4DCT-based motion model, Medical Physics 42, 2897 (2015).

Carlsson, Utilizing Problem Structure in Optimization of Radiation Therapy, Doctoral Thesis, 2008.

Cervino LI, Du J, Jiang SB. MRI-guided tumor tracking in lung cancer radiotherapy. Phys. Med. Biol. 56: 3773-3785, 2011.

Cohen E, E. J. Bernhard and W. G. McKenna, "How does radiation kill cells?", Elsevier Science, pp. 77–83, 1999.

Colgan R., McClelland J., McQuaid D., Evans P M., Hawkes D., Brock J., Landau D. and Webb S., Planning lung radiotherapy using 4D CT data and a motion model, Phys. Med. Biol. 53**,** 5815–5830, 2008.

Constantin DE., Fahrig R., Keall P., A study of the effect of in-line and perpendicular magnetic fields on beam characteristics of electron guns in medical linear accelerators. Med Phys. 38: 4174-4185, 2011.

Crijns SP., Kok JG., Lagendijk JJ., et al. Towards MRI-guided linear accelerator control: Gating on an MRI accelerator. Phys. Med. Biol. 56: 4815-4825, 2011.

Crijns SP., Raaymakers BW., Lagendijk JJ., Proof of concept of MRI-guided tracked radiation delivery: Tracking one-dimensional motion. Phys. Med. Biol. 57: 7863-7872, 2012.

Crijns SP., Raaymakers BW., From static to dynamic 1.5T MRI-linac prototype: impact of gantry position related magnetic field variation on image fidelity. Phys. Med. Biol. 59: 3241, 2014.

Dawson LA., Sharpe MB., Image-guided radiotherapy: rationale, benefits, and limitations, Lancet Oncol 2006; 7: 848–58, 2006.

Dewey W.C, Clifton C. Ling, Raymond E. Meyn, Radiation-induced apoptosis: Relevance to radiotherapy, International Journal of Radiation Oncology Biology Physics, Volume 33, Issue 4, 1, Pages 781–796, 1995

Dobler B., Koelbl O., Bogner L., Pohl F., Direct machine parameter optimization for intensity modulated radiation therapy (IMRT) of oropharyngeal cancer – a planning study, Journal of applied clinical medical physics, Volume 10, Number 4, Fall 2009.

Elmpt W., Nijsten S., Petit S., Mijnheer B. , Lambin P., and Dekker A.,"3D in vivo dosimetry using megavoltage cone-beam CT and EPID dosimetry", Int. J. Radiat. Oncol., Biol., Phys. 73, 1580−1587 (2009).

Elmpt W., Petit S., De Ruysscher D., Lambin P., and Dekker A., "3D dose delivery verification using repeated cone-beam imaging and EPID dosimetry for stereotactic body radiotherapy of non-small cell lung cancer", Radiother. Oncol. 94, 188−194 (2010).

Eriksson D., Stigbrand T., Radiation-induced cell death mechanisms. Tumor Biol. 31:363–372, 2010.

Fallone BG., The rotating biplanar linac-magnetic resonance imaging system. Seminars in Radiation Oncology. 24: 200-202, 2014.

Fassi A., Seregni M., Riboldi M., Cerveri P., Sarrut D., Ivaldi G., Tabarelli de Fatis P., Liotta M. e Baroni G., Surrogate-driven deformable motion model for organ motion tracking in particle radiation therapy, Physics in Medicine & Biology, 2015.

Fayad H., Buerger C., Tsoumpas C., et al. A Generic Respiratory Motion Model Based on 4D MRI Imaging and 2D Image Navigators. IEEE NSS/MIC. 4058-4061, 2012.

Fayad H., Clement J.F., Pan T., Roux C., Cheze C., Rest I.e., Pradier O. and Visvikis O., Towards a Generic Respiratory Motion Model for 4D CT Imaging of the Thorax IEEE Nucl. Sci. Symp. Conf. Rec. 2009 , Page(s): 3975 – 3979, 2009.

RTOG 0617 : A randomized phase III comparison of standard- dose (60 Gy) versus High-Dose (74 Gy) Conformal radiotherapy with concurrent and consolidation carboplatin/paclitaxel +/- cetuximab (ind #103444) in patients with stage IIIA/IIIB non-small cell lung cancer, Study Team (1/19/16)

Fuangrod T., Woodruff HC., van Uytven E., et al. A system for EPID-based real-time treatment delivery verification during dynamic IMRT treatment. Med Phys. 40: 1-11, 2013.

Ge Y., O'Brein R., Keall P., Real-time tumor deformation tracking using dynamic multileaf collimator (DMLC). Int J Radiat Oncol Biol Phys. 84: S83, 2012.

Gianoli C., Riboldi M., Spadea MF., et al. A multiple points method for 4D CT image sorting. Med Phys. 38: 656-667, 2011.

Glitzner M., Crijns S.P.M, Denis de Senneville B., Kontaxis C. , Prins F.M., Lagendijk J.J.W. and Raaymakers B.W., On-line MR imaging for dose validation of abdominal radiotherapy, Phys. Med. Biol. 60, 8869–8883, 2015

Goraj A., Steven F. de Boer, Impact of the number of control points has on isodose distributions in a dynamic multileaf collimator intensity-modulated radiation therapy delivery, Medical Dosimetry 37, 412-416, 2012.

Hardemark B., Liander A., Rehbinder H., Lof J., Direct Machine parameter optimization, Pinnacle3 White Paper Nr. 4535 983 02483, Philips (2004).

Herman JM., Balter JM., Jaffray D., et al. Clinical use of electronic portal imaging: Report of AAPM Radiation Therapy Committee Task Group 58. Med Phys. 28: 712-737, 2001.

http://au.mathworks.com/products/image/

http://plastimatch.org/

http://www.fei.com/software/amira-3d-for-life-sciences/

https://www.slicer.org/

Hurwitz M., Williams C.L., Mishra P., Rottmann J., Dhou S., Wagar M., Mannarino E., Mak R. H., and Lewis J. H., ″Generation of fluoroscopic 3D images with a respiratory motion model based on an external surrogate signal,″ Phys. Med. Biol. 60, 521–535 (2014).

International Commission on Radiation Units and Measurements, «Report 36. microdosimetry,» 1983.

International Commission on Radiation Units and Measurements, «Report 50. prescribing, recording and reporting photon beam,» 1993.

International Commission on Radiation Units and Measurements, «Report 51. quantities and units in radiation protection dosimetry,» 1993.

International Commission on Radiation Units and Measurements, «Report 62. prescribing, recording and reporting photon beam,» 1999.

Ionascu D., Jiang S.B., Nishioka S., Shirato H., Berbeco R.I., Internal-external correlation investigations of respiratory induced motion of lung tumors, Med Phys., Sept 2007.

Jaffray D., Carlone MC., Milosevic MF., et al. A Facility for Magnetic Resonance–Guided Radiation Therapy. Seminars in Radiation Oncology. 24: 193-195, 2014.

Jaffray D., Image-guided radiotherapy: from current concept to future perspectives, Nat. Rev. Clin. Oncol. 9, 688-699, 2012.

Kamino Y., Takayama K., Kokubo M., et al. Development of a four-dimensional image-guided radiotherapy system with a gimbaled X-ray head. Int J Radiat Oncol Biol Phys. 66: 271–278, 2006.

Karzmark CJ., Nunan CS., Tanabe E., Medical Electron Accelerators. McGraw-Hill. 1993.

Keall P., 4-Dimensional Computed Tomography Imaging and Treatment Planning, Seminars in Radiation Oncology, Vol 14, No 1:pp 81-90, 2004.

Keall P., Barton M., Crozier S., The Australian magnetic resonance imaging-linac program. Seminars in Radiation Oncology. 24: 203-206, 2014.

Keall P., Kini VR., Vedam SS., Motion adaptive x-ray therapy: a feasibility study. Med Phys. 46:1-10, 2001.

Keall P., Mageras GS., Balter JM., et al. The Management of Respiratory Motion in Radiation Oncology. Med Phys. 33:3874-3900, 2006b.

Keall P. J., Kini VR., Vedam SS. and Mohan R., "Potential radiotherapy improvements with respiratory gating," Australas. Phys. Eng. Sci. Med. , 2002.

Keall P., Vedam S., George R., Bartee C., Siebers J., Lerma Fritz, Weiss E. and Chung T., The clinical implementation of respiratory gated intensity-modulated radiotherapy, Medical Dosimetry, Vol. 31, No. 2, pp.152-162, 2006a.

Kilby W., Dooley JR., Kuduvalli G., et al. The CyberKnife® Robotic Radiosurgery System in 2010. Technology in Cancer Research and Treatment. 9: 433-452, 2010.

Kim T., Pollock S., Lee D., O'Brien R. and Paul Keall, Audiovisual biofeedback improves diaphragm motion reproducibility in MRI, Med Phys.; 39(11): 6921–6928, 2012.

Kolling S., Oborn B., Keall P.. Impact of the MLC on the MRI field distortion of a prototype MRI-linac. Med Phys.40:121705, 2013.

Kooy H.M et al, "Monitor unit calculations for range-modulated spread-out Bragg peak fields" Phys. Med. Biol. 48 2797-2808, 2003.

Korreman SS. Motion in radiotherapy: photon therapy. Phys. Med. Biol. 57: 161–191, 2012.

Kubo HD, Hill BC. Respiration gated radiotherapy treatment: A technical study. Phys. Med. Biol. 41:83-91, 1996.

Lagendijk JJW., Raaymakers BW., van Vulpen M. The magnetic resonance imaging-linac system. Seminars in Radiation Oncology. 24:207-209, 2014.

Langen KM., Jones DT. Organ motion and its management. Int J Radiat Oncol Biol Phys. 50:265-78, 2001.

Lof J., Rehbinder H., McNutt T., Johnson S., P^3IMRT: Inverse Planning Optimization, Pinnacle^3 White Paper No. 4535 983 02479, 2003.

Lu, W., Low, D.A., Parikh, P.J., Nystrom, M.M., El Naqa, I.M., Wahab, S.H., Handoko, M., Fooshee, D., Bradley, J.D., Comparison of spirometry and abdominal height as four-dimensional computed tomography metrics in lung. Medical Physics 32, 2351–2357, 2005.

Mackie T. R, Bielajew A. F., Rogers D. W. O, Battista J.J, Generation of photon energy deposition using the EGS Monte Carlo code, Phys. Med. Biol., Vol. 33, No 1, 1-20, 1988.

Mackie T.R, Reckwerdt P.J., Gehring M. A., Holmes T.W., Kubsad S.S., Thomadsen B.R., Sanders C.A., Paliwal B.R., Kinsella T.J., Clinical implementation of the convolution/superposition method, Proceedings of the Xth ICCR, 322-235 (1990).

Mackie T.R., Ahnesjoe A., Dickof P., Snider A., Development of a convolution/superposition method for photon beams. Use of Comp. In Rad. Ther., 107-110 (1987).

Maintz JBA., Viergever MA., A survey of medical image registration. Medical Image Analysis. 2: 1-36, 1998b.

Maintz JBA., Viergever MA., An overview on Medical Image Registration Methods. Utrecht University Repository, 1998a.

Mazur T., Fischer-Valuck B., Wang Y., Yang D., Mutic S., and Li H., SIFT-based dense pixel tracking on 0.35 T cine-MR images acquired during image guided-radiation therapy with application to gating optimization, Medical Physics 43, 279 (2016).

McClelland J.R., Hawkes D.J., Schaeffter T., King A.P., Respiratory motion models: A review. Medical Image Analysis 17 , 2013.

McKinnon G. C. and Bates R.H.T., Towards imaging the beating heart usefully with a conventional CT scanner, IEEE Trans. Biomed. Eng. BME-28(2), 123–127 (1981).

McNutt T., "Dose calculations - collapsed cone convolution superposition and delta pixel beam," Pinnacle3 White Paper, (2007).

McRobbie DW., Moore EA., Graves MJ., et al. MRI: from picture to proton. New York: Cambridge University Press, 2006.

Menard C., van der Heide U. Introduction: Systems for Magnetic Resonance Image Guided Radiation Therapy. Seminars in Radiation Oncology. 24, 2014.

Murphy MJ., Dieterich S. Comparative performance of linear and nonlinear neural networks to predict irregular breathing. Phys. Med. Biol. 51: 5903-5914, 2006.

Mutic S., Dempsey JF., The ViewRay System: Magnetic Resonance – Guided and Controlled Radiotherapy. Seminars in Radiation Oncology. 24: 196-199, 2014.

Oborn B., Metcalfe PE., Butson MJ., et al. Monte Carlo characterization of skin doses in 6MV transverse field MRI linac systems: Effect of field size, surface orientation, magnetic field strength and exit bolus. Med Phys. 37:5208-5217, 2010.

Oborn B., Metcalfe PE., Butson MJ. Electron contamination modeling and skin dose in 6MV longitudinal field MRIgRT: Impact of the MRI and MRI fringe field. Med Phys. 39:874-890, 2012.

Paganelli C., Peroni M., Pennati F., Baroni G., Summer P., Bellomi M., Riboldi M. Scale invariant feature transform as feature tracking method in 4D imaging: A feasibility study,. 34th Annual International Conference of the IEEE (EMBS) 2012.

Paganelli C., Peroni M., Baroni G., Riboldi M., Quantification of organ motion based on an adaptive image-based scale invariant feature method, Med Phys., 40(11):111701, 2013a.

Paganelli C., Peroni M., Riboldi M., Sharp GC., Ciardo D., Alterio D., Orechhia R.m, Varoni G., Scale invariant feature transform in adaptive radiation therapy: a tool for deformable image registration assessment and re-planning indication, Phys Med Biol.; 58(2):287-99, 2013b.

Paganelli C., Seregni M., Fattori G., Summers P., Bellomi M., Baroni G., Riboldi M. Magnetic resonance imaging-guided versus surrogate-based motion tracking in liver radiation therapy: A prospective comparative study International Journal of Radiation Oncology Biology Physics, 91: 840-848, 2015a.

Paganelli C., Summers P., Bellomi M., Baroni G. and Riboldi M., Simulation of abdominal MRI sequences in a computational 4D phantom for MRI-guided radiotherapy Computer Assistance in Radiation Therapy Workshop, MICCAI, Munich, October 9th 2015b.

Paganelli C., Summers P., Baroni G., Bellomi M. and Riboldi M., A global motion model for a daily 4DMRI, IEEE International Symposium on Biomedical Imaging, Brooklyn, NY, 16-19 April 2015c.

Pinnacle, [online]. Available: www.medical.philips.com

Pinnacle, [online]. Available: http://www.usa.philips.com/healthcare/solutions/radiation-oncology/radiation-treatment-planning

Plathow C., Leys S., Fink C., Puderbach M., Hosch W., Schm Ahl A, Debus J., Kauczor H., Analysis of intrathoracic tumor mobility during whole breathing cycle by dynamic MRI, International Journal of Radiation Oncology, Elsevier Inc 2004.

Raaymakers BW., Lagendijk JJW., Overweg J., et al. Integrating a 1.5 T MRI scanner with a 6 MV accelerator: proof of concept. Phys. Med. Biol. 54: 229–37, 2009.

Rietzel E., Chen GT.. Improving retrospective sorting of 4D computed tomography data. Phys. Med. Biol. 33:377-379, 2006.

Rit S., Van Herk M., Zijp L.B.Sc. and Sonke J.J., Quantification of the Variability of Diaphragm Motion and Implications for Treatment Margin Construction, Int J Radiat Oncol Biol Phys. 82(3):399-407, 2012.

Sarrut D., Deformable Registration for Image-Guided Radiation Therapy. Med Phys. 1–38. 2006.

Scarfe W. C., Farman A. G., What is Cone-Beam CT and How Does it Work?, Dent Clin N Am 52 (2008).

Shackleford J.A., Kandasamy N., Sharp G.C, On developing B-spline registration algorithms for multi-core processors, Physics in Medicine and Biology, Vol 55, No 21, pp 6329-6351, Nov 7, 2010.

Shieh C-C., Kipriditis J., O'Brien B., Kuncic Z., Keall P.J., Image quality in thorachic 4D cone-beam CT: A sensitivity analysisof respiratory signal, binning method, reconstruction algorithm, and projection angular spacing, Medical Physics, Vol.41, No.4, April 2014.

Shirato H., Shimizu S., Kunieda T., et al. Physical aspects of a real-time tumor-tracking system for gated radiotherapy. Int J Radiat Oncol Biol Phys. 48: 1187–1195, 2000.

Stemkens B., Rob HN., Tijssen R.H.N., Denis de Senneville B., Jan J W Lagendijk J.J.W and Van den Berg C.A.T, Image-driven, model-based 3D abdominal motion estimation for MR-guided radiotherapy, Phys. Med. Biol. 61 5335–5355 (2016).

Tryggestad E., Flammang A., Hales R., et al. 4D tumor centroid tracking using orthogonal 2D dynamic MRI: Implications for radiotherapy planning. Med Phys. 40: 091712. 2013a.

Tsui B.M.W, 4D XCAT phantom for multimodality imaging research, Med Phys. 2010.

Turner, Atoms, Radiation, and Radiation Protection, 2007.

Vandemeulebroucke J., Kybic J., Clarysse P. and Sarrut D., Respiratory Motion Estimation from Cone-Beam Projections Using a Prior Model, Springer-Verlag Berlin Heidelberg 2009.

Varian, [online]. Available: http://www.varian.com/us/oncology/radiation_oncology/linac/

Vedam S.S., Keall P.J, Kini VR, Mostafavi H., Shukla HP, Mohan R, Acquiring a four-dimensional computed tomography dataset using an external respiratory signal. Phys Med Biol. 48(1):45-62, 2003a.

Vedam SS., Kini VR., Keall PJ., et al. Quantifying the predictability of diaphragm motion during respiration with a noninvasive external marker. Med Phys. 30:505–513, 2003b.

Veiga C., Lourenco A. M., Mouinuddin S., van Herk M., Modat M., Ourselin S., Royle G., McClelland J., Toward adaptive radiotherapy for head and neck patients: Uncertainties in dose warping due to the choice of deformable registration algorithm, Medical Physics 42, 760 (2015).

Webb S., The physical basis of IMRT and inverse planning, The British Journal of Radiology, 76 (2003), 678–689, 2003.

Withers, Biologic Basis for Altered Fractionation Schemes, Cancer 552086-2095, 1985.

Wolthaus JW., Sonke JJ., van Herk M., and Damen EM., Reconstruction of a time-averaged midposition CT scan for radiotherapy planning of lung cancer patients using deformable registration, Med. Phys. 35, 3998 (2008).

Wong, Sharpe MB., Jaffray D., et al. The use of active breathing control (ABC) to reduce margin for breathing motion. Int J Radiat Oncol Biol Phys. 44:911-919,1999.

Xing L., Siebers J. and Paul Keall, Computational Challenges for Image-Guided Radiation Therapy: Framework and Current Research, Semin Radiat Oncol 17:245-257, 2007.

Xing L., Thorndyke B., Schereibmann E., Yong Yang, Tian-Fang, Gwe-Yakin, Luxton G., Koong A., Overview of image-guided radiation therapy, Med Dosim 31(2):91-112, 2006

Yu CX, Tang G. Intensity-modulated arc therapy: principles, technologies and clinical implementation. Phys. Med. Biol. 56: R31–R54, 2011.

Zeng R., Fessler JA., Balter JM., et al. Iterative sorting for four-dimensional CT images based on internal anatomy motion. Med Phys. 5:917–926, 2008.

Acknowledgments

At the end of our university course, we would like to thank all the people who help us during these years, especially in the last months.

First of all, Prof. Marco Riboldi for giving us the opportunity to work at this project, for his willingness and, above all, for the chance to undertake part of the thesis in Sydney.

The second thank is for Prof. Paul Keall, who hosts us at the University of Sydney, for his support and for his valuable advices whenever we had a problem to overcome.

We'd like also to thank Dr. Chiara Paganelli who supports and follows us, with attention and patience, step by step, also when we were in the other part of the world, sharing with us the best and worst moments.

Another thank is for all the researchers of the Australian lab, especially to Brendan Whelan, not directly involved in this work, that advised and helped us.